amU
Aix Marseille Université

NNT : à remplir

THÈSE DE DOCTORAT

Soutenue à Aix-Marseille Université
le 26 novembre 2024 par

Kishore IYER

Looking for anyons in the fractional quantum Hall effect

Discipline
Physique et Sciences de la Matière

Spécialité
Physique Théorique et Mathématique

École doctorale
ED 352 Physique et Sciences de la Matière

Laboratoire/Partenaires de recherche
Centre de Physique Théorique, UMR 7332 ; CNRS

Composition du jury

Christophe Mora Professeur Laboratoire MPQ, Univ. Paris Cité	Rapporteur
Anne ANTHORE Professeure C2N, Univ. Paris Saclay, Univ. Paris Cité	Rapporteure
Benoît DOUÇOT Directeur de recherche LPTHE, CNRS	President de jury
Thibaut JONCKHEERE Directeur de recherche CPT, CNRS	Directeur de thèse
Jérôme RECH Chargé de recherche CPT, CNRS	Codirecteur de thèse
Thierry MARTIN Professeur CPT, Aix-Marseille Université	Membre invité

CPT

cnrs

Affidavit

I, undersigned, Kishore Narayanan Iyer, hereby declare that the work presented in this manuscript is my own work, carried out under the scientific supervision of Thibaut Jonckheere, Jérôme Réch, Benoît Grémaud, and Thierry Martin, in accordance with the principles of honesty, integrity and responsibility inherent to the research mission. The research work and the writing of this manuscript have been carried out in compliance with both the French national charter for Research Integrity and the Aix-Marseille University charter on the fight against plagiarism.

This work has not been submitted previously either in this country or in another country in the same or in a similar version to any other examination body.

Marseille, 28 September 2024.



Publications and conferences

Articles related to this thesis

1. K. Iyer, F. Ronetti, B. Grémaud, T. Martin, J. Rech, and T. Jonckheere, "Finite width of anyons changes their braiding signature", *Physical Review Letters*, 132, 216601 (2024).
2. K. Iyer, T. Martin, J. Rech, and T. Jonckheere, "Quasiparticle Andreev reflection in the Laughlin fractions of the fractional quantum hall effect", *Physical Review B*, 108, 155404 (2023).
3. K. Iyer, J. Rech, T. Jonckheere, L. Raymond, B. Grémaud, and T. Martin, "Colored delta-T noise in fractional quantum Hall liquids", *Physical Review B*, 108, 245427, (2023).
4. K. Iyer, F. Ronetti, B. Grémaud, T. Martin, J. Rech, and T. Jonckheere, "Photoassisted shot noise probes multiple charge carriers in the fractional quantum Hall effect", arXiv:2502.15909, *manuscript submitted for publication.*
5. K. Iyer *et al.*, "Generalized Abelian anyon collider", *manuscript in preparation.*

Additional research during the course of the thesis

6. K. Iyer, A. Ratnakar, S. Rao, and S. Das, "Multiple species of Majorana zero modes in reconstructed quantum Hall edge", *Physical Review B 110, L161302* (2024).
7. K. Iyer, A. Ratnakar, A. Mukhopadhyay, S. Rao, and S. Das, "Spontaneous fractional Josephson current in parafermion junctions", *Physical Review B*, 107, L121408 (2023).

Participation in conferences and schools

1. Journées de la Matière Condensée, Marseille, France, October 2024.
   Talk: K. Iyer, A. Ratnakar, S. Rao, S. Das. *Multiple species of Majorana zero modes in reconstructed quantum Hall edges*

2. Topological Matter School, San Sebastian, Spain, August 2024.
   Poster: K. Iyer. *Fusion multiplicity from tunneling conductance of non-Abelian anyons*

3. Topological Order: Anyons and Fractons in Les Houches, France, April 2024.
   Poster: K. Iyer. *Probing fusion channels in non-Abelian fractional quantum Hall effect*

4. GDR Quantum Mesoscopic Physics – Plenary Session in Aussois, France, November 2023
   Talk: K. Iyer, F. Ronetti, B. Grémaud, T. Martin, J. Rech, T. Jonckheere. *Finite width of anyons changes braiding signatures*

5. Rencontres de Moriond – Mesocopic Physics, in La Thuile, Italy, March 2023.
   Poster: K. Iyer, T. Martin, J. Rech, T. Jonckheere. *Quasiparticle Andreev reflection in Laughlin fractional quantum Hall effect*

6. Topological Quantum Matter: theory and applications in Genova, Italy, March 2022.
   Short talk: K. Iyer, A. Ratnakar, S. Rao, S. Das. *Electrically induced fractional Josephson effect of parafermions*

To my amma, Apeetha,
for her unconditional love.

Acknowledgements

It is hard to believe that it is time to write another acknowledgment – this one really snuck up on me.

First, I would like to extend my deepest gratitude to all the members of the Nanophysics team at CPT. Their contributions were invaluable for my thesis, and the collaborative environment of the team greatly enhanced my experience. I thank Thibaut Jonckheere, for all the insightful discussions. He was always ready to listen to whatever ideas I brought up, offering both encouragement and constructive criticism that helped me progress. I am grateful to Thierry Martin for nominating me for this PhD – our discussions, especially at the beginning of my time in Marseille, played a crucial role in shaping the years that followed. I thank Jérôme Réch for his keen eye, a strong sense of rigor, and wizardry with integrals – I can only hope to have absorbed a fraction of those! It was always a pleasure to discuss with Benoît Grémaud, Flavio Ronetti, and Laurent Raymond, whose openness and enthusiasm made for enlightening conversations. I especially remember the group discussions with the entire team, which were as fun as they were productive.

I was fortunate to collaborate regularly with our experimental colleagues at Gwendal Fève's group, who has a remarkable ability to explain experiments in a manner that theorists could follow. I am grateful for illuminating discussions with Ulf Gennser, Melanie Ruelle, Elric Frigerio, and Gerbold Ménard. I am deeply grateful to my academic mentor, Sumathi Rao, for introducing me to condensed matter physics, and to Sourin Das for his unique perspectives. Their guidance over the years has been truly invaluable. I sincerely thank Sunil Patwardhan for his mentorship during my high school years and for inspiring me to pursue science.

This thesis does mark a milestone in my life, and getting through these years was much more than just physics. I have been truly privileged to have people who stood by me during tough times and made the good moments even better.

I want to thank my colleagues at CPT – Asier, Mathilde, Gloria, Toto, Willem, Antoine, Sami, Kenza, Sophie, Aurélien, Rémy, Christian, Siméon, Sucheta, Juliette, Valentin, Arthur, Patricia, Louis, and many others – for making everyday life in Marseille so much more enjoyable. From daily lunches, hikes in the Calanques to hangouts at La Plaine and spirited volleyball games, I'm grateful for the time I've spent with you all. In France, where the labs typically empty out by 6pm, I was lucky to find fellow night owls – Alex, Yohann, Noé, and Vijay. Those sandwiches and late-night hangouts are something I looked forward to, and will always remember. Special mention to Alex for never hesitating

to wander down a dodgy street or to explore an abandoned building with me. Noé and Bruno, thank you for being pleasant office mates, and for the unforgettable times at conferences. And to Amulya, who joined us later – thank you for bringing *Dilli vaale* vibes into the office, and for our earlier fruitful collaborations. Yogesh, Chandrashekhar and Nilanjana, thank you for the delicious food, long conversations, and many strolls on the streets of Marseille.

I am incredibly grateful to Sanchit, Renuka, Pradhan, Sai, Swarali, Rohin, Shrey, Adithya, JK, and Khalak who, despite being scattered across countries and continents, were just a screen away. The calls that started as an effort to lift Sai's spirits ended up filling all our lives (well, at least mine) with warmth and laughter. Shoutout to Shrey for always showing up and keeping the calls alive! Pradhan, Sai, Khalak, Govindarajan, Srikrishna, and Adarsh – our trips and celebrations together have been nothing short of legendary. From push-ups in the streets of Paris and narrowly escaping a scam in Florence, to Diwali in Marseille, every moment with you guys has been an adventure! I'm also grateful to Sabuj, Keshav, Diksha, Aman, Ashish, Ankit, and Numash for the wild hangouts in Bangalore. Whether it was the late-night escapades or catching up after a long time, those times will always be special to me. Vicky, Jayant and Karthic *anna*, I'm grateful for the wisdom you've shared with me over the years. To Devang, Bhavesh, Jigar, and Swastik – our experiences together are countless, and each one has shaped me significantly. Thank you for being the ones I can always count on.

Khalak, thank you for everything. For your unwavering support and for braving countless inconvenient flights – I promise I'll make it up to you! Most of all, for your contagious enthusiasm. I'm so lucky to have you in my life, and I can't wait for our future together. To my father, Narayanan – thank you *appa* for setting standards I always look up to. Your commitment to principles and limitless patience never cease to amaze me. I am grateful for the reassurance you have given me in the toughest times. Finally, to my mom and first teacher, Apeetha – your grit continues to inspire me every day. Thank you *amma* for planting the first seeds of my interest in science, for your guidance in forging my own path, and for always motivating me to pursue my interests. And, of course, for waking me up each morning with a smile. I miss you every single day.

Abstract

Anyons are particles intermediate between bosons and fermions, characterized by fractional braiding phase and predicted to exist in two spatial dimensions. These exotic particles have found a solid experimental footing in the fractional quantum Hall effect (FQHE). Fundamental interest and potential technological applications have fuelled intense pursuit of anyons in the FQHE in the past several decades. While the fractional charge of anyons is experimentally verified since the 90s, the more exotic scaling dimension (signifies strength of anyon correlations) and fractional braiding phase are only recently beginning to be understood. However, the most convincing agreement between theory and experiment is restricted to the simplest Laughlin fractions of the FQHE. Indeed, experiments fail to reliably measure all the predicted charges in non-Laughlin states like $\nu = 2/3$ or $2/5$. Perhaps the most glaring issue concerns the braiding phase of anyons: the *anyon collider* experiment at $\nu = 2/5$ *qualitatively* disagrees with theory.

This thesis aspires to fill in these gaps in the understanding of anyons in non-Laughlin FQHE. We theoretically calculate quantities measurable in contemporary experiments, such as current and noise, that could unambiguously characterize the topological properties of anyons in general Abelian FQHE, while being mindful of complications that might cause deviations from simple theoretical predictions.

We identify photo-assisted shot noise (PASN) as a robust probe of fractional charges when different types of charges coexist in FQHE, as is true in non-Laughlin states. We illustrate the inadequacy of traditional probes in the latter scenario and demonstrate the sensitivity of PASN to all the charges under standard experimental conditions. Similarly, our exploration of Andreev reflection-like processes of fractionally charged anyons offers insights into the transport properties of fractional charges, shedding light on recent and older experiments. We also study a temperature biased-noise in general Abelian FQHE, which we demonstrate to distinguish anyonic scaling dimensions from non-anyonic ones.

Investigating the braiding phase of anyons, we show how time-domain braiding processes behave in a general Abelian FQHE. This allows us to generalize the theory of the anyon collider to address any Abelian FQHE state. Leveraging the generality of the latter model, we look for ingredients that could explain the discrepancies in $\nu = 2/5$ FQHE. We are led finally to the finite width of anyons, an aspect often overlooked. We show that the finite width of anyons, even extremely small, has a dramatic impact on the braiding signatures. Taking the latter into account resolves the discrepancy by quantitatively explaining the anyon collider at $\nu = 2/5$.

Résumé

Les anyons sont des particules intermédiaires entre les bosons et les fermions, caractérisées par une phase de d'échange fractionnaire. Ces particules exotiques ont trouvé une base expérimentale solide dans l'effet Hall quantique fractionnaire (FQHE). L'intérêt fondamental et les applications technologiques potentielles ont alimenté une recherche intense des anyons dans l'effet Hall quantique fractionnaire au cours des dernières décennies. Alors que la charge fractionnaire des anyons est vérifiée expérimentalement depuis les années 90, la dimension d'échelle plus exotique et la phase de tressage fractionnaire ne commencent que récemment à être comprises. Cependant, l'accord le plus convaincant entre la théorie et l'expérience se limite aux fractions de Laughlin les plus simples de la FQHE. En effet, les expériences ne parviennent pas à mesurer de manière fiable toutes les charges prédites dans les états non-Laughlin comme $\nu = 2/3$ ou $2/5$. Le problème le plus flagrant concerne peut-être la phase de tressage des anyons : l'expérience *anyon collider* à $\nu = 2/5$ n'est pas en accord avec la théorie même qualitativent.

Cette thèse vise à combler ces lacunes dans la compréhension des anyons dans FQHE non-Laughlin. Nous recherchons des quantités mesurables expérimentalement, telles que le courant et le bruit, qui pourraient caractériser sans ambiguïté les propriétés topologiques des anyons dans l'FQHE abélienne générale, tout en tenant compte des complications qui pourraient causer des déviations par rapport aux prédictions théoriques simples.

Nous identifions le bruit de grenaille photo-assisté (PASN) comme une sonde robuste des charges fractionnaires lorsque différents types de charges coexistent dans FQHE, comme c'est le cas dans les états non-Laughlin. Nous illustrons l'inadéquation des sondes traditionnelles dans ce dernier scénario et démontrons la sensibilité du PASN à toutes les charges dans des conditions expérimentales standard. Notre exploration des processus de type réflexion d'Andreev d'anyons chargés fractionnellement donne un aperçu des propriétés de transport des charges fractionnaires, en mettant en lumière des expériences récentes et plus anciennes. Nous étudions également un bruit biaisé par la température dans la FQHE abélienne générale, dont nous démontrons qu'il permet de distinguer les dimensions d'échelle anyoniques de celles qui ne le sont pas.

En étudiant la phase de tressage des anyons, nous montrons comment les processus de tressage dans le domaine temporel se comportent dans une FQHE abélienne générale. Cela nous permet de généraliser la théorie du collisionneur d'anyons pour traiter n'importe quel état FQHE abélien. En tirant parti de la généralité de ce dernier modèle, nous recherchons des ingrédients qui pourraient expliquer les désaccords dans $\nu = 2/5$ FQHE. Nous sommes

finalement conduits à la largeur finie des anyons, un aspect souvent négligé. Nous montrons que la largeur finie des anyons, même extrêmement petite, a un impact dramatique sur les signatures de tressage. sur les signatures de tressage. La prise en compte de cette dernière nous permet d'expliquer quantitativement le collisionneur d'anyons à $\nu = 2/5$. La résolution de ce désaccord est une résultat important de cette thèse.

Résumé étendu en Français

Introduction

La matière condensée, qui se compose d'un assemblage dense d'atomes et d'électrons, présente une variété de propriétés physiques qui se traduisent par différentes *phases* de la matière. Celles-ci comprennent les solides et les liquides ordinaires, ainsi que les supraconducteurs ou superfluides exotiques, entre autres. Les propriétés physiques des différentes phases dépendent non seulement des particules constitutives et de leurs interactions, mais aussi de leur disposition dans le matériau. Les symétries, c'est-à-dire les transformations qui laissent le système inchangé, constituent un aspect crucial de cet arrangement. Par exemple, l'eau présente une symétrie de translation continue, où les molécules sont réparties de manière aléatoire, tandis que la glace présente une symétrie de translation discrète en raison de sa structure cristalline. Le passage de l'eau à la glace implique des changements abrupts dans les symétries et les propriétés locales telles que la densité. Landau a lancé l'idée que les symétries caractérisent complètement les phases de la matière et que les transitions entre les phases impliquent une rupture de symétrie et des changements abrupts dans les propriétés locales du système. En raison de son succès phénoménal, les physiciens ont cru pendant une grande partie du 20e siècle que le cadre de Landau capturait tous les ordres et transitions de phase possibles dans les systèmes de matière condensée.

La découverte de l'effet Hall quantique (QHE) a fait voler en éclats le paradigme de Landau sur la matière condensée. L'effet Hall quantique consiste en des électrons confinés dans un plan 2D soumis à un fort champ magnétique. Alors que l'effet Hall classique se traduit par une évolution linéaire de la résistivité de Hall (R_H) en fonction du champ magnétique, l'effet Hall quantique se caractérise par une R_H quantifiée à des valeurs entières ou fractionnaires du quantum de résistance. En effet, lorsque le champ magnétique est modifié progressivement, R_H reste constant aux valeurs quantifiées avant de passer brusquement à la valeur quantifiée suivante. Ces sauts abrupts rappellent les transitions de phase, ce qui suggère que les QHE de différents R_H constituent des phases distinctes de la matière. Cependant, contrairement au paradigme de Landau, les symétries du système restent les mêmes dans tous les états QHE.

Cette observation a conduit à l'idée de l'ordre *topologique*. En effet, si les différents états QHE ont des symétries identiques, ils diffèrent par leurs propriétés *topologiques*. On peut considérer que la topologie en mathématiques a commencé avec la résolution

par Euler du problème des sept ponts de Königsberg. Ce dernier problème cherchait un chemin traversant exactement une fois chacun des sept ponts de la ville. Euler a prouvé qu'un tel chemin n'existe pas, en soulignant que le résultat ne dépend pas de détails tels que la longueur des ponts ou les distances entre eux, mais uniquement des connexions entre les différentes parties de la ville.

De même, en physique, certaines propriétés des matériaux ne dépendent pas de détails tels que la distribution des atomes et des électrons ou les interactions précises entre eux, mais de propriétés globales, non locales, telles que les lacunes dans la structure de bande du système ou le nombre de trous dans le collecteur sur lequel vit le système. Dans le cas de l'effet Hall quantique entier (R_H quantifié en valeurs entières du quantum de résistance), les propriétés topologiques sont capturées par le nombre de Chern, une propriété non locale du système qui change en même temps que le R_H quantifié. Le nombre de Chern est indépendant des symétries mais dépend plutôt de la façon dont la phase des états quantiques s'enroule autour de l'espace des moments du système. La manifestation la plus frappante des phases topologiquement ordonnées est le système à forte interaction de l'effet Hall quantique fractionnaire (FQHE) (R_H quantifié en valeurs fractionnaires du quantum de résistance). Ici encore, l'ordre n'est pas capturé par les symétries, mais par des propriétés telles que la dégénérescence robuste de l'état fondamental, les états de bord chiraux et les excitations émergentes des *anyons*. Les anyons sont des particules intermédiaires entre les fermions et les bosons, qui donnent lieu à des phases fractionnaires lorsqu'ils sont échangés. La valeur précise de ces dernières phases fractionnaires est une quantité clé caractérisant les phases topologiquement ordonnées de la matière.

Au-delà de leur intérêt fondamental, les phases topologiquement ordonnées sont considérées comme des blocs de construction potentiels pour des ordinateurs quantiques évolutifs. Bien que des ordinateurs quantiques ayant fait leurs preuves avec quelques centaines de qubits aient été construits dans de nombreuses plates-formes physiques, le passage à l'échelle d'un ordinateur quantique fonctionnel reste un défi. Le principal obstacle réside dans le fait que les superpositions de qubits sont susceptibles d'être perturbées localement par l'environnement. Les qubits construits à partir de phases topologiques offrent une alternative intéressante. Le meilleur exemple est celui des anyons issus de l'effet FQHE 5/2. Deux de ces anyons, lorsqu'ils sont réunis, forment un qubit. Si les anyons sont très éloignés l'un de l'autre, toute perturbation locale ne perturbe qu'un seul anyon et ne peut donc pas changer l'état des deux anyons. Un tel qubit est donc intrinsèquement résistant aux perturbations locales, ce qui souligne son avantage par rapport à d'autres plateformes de qubits.

Les promesses technologiques et l'intérêt fondamental ont tous deux alimenté une recherche théorique et expérimentale intense sur les anyons dans la FQHE au cours des dernières décennies. La physique de l'effet FQHE, qu'il s'agisse du *bulk* (l'intérieur du materiau) ou de l'état de bord, est une histoire riche, complexe et évolutive. Cependant, en raison du gran *gap* des états quantiques du *bulk*, la plupart des expériences sondent l'effet FQHE à travers ses bords chiraux sans *gap*, ce qui permet néanmoins de mieux

comprendre les excitations des anyons de la FQHE. Les anyons sur les bords de la FQHE peuvent être étudiés en excitant les bords par un potentiel externe et en mesurant la réponse résultante. En particulier, le rapprochement de bords opposés pour former un contact ponctuel quantique permet aux anyons de traverser les bords par effet tunnel. C'est une stratégie qui a permis des mesures remarquables des propriétés topologiques des anyons. En effet, à la suite de propositions théoriques initiales, la charge fractionnelle des anyons a été vérifiée expérimentalement à la fin des années 90 dans le cadre de telles expériences d'effet tunnel. Cependant, malgré des décennies d'efforts expérimentaux et de propositions théoriques innovantes, la vérification expérimentale des propriétés plus complexes comme la dimension d'échelle (*scaling dimensions*) et des statistiques d'échange (aussi appelée tressage) des anyons est restée longtemps hors de portée.

Ces efforts ont porté leurs fruits ces dernières années, avec la détection expérimentale sans ambiguïté des statistiques de tressage fractionnaire par plusieurs groupes dans le système $\nu = 1/3$ FQHE. L'état $\nu = 1/3$ appartient aux séries dites de Laughlin. Il s'agit de la manifestation la plus simple de l'effet FQHE, où le système possède un seul état de bord chiral et un type unique d'anyon. En raison notamment de leur simplicité, l'accord le plus convaincant entre la théorie et les expériences se limite aux états FQHE de Laughlin. Il est intéressant de noter que, toujours dans l'effet FQHE $\nu = 1/3$, la dimension d'échelle des anyons a suscité un vif débat, les diverses expériences étant en profond désaccord les unes avec les autres.

Les états FQHE non-Laughlin ou Jain, cousins relativement complexes de la FQHE de Laughlin, abritent de multiples états de bord chiraux. Ces états abritent notamment différents types d'anyons qui coexistent dans le système. Chaque type d'anyon porte un charge, un dimension d'échelle et un phase de tressage propre et mutuelle différente, ce qui se traduit par un ordre topologique plus riche que dans les états de Laughlin. Cependant, les expériences sur l'effet FQHE non-Laughlin montrent un accord nettement plus limité avec les prédictions théoriques que celles sur les états de Laughlin. Ceci est certainement vrai dans le cas des mesures de charge fractionnaire. En effet, dans les états non-Laughlin comme $\nu = 2/3$ et $2/5$, il est prévu que différentes charges soient présentes. Cependant, la plupart des expériences n'observent qu'une seule de ces charges, tandis que l'interprétation des expériences qui ont observé les différentes charges a été remise en question par des résultats récents. Alors que la situation avec les charges fractionnaires est préoccupante, la question de la phase de tressage dans $\nu = 2/5$ est plus problématique. Dans ce dernier système, les expériences sondant la phase de tressage sont en désaccord avec les prédictions théoriques, non seulement sur le plan quantitatif, mais aussi sur le plan qualitatif. Le comportement étrange des anyons dans ce système ne trouve pas d'explication facile. Il est nécessaire d'aborder ces divergences dans la poursuite d'une meilleure compréhension des anyons dans la FQHE.

Cette thèse est donc consacrée à l'étude théorique des propriétés exotiques des anyons dans un système FQHE général (abélien), conduisant à une caractérisation de la phase topologique de la FQHE. Pour être plus précis, nous identifions des quantités mesurables

qui peuvent conduire à une mesure non ambiguë des propriétés topologiques des anyons – charge, dimension d'échelle, et bien sûr, les statistiques de tressage – dans les FQHE non-Laughlin.

Effet Hall quantique fractionnaire

Le chapitre 1 présente l'effet Hall quantique fractionnaire (FQHE) comme un système physique concret dont les excitations fondamentales sont des anyons. Pour commencer, nous considérons la notion de particules identiques et démontrons comment, dans deux dimensions spatiales, des particules avec des statistiques entre fermions et bosons peuvent apparaître. En effet, imaginons deux particules A et B. Considérons maintenant que la particule B décrit une trajectoire circulaire autour de la particule A. En trois dimensions spatiales, cette trajectoire circulaire peut être soulevée au-dessus de la particule A, déformant la trajectoire jusqu'à la transformer en l'opération d'identité, ce qui revient à ne pas exécuter le mouvement circulaire. Cependant, en deux dimensions spatiales, cela n'est pas possible. La troisième dimension étant absente, toute trajectoire de la particule B effectuant une boucle complète autour de A est topologiquement distincte des autres trajectoires de B ne contournant pas A. Cette possibilité exotique en deux dimensions donne naissance aux anyons, des particules exotiques dotées de statistiques d'échange fractionnaires, comme nous l'avons vu précédemment.

Un système physique concret hébergeant des anyons est l'effet FQHE. L'effet FQHE est caractérisée par de fortes interactions de Coulomb entre les électrons et une dégénérescence macroscopique importante de l'état fondamental. Une approche théorique ou numérique directe de ce problème n'est donc pas possible. Des avancées sur le plan théorique ont été réalisées par Laughlin, qui, au lieu de dériver une solution en diagonalisant l'hamiltonien, a simplement écrit la fonction d'onde. La forme de la fonction d'onde dite de Laughlin a été motivée par les symétries du problème et les statistiques de Fermi-Dirac des électrons. La fonction d'onde de Laughlin explique naturellement l'existence de plateaux de résistivité de Hall de $1/m$ fois la résistance de Hall, où m est un entier impair. Plus intéressant encore, les excitations de la fonction d'onde de Laughlin sont des anyons ! En effet, on peut montrer explicitement que les excitations portent une charge fractionnaire et, surtout, qu'elles présentent des statistiques d'échange fractionnaires.

La fonction d'onde de Laughlin explique naturellement la série de plateaux de résistivité Hall se produisant à des valeurs fractionnaires de $\nu = 1/m$ avec m un entier impair. Cette dernière série d'états de Hall quantique fractionnaires est maintenant appelée la série de Laughlin. Il existe cependant d'autres plateaux à des valeurs fractionnaires telles que $\nu = 2/5,\ 2/3,\ 3/7$, et ainsi de suite, qui n'entrent pas dans la série de Laughlin. Ces plateaux restent inexpliqués par la fonction d'onde de Laughlin. Une extension naturelle de la fonction d'onde de Laughlin explique ces derniers plateaux non-Laughlin. Les excitations anyoniques elles-mêmes sont supposées exister dans une phase FQHE, ce qui

conduit à un terme supplémentaire dans la fonction d'onde. Les plateaux de résistivité prédits par les fonctions d'onde dites hiérarchiques correspondent bien aux plateaux observés expérimentalement au-delà de la série de Laughlin. Une autre explication des états non-Laughlin est la théorie du fermion composite. Dans cette théorie, les électrons sont supposés former des états liés avec un nombre pair de quanta de flux magnétique, appelés fermions composites. Les plateaux fractionnaires de l'effet Hall quantique des électrons peuvent alors être compris comme les plateaux entiers de l'effet Hall quantique des fermions composites. Néanmoins, les deux images des fonctions d'onde hiérarchiques et des fermions composites sont largement compatibles l'une avec l'autre.

Bien que ces différentes fonctions d'onde offrent une explication microscopique convaincante de la FQHE, nous nous intéressons également à des descriptions plus simples du phénomène, dans un souci de simplicité théorique. La théorie de Chern-Simons fournit une description efficace et à grande échelle de l'effet FQHE, capturant les caractéristiques toopologiques importantes telles que la résistivité de Hall quantifiée fractionnaire, les excitations anyoniques émergentes et les états de bord chiraux.

Plusieurs éléments indiquent que le terme de Chern-Simons devrait décrire la physique du Hall quantique. Tout d'abord, les symétries. L'effet Hall quantique préserve la symétrie de translation et de rotation et, bien sûr, l'invariance de jauge, mais brise les symétries de retournement temporel et de parité. Le terme de dimension d'échelle la plus basse qui satisfait ces exigences de symétrie en deux dimensions spatiales est le terme de Chern-Simons. L'existence d'anyons dans la FQHE, comme le montre la fonction d'onde de Laughlin, est un autre indice fort. Il est bien connu que le terme de Chern-Simons lie les flux aux charges. Un composite flux-charge est en effet un prototype d'anyons, ce qui indique le lien entre la FQHE et la théorie de Chern-Simons. L'effet FQHE abélien général est décrit par N champs de jauge de Chern-Simons, le couplage entre les différents champs de Chern-Simons étant donné par ce que l'on appelle la matrice K. Les excitations du champ de Chern-Simons présentent un comportement anyonique, la charge et les statistiques de tressage des anyons étant directement liées à la matrice K.

L'analyse microscopique et les études de la théorie des champs effectifs établissent fermement l'existence d'anyons dans l'effet FQHE. L'étape suivante consiste à relever le défi de sonder expérimentalement ces anyons pour vérifier leur existence. L'un des principaux problèmes réside dans le fait que le système FQHE est fermé : l'écart d'énergie entre les niveaux de Landau est important, ce qui empêche le transport des anyons dans le *bulk* et, partant, l'étude de leur réponse à des stimuli externes. Cependant, près du bord de l'échantillon, les niveaux de Landau se courbent et croisent le niveau de Fermi, créant ainsi des états de bord sans *gap*. Cela fait du bord un terrain de jeu naturel pour l'étude de la réponse des anyons aux forces externes.

Dans le **chapitre** 2, nous considérons donc naturellement la théorie de Chern-Simons sur un système borné, semblable à un véritable système FQHE. Par des arguments d'invariance de jauge, nous montrons que la physique du bord est décrite par un liquide de Luttinger chiral ou un champ bosonique libre chiral. Il est important de noter que le fait de

partir de l'action de Chern-Simons permet de mettre en évidence la correspondance entre le *bulk* et le bord de l'échantillon. Puisque la théorie du bord hérite de la même matrice K que celle du *bulk*, les anyons sur le bord possèdent les mêmes propriétés topologiques - statistiques de charge et d'échange - que les anyons dans le *bulk*.

L'étude de la physique des anyons sur les bords nécessite de nombreux outils théoriques. Nous développons une approche progressive pour décrire la physique des bords de la FQHE, à partir d'une action de liquide de Luttinger chiral et de données phénoménologiques. Ainsi, tous les anyons existant sur les bords peuvent être facilement déterminés. Les anyons sont sondés en pilotant les bords en appliquant une différence de tension ou de température. Les tensions sont couplées aux bords FQHE en ajoutant un terme de couplage à l'hamiltonien du bord, qui prend en compte l'effet de la tension sur les liquides de Luttinger chiraux sur le bord. Les courants résultants sont partitionnés au niveau des contacts ponctuels quantiques (QPC) - un dispositif qui réunit les bords opposés de la FQHE - ce qui nous permet de sonder la nature anyonique des particules transportant les courants. Les QPC sont décrits théoriquement par un terme d'interaction dans l'hamiltonien, qui rend compte de l'effet tunnel des anyons entre les bords rapprochés par les QPC. Pour calculer les observables physiques associées au flux d'anyons partitionnés, telles que le courant moyen ou le bruit de courant, nous utilisons des techniques de la théorie quantique des champs hors équilibre. En effet, comme les bords sont entraînés hors de l'équilibre par la différence de tension ou de température, nous utilisons le formalisme de la fonction de Greens de Keldysh hors équilibre. Nous mettons l'accent sur la mesure non ambiguë de trois propriétés topologiques clés des anyons : la charge, la dimension d'échelle et les statistiques d'échange. Ces propriétés peuvent être sondées dans des expériences de bord en mesurant différentes quantités, et utilisées pour caractériser l'état FQHE.

En effet, des expériences récentes ont permis de mesurer avec succès ces propriétés des anyons. Cependant, comme mentionné précédemment, l'accord entre la théorie et l'expérience n'est solide que pour les fractions de Laughlin les plus simples de la FQHE. Dans les fractions non-Laughlin telles que $\nu = 2/3$ ou $\nu = 2/5$, il existe des problèmes dans la mesure des trois quantités citées ci-dessus. Cette thèse présente donc différentes pistes pour surmonter les défis de la mesure non ambiguë de la charge, de la dimension d'échelle et des statistiques de tressage des anyons dans les systèmes FQHE non-Laughlin. Les contributions originales de cette thèse sont résumées dans les sections suivantes.

Charge fractionnaire

Les charges fractionnaires ont été observées pour la première fois par des mesures de bruit de grenaille en courant continu d'anyons passant par un contact ponctuel quantique (QPC) dans l'effet Hall quantique fractionnaire (FQHE). Cette dernière mesure est aujourd'hui la technique de référence pour mesurer la charge des anyons. Cependant, dans les scénarios où l'on s'attend à ce que différents types de charges s'infiltrent simultanément au QPC, il

est difficile de déterminer les charges individuelles à l'aide de mesures du bruit de grenaille en courant continu.

Une alternative prometteuse explorée au chapitre 3 est l'étude du bruit de grenaille sous l'influence d'une tension alternative périodique, appelée *bruit de grenaille photo-assisté* (PASN). Dans la FQHE de Laughlin, le PASN a été démontré comme un outil complémentaire pour les diagnostics de charge fractionnaire. Nous étudions donc le PASN dans l'effet FQHE abélien général, où différents types de charges sont transmises simultanément dans le QPC. Les calculs théoriques sont effectués dans le cadre du formalisme de Floquet. Il est naturel de constater que l'état fondamental de la théorie des bords, piloté par une tension alternative, peut être interprété comme une superposition d'états dont l'énergie est quantifiée par la fréquence du courant alternatif. Les transitions vers les états d'énergie supérieure et inférieure sont effectuées par l'absorption et l'émission de photons provenant du courant alternatif, d'où le nom de bruit photo-assisté.

Appliquée au cas spécifique de $\nu = 2/3$ FQHE, notre analyse révèle que le PASN est une sonde robuste pour détecter différents types de charges passant par effet tunnel dans un QPC. Il esr remarquable que le PASN reste efficace même lorsque l'effet tunnel d'un type de charge est significativement moins important que les autres. Nous montrons que même dans des conditions facilement accessibles dans les expériences contemporaines, le PASN combiné à des mesures de bruit de grenaille en courant continu constitue une sonde efficace de plusieurs types de charges passant simultanément dans le QPC.

Alors que des décennies d'efforts théoriques et expérimentaux ont établi que les charges fractionnaires sont une caractéristique intrinsèque des quasiparticules anyoniques FQHE, il reste encore beaucoup à comprendre sur leurs propriétés de transport. L'intuition des propriétés de transport élastique des électrons dicte que les particules confrontées à une barrière opaque sont réfléchies. Cette intuition ne s'applique pas aux anyons. En effet, les anyons peuvent subir un processus plus exotique, dans lequel ils empruntent d'autres anyons au système FQHE pour former un électron qui est transmis à travers la barrière (qui n'est opaque que pour les anyons, mais pas pour les électrons). Ce processus rappelle la réflexion d'Andreev qui se produit dans une jonction entre un supraconducteur et un métal normal. Le chapitre 4 est consacré à l'étude théorique de ce processus exotique de réflexion d'Andreev des quasiparticules anyoniques dans l'effet FQHE.

Expérimentalement, cette possibilité est réalisée dans une géométrie comprenant deux contacts ponctuels quantiques (QPC). Le premier QPC est polarisé avec une tension importante, émettant un flux d'anyons sur les bords opposés. Ces derniers anyons voyagent le long du bord et sont incidents sur un QPC qui est accordé dans un régime qui n'admet que le passage des électrons. Ce dernier QPC est donc opaque aux anyons. Le décalage de charge entre les entités passant par les deux QPC donne lieu à un phénomène de réflexion de type Andreev dans ce système FQHE. La quasiparticule anyonique de charge fractionaire qui arrive sur le deuxième QPC déclenche la transmission d'un électron et, par conservation de la charge, des quasi-trous anyoniques sont réfléchis.

Les signatures des processus de réflexion de type Andreev se trouvent dans les corrélations croisées et les autocorrélations de courant, qui ont été mesurées expérimentalement récemment. Nous fournissons ici un calcul complet des corrélations de courant, en parfait accord avec les expériences récentes. De plus, nous mettons en lumière la dépendance en température de ce processus de réflexion de type Andreev, fournissant ainsi une explication possible aux expériences paradoxales précédentes.

Dimension d'échelle

La dimension d'échelle des anyons sur les bords de la FQHE est une autre manifestation importante des propriétés topologiques exotiques des anyons. Cette dernière quantité correspond à l'exposant caractérisant la décroissance du corrélateur anyonique, et fait actuellement l'objet d'intenses recherches. Cependant, comparée à d'autres propriétés des anyons, la dimension d'échelle est beaucoup plus sensible à la physique non universelle des bords de FQHE. Cette sensibilité a conduit à des divergences significatives entre la théorie et l'expérience, même pour les états de Laughlin les plus simples. Il est donc crucial d'identifier des sondes plus fiables de la dimension d'échelle des anyons.

À cette fin, dans le chapitre 5, nous explorons le bruit induit par une différence de température dans l'effet FQHE, appelé bruit ΔT. Cela se produit lorsque deux bords de l'FQHE à des températures différentes sont connectés par un contact ponctuel quantique (QPC). Bien que la symétrie particule-trou du QPC se traduise par un courant net nul, le bruit diffère du bruit d'équilibre, ce qui conduit à un bruit d'excès mesurable.

Nous calculons le bruit ΔT à fréquence finie dans un système FQHE abélien général. Ce bruit présente des différences marquées selon que les anyons ou les électrons traversent le QPC par effet tunnel. Pour l'effet tunnel des anyons, l'excès de bruit ΔT est négatif sur une large gamme de fréquences, alors que l'effet tunnel des électrons produit toujours un excès de bruit positif. Plus généralement, l'excès de bruit ΔT à fréquence finie ne devient négatif que lorsque la dimension d'échelle des particules à effet tunnel est inférieure à un - une caractéristique des anyons. Même lorsque des effets de bord non universels modifient la dimension d'échelle, le bruit ΔT à fréquence finie fournit une méthode robuste pour distinguer l'effet tunnel des quasiparticules anyoniques de l'effet tunnel non anyonique au niveau du QPC.

Phase de tressage

Les statistiques de tressage fractionnaire sont sans aucun doute l'aspect le plus exotique et le plus caractéristique des anyons. Alors que la tresse implique généralement le déplacement d'un anyon autour d'un autre dans l'espace 2D, les bords du Hall quantique fractionnaire

équipés de contacts ponctuels quantiques (QPC) offrent une méthode plus abstraite pour ce processus. Dans le régime de rétrodiffusion faible, les QPC réunissent deux bords du systèmd FQHE, une petite région du système de l'FQHE se trouvant entre les bords. Cette configuration permet aux anyons approchant le QPC (à partir d'une source non spécifiée) de se tresser avec les excitations virtuelles anyon-antianyon générées au QPC. Contrairement au tressage conventionnel d'anyons dans l'espace 2D, ce processus est plus abstrait. Le tressage conventionnel d'anyons n'est pas réalisable dans un système à 1D comme les bords de l'effet FQHE. Au lieu de cela, comme indiqué au chapitre 6 l'ordonnancement temporel des anyons entrants par rapport aux paires anyon-antianyon générées au QPC introduit effectivement une deuxième dimension, permettant un tressage en $1 + 1$D.

Le chapitre 7 explore la physique du collisionneur anyon. L'expérience du collisionneur d'anyons a marqué la première démonstration expérimentale des statistiques anyoniques dans l'FQHE de Laughlin $\nu = 1/3$. Le dispositif comprend deux flux dilués d'anyons qui se rencontrent à un QPC. Initialement, on pensait que les anyons des deux flux entraient en collision et s'excluaient spatialement l'un l'autre, le regroupement (*bunching*) ou l'*antibunching* des anyons étant intermédiaire entre les fermions et les bosons. Cependant, une analyse plus poussée a révélé que c'est plutôt le processus de tressage dans le domaine temporel évoqué au paragraphe précédent qui se produit dans cette configuration. Les anyons des flux entrants se tressent avec les paires anyon-antianyon générées au QPC où les deux faisceaux se rencontrent. Les signes de ces processus de tressage se manifestent dans diverses observables physiques, notamment les corrélations croisées des courants de sortie du QPC.

Alors que l'expérience s'accorde très bien avec la théorie à $\nu = 1/3$, la même expérience à $\nu = 2/5$ est en profond désaccord avec les prédictions théoriques. Ces dernières sont basées sur l'interpolation des résultats de Rosenow, qui ne tient pas compte des complexités des fractions de remplissage non-Laughlin. Cette approche simpliste n'intègre pas les effets non triviaux sur le bord qui pourraient conduire à de fortes déviations par rapport aux calculs de la théorie du bord de l'effet FQHE Laughlin.

Nous généralisons donc la théorie du collisionneur d'anyons à un état FQHE abélien arbitraire comprenant plusieurs modes bosoniques sur le bord, et différents types d'anyons transmis au niveau du QPC. Les multiples modes bosoniques peuvent être co-propageants (comme dans $\nu = 2/5$) ou contra-propageants (comme dans $\nu = 2/3$).

Nous appliquons notre théorie à deux systèmes FQHE : $\nu = 2/3$ et $\nu = 2/5$. Dans le système $\nu = 2/3$, nous fournissons des prédictions explicites pour différents scénarios de tressage d'anyons, en prévision d'expériences futures. D'autre part, étant donné les résultats expérimentaux existants dans le système $\nu = 2/5$, l'objectif est de réconcilier la théorie et l'expérience. Notre modèle comprenant plusieurs modes bosoniques sur chaque bord, et différents types d'anyons tunnelant aux QPCs, nous permet d'avancer dans cette direction. Nous étudions les conséquences d'effets non triviaux sur le bord, tels que les interactions intermodes, la reconstruction du bord et l'effet tunnel de différents types

d'anyons. Bien que le fossé entre la théorie et l'expérience ne soit pas comblé de manière satisfaisante, cette étude donne des indications cruciales sur la manière dont la physique du collisionneur d'anyons est façonnée par ces ingrédients non triviaux, ce qui conduit à une compréhension plus complète des statistiques de tressage d'anyons dans les systèmes FQHE non-Laughlin.

Dans le chapitre 8, nous examinons un aspect de la physique des anyons qui a été négligé jusqu'à présent : la largeur finie des anyons. Alors que les objets physiques ont généralement une largeur finie, cette caractéristique est souvent négligée lorsque la largeur est petite par rapport aux autres échelles de longueur du système. Cependant, pour les anyons, nous montrons que même lorsque leur largeur est inférieure de plusieurs ordres de grandeur à d'autres échelles physiques pertinentes, elle joue un rôle crucial en influençant les signatures de tressage.

Nous commençons par calculer le courant d'effet tunnel d'un seul anyon de largeur finie incident sur un contact ponctuel quantique (QPC), ce qui permet de comprendre clairement l'impact de la largeur de l'anyon sur les observables physiques dans un cadre simplifié. Après avoir compris l'idée clé, nous étendons la théorie du collisionneur d'anyons en tenant compte de la largeur finie des anyons entrants. Nous sommes ainsi en mesure de montrer que la largeur finie des anyons entraîne une diminution de la phase de tressage effective dans le domaine temporel qui se produisent dans le collisionneur d'anyons. Cette découverte nous conduit à une résolution satisfaisante du problème identifié dans le chapitre précédent.

Nous établissons en outre une relation directe entre la largeur des anyons et la transparence des QPCs sources, reliant ainsi la largeur des anyons à une quantité contrôlable expérimentalement. Nous constatons que la largeur des anyons pour laquelle un accord est trouvé avec les expériences à $\nu = 2/5$ FQHE est compatible avec les valeurs de transparence des QPC utilisées dans les expériences. En explorant davantage ce lien, nous comparons la théorie et l'expérience à $\nu = 1/3$, en faisant varier la transparence QPC, et nous trouvons un accord solide, ce qui place notre théorie sur une base quantitative solide.

Perspectives

Cette thèse contribue à approfondir notre compréhension des anyons dans un état abélien général de FQHE. Nous proposons non seulement des techniques pour mesurer sans ambiguïté la charge fractionnaire, la dimension d'échelle et les statistiques de tressage des anyons, mais nous tenons également compte de la physique des bords qui pourrait conduire à des observations différentes des prédictions de la théorie la plus simple. La thèse résout de nombreux problèmes liés à la détection des anyons, mais elle ouvre également plusieurs pistes à approfondir. Dans le contexte des charges fractionnaires, il pourrait être intéressant d'utiliser le formalisme développé dans le chapitre 3 pour traiter les excitations minimales appelées Levitons sur les bords de l'effet FQHE. Il s'agit d'excitations avec

une charge entière et sans exciter de paires quasiparticules-quasitrous supplémentaires, potentiellement utiles dans les applications de qubits volants.

Alors que nous avons abordé les processus similaires à la réflexion d'Andreev dans l'effet FQHE de Laughlin au chapitre 4, des processus similaires qui pourraient se produire dans des fractions non-Laughlin telles que $\nu = 2/5$ restent inexplorés.: un anyon de charge $e/5$ pourrait arriver sur un QPC n'admettant queanyons de charge $e/3$,

Le gradient de température entre les bords, étudié au chapitre 5 a fourni des informations précieuses sur la dimension d'échelle des anyons. Cependant, les gradients thermiques dans les configurations impliquant de multiples contacts quantiques ponctuels pourraient également fournir des informations sur les statistiques de tressage. Au-delà de l'effet FQHE, cela pourrait avoir des implications pour les états liquides de spin chiraux où les excitations anyoniques sont neutres.

La configuration du collisionneur d'anyons décrite dans les chapitres 6-8 a permis une observation remarquable des statistiques de tressage anyonique dans les systèmes $\nu = 1/3$ et $\nu = 2/5$ par le biais des processus de tressage dans le domaine temporel. Cependant, comme nous l'avons vu, la largeur finie des anyons conduit à une phase de tressage effectivement plus petite expérimentée par le système. La géométrie de Fabry-Pérot, où les anyons de bord se tressent avec les anyons du *bulk* au sens conventionnel, mise en oeuvre à $\nu = 2/5$ est toujours en accord avec les prédictions des anyons de largeur nulle. Il est donc intéressant d'étudier la combinaison entre le tressage des anyons dans le domaine temporel et le tressage conventionnel des anyons dans le domaine $2D$. Le système Fabry-Pérot offre un moyen naturel d'étudier cette combinaison. En effet, nous pouvons imaginer l'envoi d'un flux dilué d'anyons sur l'interféromètre de Fabry-Pérot via un QPC source en amont. Les anyons entrants ne tressent pas seulement dans le domaine temporel avec les anyons qui tunnelent dans le QPC, mais aussi dans l'espace avec les anyons du *bulk* situés dans l'ilot entre les deux QPC de l'interféromètre de Fabry-Pérot. L'étude de cette combinaison pourrait permettre de mieux comprendre la physique des anyons.

Enfin, bien que cette thèse se soit concentrée sur les anyons abéliens, la promesse technologique des phases topologiques concerne les états FQHE non abéliens. Alors que l'existence des anyons abéliens a été établie expérimentalement, il n'y a pas encore de preuve de l'existence d'anyons non abéliens prédits par exemple pour les facteurs de remplissage $\nu = 5/2$ et $\nu = 12/5$ dams l'effet FQHE. Il y a donc une forte motivation pour considérer la géométrie des collisionneurs d'anyons dans le contexte de l'effet FQHE non abélienne, dans l'espoir de trouver une trace non ambiguë du caractère non abélien des anyons.

Contents

Introduction **1**

1. Quantum Hall effect: bulk **7**
1.1. Anyons . . . 7
1.2. Quantum Hall effect . . . 8
1.2.1. Classical Hall effect . . . 10
1.2.2. Integer quantum Hall effect . . . 10
1.2.3. Fractional quantum Hall effect . . . 15
1.3. Chern-Simons approach to fractional quantum Hall . . . 22
1.3.1. Level Quantization of Chern-Simons theory . . . 22
1.3.2. Chern-Simons theory for Laughlin fractions . . . 23
1.3.3. Chern-Simons theory for hierarchical fractions . . . 25
1.4. Conclusion . . . 28

2. Quantum Hall effect: edge **29**
2.1. Chiral Luttinger liquids from Chern-Simons theory . . . 29
2.1.1. Charge density operator on the edge . . . 31
2.1.2. Quasiparticle operators on the edge . . . 32
2.1.3. Change of basis . . . 33
2.2. Edge theory of FQHE: a bottom-up approach . . . 34
2.2.1. Finding the electron and anyon operators . . . 36
2.2.2. Important measurable quantities of anyons . . . 37
2.2.3. Anyon and electron operators . . . 38
2.3. Probing anyons using transport . . . 39
2.3.1. Coupling a voltage to the edge . . . 41
2.3.2. Quantum point contacts in FQHE . . . 41
2.3.3. Tunneling Hamiltonian: weak- and strong-backscattering regimes 43
2.3.4. Tunneling current . . . 44
2.3.5. Keldysh formalism . . . 44
2.4. Review of FQHE edge experiments . . . 49
2.4.1. Fractional charge . . . 50
2.4.2. Scaling dimension . . . 54
2.4.3. Braiding phase . . . 56

3. Photoassisted shot noise **59**
3.1. Preliminaries . . . 59
3.1.1. Shortcomings of DC shot noise . . . 60
3.1.2. Introduction to photoassisted shot noise . . . 63
3.2. Floquet formalism for Abelian FQHE edges . . . 65
3.3. Photoassisted shot noise: general Abelian FQHE . . . 67
Tien-Gordon relation of PASN in Abelian FQHE . . . 69
3.4. Photoassisted shot noise in $\nu = 2/3$ FQHE . . . 70
Non-universal scaling dimension . . . 73
3.5. Discussion and conclusion . . . 74

4. Quasiparticle Andreev Reflection **76**
4.1. Preliminaries . . . 76
4.2. System description . . . 78
4.3. Theoretical model . . . 80
4.4. Physical measurables . . . 81
4.4.1. Cross-correlations . . . 82
4.4.2. Auto-correlations . . . 85
4.4.3. Tunneling current . . . 86
4.5. Finite temperature . . . 87
4.6. Discussion of results . . . 88
4.7. Comparison with experiments . . . 90
4.8. Conclusion . . . 92

5. Finite-frequency ΔT noise **93**
5.1. Preliminaries . . . 93
5.1.1. Finite-frequency noise . . . 94
5.1.2. Zero-frequency ΔT noise in Fermi liquids . . . 96
5.2. ΔT emission noise in FQHE . . . 97
5.2.1. Expansion in the temperature gradient . . . 100
5.3. ΔT emission noise probes scaling dimension . . . 102
5.3.1. Laughlin fractions . . . 102
5.3.2. Comparison with zero-frequency ΔT noise . . . 104
5.3.3. Non-Laughlin fractions . . . 105
5.3.4. Non-chiral Luttinger liquids . . . 106
5.3.5. Consolidating the results . . . 106
5.4. Discussion and conclusion . . . 107

6. Time-Domain Braiding **110**
6.1. Heuristic discussion . . . 111
6.2. Tunneling current: single anyon in general Abelian FQHE . . . 117

7. Generalized Abelian Anyon Collider **127**
7.1. Upstream QPC as anyon sources: the anyon collider . . . 128
7.1.1. Theoretical framework . . . 129
7.1.2. Tunneling current due to N anyons . . . 131
7.1.3. Poisson-averaged tunneling current . . . 133
7.2. Generalizing the anyon collider . . . 134
7.2.1. Theoretical framework . . . 135
7.2.2. Tunneling current . . . 136
7.2.3. Asymmetry of incoming currents . . . 140
7.3. Non-equilibrium bosonization . . . 141
7.3.1. Definition . . . 142
7.3.2. Tunneling noise . . . 144
7.4. Cross-correlations and generalized Fano factor . . . 145
7.5. Experimental status . . . 148
7.5.1. $\nu = 1/3$ . . . 148
7.5.2. $\nu = 2/5$ . . . 149
7.6. $\nu = 2/3$: predictions from the generalized model . . . 150
7.6.1. Charged mode braiding . . . 151
7.6.2. Neutral mode braiding . . . 152
7.7. $\nu = 2/5$: attempts to bridge theory and experiment . . . 154
7.7.1. Various edge models . . . 155
7.7.2. $2e/5$ anyons . . . 156
7.7.3. Killing the neutral mode . . . 159
7.7.4. Different topological class . . . 160
7.7.5. Interactions . . . 161
7.8. Conclusion . . . 162

8. Finite width anyons **164**
8.1. Tunneling current due to a single anyon . . . 165
8.2. Finite width anyons in the anyon collider . . . 170
8.2.1. Non-equilibrium correlator of finite-width anyons . . . 171
8.2.2. Tunneling current due to finite-width anyons . . . 173
8.2.3. Tunneling noise, cross-correlation noise, and $P-$value . . . 174
8.2.4. Behavior of finite-width phase . . . 176
8.2.5. Finite width changes sign of tunneling current . . . 177
8.3. Scaled width and source QPC transparency . . . 179
8.4. Comparison with experiment . . . 181
8.4.1. $\nu = 2/5$ . . . 181
8.4.2. $\nu = 1/3$ . . . 181
8.5. Discussion and conclusion . . . 183

Perspectives **185**

A. Berry Phase **188**

B. Bosonic Greens Function **190**
B.1. Derivation of bosonic Greens function for a single chiral boson 190
B.2. Extension to multiple chiral bosons 192
B.3. Correlation function of exponentiated boson operators 193
B.3.1. Single harmonic oscillator 193
B.3.2. Bosonic fields 194
B.4. Quasiparticle Greens function 195

C. DC shot noise: general Abelian edge **196**

D. Finite-frequency ΔT noise: C_2 analytics **200**

E. Quasiparticle Andreev Reflection: Integrals **203**
E.1. Zero temperature: useful contour integrals 203
E.2. Finite temperature calculation 204
E.2.1. $t-$ and t_1-integrals 204
E.2.2. $\tilde{t}-$integral 205
E.2.3. t_2-integral 206
E.2.4. Final $\tau-$integral 207

F. Time-domain braiding phase from 4−branch Keldysh contour **209**

G. Anyon Collider: Fluctuation-Dissipation Theorem **212**

Introduction

Condensed matter, which consists of densely packed atoms and electrons, exhibits a variety of physical properties resulting in different *phases* of matter [1]. The phases of matter range from mundane solids or liquids, to exotic superconductors or superfluids. The physical properties of different phases depend not just on the constituent particles and their interactions but also on their arrangement or *order* in the material. A crucial aspect of the order is symmetries—transformations that leave the system unchanged. For example, water has continuous translational symmetry, where molecules are randomly distributed, while ice has discrete translational symmetry due to its crystalline structure. The transition from water to ice involves abrupt changes in symmetries and local properties such as density. Landau pioneered the idea that the symmetries completely characterize phases of matter, and phase transitions involve symmetry-breaking and abrupt changes in local properties of the system [2, 3]. Due to its phenomenal success, for much of the 20th century, physicists believed that Landau's framework captured all possible orders and phase transitions in condensed matter systems.

The discovery of the quantum Hall effect (QHE) shattered the Landau paradigm of condensed matter [4–8]. QHE consists of electrons confined in a 2D plane subjected to a strong magnetic field. While the classical Hall effect [9] yields a linearly evolving Hall resistivity (R_H) with respect to magnetic field, the QHE features quantized R_H at integer or fractional values of the resistance quantum. Indeed, as the magnetic field is changed gradually, R_H remains constant at the quantized values before abruptly jumping to the next quantized value. These abrupt jumps are reminiscent of phase transitions, suggesting that QHE of different R_H comprise distinct phases of matter. However, in defiance of the Landau paradigm, the symmetries of the system remain the same in all the QHE states.

This observation led to the idea of *topological order* [10, 11]. Indeed, while the different QHE states have identical symmetries, they differ in their *topological* properties. Topology in mathematics can be thought to begin with Euler's resolution of the Seven Bridges of Königsberg problem. The latter problem sought a path crossing each of the city's seven bridges exactly once. Euler proved that such a path does not exist, emphasizing that the result depends not on the details such as lengths of the bridges or the distances between them, but solely on the connections between the different parts of the city.

Similarly, in physics, some properties of materials do not depend on details such as the distribution of atoms and electrons or the precise interactions between them, but on global, non-local properties such as gaps in the band structure of the system or the

number of holes in the manifold on which the system lives [12]. In the case of the integer quantum Hall effect (R_H quantized to integer values of the resistance quantum), the topological properties are captured by the *Chern number*, a non-local property of the system that changes along with the quantized R_H. The Chern number is independent of the symmetries, but rather depends on how the phase of the wavefunction winds around the momentum space of the system [7]. The most striking manifestation of topologically ordered phases is the strongly interacting system of the fractional quantum Hall effect (FQHE) (R_H quantized to fractional values of the resistance quantum). Here, the order is again captured not by the symmetries, but by properties such as robust ground-state degeneracy, chiral edge states, and emergent *anyon* excitations [10]. Anyons are particles intermediate between fermions and bosons, giving rise to fractional phases when exchanged [13–15]. The precise value of the latter fractional phases is a key quantity characterizing topologically ordered phases of matter.

Beyond their fundamental interest, topologically ordered phases are believed to be potential building blocks for scalable quantum computers [16, 17]. While proof-of-concept quantum computers have been built in many physical platforms, scaling up to a working quantum computer remains a challenge. The primary impediment is that qubit superpositions are susceptible to local perturbations by the environment. Qubits built from topological phases offer a compelling alternative. The best example is the anyons arising in the 5/2 FQHE [18, 19]. Two of the latter anyons, when brought together, form a qubit. If the anyons are far away from each other, any local perturbation disturbs only a single anyon and hence cannot change the two-anyon state. Such a qubit is thus inherently robust against local perturbations, underscoring their advantage against other qubit platforms.

Technological promise and fundamental interest, have both fueled intense theoretical and experimental pursuit of anyons in the FQHE in the past few decades [20]. The physics of the FQHE spanning both its bulk and edge states is a rich, complex, and evolving story [21]. However, owing to a large gap of the bulk quantum states, most experiments probe the FQHE through its gapless chiral edges, nevertheless providing profound insight into the anyon excitations of FQHE [22–24]. Anyons on FQHE edges can be investigated by exciting the edges by an external drive and measuring the resulting response. In particular, bringing opposite edges together forming quantum point contacts [25] to allow anyon tunneling across the edges, is a strategy that has allowed remarkable measurements of the topological properties of anyons [26–28]. Indeed, following initial theoretical proposals [29], the fractional charge of anyons was experimentally verified in the late 90s in such tunneling experiments [30–32]. Yet despite decades of experimental efforts and innovative theoretical proposals (see Ref. [20] for a review), experimental verification of the arguably more exotic, scaling dimension (quantity that controls edge anyon correlations) and braiding phase of anyons remained out of reach for a long time.

The efforts have yielded fruit in the past few years, with unambiguous experimental detection of fractional braiding phase by several groups in the $\nu = 1/3$ FQHE system [33–42]. The $\nu = 1/3$ state belongs to so-called Laughlin series. These are the simplest

manifestation of FQHE, where the system has a single chiral edge state, and a unique type of anyon existing in the system. Owing in part to their simplicity, the most convincing agreement between theory and experiments is restricted to the Laughlin FQHE states. It is noteworthy that still in the $\nu = 1/3$ FQHE, the scaling dimension of anyons has sparked a lively debate with various experiments in strong disagreement with each other [43–45].

The non-Laughlin or Jain FQHE states [46, 47], relatively complex cousins of the Laughlin FQHE, host multiple chiral edge states [23, 24]. Notably, these states host various types of anyons that coexist within the system. Each type of anyon carries different charges, scaling dimensions, and self- and mutual braiding phases, resulting in a richer topological order compared to Laughlin states. However, experiments on non-Laughlin FQHE show a markedly limited agreement with theoretical predictions compared to those on Laughlin states. This is certainly true in the case of fractional charge measurements. Indeed, in non-Laughlin states like $\nu = 2/3$ and $2/5$, different charges are predicted to tunnel across QPCs [24, 48]. However, most experiments see only one of these charges, while the interpretation of experiments that did witness the different charges [49–51] has been questioned by recent results [43, 52]. While the situation with fractional charges is concerning, the issue with braiding phase in $\nu = 2/5$ is more problematic [37–39]. In the latter system, experiments probing the braiding phase disagree with theoretical predictions, not only quantitatively but even at a qualitative level. The odd behavior of anyons in this system finds no easy explanation. It is necessary to address these discrepancies in the pursuit of a better understanding of anyons in the FQHE.

This thesis is geared towards detection of the exotic properties of anyons in a general (Abelian) FQHE system, leading to a characterization of the topological phase of the FQHE. To be more precise, we theoretically identify quantities that can lead to an unambiguous measurement of the topological properties of anyons – charge, scaling dimension, and of course, the braiding phase – in non-Laughlin FQHE. As alluded to above, transport of anyons across quantum point contacts (QPC) of FQHE edges has proved to be a prolific source of information on the topological properties of anyons. We hence theoretically analyze non-equilibrium transport of anyons on FQHE edges, in setups involving one or many QPCs. We calculate quantities measurable in experiments, such as current and noise, using chiral Luttinger liquid theory of FQHE edges and the Keldysh non-equilibrium Greens function formalism. We consider different non-equilibrium drives such as constant and time-dependent voltage drives, or temperature bias across the FQHE edges, creating current and/or noise across the QPC. Being mindful of non-universal physics arising in FQHE edges, these non-equilibrium quantities are shown to provide a measure of the topological properties of anyons in non-Laughlin FQHE.

Summary of the thesis

Chapters 1 and **2** are introductory. They recall well-established results and also discuss very recent progress, placing the original findings of this thesis in a broader context. Moreover, these chapters outline the technical tools employed throughout this thesis.

Chapter 1 introduces the notion of anyons and firmly establishes the existence of anyons in the fractional quantum Hall effect. First, a microscopic description of anyons is given via Laughlin's wavefunction and its generalizations. We then outline an effective description of the FQHE via the Chern-Simons theory. While the Chern-Simons theory of FQHE is interesting in its own right, the primary motivation to recall it in this thesis is the easy connection to the edge physics of FQHE. Indeed, while Chapter 1 focuses solely on anyons in the bulk of the FQHE, these remain difficult to probe in experiments.

In **Chapter 2** we shift our attention to the FQHE edges. It is here that the Chern-Simons theory of FQHE comes in handy. Using gauge invariance arguments, we show that edge physics is described by chiral bosons, and more importantly, we highlight that anyons on FQHE edges carry identical topological properties to those in the bulk. Chapter 2 continues from here to build the technical tools used throughout this thesis. We first develop a bottom-up approach to describing FQHE edge physics. This approach starts from a chiral boson action that takes phenomenological inputs, allowing us to find the anyons existing on an arbitrary Abelian FQHE edge system, and all the topological properties of these anyons. We focus on three key properties of anyons: fractional charge, scaling dimension, and braiding phase. We subsequently introduce the technical description of quantum point contacts (QPC), one of the most fundamental devices used to probe anyons in FQHE. This naturally leads to the Keldysh formalism, the method used throughout this thesis to calculate non-equilibrium quantum averages of measurable physical quantities such as currents and noises. The chapter concludes with a review of recent edge experiments that probe the aforementioned topological properties of anyons, placing the original findings of this thesis in context.

Chapters 3–8 comprise the original findings of this thesis. The thesis admits a natural division into investigations on the three properties of anyons quoted above. Chapters 3 and 4 focus on phenomena associated with fractional charges of the anyons in FQHE, while Chapter 5 concerns scaling dimension of the anyons. Chapters 6–8 investigate the most exotic and defining feature of anyons: fractional braiding phase. We now quickly summarize the content of each chapter.

Chapter 3 is devoted to finding robust probes of fractional charges tunneling at QPCs in non-Laughlin fractions of FQHE. We first highlight the inadequacies of the traditional diagnostic of fractional charges – DC shot noise – when different types of fractional charges tunnel simultaneously at the QPCs. We then introduce the noise due to an AC voltage, called the photoassisted shot noise (PASN), as an alternative probe of the fractional charges. To theoretically analyze the PASN in general Abelian FQHE

edges, we develop a Floquet formalism encompassing multiple bosons on each edge, and different types of charges tunneling at the QPCs. Our analysis applied to the $\nu = 2/3$ FQHE reveals PASN to be a robust probe of different charges tunneling simultaneously at the QPCs in standard experimental conditions.

Chapter 4 investigates the transport properties of anyons carrying a fractional charge. Indeed, intuition based on electronic quantum transport does not apply to fractionally charged anyons, for instance when they are incident on opaque barriers. We investigate such a scenario in this chapter, where anyons in the Laughlin FQHE are incident on a QPC which allows only electrons to go through. This results in an Andreev reflection-like process where an electron is transmitted through the QPC, while two anti-anyons are reflected from the QPC. The signatures of these exotic processes are available in the cross- and auto-correlations of the currents measured on the two arms of the QPC. We explicitly calculate the latter quantities at zero as well as finite temperatures. Our finite temperature results allow us to shed light on older experiments, and find an excellent agreement with recent experiments that probe this process.

Chapter 5 concerns the scaling dimension of anyons in the FQHE. Here, we consider a QPC in a general Abelian FQHE where the two edges are held at different temperatures. While particle-hole symmetry of the QPC implies a net-zero current due to a temperature gradient, there can nevertheless be a non-zero excess noise in the system, called the ΔT noise. In this chapter, we calculate the finite-frequency ΔT noise in a general Abelian FQHE. Our results show that this noise can take negative values when anyons tunnel through the QPC, whereas electron tunneling always produces a positive value. More generally, we find that scaling dimensions less than one – a characteristic of anyons on FQHE edges – gives a negative excess ΔT noise across a wide range of frequencies, while scaling dimensions greater than one give a strictly positive excess ΔT noise. Hence, finite-frequency ΔT noise is positioned as a robust probe of anyonic scaling dimensions.

Chapter 6 introduces the idea of time-domain braiding of anyons. We start with a heuristic discussion of time-domain braiding processes with a simple toy example of a single anyon incident on a QPC. Having understood the key physical ingredients, we show in full rigor the time-domain braiding of anyons in a general Abelian FQHE for the same toy example.

Chapter 7 investigates the anyon collider, a realistic experimental geometry that probes the time-domain braiding of anyons. We first recall the theory of anyon collider already established for Laughlin fractions before generalizing these ideas to address non-Laughlin fractions of the FQHE, incorporating ingredients such as multiple bosonic modes on the edges, and different types of anyons tunneling at the QPCs. The generalization allows us to address complexities that arise in the non-Laughlin states. In particular, we first use our generalized model to provide explicit predictions for different anyon braiding scenarios in the $\nu = 2/3$ FQHE in anticipation of future experiments. We then address the $\nu = 2/5$ FQHE where experiments strongly disagree with naive theoretical predictions. Leveraging the generality of our model, we account for non-trivial edge

physics of non-Laughlin FQHE such as interactions and edge reconstruction, among others. While this investigation fails to satisfactorily resolve the disagreement between theory and experiment at $\nu = 2/5$, it provides crucial insight on how non-trivialities on the edge affect the measurement of braiding phase.

Chapter 8, the concluding chapter, provides a resolution of the discrepancy between theory and experiment of the anyon collider at $\nu = 2/5$ FQHE. Here, we account for the finite width of anyons, an aspect typically overlooked. We begin by illustrating the dramatic impact of the finite width of anyons with the toy example of a single anyon incident on a QPC. The chapter then naturally proceeds to incorporate the finite width of anyons in the theory of the anyon collider. Along the way, we establish a direct relation between the width of anyons and the transparency of the QPCs emitting those anyons. With this, we achieve a quantitative agreement with the anyon collider experiment at $\nu = 2/5$ FQHE.

The thesis concludes with comments on new avenues opened up by the research carried out in this thesis.

How to read this thesis?

The most natural way to read this thesis is in the order it is presented. Readers unfamiliar with anyons and FQHE might find it useful to go over Chapter 1 and Section 2.1. While Sections 1.3 and 2.1 are quite technical and provide a complementary perspective to the discussion of Section 1.2, the theoretically inclined reader might find it rewarding to go through the former sections (and the references therein).

However, the reader familiar with FQHE physics should feel free to skip Chapter 1 and Section 2.1. Readers familiar with anyons and FQHE but not the edge physics of FQHE, might find it useful to go through Sections 2.2–2.4. Even the experts in this area might benefit by glossing over the latter sections as they set the notations used throughout this thesis and place the original findings of the thesis within the context of contemporary research on anyons in the FQHE.

Nevertheless, the experts on FQHE edge theory can jump to any of the core chapters as an attempt is made to make each chapter self-contained. Exceptionally, Chapter 6 is designed as an introduction to the physics considered in Chapters 7 and 8. The average reader is likely to find it useful to go through Chapters 6–8 in the presented order. However, the expert might not find it too difficult to jump from Chapter 6 to Chapter 8.

Chapter 1.

Quantum Hall effect: bulk

This chapter introduces the fractional quantum Hall effect (FQHE) as a concrete physical system that hosts anyons—particles intermediate between fermions and bosons. To start with, we consider the notion of identical particles and demonstrate how, in two spatial dimensions, particles with statistics between fermions and bosons can arise. Next, we briefly review the classical Hall effect and introduce the Hall resistivity. From there, the chapter transitions naturally into the integer quantum Hall effect (IQHE), where we discuss quantized Hall conductivity and essential concepts such as Landau levels and edge states.

Building on this theoretical foundation, we delve into the physics of the FQHE. We present Laughlin's wavefunction, which offers a compelling microscopic explanation of the FQHE. Importantly, we show that the excitations of the Laughlin state exhibit anyonic behavior. We also introduce the hierarchical states of FQHE, that form the core focus of this thesis. The chapter concludes with a discussion of the effective field theory for the FQHE, based on Chern-Simons theory. This sets the stage for understanding edge physics of FQHE, a topic that will be further developed in the next chapter and employed throughout the thesis.

1.1. Anyons

We start by examining the notion of identical particles familiar to us from undergraduate quantum mechanics. We consider two identical particles A and B to be placed at positions r_A and r_B respectively. If the two particles are exchanged, all the probability must remain the same. That is, $|\psi(r_A, r_B)|^2 = |\psi(r_B, r_A)|^2$. Hence, the two states are related at most by a phase

$$\psi_{r_A,r_B} = e^{i\pi\lambda}\psi_{r_B,r_A}. \tag{1.1}$$

Exchanging the particles one more time, we find:

$$\psi_{r_A,r_B} = e^{2i\pi\lambda}\psi_{r_A,r_B}, \tag{1.2}$$

and since the two states on the left and right sides are the same, $e^{2i\pi\lambda} = 1$ is imposed. Hence, we find $\lambda = \pm 1$ corresponding to bosons or fermions respectively.

In the above arguments, the exchange was thought to be an instantaneous process leading to the phase $e^{i\pi\lambda}$. However, physically an exchange is affected by moving say particle A to the other side of particle B. A double exchange then implies that particle A is taken in a circle around B. Thinking in terms of adiabatic paths makes the result above transparent [13]. In three spatial dimensions, a double exchange of particles is topologically equivalent to no exchange at all. This is because the circular path of one particle around another can be lifted into the third dimension and continuously deformed into a single point, as illustrated in Figure 1.1.

In two spatial dimensions, this reasoning breaks down. Without a third dimension, the path of particle B around A cannot be deformed into a point. As a result, a single circular path of particle B around A is topologically distinct from no path at all. Likewise, one circular path is different from two circular paths or even a path in the opposite direction. This distinct topological behavior in two dimensions gives rise to a new class of particles, where the exchange phase λ can take *any* value between 0 and 1 unlike in three dimensions. These particles are known as *anyons*.

It is fascinating to imagine exotic particles that could exist in two dimensions, but the reality is that we live in a three-dimensional world. However, experimental advances have made it possible to simulate effectively two-dimensional physics in laboratory settings. In fact, the band structures of real three-dimensional solid-state materials admit one-dimensional quantum wells [53]. When the width of these wells is comparable to the de Broglie wavelength of the electrons, the system begins to resemble the prototypical particle-in-a-box problem. In these quantum wells, electrons are confined vertically but are free to move along the two-dimensional plane. The wells support quantized energy states, separated by energy gaps. At sufficiently low temperatures, the electrons are confined to the lowest energy state, and their motion in the vertical direction is heavily suppressed, rendering the system effectively two-dimensional. This setup makes quantum wells strong candidates for hosting anyons. As we will explore in the upcoming sections, anyons do indeed emerge in these systems, but only under specific and demanding conditions, such as ultra-high magnetic fields and strong Coulomb interactions between electrons.

1.2. Quantum Hall effect

The main goal of this section is to demonstrate that the fractional quantum Hall effect (FQHE) provides a platform hosting anyons. To build up to this, we first offer a brief

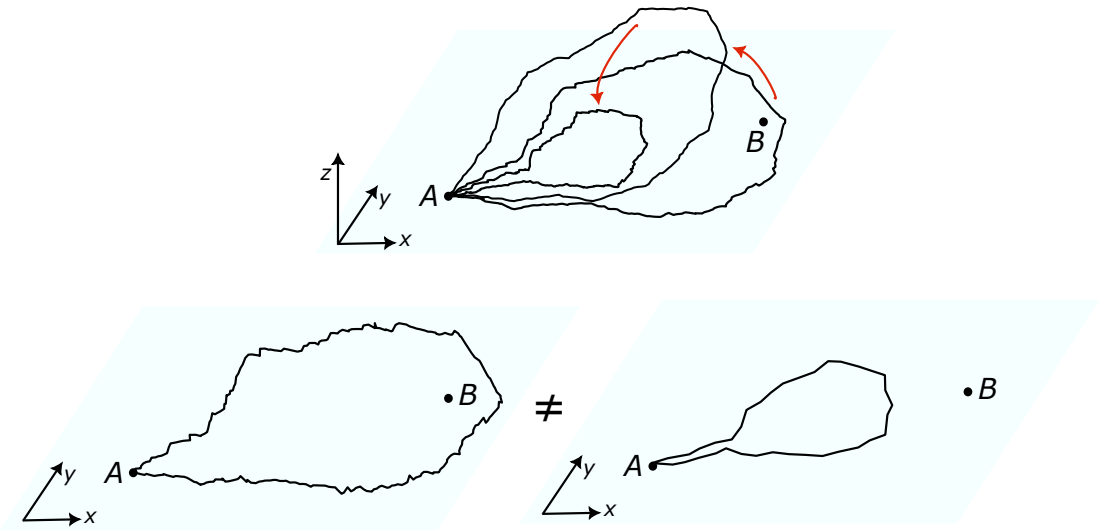


Figure 1.1.: Topology of paths in (top) three and (bottom) two spatial dimensions. (Top) Depicts a closed loop of particle A around particle B. The third dimension allows to lift the path and deform it into a path where particle A has not gone around B. (Bottom) In 2D the above operation is not possible since the third dimension is absent. Particle B poses on obstruction to deforming the path within the 2D plane. Thus, the path where particle A has gone around B is topologically distinct from the path where it has not.

review of the classical Hall effect and the non-interacting physics of the integer quantum Hall effect (IQHE). The basic understanding will set the stage for a deeper exploration of the FQHE, where the strong electron interactions gives rise to anyons.

1.2.1. Classical Hall effect

The physics of electron transport in materials subjected to a perpendicular magnetic field is known as the Hall effect [9]. When electrons move under a voltage bias along one direction of the sheet, they experience a transverse Lorentz force due to the magnetic field applied perpendicular to the current. This causes the electrons to accumulate on one side of the sheet, generating a voltage across the transverse direction. The relationship between this transverse voltage and the longitudinal current defines the Hall resistivity R_H, which is expressed as:

$$R_H = \frac{B}{ne} \tag{1.3}$$

where n denotes the electron density of the sample, B denotes the magnetic field, and e the electronic charge. This phenomenon is well explained within Drude's classical transport theory [54]. The Hall effect has yielded important information on the charge carriers in a material, crucially, whether the current is carried by electrons or holes.

1.2.2. Integer quantum Hall effect

Several decades later, Hall resitivity was measured in materials under extreme circumstances, compared to the conditions where classical Hall effect is observed. Instead of a thin metallic sheet, experiments analyzed electrons confined to two spatial dimensions, called two-dimensional electron gas (2DEG). 2DEGs are found in silicon-based MOSFET and GaAs-GaAlAs heterostructures, among other materials [53]. The 2DEG were subjected to ultra-low temperatures and strong magnetic field B, and measurements akin to the classical Hall effect were performed in this system. The results were striking. Experiments revealed that the linear B dependence of R_H, under the demanding conditions described above, is replaced by quantized plateaus [4], as shown in Figure 1.2. The Hall resistivity remains constant over a range of magnetic fields, before abruptly jumping to the next plateau. The Hall resistivity on the plateaus takes the values

$$R_H = \frac{h}{e^2}\frac{1}{\nu}. \tag{1.4}$$

The number ν was measured to be an integer with an accuracy of one in a billion, lending the name integer quantum Hall effect (IQHE) to this phenomenon. The value of the resistivity is independent of the details of the sample or even the material. Given the

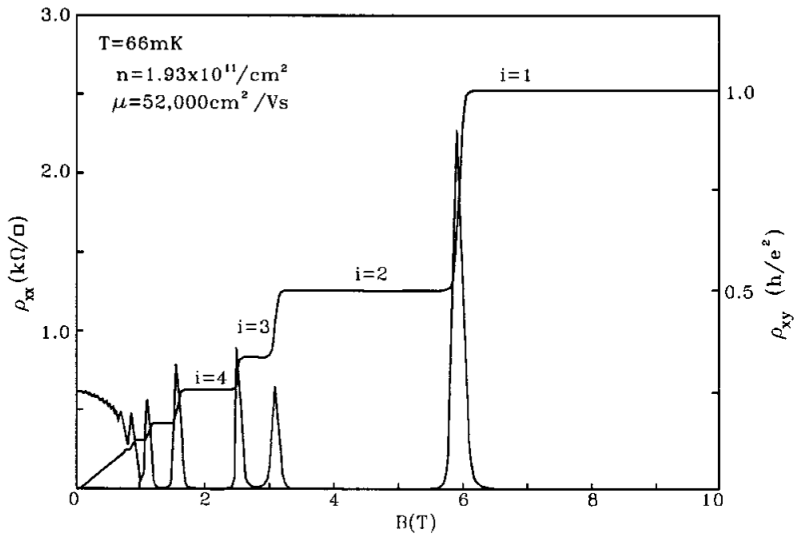


Figure 1.2.: Quantized Hall resistance plateaus in 2DEGs under high magnetic field. i corresponds to ν in Equation (1.4). Figure taken from Ref. [6]

immunity of the Hall resistance value to any details, measurements of Hall resistance are now a standard for the unit of resistance.

The salient features of IQHE can be understood by a semiclassical description. Applying a strong magnetic field on 2D system of electrons confines their movement strongly. Even under a voltage bias, the electrons would be localized, executing a cyclotron motion of radius $l_B = \sqrt{\hbar/eB}$. The latter quantity is called the magnetic length. The story ends here for an infinite sample – infinite Hall resistivity. However, experiments do witness a non-zero R_H and experimental samples do have a boundary. Indeed, at the boundary, electrons are prevented from executing a full cyclotron orbit. They hit the boundary and move forward in one direction. Movement in the opposite direction is prohibited due to time-reversal symmetry breaking by the magnetic field. Hence we learn that the integer quantum Hall effect is characterized by an insulating bulk and a conducting chiral edge. However, this semiclassical description does not explain details such as the emergence of plateaus in R_H and the abrupt transition from one plateau to the next. Indeed, the appearance of Planck's constant in the Hall resistivity in Equation (1.4) suggests this problem to be fundamentally quantum.

Landau levels

The physics of the integer quantum Hall effect is beautifully explained by a quantum treatment of non-interacting electrons under a strong magnetic field. Let us start with a

single electron in 2D under a strong magnetic field. This is described by the Hamiltonian

$$H = \frac{1}{2m}\left(\boldsymbol{p} + e\boldsymbol{A}\right)^2 \tag{1.5}$$

where m is the mass of the electron, $\boldsymbol{p}$ denotes the momentum, and $\boldsymbol{A}$ the vector potential associated with the magnetic field, $\boldsymbol{\nabla} \times \boldsymbol{A} = B\hat{z}$. We now work in the Landau gauge taking $\boldsymbol{A} = (0, xB, 0)$. The Hamiltonian then becomes

$$H = \frac{1}{2m}\left[p_x^2 + (p_y + eBx)\right]^2. \tag{1.6}$$

Note that although the magnetic field $\boldsymbol{B}$ is invariant under translations and rotations in the (x, y) plane, the Hamiltonian above is not manifestly so. This is a consequence of the gauge choice. However, it is still translation invariant in the y direction. Hence, the wavefunction must be of the form

$$\psi_{k_y}(x, y) = e^{ik_y y} f_{k_y}(x). \tag{1.7}$$

Acting the Hamiltonian on the wavefunction above, we arrive at the momentum-dependent Hamiltonian

$$H_k = \frac{p_x^2}{2m} + \frac{m\omega_B^2}{2}\left(x + k_y l_B^2\right)^2, \tag{1.8}$$

where we have introduced the cyclotron frequency $\omega_B = eB/m$. The above Hamiltonian is that of a quantum harmonic oscillator whose center of motion is $-k_y l_B^2$. The energy eigenvalues can hence readily be written down:

$$E_n = \hbar\omega_B\left(n + \frac{1}{2}\right). \tag{1.9}$$

These harmonic oscillator-like energy levels are called Landau levels and are characteristic of charged particles under a magnetic field. They can be understood to be a quantization of the semi-classical cyclotron behavior described in the previous paragraphs. The eigenfunctions can also be expressed to be:

$$\psi_{n,k} = e^{ik_y y} H_n\left(x + k_y l_B^2\right) e^{-\left(x + k_y l_B^2\right)^2/2l_B^2}, \tag{1.10}$$

where H_n denotes Hermite polynomials. The wavefunction betrays the degeneracy of the Landau levels not apparent in the energy eigenvalues. The wavefunction depends on two quantum numbers: n and k_y, while the energy depends only on n. Hence, the degeneracy of the Landau levels is the same as the number of k_y values in the system. Let us make this statement precise by putting the system in a box. We imagine that the electrons are placed in a box of sides L_x and L_y. k_y is then quantized in units of $2\pi/L_y$. Moreover, the center of motion of the harmonic oscillator in the x direction is confined within 0 and L_x.

We hence have the inequality:

$$0 \leq k_y l_B^2 \leq L_x \implies 0 \leq k_y \leq L_x/l_B^2. \tag{1.11}$$

The number of k_y values allowed in the system, and hence the degeneracy of the Landau levels is given by:

$$N_{deg} = \frac{L_y}{2\pi}\int_0^{L_x/l_B^2} dk = \frac{L_x L_y}{2\pi l_B^2} = \frac{\phi}{\phi_0}, \tag{1.12}$$

where $\phi = L_x L_y B$ is the total magnetic flux going through the quantum Hall system, and $\phi_0 = h/e$ is the magnetic flux quantum. The degeneracy of the Landau levels is thus the same as the number of flux quanta N_ϕ. Landau levels are filled starting from the lowest ones. It is thus useful to define the notion of filling fraction of the Landau levels. Let there be N_e electrons occupying the Landau levels. The filling fraction ν is then given by:

$$\nu = \frac{N_e}{N_{deg}}. \tag{1.13}$$

Edge states

It is not a typo that the same symbol has been used in Equation (1.4) for the quantization of the R_H plateaus and also the filling fraction above. To see the connection, we need to do something more. While we counted the degeneracy of the Landau levels by placing them on a finite manifold, this is not accounted for in the Hamiltonian. A boundary bears crucial consequences for the spectrum of the problem.

Let us add a confining potential $V(x)$ at the boundary in the $x-$direction. This confining potential is large near the boundaries and quickly drops to zero into the bulk of the system. Recalling that electron wavefunctions are localized around $x = -k_y l_B^2$, the confining potential can be approximated as $V(x) \approx V(-k_y l_B^2)$. The Hamiltonian then reads

$$H_{k_y} = \frac{p_x^2}{2m} + \frac{m\omega_B^2}{2}(x + k_y l_B^2)^2 + V(-k_y l_B^2). \tag{1.14}$$

The energy eigenvalues hence are shifted by the potential, gaining a dependence on k_y or equivalently the position of the wavefunction,

$$E_n(k_y) = \hbar\omega_B\left(n + \frac{1}{2}\right) + V(-k_y l_B^2). \tag{1.15}$$

Since the potential drops to zero in the bulk and is appreciable only near the boundary, the energy of states deep in the bulk remains the same as that of the unconfined system. Close to the edges, the states gain energy. Hence, the Landau levels bend, increasing in

energy near the edges of the system as shown in Figure 1.3. Note that since the position of states is given by k_y, it is equivalent to think of energy as a function of position or k_y.

The bending of Landau levels has profound consequences on the transport properties of the system. Let us consider the velocity of the states in the $y-$direction:

$$v_y = \frac{1}{\hbar}\frac{\partial E_n(k_y)}{\partial k_y} = -\frac{l_B^2}{\hbar}\frac{\partial V}{\partial x} = -\frac{1}{eB}\frac{\partial V}{\partial x} \tag{1.16}$$

Each wavefunction thus has a different velocity. Given the profile of confining potential we consider, only the states at the edges have a non-zero velocity. Those in the bulk are stationary. Also, the shape of the potential tells us that $v_y > 0$ on the left, and $v_y < 0$ on the right.

Let us now consider what happens when a potential difference is introduced between the two edges of the system in the $x-$direction. We assume that ν Landau levels are filled. The potential difference between the edges produces a current. The total current is calculated by summing the current due to each state of the system. The latter quantity for the state $\psi_{n,k}$ is given by $I_y(k_y) = -ev_y(k_y)$. Hence, the total current is:

$$I_y = -e\nu \int \frac{dk_y}{2\pi} v_y(k_y). \tag{1.17}$$

We note that the integration over k_y concerns the states in a single Landau level. Since the velocity depends only on k_y and not on n, the contribution of multiple Landau levels is accounted for simply by multiplying with the number of filled Landau levels. Using the relation $x = -k_y l_B^2$ to change integration variables, we write:

$$I_y = \frac{e\nu}{2\pi l_B^2}\int_0^{L_x} dx \frac{1}{eB}\frac{\partial V}{\partial x} = \frac{\nu e}{h}\left[V(L_x) - V(0)\right], \tag{1.18}$$

where $V(L_x) - V(0)$ denotes the potential difference across the edges in the $x-$direction. The Hall conductivity (defined as inverse of the resistivity) is hence given by

$$\sigma_{xy} = \frac{1}{R_H} = \frac{I_y}{e\left[V(L_x) - V(0)\right]} = \nu\frac{e^2}{h} \tag{1.19}$$

consistent with the experimental observations. The Hall conductivity allow an easy interpretation in terms of the bending of Landau levels. When the Fermi level of the system lies between two Landau levels, electrons must pay a prohibitive cost of the order of $\hbar\omega_B$ to reach the unoccupied levels and thus contribute to transport. However, close to the edges, the Landau levels bend and intersect the Fermi level on both sides of the system. Thus gapless, conducting, chiral modes are realized on the edges of the system. Any Landau level that crosses the Fermi level would lead to one such chiral mode on each edge of the system. Hence, the number of edge modes has a direct correspondence with the number of filled Landau levels. At high magnetic fields, ω_B is large and only the

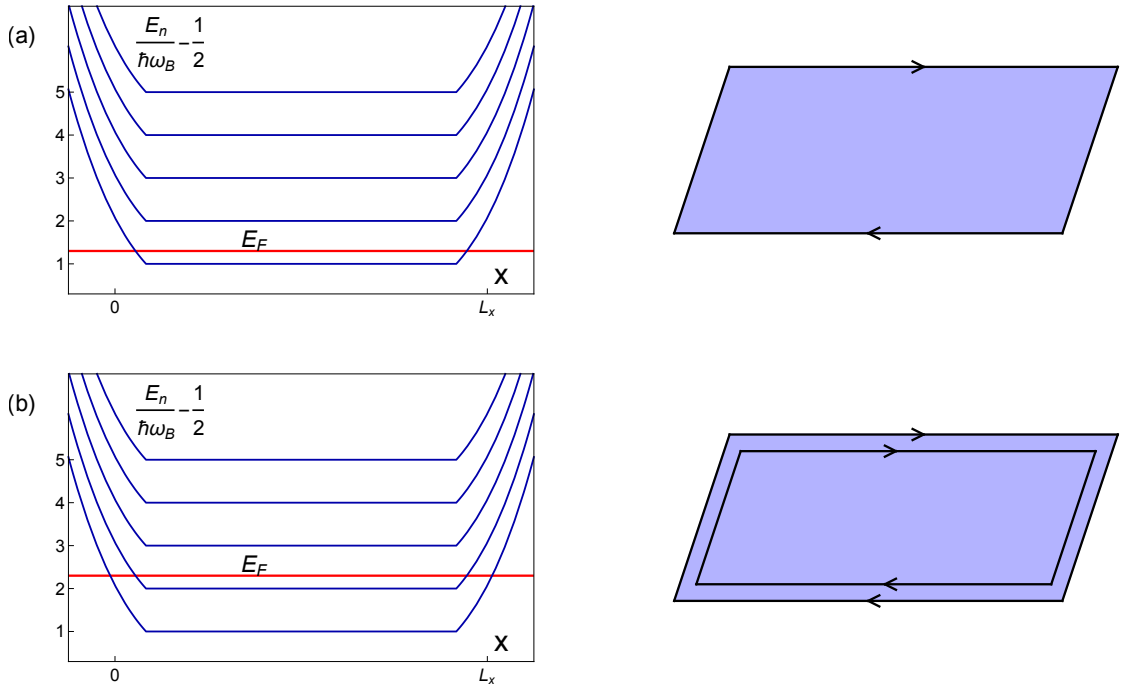


Figure 1.3.: Connection between the number of filled Landau levels and edge states. (a) The magnetic field is high, leading to a large ω_B. Only one Landau level has an energy lower than the Fermi energy E_F. The Landau level bends at the edges and intersects with the Fermi level, generating propagating modes on the edge. (b) The magnetic field is reduced, decreasing ω_B, leading to two Landau levels with an energy lower than E_F. We hence have two propagating modes on the edge.

first Landau level intersects the Fermi level. As the magnetic field is decreased, reducing ω_B, the higher Landau levels achieve an energy lower than the Fermi level (in the bulk), thus getting filled with electrons. They intersect the Fermi level at the edges, leading to additional edge modes. The process described above is depicted schematically in Figure 1.3. This interpretation fully explains the plateaus of R_H seen in Figure 1.2. The direct link between the number of filled Landau levels and the number of chiral modes appearing on the edges is the manifestation of a general phenomenon called bulk-boundary correspondence. A more striking example of this phenomenon is discussed in the next sections.

1.2.3. Fractional quantum Hall effect

While a theory of non-interacting electrons under a magnetic field was sufficient to explain the main features of the integer quantum Hall effect, experiments presented more surprises. A sample with higher mobility of electrons was subjected to stronger magnetic fields

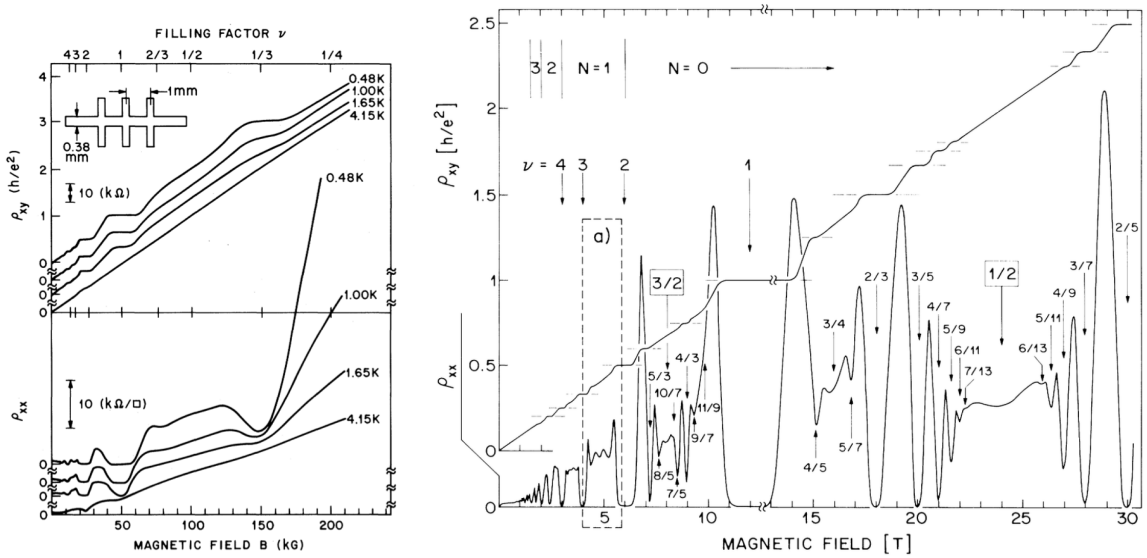


Figure 1.4.: Hall resistivity plateaus at fractional filling of Landau levels. (Left) First observation of a fractionally quantized Hall resistivity at $\nu = 1/3$, taken from Ref. [5]. (Right) Observation of fractionally quantized plateaus of Hall resistivity at a variety of rational fractions, taken from Ref. [18].

than those used previously for the integer quantum Hall effect. This experiment observed plateaus of R_H at a fractional value of the resistance quantum, $h/3e^2$ [5]. The latter resistance plateaus occurred for magnetic fields corresponding to fractional filling of the Landau levels. Further experiments revealed a plethora of plateaus at fractional filling of Landau levels [18] as shown in Figure 1.4. This phenomenon cannot be explained with non-interacting electrons. Indeed, the high mobility of electrons needed to see these plateaus emphasizes the importance of Coulomb interactions between electrons in stabilizing these phases. The Hamiltonian describing this system can hence be written as:

$$H = \sum_{i=1}^{N_e} \frac{1}{2m} \left[\boldsymbol{p}_i + e\boldsymbol{A}(\boldsymbol{r}_i)\right]^2 + \sum_{i \neq k}^{N_e} \frac{e^2}{|\boldsymbol{r}_i - \boldsymbol{r}_k|^2}. \tag{1.20}$$

The above Hamiltonian is deceptively simple. Recall the degeneracy associated with Landau levels in Equation (1.12). With partly filled Landau levels, this degeneracy assumes mammoth proportions, given the number of ways to fill up the states. For a filling fraction ν (that is fractional), since there are many ways to fill the states, the degeneracy of the system is $N_{deg} = \binom{N_\phi}{\nu N_\phi} \sim \left(\frac{1}{\nu}\right)^{\nu N_\phi} \left(\frac{1}{1-\nu}\right)^{(1-\nu)N_\phi}$, a macroscopically large number. This immediately rules out degenerate perturbation theory, even numerically. A direct theoretical approach to this problem is hence difficult.

Laughlin wavefunction

Advances on the theoretical front were made by Laughlin, who instead of deriving a wavefunction by diagonalizing the Hamiltonian, simply wrote the wavefunction down [8]. The form of the wavefunction was motivated by the symmetries of the problem and the Fermi-Dirac statistics of the electrons. Coulomb interaction manifestly preserves rotational invariance. This motivates us to consider angular momentum eigenstates. Working in the symmetric gauge to exploit the rotational invariance of the system, it can be shown that the single electron wavefunction in the lowest Landau level is:

$$\psi_{LLL,m} \sim \left(\frac{z}{l_B}\right)^m e^{-|z|^2/4l_B^2}, \tag{1.21}$$

where $z = x + iy$ is the position of the electron on the $x - y$ plane. That this is the angular momentum eigenstate is readily seen by acting the angular momentum operator $J = \hbar\left(z\partial - \bar{z}\bar{\partial}\right)$, giving us $H\psi_{LLL,m} = \hbar m\psi_{LLL,m}$. Normalizing the wavefunction and calculating the radial expectation value, one can see that these states form exponentially localized concentric rings at a radius $\sqrt{2m}l_B$. Notice that the radius depends on the angular momentum of the electron.

From the above, it is easy to build directly the two-particle wavefunction. In the two-particle system, there exists the total angular momentum $J = J_1 + J_2$ and the relative angular momentum $j = J_1 - J_2$. Restricted to the lowest Landau level, it is not too difficult to see that the eigenfunction of the angular momentum operators is given by

$$\psi_{LLL,m} \sim (z_1 + z_2)^M (z_1 - z_2)^m e^{-\left(|z_1|^2 + |z_2|^2\right)/4l_B^2}, \tag{1.22}$$

where $M = m_1 + m_2$ gives the total angular momentum and $m = m_1 - m_2$, the relative angular momentum.

While it is not possible to generalize the above arguments to a greater number of electrons, motivated by the single and two-particle wavefunctions in the lowest Landau level, Laughlin proposed the following wavefunction for the fractional quantum Hall state at filling fraction $\nu = 1/m$:

$$\psi_m(z_i) = \prod_{i<j}^{N_e} (z_i - z_j)^m e^{-\sum_{i=1}^{N_e} |z_i|^2/4l_B^2}, \tag{1.23}$$

where $z_i = x_i + iy_i$ denotes the position of the electrons on the $2D$ plane, and N_e is the total number of electrons. The Laughlin wavefunction, respecting the rotational symmetry of the problem, is an eigenfunction of the relative angular momenta of the electrons. The Fermi statistics of electrons are obeyed when m is an odd integer. When two electrons approach each other, the wavefunction strongly decays, with a zero of order m. On the

other hand, the electrons are all exponentially localized near the origin. It hence achieves a balance between attractive and repulsive forces.

We now test if the wavefunction describes the fractionally quantized Hall plateaus. The highest power of any single coordinate, say z_1 in the above wavefunction is $z_1^{m(N_e-1)}$. As can be seen by acting the angular momentum operator of z_1, the exponent represents the maximum angular momentum of the electron. Hence the maximum radius of the electron is given by $\sqrt{2mN_e}l_B$ where the -1 is negligible when N_e is macroscopically large. The area of the fractional quantum Hall system is then given by $A \sim 2\pi m N_e l_B^2$. From Equation (1.12), the degeneracy of the Landau levels is $N_{deg} = AB/\phi_0$. From the input above, we find $N_{deg} = mN_e$. Hence, the Landau level filling fraction is $\nu = N_e/N_{deg} = 1/m$, consistent with the observed quantum Hall conductance. Moreover, Laughlin exactly diagonalized the full Hamiltonian with a few electrons, finding an overwhelming overlap with the wavefunction proposed above.

Quasiholes are anyons: fractional charge and statistics

Having established that the Laughlin wavefunction successfully accounts for the fractionally quantized plateaus of the FQHE, we now turn our attention to studying the excitations above the Laughlin ground state. These excitations are generated by slightly increasing or decreasing the electronic density, which can be understood as adding or removing flux quanta in the Landau levels. Laughlin proposed that a quasihole excitation could be created by inserting a single flux quantum at a specific location, z_0, in the quantum Hall system. This insertion effectively increases the angular momentum of each electron by 1. The resulting wavefunction can be expressed as:

$$\begin{aligned}\psi_m^{+z_0}(z_i,t) = \prod_{i=1}^{N}(z_i - z_0(t)) \prod_{j<k}(z_j - z_k)^m e^{-\sum_{l=1}^{N_e}|z_l|^2/4l_B^2} \\ \equiv e^{\sum_i \log(z_i - z_0(t))}\psi_m(z_i)\end{aligned} \tag{1.24}$$

Here, the electron density vanishes at z_0, signaling a hole in the quantum Hall fluid. This quasihole has remarkable properties: a fractional charge and a fractional exchange phase. These properties are illustrated by computing the phase $e^{i\gamma}$ gathered by the quasihole as it moves in a closed loop. The phase is a sum of the dynamical contribution (which we discard by setting the energy of the quasihole to be zero) and the Berry phase which reveals the exotic properties. The Berry phase due to circular motion of a Laughlin quasihole

$$\frac{d\gamma}{dt} = i\left\langle \psi_m^{+z_0}(z_i,t) \left| \frac{d}{dt} \right| \psi_m^{+z_0}(z_i,t) \right\rangle \tag{1.25}$$

was first computed by Ref. [15], giving us:

$$\gamma = 2\pi\nu\frac{\phi}{\phi_0} \tag{1.26}$$

where ϕ denotes the flux contained in the circle of radius R. While moving in the quantum Hall fluid the quasihole picks up an Aharanov-Bohm phase due to the background magnetic field. Let e^* denote the quasihole charge. The Aharanov-Bohm phase is then given by

$$\gamma = \frac{e^*}{\hbar}\oint \boldsymbol{A}.d\boldsymbol{l} = \frac{e^*}{\hbar}\phi = 2\pi\frac{e^*}{e}\frac{\phi}{\phi_0} \tag{1.27}$$

Of course, Equations (1.26) and (1.27) must be equal since both are different manifestations of the phase gathered due to the closed loop motion of the quasihole. Comparing the two, we hence find

$$e^* = \nu e \tag{1.28}$$

establishing the fractional charge of Laughlin quasiholes.

We now consider an excited state with two quasiholes. The corresponding wavefunction is expressed as

$$\psi_m^{z_a,z_b}(z_i) = \prod_i (z_i - z_a)(z_i - z_b)\psi_m(z_i) \tag{1.29}$$

We imagine adiabatically taking z_a in a closed loop. If the closed loop taken by z_a does not contain z_b, the result is the same as before yielding a Berry phase $\gamma = 2\pi\nu\frac{\phi}{\phi_0}$. If the closed loop does contain the quasihole, there exists a modification. Since quasihole is imagined to be the insertion of flux quantum, one extra flux quantum must be added to ϕ in Equation (1.26), giving the total Berry phase here to be

$$\gamma = 2\pi\nu\frac{\phi}{\phi_0} + 2\pi\nu \tag{1.30}$$

The final term above is mathematically the consequence of the additional pole due to the term $(z_i - z_b)$ in the wavefunction.

The extra factor of $2\pi\nu$ is interpreted as the phase due to one quasiparticle going in a closed loop around another, or a braiding operation. It then follows that the exchange phase of two Laughlin quasiholes is $e^{i\pi\nu}$, where $\nu = 1/m$ is fractional. Laughlin quasiholes are anyons!

Note that we chose to work here with quasiholes, given the simplicity of the wavefunctions. Quasiparticle wavefunctions are built by removing a flux quantum, achieved by multiplying the Laughlin groundstate wavefunction with the product $\prod_i (2\partial_{z_i} - z_0)$.

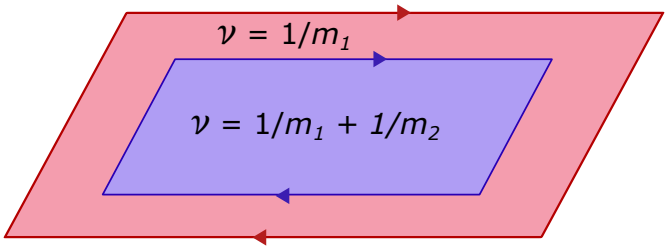


Figure 1.5.: A schematic of hierarchical FQHE states. Red represents a Laughlin FQH state of electrons of filling fraction $\nu = 1/m_1$, leading to emergent anyons. Strong interaction between the anyons forms a second Laughlin state of *anyons*, shown in blue. The total filling fraction of the FQHE is a sum of the two individual Laughlin filling fractions $\nu = 1/m_1 = 1/m_2$.

The analysis above can be adapted also for quasiparticles, yielding similar results for the fractional charge and statistics.

Hierarchical states

The Laughlin wavefunction naturally explains the series of R_H plateaus occurring at fractional values of $\nu = 1/m$ with m an odd integer. The latter series of fractional quantum Hall states is now called the Laughlin series. There however exist other plateaus at fractional filling such as $\nu = 2/5,\ 2/3,\ 3/7$, and so on, that do not fall into the Laughlin series. These remain unexplained by the Laughlin wavefunction.

A natural extension of Laughlin's arguments seems to explain many of the observed plateaus [46, 55]. Consider anyons in a Laughlin state with positions η_i, charge $e^* = \pm e/m$ and exchange phase $\alpha = \pi/m$. We imagine that these anyons form a Laughlin-like state on top of the original Laughlin state, as schematically indicated in Figure 1.5. The resulting wavefunction would take the form:

$$\psi_{m,p} \sim \prod_{i<j}^{N_a} (\eta_i - \eta_j)^{2p+1/m} \prod_{k<l}^{N_e} (z_k - z_l)^m e^{-\sum_{i=1}^{N_e} |z_i|^2} e^{-\sum_{k=1}^{N_a} |\eta_i|^2}, \tag{1.31}$$

where N_a is the number of anyons. Let us focus on the first term. Exchanging any two η yields a phase π/m, consistent with them being anyons. But how does this additional term influence the filling factor?

The maximum angular momentum of any single anyon is given by $\tilde{N}\,(2p \pm 1/m)$, where the sign depends on the charge of the anyons forming the new Laughlin state. The area of the fractional quantum Hall droplet (due to the anyons) is hence $A \sim 2\pi\,(2p \pm 1/m)\,\tilde{N} m l_B^2$. Note that we have replaced l_B^2 with $m l_B^2$ since the magnetic length of charge e/m anyons is $\sqrt{m\hbar/eB}$. Now, the number of electronic states in the Landau level is AB/ϕ_0, and hence

the number of anyon states in the Landau level is mAB/ϕ_0. The anyon filling fraction of the Landau level is then given by

$$\frac{\tilde{N}}{mN_{deg}} \equiv \nu_{anyon} = \mp\frac{1}{2pm^2 \pm m} \tag{1.32}$$

the appearance of the signs implies that filling fraction is increased by quasiparticles and decreased by quasiholes. Adding to this the filling fraction due to electrons, the filling fraction of the composite fractional quantum Hall state is:

$$\nu = \frac{1}{m} \mp \frac{1}{2pm^2 \pm m} = \frac{1}{m \pm \frac{1}{2p}}. \tag{1.33}$$

The above construction can be generalized further by forming Laughlin states of anyons in the new anyon Laughlin state. It is easy to see that the resulting filling fraction is given by:

$$\nu = \frac{1}{m \pm \frac{1}{2p_1 \pm \frac{1}{2p_2 \pm \ldots}}}. \tag{1.34}$$

Starting with $\nu = 1/3$, taking $p_i = 1$ and condensing anyons, one obtains the filling fractions of the prominently observed plateaus in fractional quantum Hall experiments: $\nu = 1/3,\ 2/5,\ 3/7,\ 4/9,\ 5/11$. It is also possible to obtain the $\nu = 2/3$ state, starting with $\nu = 1$ and $p_1 = 1$, condensing quasiholes.

We note that an alternative, perhaps more microscopic approach, albeit leading to the same results, is the theory of composite fermions [47]. In the latter, it is imagined that the fundamental excitations of the FQHE comprise bound states of electrons and an even number of magnetic flux quanta, dubbed composite fermions. FQHE is then understood very simply as an IQHE of the composite fermions, yielding remarkable agreement with experimental observations.

To summarize, hierarchical states, also known as Jain states, can be understood as fractional quantum Hall states constructed by combining Laughlin states of electrons with Laughlin states of anyons that exist in the base Laughlin state, and then iterating this process. While the Laughlin series is relatively well understood both theoretically and experimentally, there remains significant debate surrounding the non-Laughlin fractions. There are numerous candidate theories describing specific filling fractions of the FQHE and yet there is limited agreement between theory and experiment. These states are hence the central focus of this thesis.

1.3. Chern-Simons approach to fractional quantum Hall

Having dealt with the fractional quantum Hall effect from the microscopic perspective of electrons, we now seek a coarse-grained, effective description that captures the important features of the fractional quantum Hall effect. Namely, fractional quantized conductivity plateaus, emergent anyonic excitations, and chirally propagating edge states.

In this section, we will show that the Chern-Simons theory, given by the Lagrangian density

$$\mathcal{L}_{cs} = \frac{k}{4\pi}\epsilon_{\mu\nu\lambda}a_\mu\partial_\nu a_\lambda \tag{1.35}$$

captures the topological properties of FQHE [56–58]. Here, a_μ denotes the Chern-Simons gauge field, $\epsilon_{\mu\nu\lambda}$ denotes the Levi-Civita symbol and k is a constant, called the level of the Chern-Simons term. The indices $\mu,\ \nu,\ \lambda$ take values $0,\ 1,\ 2$, and Einstein summation convention is implied.

Furthermore, placing the Chern-Simons theory on a finite manifold reveals the edge physics of the FQHE through gauge invariance arguments. This approach allows to easily highlight the bulk-boundary correspondence in the FQHE: the anyons on the edge exhibit the same topological properties—such as charge and exchange phase—as those in the bulk. We leave a discussion of the edge physics to the next chapter.

There are various hints that the Chern-Simons term should describe quantum Hall physics. First, the symmetries. Quantum Hall effect preserves translation and rotational symmetry, and of course, gauge invariance, but breaks time-reversal and parity symmetries. The lowest scaling dimension term that satisfies these symmetry requirements in two spatial dimensions is the Chern-Simons term. The existence of anyons in the FQHE, as shown by the Laughlin wavefunction, is another strong hint. It is well known (as we will see below) that the Chern-Simons term binds fluxes with charges. A flux-charge composite is indeed a prototype of anyons, indicating the connection between FQHE and Chern-Simons theory [14].

1.3.1. Level Quantization of Chern-Simons theory

In this section we show that the Chern-Simons level k assumes quantized values. We start with the Chern-Simons action at finite temperature (periodic imaginary time).

$$S_{cs} = \frac{k}{4\pi}\int d^2x \int_0^\beta d\tau\ \epsilon_{\mu\nu\lambda}a_\mu\partial_\nu a_\lambda \tag{1.36}$$

where β denotes the inverse temperature. Observables are associated with gauge invariant quantities. The most fundamental gauge invariant objects in gauge theories are Wilson

loops. Let us consider a Wilson loop in the time-direction:

$$W(\boldsymbol{r}) = e^{\frac{ie}{\hbar}\int_0^\beta a_0 d\tau}. \tag{1.37}$$

The above object is also invariant under so-called large gauge transformations

$$a_0 \to a_0 + \frac{2\pi n}{\beta}\frac{\hbar}{e} \tag{1.38}$$

where n is an integer. Large refers to the fact that the gauge transformations are not continuously connected to the identity transformation. The existence of a periodic time direction, allowing the gauge field to wind around it means that the temporal component of the Chern-Simons field can be thought to be periodic in the temporal direction with periodicity $2\hbar\pi/e\beta$. Under large gauge transformations, the Chern-Simons term transforms as

$$S_{cs} \to S_{cs} + \frac{k}{2\pi}\frac{2\pi n}{\beta}\frac{\hbar}{e}\int_0^\beta d\tau \int d^2x \; f_{12}, \tag{1.39}$$

where $f_{\mu\nu} = \partial_\mu a_\nu - \partial_\nu a_\mu$. Now we imagine that the $2D$ space is a sphere, and we stick in a flux quantum inside the surface of the sphere. The spatial integral then gives $\int d^2r f_{12} = h/e$, while the temporal integral just gives β. The result is that the Chern-Simons action is not gauge invariant

$$\delta S_{cs} = \frac{k}{2\pi}\frac{2\pi n}{\beta}\frac{\hbar}{e}\frac{h}{e}\beta \tag{1.40}$$

However, the action is allowed to violate gauge invariance as long as the partition function, from which all physical observables stem, is still gauge invariant. Thus we require

$$e^{i\delta S_{cs}/\hbar} = 1 \tag{1.41}$$

This condition imposes that the Chern-Simons level k must be quantized:

$$k = m\frac{e^2}{\hbar}, \tag{1.42}$$

where m is an integer.

1.3.2. Chern-Simons theory for Laughlin fractions

Let us now couple the Chern-Simons gauge field to the electromagnetic field, which we denote by A_μ. For this, we need to look for conserved currents in the Chern-Simons theory. The only possible conserved quantity in this theory which represents the charge current

that couples to the electromagnetic field is

$$J_\mu = \frac{e^2}{h}\epsilon_{\mu\nu\lambda}\partial_\nu a_\mu. \tag{1.43}$$

The above equation tells us that the magnetic flux of the Chern-Simons theory (rhs) is the electric charge density (lhs) coupling to the electromagnetic field. Then the action including the coupling between the Chern-Simons and electromagnetic fields is given by

$$S_{cs+em}[a;A] = \frac{e^2}{\hbar}\int d^3x\ \epsilon_{\mu\nu\lambda}\left[\frac{m}{4\pi}a_\mu\partial_\nu a_\lambda + \frac{1}{2\pi}A_\mu\partial_\nu a_\lambda\right]. \tag{1.44}$$

We compute the Hall conductivity by integrating out the Chern-Simons field a_μ. For a quadratic action, this amounts to simply plugging in the equation of motion $a_\mu = -\frac{1}{m}A_\mu$ into the action, giving us:

$$S_{\text{eff}}[A] = \frac{e^2}{\hbar}\frac{1}{4\pi m}\int d^3x\ \epsilon_{\mu\nu\lambda}A_\mu\partial_\nu A_\lambda \tag{1.45}$$

where the subscript eff denotes that the dynamical gauge field has been integrated out. This theory gives us the response of the Chern-Simons gauge field to the electromagnetic fields (and nothing more). The currents produced by the electromagnetic field are given by $\langle J_\mu\rangle = \delta S_{\text{eff}}[A]/\delta A_\mu$ which yields for the effective action of Equation (1.45):

$$\langle J_i\rangle = \frac{1}{m}\frac{e^2}{2\pi\hbar}\ \epsilon_{i\nu\lambda}\partial_\nu a_\lambda = \frac{1}{m}\frac{e^2}{2\pi\hbar}\epsilon_{ij}E_j, \tag{1.46}$$

where E_j denotes the electric field in the $j-$direction. The above equation gives the fractionally quantized Hall conductivity of FQHE

$$\sigma_{xy} = \frac{\langle J_1\rangle}{E_2} = \frac{1}{m}\frac{e^2}{h} \tag{1.47}$$

as long as m is an odd integer. Hence, the Chern-Simons term describes (fermionic) Laughlin FQHE state when the Chern-Simons level is an odd integer.

To see now the anyons with fractional charge and statistics, we couple the Chern-Simons gauge field to its own current, j_μ. Indeed, elementary density fluctuations of the Chern-Simons gauge field will turn out to be anyons. To this end, we add the following term to the action

$$\Delta S = \int d^3x\ a_\mu j_\mu. \tag{1.48}$$

In the absence of the background electromagnetic field, we have the following equation of motion:

$$j_\mu = \frac{me^2}{h}\epsilon_{\mu\nu\lambda}\partial_\nu a_\lambda. \tag{1.49}$$

Consider a localized unit charge (of the Chern-Simons field) at location $\boldsymbol{x_0}$. The latter is given by source current $j_1 = j_2 = 0$, $j_0 = e\delta^2(\boldsymbol{x} - \boldsymbol{x_0})$. Employing this source in Equation (1.49):

$$f_{12} = \frac{h}{em}\delta^2(\boldsymbol{x} - \boldsymbol{x_0}) \tag{1.50}$$

Hence, the effect of the Chern-Simons term is to attach a flux h/em to particles of charge e (where the charge is under the Chern-Simons field, not the electromagnetic field). As we saw in Equation (1.43), the flux of the Chern-Simons field gives the charge of the electromagnetic field. Hence, using Equations (1.43) and (1.50):

$$J_0 = \frac{e^2}{h}f_{12} = \frac{e}{m}\delta^2(\boldsymbol{x} - \boldsymbol{x_0}) \tag{1.51}$$

which shows the fractional charge of excitations in Chern-Simons theory. The fractional statistics of these excitations can be computed with a simple Aharanov-Bohm phase calculation. Each particle of charge e in the Chern-Simons theory necessarily carries also a flux h/em. Carrying one particle in a closed loop around another yields an Aharanov-Bohm phase $e^{\frac{i}{\hbar}e\times h/em} = e^{2\pi i/m}$. Hence, the phase for a single exchange is $e^{i\pi/m}$.

1.3.3. Chern-Simons theory for hierarchical fractions

Having understood the effective description of Laughlin FQHE, we proceed to more general hierarchical states of composite fractions. The approach of building wavefunction for the hierarchical states in Section 1.2.3 was to start from a Laughlin state, and assume that the Laughlin anyons form another fractional quantum Hall state with a Laughlin filling fraction. We use a similar line of thought to build Chern-Simons theories for the composite fractions.

The Laughlin Chern-Simons field a_μ is thought to be an emergent gauge field born out of strong electron interactions. The electromagnetic field A_μ couples to a current given by a_μ. The emergent theory, whose dynamics is described by a Chern-Simons term, hosts anyons.

We can similarly imagine that the strong interactions between the anyons give rise to another emergent gauge field $\tilde{a}$. Similar to Equation (1.43), the new gauge field $\tilde{a}_\mu$ forms a current $\tilde{j}_\mu = e^2\epsilon_{\mu\nu\lambda}\partial_\nu\tilde{a}_\lambda/h$ to which a_μ couples. $\tilde{a}_\mu$ is also endowed with dynamics via a

Chern-Simons term. The full action then reads

$$S_{cs+em}[a,\tilde{a},A] = \frac{e^2}{2\pi\hbar}\int d^3x\ \epsilon_{\mu\nu\lambda}\left[A_\mu\partial_\nu a_\lambda + \frac{m}{2}a_\mu\partial_\nu a_\lambda + a_\mu\partial_\nu\tilde{a}_\lambda + \frac{\tilde{m}}{2}\tilde{a}_\mu\partial_\nu\tilde{a}_\lambda\right] \quad (1.52)$$

As before, we integrate out the emergent gauge fields $\tilde{a}$ and a to calculate the Hall conductivity. Repeating the same steps, we find:

$$\sigma_{xy} = \frac{1}{m - \frac{1}{\tilde{m}}}\frac{e^2}{h} \quad (1.53)$$

consistent with Equation (1.34) of the hierarchical wavefunctions. The charge of the resulting quasiparticles can be also be computed as before by plugging in a source charge e of each gauge field. For a charge coupling to a, we find

$$f_{12} = \frac{h}{e}\frac{1}{m - \frac{1}{\tilde{m}}}\delta^2(\boldsymbol{x} - \boldsymbol{x_0}), \quad (1.54)$$

and for a charge coupling to $\tilde{a}$

$$f_{12} = \frac{h}{e}\frac{1}{m\tilde{m} - 1}\delta^2(\boldsymbol{x} - \boldsymbol{x_0}). \quad (1.55)$$

By comparison with Equation (1.43), we find the quasiparticle charges to be $e^* = e/(m - 1/m),\ e/(m\tilde{m} - 1)$. For the $\nu = 2/5$ state, we have $m = 2$ and $\tilde{m} = -1$, giving us $e^* = e/5,\ 2e/5$.

It is possible to generalize this construction by adding more Chern-Simons gauge fields. The resulting states can be shown to have a filling fraction

$$\nu = \frac{1}{m \pm \frac{1}{\tilde{m}_1 \pm \frac{1}{\tilde{m}_2 \pm \ldots}}} \quad (1.56)$$

consistent with the result calculated before starting from microscopic wavefunctions in Equation (1.34). Such a theory contains N emergent gauge fields, $a_{\mu i},\ i = 1, \ldots, N$ and the action describing it can be readily written down as

$$S_{cs+em}[a_i, A] = \frac{e^2}{h}\int d^3x\ \sum_{ij}\epsilon_{\mu\nu\lambda}\left[\frac{1}{4\pi}K_{ij}a_{\mu i}\partial_\nu a_{\lambda j} + \frac{1}{2\pi}\delta_{ij}Q_i A_\mu\partial_\nu a_{\lambda j}\right] \quad (1.57)$$

where the $K-$matrix describes the various Chern-Simons couplings. The current operator coupling to the electromagnetic field is

$$J_\mu = \frac{e^2}{h}\sum_i Q_i J_{i\mu} = \frac{e^2}{h}\sum_i Q_i\epsilon_{\mu\nu\lambda}\partial_\nu a_{\lambda i} \quad (1.58)$$

where $J_{i\mu} = \epsilon_{\mu\nu\lambda}\partial_\nu a_{\lambda i}$ is current of the $i-$th emergent gauge field. Charge vector Q_i specifies the combination of the emergent gauge fields that couples to the electromagnetic field.

Integrating out the dynamical gauge fields from the action we find the equation of motion of the above theory:

$$K_{ij}a_{j\lambda} = -Q_i A_\lambda. \tag{1.59}$$

From this, following similar steps as the Laughlin case, we find the filling fraction to be

$$\nu = \sum_{ij}(K^{-1})_{ij}Q_iQ_j. \tag{1.60}$$

Let us now add excitations in the theory. The most general quasiparticle is composed of excitations or vortices from each Chern-Simons gauge field. Denoted $\psi_{\boldsymbol{g_\alpha}}$, the quasiparticle is labelled by an $N-$component vector $\boldsymbol{g}_\alpha$. This quasiparticle is modeled by adding a source term to the action:

$$\Delta S = \int d^3x \; g_{\alpha i}a_{\mu i}j_\mu \tag{1.61}$$

where $g_{\alpha i}$ denotes the number of units of $a_{\mu i}$ that make up the quasiparticle $\psi_{\boldsymbol{g_\alpha}}$. Let us compute the equation of motion of $S_{cs} + \Delta S$, taking $A_\mu = 0$ for the moment. This gives us

$$g_{\alpha i}j_\mu = \frac{e^2}{h}K_{ij}\epsilon_{\mu\nu\lambda}\partial_\nu a_{\lambda j} \tag{1.62}$$

Considering a stationary quasiparticle, we take $j_1 = j_2 = 0$, and $j_0 = e\delta^2(\boldsymbol{x} - \boldsymbol{x_0})$. We hence have

$$(f_{12})_j = \frac{h}{e}g_{\alpha i}(K^{-1})_{ij}\delta^2(\boldsymbol{x} - \boldsymbol{x_0}) \tag{1.63}$$

Plugging the above into Equation (1.58), the charge of quasiparticle $\psi_{\boldsymbol{g_\alpha}}$ is found to be:

$$q_{\boldsymbol{g}_\alpha} = \sum_{ij} g_{\alpha i}(K^{-1})_{ij}Q_j. \tag{1.64}$$

We again compute the exchange phase with an Aharanov-Bohm phase calculation. The Chern-Simons flux attached to each quasiparticle $\psi_{\boldsymbol{g_\alpha}}$ is $\sum_i \frac{h}{e}g_{\alpha i}(K^{-1})_{ij}$, and the charge of each quasiparticle (under the Chern-Simons fields, not the electromagnetic field) is $e\sum_j g_{\alpha j}$. The Aharanov-Bohm phase is then given by $e^{\frac{i}{\hbar}\sum_{ij} g_{\alpha i}(K^{-1})_{ij}g_{\alpha j}} = e^{i2\pi\sum_{ij} g_{\alpha i}(K^{-1})_{ij}g_{\alpha j}}$. The

exchange phase is hence given by

$$\theta_{\boldsymbol{g_\alpha g_\alpha}} = \pi \sum_{ij} g_{\alpha i}(K^{-1})_{ij} g_{\alpha j}. \tag{1.65}$$

By the same arguments, it is easy to see that the exchange phase between quasiparticles $\psi_{\boldsymbol{g_\alpha}}$ and $\psi_{\boldsymbol{g_\beta}}$ is

$$\theta_{\boldsymbol{g_\alpha g_\beta}} = \pi \sum_{ij} g_{\alpha i}(K^{-1})_{ij} g_{\beta j} \tag{1.66}$$

1.4. Conclusion

This chapter introduced the notion of anyons, particles that are intermediate between fermions and bosons, carrying a fractional exchange phase. We showed that these exotic particles have found home in the fractional quantum Hall effect (FQHE), a system characterized by strong electronic interactions.

The existence of anyons in the FQHE was shown by two different approaches. First, we outline a microscopic description of FQHE using the Laughlin wavefunction and its generalized avatars. It is shown that these wavefunctions naturally explain the experimentally observed FQHE plateaus and that their excitations are anyons. Next, we considered a coarse-grained, effective field theory description of the FQHE physics with the Chern-Simons theory. Here too, we showed that the FQHE hosts anyonic excitations. The latter sets the stage for exploring the edge physics of FQHE, the central focus of this thesis, and the subject of the next chapter.

Chapter 2.

Quantum Hall effect: edge

The previous chapter firmly established the existence of anyons in the FQHE. Now, we address the challenge of experimentally probing these anyons to verify their existence. A major issue is that the FQHE system is gapped. The energy gap between Landau levels is huge, preventing anyon transport in the bulk. However, near the edge of the sample, Landau levels bend and intersect the Fermi level, creating gapless edge states. This makes the edge a natural playground for investigating the response of anyons to external drives.

In this chapter, we begin by placing the Chern-Simons theory on a bounded manifold, akin to a real FQHE system. Using gauge invariance arguments, we show that the edge physics is described by a chiral Luttinger liquid or a chiral free bosonic field. Importantly, starting from the Chern-Simons action allows to highlight the bulk-boundary correspondence, showing that the anyons at the edge possess the same topological properties—charge and exchange statistics—as the anyons in the bulk.

We then introduce the technical tools needed to study edge physics in the FQHE. We develop a bottom-up approach to describing FQHE edge physics, starting from a chiral Luttinger liquid action and phenomenological inputs. We emphasize on three key topological properties of anyons: charge, scaling dimension, and exchange statistics. These properties can be probed in edge experiments and used to characterize the FQHE state. We also describe the theoretical framework for quantum point contacts, an indispensable device in FQHE edge experiments, and the Keldysh formalism, the technical tool employed throughout this thesis. The chapter concludes with a review of state-of-the-art experiments that probe the aforementioned properties, highlighting the challenges faced. The latter underscores the motivations for the research carried out in this thesis.

2.1. Chiral Luttinger liquids from Chern-Simons theory

We consider now a single Chern-Simons term placed on a space with a boundary. For concreteness, we assume that the Chern-Simons term exists in the lower half of the $x - y$

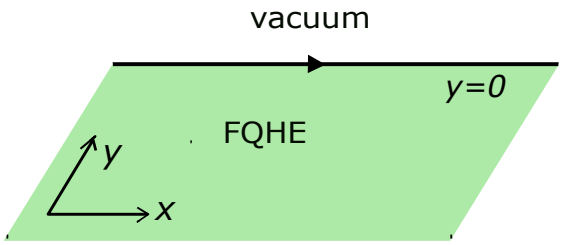


Figure 2.1.: FQHE on a bounded manifold. $y < 0$ contains the FQHE system, and $y > 0$ is vacuum. The interface between FQHE and vacuum hosts a chirally propagating boson.

plane, with vacuum in $y > 0$.

$$S_{cs} = \int dxdt \int_{-\infty}^{0} dy\ \epsilon_{\mu\nu\lambda} a_\mu \partial_\nu a_\lambda \tag{2.1}$$

Consider now a gauge transformation $a_\mu \to a_\mu + \partial_\mu \omega$, giving us an extra piece

$$\delta S_{cs} = \int dxdt\ \omega \left(\partial_t a_x - \partial_x a_t\right)\Big|_{y=0}, \tag{2.2}$$

rendering the Chern-Simons action gauge dependent. To fix this, we impose that only those gauge transformations that vanish at $y = 0$ are allowed. By restricting the allowed gauge transformations, one is removing some redundancies in the description. This amounts to introducing new physical degrees of freedom into the system. To derive an action for these new degrees of freedom, we choose a gauge $a_t + v a_x = 0$, where v is a parameter we introduce. We subsequently employ a coordinate transformation $t' = t$, $x' = x - vt$, $y' = y$. In these coordinates, the gauge field transforms as $a'_{t'} = a_t + v a_x$, $a'_{x'} = a_x$, and $a'_{y'} = a_y$. The gauge fixing condition hence reduces to $a'_{t'} = 0$. By the equation of motion of $a'_{t'}$, the gauge fixing gives the constraint $f'_{x'y'} = 0$. The latter constraint is solved by the solutions $a'_{x'} = \partial_x \phi$ and $a'_{y'} = \partial_y \phi$, where ϕ is an arbitrary smooth function of the coordinates. This solution is pure gauge. However the restricted gauge transformations at the boundary means that ϕ will become a physical variable at $y = 0$. To see this, let us plug the above solution into the Chern-Simons action, setting $a'_{t'} = 0$:

$$\begin{aligned} S_{cs} &= \frac{1}{4\pi} \int dx'dy'dt'\ \left[\partial_{x'}\phi \partial_{t'}\partial_{y'}\phi - \partial_{y'}\phi\partial_{t'}\partial_{x'}\phi\right], \\ &= \frac{1}{4\pi} \int dx'dt'\ \partial_{t'}\phi\partial_{x'}\phi\Big|_{y=0}. \end{aligned} \tag{2.3}$$

Transforming back to the unprimed coordinates, we have the action

$$S = \frac{1}{4\pi} \int dxdt \left[-\partial_t\phi\partial_x\phi - v(\partial_x\phi)^2\right]. \tag{2.4}$$

The above equation describes a chirally propagating bosonic field, with v representing the velocity of propagation. This system is also called a chiral Luttinger liquid. We conclude that Chern-Simons theory hosts a chiral boson at its boundary. It should be straightforward to see that a fractional quantum Hall system with N emergent Chern-Simons terms will host N chiral Luttinger liquids on its boundary, since the $K-$matrix of Equation (1.57) can be diagonalized. The resulting action is given by:

$$S = \frac{1}{4\pi} \int dxdt \sum_{ij} [-K_{ij}\partial_t \phi_i \partial_x \phi_j - V_{ij}\partial_x \phi_i \partial_x \phi_j] \tag{2.5}$$

where the theory is quantized by the commutator:

$$[\phi_i(x), \phi_j(y)] = i\pi (K^{-1})_{ij} \text{sgn}\,(x-y)\,. \tag{2.6}$$

We emphasize that the edge theory inherits the same $K-$matrix as the bulk, a manifestation of the bulk-edge correspondence. As we will see subsequently, the anyon operators on the edge have the same charge and statistics as those in the bulk. Thus, the *topological* properties of the bulk and the edge are equivalent.

We are now confronted with two major questions. What is the charge density operator on the edge that couples to the electromagnetic field? What do the quasiparticle or anyon operators $\psi_{\boldsymbol{g_\alpha}}$ look like on the edge?

2.1.1. Charge density operator on the edge

The conventional coupling term to the electromagnetic field is given by:

$$\Delta S = \frac{1}{2\pi} \int d^3x \sum_i Q_i \epsilon_{\mu\nu\lambda} A_\mu \partial_\nu a_{\lambda i}. \tag{2.7}$$

The above piece of the action, while invariant under gauge transformations of a_μ, is not so under those of A_μ in the presence of a boundary. We do not have the freedom to restrict gauge transformations of A_μ as the latter exists even outside the quantum Hall system in contrast to a_μ. This is easily fixed. We integrate by parts and discard the boundary term:

$$\Delta S = \frac{1}{2\pi} \int d^3x \sum_i Q_i \epsilon_{\mu\nu\lambda} a_{\lambda i} \partial_\nu A_\lambda. \tag{2.8}$$

The above action is invariant under restricted gauge transformations of a_μ, as we have imposed, and arbitrary gauge transformations of A_μ, as required. We now choose a gauge

where $A_y = 0$ and work in the primed coordinates. The coupling term becomes:

$$\begin{aligned}\Delta S &= \frac{1}{2\pi}\int d^3x \sum_i Q_i \partial_{y'}\phi_i \left(\partial_{t'}A'_{x'} - \partial_{x'}A'_{t'}\right) \\ &= \frac{1}{2\pi}\int dxdt \sum_i Q_i \phi_i \left(\partial_{t'}A'_{x'} - \partial_{x'}A'_{t'}\right)\Big|_{y'=0}.\end{aligned} \tag{2.9}$$

Integrating the above equation by parts, we have:

$$\Delta S = \frac{1}{2\pi}\int dxdt \sum_i Q_i \left(A'_{x'}\partial_{t'}\phi_i - A'_{t'}\partial_{x'}\phi_i\right)\Big|_{y'=0}. \tag{2.10}$$

The equation of motion of the chiral bosons implies that the first term above vanishes. Writing the second term in the unprimed coordinates, the physical picture becomes clear.

$$\Delta S = \frac{1}{2\pi}\int dxdt \sum_i Q_i \left(A_t - vA_x\right)\partial_x\phi_i\Big|_{y'=0} \tag{2.11}$$

The quantity coupling to A_t is the charge density. Hence, we find

$$\rho = \sum_i Q_i\rho_i = \frac{1}{2\pi}\sum_i Q_i\partial_x\phi_i \tag{2.12}$$

where $\rho_i = \partial_x\phi_i/2\pi$.

2.1.2. Quasiparticle operators on the edge

Adding quasiparticles to the theory implies a change in the density of the emergent gauge fields. From Equations (1.58) and (1.63), the change in density of $a_{\mu i}$ due to the quasiparticle $\psi_{\boldsymbol{g_\alpha}}$ is given by $eg_{\alpha i}(K^{-1})_{ij}$. The same condition should hold on the edge. When $\psi_{\boldsymbol{g_\alpha}}$ is inserted on the edge, the edge density ρ must hence satisfy

$$\int dx\ \rho(x) = g_{\alpha i}(K^{-1})_{ij}. \tag{2.13}$$

Additionally, the operator $\psi_{\boldsymbol{g_\alpha}}$ must be a local operator, that is, it creates a charge excitation at a specified location. A local operator is required to satisfy following commutation with the density operator:

$$[\rho_i(x), \psi_{\boldsymbol{g_\alpha}}(y)] = g_{\alpha j}(K^{-1})_{ij}\delta(x-y)\psi_{\boldsymbol{g_\alpha}}(y). \tag{2.14}$$

Equations (2.6) and (2.14) together fix the form of the quasiparticle operator $\psi_{\boldsymbol{g_\alpha}}$. Indeed, using the Baker-Campbell-Hausdorff relations, it is not difficult to see that the quasiparticle

operators must take the form:

$$\psi_{\boldsymbol{g_\alpha}}(x) \sim e^{i\sum_j g_{\alpha j}\phi_j(x)} \equiv e^{i\boldsymbol{g_\alpha}\cdot\boldsymbol{\phi}(x)} \tag{2.15}$$

where normal ordering is implied. The charge carried by this operator can be checked by its commutator with the electronic density operator.

$$[\rho(x), \psi_{\boldsymbol{g_\alpha}}(y)] = e\sum_{ij} Q_i (K^{-1})_{ij} g_{j\alpha} \delta(x-y)\psi_{\boldsymbol{g_\alpha}}(y) \equiv q_{\boldsymbol{g}_\alpha}\delta(x-y)\psi_{\boldsymbol{g_\alpha}}(y). \tag{2.16}$$

The charge $q_{\boldsymbol{g}_\alpha}$ of the operator $\psi_{\boldsymbol{g_\alpha}}$ is hence

$$q_{\boldsymbol{g}_\alpha} = e\sum_{ij} Q_i (K^{-1})_{ij} g_{j\alpha}. \tag{2.17}$$

The exchange statistics of the anyon operators $\psi_{\boldsymbol{g_\alpha}}$ and $\psi_{\boldsymbol{g_\beta}}$ is found by simply exchanging the operators, employing Equation (2.6):

$$\psi_{\boldsymbol{g_\alpha}}(x)\psi_{\boldsymbol{g_\beta}}(y) = e^{i\pi\sum_{ij} g_{\alpha i}(K^{-1})_{ij} g_{\beta j}\mathrm{sgn}(x-y)}\psi_{\boldsymbol{g_\beta}}(y)\psi_{\boldsymbol{g_\alpha}}(x), \tag{2.18}$$

giving us the exchange statistics to be

$$\theta_{\boldsymbol{g_\alpha g_\beta}} = \pi\sum_{ij} g_{\alpha i}(K^{-1})_{ij} g_{\beta j} \tag{2.19}$$

We find the properties of anyons on the edge such as charge and statistics are identical to those in the bulk. This is of course no coincidence. It is a consequence of the fact that the edge theory inherits the $K-$matrix from the bulk Chern-Simons theory and all the excitations have properties stemming from the latter.

2.1.3. Change of basis

We now perform a change of basis of bosonic fields of the action in Equation (2.5). We transform to a basis where the $K-$matrix is reduced to a signature matrix, $K''_{ij} = \pm\delta_{ij}$. That is, $K'' = \mathrm{diag}\,(1,\ldots,-1,\ldots) \equiv \boldsymbol{\chi}$. Note that quantities in the new basis are denoted with a double prime. The action then reads:

$$S = \frac{1}{4\pi}\int dxdt \sum_{j=1}^{N}\left[-\chi_j \partial_x\phi''_j\partial_t\phi''_j - v_j(\partial_x\phi''_j)^2\right], \tag{2.20}$$

where $v_j > 0$ denote the propagation velocity of the $j-$th bosonic field. Computing the equation of motion shows that $\chi_j = \pm$ denotes the chirality of the $j-$th bosonic field.

The commutator of the bosonic fields now reads

$$\left[\phi_j''(x), \phi_k''(y)\right] = i\pi\delta_{jk}\chi_j \text{Sign}(x-y). \tag{2.21}$$

In this basis, the filling fraction of Equation (1.60) is written as:

$$\nu = \sum_j \chi_j Q_j^{''2}. \tag{2.22}$$

The parameters Q_j'' admit a more physical interpretation. A defining feature of the FQHE is that the conductance of the edge is the same as the bulk filling fraction. If there are multiple bosonic fields on the edge, their individual conductance must add up (or subtract, if counter propagating) to yield the edge conductance. Hence, $Q_j''^2$ can be interpreted as the conductance of the $j-$th bosonic field. The charge and statistics of the anyon operators ψ_{g_α} are given in this basis by:

$$q_{\boldsymbol{g}_\alpha} = \sum_j Q_j''\chi_j g_{\alpha j}'' \equiv \boldsymbol{Q''} * \boldsymbol{g_\alpha''} \tag{2.23}$$

$$\theta_{\boldsymbol{g_\alpha'' g_\beta''}} = \pi \sum_j g_{\alpha j}''\chi_j g_{\beta j}'' \equiv \pi \boldsymbol{g_\alpha''} * \boldsymbol{g_\beta''} \tag{2.24}$$

where $\boldsymbol{A} * \boldsymbol{B} \equiv \sum_i \chi_i A_i B_i$.

Physically the transformation to the primed basis implies that the smallest charge of each Chern-Simons gauge field can be less than e, even under their own current. But this does not change any physics. It only shuffles numbers from the $K-$matrix onto the parameters Q_i'' and $g_{\alpha i}''$. Although not stated explicitly to avoid confusion, in the unprimed basis, the parameters Q_i and $g_{\alpha i}$ are constrained to assume integer values. With the basis transformation suggested above, Q_i'' and $g_{\alpha i}''$ can assume fractional or even irrational values.

In what follows, we will always work in the basis where the $K-$matrix is reduced to its signature, that is, the double primed basis. With this in mind, we henceforth drop the primes on the quantities ϕ_i'', Q_i'' and $g_{\alpha i}''$ and write them simply as ϕ_i, Q_i and $g_{\alpha i}$.

2.2. Edge theory of FQHE: a bottom-up approach

We now describe a constructive approach to the edge excitations of an Abelian fractional quantum Hall edge. As we saw in the previous section, FQHE edges host chiral Luttinger liquids. A general Abelian quantum Hall edge is hence described by the action of N

independent chiral Luttinger liquids [24, 48]:

$$S = \frac{1}{4\pi} \int dxdt \sum_{j=1}^{N} \left[-\chi_j \partial_x \phi_j \partial_t \phi_j - v_j (\partial_x \phi_j)^2 \right], \tag{2.25}$$

where ϕ_j denote the bosonic modes on the edge, $v_j > 0$ denote the propagation velocity of $j-$th bosonic mode, and $\chi_j = \pm 1$ denote their chiralities, with $j \in \{1, \ldots, N\}$. The edge is alternatively described by the Hamiltonian

$$H_0 = \frac{1}{4\pi} \int dxdt \sum_{j}^{N} v_j (\partial_x \phi_j)^2. \tag{2.26}$$

The bosonic fields satisfy commutation relations given by:

$$[\phi_j(x,t), \phi_k(x',t')] = i\chi_j \pi \delta_{jk} \text{Sign}(X_j - X'_k), \tag{2.27}$$

where $X_j = -\chi_j x + v_j t$. The dynamics of the bosonic fields is contained in their two-point correlation function or Greens function:

$$\mathcal{G}_j(x_1 - x_2, t_1 - t_2) = \langle \phi_j(x_1, t_1) \phi_j(x_2, t_2) \rangle - \langle \phi_j(0,0) \phi_j(0,0) \rangle, \tag{2.28}$$

where the average is taken on the ground state of the bosonic theory. This object, derived rigorously in Appendix B, takes the following form at a finite temperature T:

$$\mathcal{G}_j(x,t) = \log \left\{ \frac{\sinh(i\pi T \tau_0)}{\sinh\left[\pi T \left(i\tau_0 + t - \chi x / v\right)\right]} \right\}, \tag{2.29}$$

and at zero temperature, it is expressed simply as:

$$\mathcal{G}_j(x,t) = \log \left(\frac{i\tau_0}{i\tau_0 + t - \chi x / v} \right), \tag{2.30}$$

for all j. The charge density ρ and the current I on the edge are given by

$$\begin{aligned} \rho &= \frac{1}{2\pi} \sum_j Q_j \partial_x \phi_j \\ I &= -\frac{1}{2\pi} \sum_j v_j Q_j \partial_t \phi_i, \end{aligned} \tag{2.31}$$

where Q_j^2 is the conductance of the j-th bosonic mode, e is the electronic charge, and h the Planck's constant. The topologically quantized conductance of the edge is related to

the bulk filling fraction ν of the FQHE liquid via:

$$\sum_i \chi_i Q_i^2 = \nu. \tag{2.32}$$

As we saw in Section 2.1.2, locality of the excitations imposes that quasiparticle operators on the edge should be of the form:

$$\psi_{\boldsymbol{g}} \sim e^{i\boldsymbol{g}.\boldsymbol{\phi}}, \tag{2.33}$$

where $\boldsymbol{g} = (g_1, \ldots, g_N)$ labels different anyon excitations, and $\boldsymbol{\phi} = (\phi_1, \ldots, \phi_N)$. We emphasize that vectors with N components are denoted in bold throughout this thesis.

2.2.1. Finding the electron and anyon operators

The anyon/quasiparticle operators admitted by a given edge theory are found in the following manner. First, we find a set of N electron operators $\psi_{\boldsymbol{e_\alpha}} = e^{i\boldsymbol{e_\alpha}.\boldsymbol{\phi}}$ on the edge by demanding it to satisfy the following relations expected of an electron:

$$\begin{aligned} \{\psi_{\boldsymbol{e_\alpha}}(x,t), \psi_{\boldsymbol{e_\alpha}}(x',t)\} &= 0, \\ \psi_{\boldsymbol{e_\alpha}}(x,t)\psi_{\boldsymbol{e_\beta}}(x',t) \pm \psi_{\boldsymbol{e_\beta}}(x',t), \psi_{\boldsymbol{e_\alpha}}(x,t) &= 0, \\ [\rho(x,t), \psi_{\boldsymbol{e_\alpha}}(x',t)] &= \delta(x-x')\psi_{\boldsymbol{e_\alpha}}(x,t). \end{aligned} \tag{2.34}$$

A given set of N electron operators defines a topological class of the quantum Hall system. The topological class of quantum Hall system is conveniently characterized by the $K-$matrix:

$$K_{\alpha\beta} = \boldsymbol{e}_\alpha * \boldsymbol{e}_\beta, \tag{2.35}$$

where $\boldsymbol{A} * \boldsymbol{B} \equiv \sum_i \chi_i A_i B_i$.

Once the electron operators have been determined, the anyon operators are found simply. Only operators satisfying trivial braiding with electrons are allowed to exist in the theory. Indeed, since electrons must be physically measurable, they cannot be multi-valued with respect to any other operator. Hence, all the allowed anyon operators $\psi_{\boldsymbol{g}} = e^{i\boldsymbol{g}.\boldsymbol{\phi}}$ are found by demanding that they braid trivially with the electrons:

$$\psi_{\boldsymbol{g}}(x,t)\psi_{\boldsymbol{e_\alpha}}(x',t) \pm \psi_{\boldsymbol{g}}(x',t), \psi_{\boldsymbol{e_\alpha}}(x,t) \;=\; 0. \tag{2.36}$$

We emphasize that the parameters N, $\boldsymbol{Q}$, and $\boldsymbol{\chi}$ here are phenomenological, with the values chosen being motivated by experimental observations. Once fixed, they can give rise to several solutions of N electron operators, each of which uniquely characterizes quantum Hall states via the K-matrix.

2.2.2. Important measurable quantities of anyons

A primary objective of this thesis is to devise experimental protocols that could unambiguously measure each component of the $K-$matrix, thus characterizing the fractional quantum Hall state. Anyon operators are characterized by the following important physical properties, some of which have been already discussed.

- **Charge:** The charge of quasiparticle $\psi_{\boldsymbol{g_\alpha}}$ is denoted $q_{\boldsymbol{g}_\alpha}$ and is given by:

$$q_{\boldsymbol{g}_\alpha} = \boldsymbol{g_\alpha} * \boldsymbol{Q}\ e. \tag{2.37}$$

- **Scaling dimension:** Scaling dimension of anyons is a property we have not encountered yet. Our discussion of anyons in Chapter 1 was in the bulk which is gapped due to large ω_B. In the absence of dynamics, the scaling dimension is unimportant. However, the edge being gapless admits dynamics described by Equation (2.26). Here, the scaling dimension of anyons starts playing an important role – it describes how quickly the anyon correlations decay – as we will see. The scaling dimension is given by:

$$\delta_{\boldsymbol{g}_\alpha} = \sum_i g_{\alpha i}^2. \tag{2.38}$$

- **Exchange phase:** The most striking property of anyons is their fractional exchange or braiding phase. The mutual exchange phase of the two anyons $\psi_{\boldsymbol{g_\alpha}}$ and $\psi_{\boldsymbol{g_\beta}}$ is given by

$$\theta_{\boldsymbol{g_1 g_2}} \equiv \pi\lambda_{\boldsymbol{g_1 g_2}} = \pi\ \boldsymbol{g_1 . g_2}. \tag{2.39}$$

  Throughout this thesis, we will use the above notations of exchange statistics interchangeably.

For tunneling of anyons at a quantum point contact (to be described in the forthcoming section), within a low energy approximation, the anyons with the lowest scaling dimension dominantly tunnel. Hence, the ones with higher scaling dimensions are usually ignored. The lowest scaling dimension anyon operators also bear a relation with the $K-$matrix, given by:

$$(K^{-1})_{\alpha\beta} = \boldsymbol{g_\alpha} * \boldsymbol{g_\beta}. \tag{2.40}$$

Given the direct relation between the above quantities and the $K-$matrix, unambiguous measurement of these quantities leads to a characterization of the FQHE.

2.2.3. Anyon and electron operators

Laughlin states

Laughlin states are observed for the FQHE at filling factor $\nu = 1/(2m+1)$ (with m an integer). The edge theory is described by a single Luttinger liquid ($N = 1$), with $\boldsymbol{Q} = (\sqrt{\nu})$, and $\boldsymbol{g} = (\sqrt{\nu})$. This gives for the electron operator, $\boldsymbol{e} = (1/\sqrt{\nu})$ and hence a trivial K-matrix, $(1/\nu)$. This recovers the results expected for Laughlin systems: the quasiparticle operator is given by $\psi_{\boldsymbol{g}} \sim e^{i\sqrt{\nu}\phi}$, quasiparticle charge is $q_{\boldsymbol{g}} = \nu e$, the exchange statistics is $\theta_{\boldsymbol{gg}} = \pi\nu$, and finally the scaling dimension is $\delta_{\boldsymbol{g}} = \nu$.

$\boldsymbol{\nu = 2/5}$

Theoretically describing the $\nu = 2/5$ FQHE state requires two chiral Luttinger liquids on the edge ($N = 2$) [23]. Indeed, recall the discussion around Figure 1.5, where hierarchical states are shown to be composed of several Laughlin states. Indeed, $\nu = 2/5$ has been thought to be composed of Laughlin $\nu = 1/3$ and $1/15$ states [24], consistent with experiments [37]. This leads us to take $\boldsymbol{q} = (\sqrt{1/3}, \sqrt{1/15})$. Both modes propagate in the same direction, hence $\boldsymbol{\chi} = (+1, +1)$. This choice of $\boldsymbol{q}$ and $\boldsymbol{\chi}$ satisfies Equation (2.32) and gives us the following lowest scaling dimension electron operators:

$$\begin{aligned} \boldsymbol{e_1} &= \left(-2/\sqrt{3}, -\sqrt{5/3}\right), \\ \boldsymbol{e_2} &= \left(-\sqrt{3}, 0\right), \end{aligned} \tag{2.41}$$

and hence using Equation (2.35) the $K-$matrix

$$K = \begin{pmatrix} 3 & 2 \\ 2 & 3 \end{pmatrix}. \tag{2.42}$$

From these, it can then be shown that there exist two anyons of the lowest scaling dimension, having charge $e/5$. They are given by $e^{i\boldsymbol{g_1}\cdot\boldsymbol{\phi}}$ and $e^{i\boldsymbol{g_2}\cdot\boldsymbol{\phi}}$, where:

$$\begin{aligned} \boldsymbol{g_1} &= \left(0, \sqrt{3/5}\right) \\ \boldsymbol{g_2} &= \left(\sqrt{1/3}, -2/\sqrt{15}\right) \end{aligned} \tag{2.43}$$

Both of these charge $e/5$ anyons have the same scaling dimension $\delta_{\boldsymbol{g_1}} = \delta_{\boldsymbol{g_2}} = 3/5$. Their exchange statistics is given by $\theta_{\boldsymbol{g_1 g_1}} = \theta_{\boldsymbol{g_2 g_2}} = \theta_{\boldsymbol{g_1 g_2}} = 3\pi/5$.

We note that there exists also an anyon of charge $2e/5$ that has an even lower scaling dimension. We usually ignore the latter as it is not observed in experiments under typical applied voltages and temperatures.

$\nu = 2/3$

$\nu = 2/3$ edge also admits an edge structure with two chiral Luttinger liquids on the edge ($N = 2$). Experiments witness a charge mode of conductance $2/3$ and a *neutral* mode that propagates in the opposite direction [48, 59]. This is given by the charge vector $\boldsymbol{Q} = (\sqrt{2/3}, 0)$ and chirality vector $\boldsymbol{\chi} = (+1, -1)$, satisfying Equation (2.32). From these inputs, we obtain the electron operators [48]:

$$\begin{aligned} \boldsymbol{e_1} &= \left(\sqrt{3/2}, \sqrt{1/2}\right), \\ \boldsymbol{e_2} &= \left(\sqrt{3/2}, -\sqrt{1/2}\right), \end{aligned} \tag{2.44}$$

and hence the $K-$matrix

$$K = \begin{pmatrix} 1 & 2 \\ 2 & 1 \end{pmatrix}. \tag{2.45}$$

We can then find the allowed anyon operators by demanding they braid trivially with the electrons. This gives us *three* operators all with the same scaling dimension:

$$\begin{aligned} \boldsymbol{g_1} &= \left(\sqrt{1/6}, \sqrt{1/2}\right), \\ \boldsymbol{g_2} &= \left(\sqrt{1/6}, -\sqrt{1/2}\right), \\ \boldsymbol{g_3} &= \left(\sqrt{2/3}, 0\right). \end{aligned} \tag{2.46}$$

The anyons $\psi_{\boldsymbol{g_1}}$ and $\psi_{\boldsymbol{g_2}}$ both have a charge $e/3$, while $\psi_{\boldsymbol{g_3}}$ has a charge $2e/3$. All of them have the same scaling dimension $\delta_{\boldsymbol{g_1}} = \delta_{\boldsymbol{g_2}} = \delta_{\boldsymbol{g_3}} = 2/3$. Their exchange statistics are given by $\theta_{\boldsymbol{g_1 g_1}} = \theta_{\boldsymbol{g_2 g_2}} = -\pi/3$, $\theta_{\boldsymbol{g_1 g_2}} = 2\pi/3$, $\theta_{\boldsymbol{g_3 g_3}} = 2\pi/3$, $\theta_{\boldsymbol{g_1 g_3}} = \theta_{\boldsymbol{g_2 g_3}} = \pi/3$.

We note that the above is the exchange statistics of the anyons when the excitations on each bosonic mode are bound together. Since the charge and neutral modes in $\nu = 2/3$ have opposite chiralities, when an anyon is emitted on the edge, the charge and neutral excitations propagate in opposite directions. In this case, it is necessary to be more careful and calculate statistics of the excitations that are actually exchanged/braided.

2.3. Probing anyons using transport

Quantum transport concerns the impact of quantum processes on the flow of currents. In the context of anyons, quantum transport deals with the response of quantum Hall edges to non-equilibrium drives. Of course, since the bulk of FQHE is gapped, it is difficult to experimentally probe anyons in the bulk. But as discussed in Section 2.1, the bulk-edge

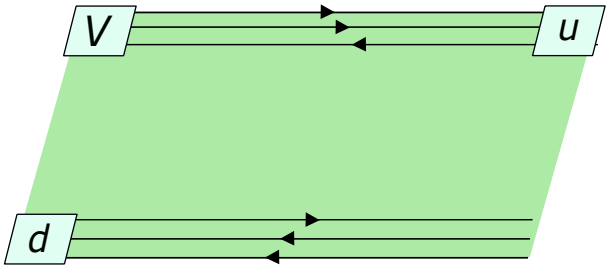


Figure 2.2.: A voltage V is introduced on an arbitrary Abelian FQHE edge using a "contact".

correspondence implies that anyons on the edge have the same properties such as charge and statistics, as those in the bulk. Hence studying responses of the edge theory to external drives, such as a potential difference or temperature difference between edges connected by a QPC, could shed light on the exotic properties of anyons. This section hence aims to lay down all the technical tools to study transport phenomena in FQHE edges, used throughout this thesis.

One of the simplest ways to drive the edge out of equilibrium is by applying a voltage bias, generating an electric current. Indeed, measuring the transverse voltage induced by a longitudinal current along a quantum Hall edge allows us to observe the fractionally quantized Hall plateaus. We hence start this section by theoretically describing how external voltages couple to FQHE edges. However, our main interest lies in examining the granularity of the current. In the FQHE, the elementary charge carriers are not electrons but anyons, which, as we have shown, often carry a fraction of the electronic charge. Accessing this current granularity can provide precious information about the nature of anyons. To achieve this, the opposite edges of the system can be brought close together, forming a structure known as a quantum point contact (QPC). The QPC enables the study of individual charge carriers (which we suppose are anyons) of the current. A significant part of this section is thus devoted to laying down the theoretical description of QPCs in FQHE.

To rigorously analyze transport phenomena in FQHE edges, we employ the Keldysh non-equilibrium Greens function formalism. As the name suggests, this technique is geared towards studying non-equilibrium phenomena in quantum systems, and hence allows to model the response of FQHE edges to external drives. As the Keldysh formalism constitutes the technical cornerstone of this thesis, we conclude this section with a brief recap of the important details of the latter formalism.

2.3.1. Coupling a voltage to the edge

Let us start by understanding how a voltage $V(x,t)$ couples to FQHE edges. Experimentally, voltages are into the edges via a contact as schematically shown in Figure 2.2. Of course, voltage couples to the electron density on the edge. This is accounted for with an additional term in the Hamiltonian:

$$H_V = \sum_j \frac{Q_j}{2\pi} \int dx V(x,t) \partial_x \phi_j(x,t). \tag{2.47}$$

The equation of motion of the full Hamiltonian $H_0 + H_V$ is:

$$(\partial_x - v_i \partial_t)\phi_j(x,t) = Q_j V(x,t). \tag{2.48}$$

From the above, it is straightforward to see that the effect of the voltage is accounted for with a simple rescaling of the bosonic fields.

$$\phi_j(x,t) \longrightarrow \phi_j(x,t) + Q_j \int_{-\infty}^{t} dt' V(x',t') \tag{2.49}$$

Since the edges are chiral, we can express the time and position dependence of the voltage as

$$\phi_j(x,t) \longrightarrow \phi_j(x,t) + Q_j \int_{-\infty}^{t} dt' V(t' - x'/v_i) \tag{2.50}$$

where the voltage contact has been assumed to be semi-infinite. With a coordinate transformation $t \longrightarrow t - x'/v_j$, we change the argument of the voltage and also the limits of the integral. The constant coming from x'/v_j part of the limit can be shown to get cancelled (since we will always consider bilinear anyon operators). This part is hence safely discarded, giving us the final expression for voltage coupling to FQHE edge modes:

$$\phi_j(x,t) \longrightarrow \phi_j(x,t) + Q_j \int_{-\infty}^{t} dt' V(t'). \tag{2.51}$$

2.3.2. Quantum point contacts in FQHE

Driving an edge with a voltage creates a current along the edge, which is imagined to be composed of discrete charge carriers. In the fractional quantum Hall effect, the most fundamental constituents of charge are not electrons anyons. However, to probe the granularity of the current, and consequently the physics of discrete anyons it is necessary to split the current into two. Since the bulk of FQHE is gapped, the only way to split the current on the edges is to somehow bring the two opposite edges close. Indeed, this can be achieved by depleting the 2DEG in a confined region as shown in Figure 2.3. This

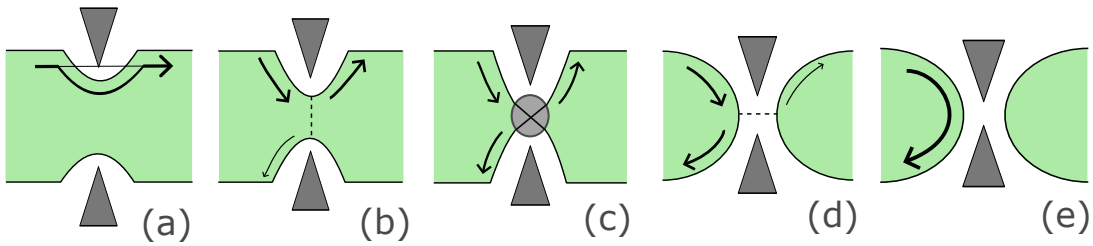


Figure 2.3.: Operating regimes of a quantum point contact (QPC) controlled by top gates (in grey). (a) The fully open regime: the incoming current on the upper edge is fully "forward-scattered". (b) The gates are used to slightly deplete the FQHE, bringing the opposite edges closer. The current is largely forward-scattered on the same edge. A tiny amount of current is "back-scattered" to the lower edge. This regime is called the weak-backscattering regime and is described by tunneling of anyons. (c) Pinching the edges together further, we arrive at the intermediate regime. Here, forward- and back-scattered currents are of the same magnitude. This regime mostly evades theoretical description in FQHE. (d) The gates almost break the FQHE in half, leaving vacuum between the edges. Most of the incoming current is back-scattered, and a tiny amount is forward-scattered. This regime is dubbed strong-backscattering regime, and is described by tunneling of electrons between the edges. (e) The gates break the FQHE in two and the incoming current is fully back-scattered.

device is called a quantum point contact, which allows tunneling of excitations between the edges, possibly granting us access to the physics of individual anyons.

There are several possible configurations of the quantum point contact (QPC), as shown in Figure 2.3. A voltage is applied on the top edge, giving rise to an incoming current. The current incident on the QPC is split into a transmitted part, flowing to the lower edge, and a reflected part, continuing on the upper edge. The configurations shown in Figure 2.3 differ in the proportions of current transmitted to the lower edge. (a) describes a trivial scenario where the QPC is fully open. The incoming current continues fully on the upper edge. In (b), the QPC is slightly closed forming the so-called weak-backscattering regime. Most of the current continues on the upper edge and a small fraction is transmitted to the lower edge. (c) continues to close the QPC, yielding a situation with arbitrary reflected and transmitted current. (d) Further closes the QPC and almost pinches off the FQHE bar, separating it into two parts. We end up with a situation where most of the current is transmitted to the lower edge and a tiny fraction is reflected on the upper edge. This situation is called the strong-backscattering regime. (e) represents a scenario where the QPC is fully closed, and all the current is transmitted to the lower edge.

Scenarios (a) and (e) are trivial where all the current is fully reflected or transmitted respectively. These hence require no further ingredients in their theoretical description. On the other hand, the non-linearity (with respect to applied voltage) inherent in FQHE edge tunneling current (see Equation (2.78)) mean that (c) mostly evades a theoretical

description. It is possible to theoretically describe the remaining two regimes in terms of single-particle tunneling events.

2.3.3. Tunneling Hamiltonian: weak- and strong-backscattering regimes

The weak-backscattering regime of the QPC brings together the two edges, leaving a small amount of the FQHE in between the edges. It could hence admit anyons tunneling across the edges. The full Hamiltonian describing this process is $H = H_0 + H_T$. H_0 is the free Hamiltonian of the two edges.

$$H_0 = \frac{1}{4\pi} \int dx \sum_i^N v_i \left[(\partial_x \phi_i^u)^2 + (\partial_x \phi_i^d)^2 \right] \tag{2.52}$$

The tunneling process is described by adding an anyon hopping term in the Hamiltonian

$$H_T(t) = \sum_\alpha \Gamma_{\boldsymbol{g}_\alpha} \left[\psi^{u\dagger}_{\boldsymbol{g}_\alpha}(0,t)\psi^d_{\boldsymbol{g}_\alpha}(0,t) + \psi^{d\dagger}_{\boldsymbol{g}_\alpha}(0,t)\psi^u_{\boldsymbol{g}_\alpha}(0,t) \right], \tag{2.53}$$

where $\Gamma_{\boldsymbol{g}_\alpha}$ is the tunneling amplitude associated with the tunneling of quasiparticle $\psi_{\boldsymbol{g}_\alpha}$. The sum over α accounts for all anyonic quasiparticles that exist on the edges. Indeed, we imagine that all the anyons that exist on the FQHE edges can tunnel between them. The superscripts u/d denote operators on the upper/lower edge. For theoretical simplicity, we have assumed that the tunneling process occurs at a single spatial location $x = 0$. As the above Hamiltonian describes tunneling of anyons from one edge to another, it is referred to as the *tunneling Hamiltonian*. Keeping in mind that the anyon operators on the edge are complex, exponentiated boson operators, it is possible to compactly express the tunneling Hamiltonian in the following manner:

$$H_T(t) = \sum_\alpha \sum_{\epsilon=\pm} \Gamma_{\boldsymbol{g}_\alpha} \left[\psi^{u\dagger}_{\boldsymbol{g}_\alpha}(0,t)\psi^d_{\boldsymbol{g}_\alpha}(0,t) \right]^\epsilon, \tag{2.54}$$

where the sum over ϵ takes care of the two Hermitian conjugate tunneling terms.

In the strong-backscattering regime, while the QPC brings together the upper and lower edges, it breaks the FQHE into two. It leaves a vacuum between the left and right parts of the FQHE. Since anyons are emergent quasiparticles existing only in the FQHE, any tunneling of charges must be mediated via electrons. We can describe this regime with a similar tunneling Hamiltonian comprising electron operators:

$$H_T(t) = \sum_\alpha \sum_\epsilon \left[\Gamma_{\boldsymbol{e}_\alpha} \psi^{u\dagger}_{\boldsymbol{e}_\alpha}(0,t)\psi^d_{\boldsymbol{e}_\alpha}(0,t) \right]^\epsilon. \tag{2.55}$$

Again, we imagine that all electrons existing on the edges can tunnel across the edges. This is accounted for with the sum over α, the different types of electrons. Note that we retain the notation u/d for consistency, but in this regime, one thinks of the upper and lower edges splitting into two halves, forming the right and left edges, as shown in Figure 2.3(d). These new edges are described by the same chiral Luttinger liquid theory and the notation above does not lead to discrepancies. With the above nuances in mind, as far as the theoretical calculations are concerned, the strong-backscattering regime can be described identically as the weak-backscattering regime. The latter can be understood to be a special case of the former with tunneling operators representing electrons.

2.3.4. Tunneling current

How does tunneling of anyons at a QPC modify the currents on the edges? More precisely, what is the current tunneling from the upper edge to the lower edge? To answer this question, we calculate the rate of change of the charge of the lower edge. The charge on the lower edge is obtained as an integral of its charge density:

$$\bar{Q}^d = \int dx\ \rho^d(x). \tag{2.56}$$

The rate of change of charge is then given by the commutator of the charge with the Hamiltonian, $H = H_0 + H_T$:

$$I_T(t) \equiv \frac{d\bar{Q}^d}{dt} = \left[\bar{Q}^d, H_0 + H_T\right] = \left[\bar{Q}^d, H_T\right]. \tag{2.57}$$

Using Baker-Campbell-Hausdorff relations we find

$$I_T(t) = \sum_{\alpha} \sum_{\epsilon} i\epsilon q_{\boldsymbol{g}_\alpha} \left[\Gamma_{\boldsymbol{g}_\alpha} \psi^{u\dagger}_{\boldsymbol{g}_\alpha}(0,t)\psi^{d}_{\boldsymbol{g}_\alpha}(0,t)\right]^{\epsilon}. \tag{2.58}$$

One finds the anyons charge sitting in the expression above. This suggests that a proper analysis of this quantity may allow us to characterize anyons and the FQHE state. We have in mind to calculate the expectation value or higher moments of the tunneling current in the ground state of the system.

2.3.5. Keldysh formalism

Keldysh non-equilibrium Greens function formalism is the standard tool to calculate correlation functions in non-equilibrium quantum systems. In this thesis, we want to calculate averages and higher moments of the tunneling current operator in Equation (2.58) under a non-equilibrium drive, among other things. With this motivation to theoretically analyze non-equilibrium transport phenomena in FQHE edges, we briefly summarize the

key technical details of the Keldysh formalism, before quickly describing how the latter formalism applies to FQHE edges.

Technical introduction

As stated before, to probe the physics of anyons, we want to calculate moments of the tunneling current operator. Consider the system to be described by the Hamiltonian $H = H_0 + H_T(t)$, where H_0 is the free, non-interacting term (that can be solved exactly) while $H_T(t)$ is a perturbative interaction term.

When calculating observables related to the operator $I_T(t)$, one is confronted with time-ordered correlators of the form:

$$O(\{t_k\}) = \left\langle T\left\{\tilde{I}_T(t_1)\tilde{I}_T(t_2)\tilde{I}_T(t_3)\dots\right\}\right\rangle. \tag{2.59}$$

Here, the operators with a tilde are in the Heisenberg representation, T denotes time ordering on the real-time axis, and the average is calculated between the initial and final states of the system. Calculation of correlators typically relies on Wick's theorem, which allows to express time-ordered operator products as normal-ordered operator products, thus expressing a complicated correlator in terms of products of two-point correlators. The Heisenberg representation however is unwieldy to calculate correlation functions since all the time dependence is hidden in the operators, while Wick's theorem demands non-interacting operators (the action of the operators on the states of the non-interacting theory must be known). To work around this, it is far more convenient to use the interaction representation, where the non-trivial time dependence is shifted to the so-called $S-$matrix:

$$S(t,t') = T\exp\left[-i\int_{t'}^{t} d\bar{t}\; H_T(\bar{t})\right]. \tag{2.60}$$

Thus we can express the time-ordered correlator as:

$$O(\{t_k\}) = \langle f|\, T\left\{S(\infty,-\infty)I_T(t_1)I_T(t_2)\dots\right\}|0\rangle\,, \tag{2.61}$$

where $|0\rangle$ denotes the state of the system at $-\infty$ and $|f\rangle$ denotes the state of the system at $+\infty$, and the operators are all in the interaction representation. The operators now carry only a trivial time dependence, and their action on the states of the non-interacting theory is known. However, there exists another obstacle to employing Wick's theorem: in general, the time-evolved final state may be quite different from the eigenstates of the initial non-interacting theory. Hence, the action of the operators on the latter state may not be known.

In equilibrium QFT, it is argued that the final state is the same as the initial state up to a phase [60]. The claim can be shown by adiabaticity arguments [61]. Indeed, one imagines starting from the non-interacting theory H_0 in the asymptotic past, characterized

by the state $|0\rangle$. The interaction term H_T is imagined to be turned on adiabatically slowly, such that the system remains in the same state throughout the process. The interactions peak close to $t = 0$, and are then again imagined to be turned off adiabatically going into the asymptotic future. Throughout this process, adiabaticity implies that the system remains in the same state. Thus, the initial and final state are related by $|f\rangle = e^{i\gamma}|0\rangle$ where $e^{i\gamma} = \langle 0| S(\infty, -\infty)|0\rangle$. With this assumption, the correlator is expressed as:

$$O(\{t_k\}) = \frac{\langle 0| T\{S(\infty, -\infty) I_T(t_1) I_T(t_2) \dots\} |0\rangle}{\langle 0| S(+\infty, -\infty)|0\rangle}. \tag{2.62}$$

This is the traditional starting point of equilibrium QFT calculations. Typically, the $S-$matrix (whose expression is given in Equation (2.60)) is expanded perturbatively and all the terms of the sum can be evaluated using Wick's theorem.

The key step that enabled utilizing the powerful technique of Wick's theorem in equilibrium QFT is the argument of adiabaticity, putting the initial and final states to be the same. Unfortunately, we no longer afford this luxury in non-equilibrium QFT. Indeed, the adiabatic theorem simply fails in non-equilibrium scenarios. Let us understand this with a simple example. Consider two edge states of the quantum Hall effect. We drive the system out of equilibrium by coupling the upper edge to a voltage source. In the asymptotic past, while the upper edge is populated with particles due to the voltage, the lower edge is fully unpopulated. Let us now imagine slowly turning on an interaction, allowing the tunneling of particles across the edges (due to a QPC, for example). The instant the tunneling is turned on, adiabatically or not, particles start pouring into the lower edge. Of course, if the tunneling is turned back off, the system is not going to return to anything close to the initial state where the lower edge was completely unpopulated. Hence, in non-equilibrium QFT, the initial and final states are expected to be fundamentally different in general. The time-ordered average thus goes back to the form:

$$O(\{t_k\}) = \langle f| T\{S(\infty, -\infty) I_T(t_1) I_T(t_2) \dots\} |0\rangle, \tag{2.63}$$

where we cannot employ Wick's theorem. Keldysh proposed a very simple solution to this problem. First, we note that the relation $|f\rangle = S(\infty, -\infty)|0\rangle$ between the initial and final states still holds (only the $S-$matrix is no longer a phase). This allows us to express the operator average as:

$$O(\{t_k\}) = \langle 0| S(-\infty, \infty) T\{S(\infty, -\infty) I_T(t_1) I_T(t_2) \dots\} |0\rangle. \tag{2.64}$$

Notice that it seemingly takes on a form similar to Equation (2.62), where the operators are now sandwiched between the initial states. However, this comes at the expense of introducing the $S-$matrix that time evolves the system from $+\infty$ back to $-\infty$. Crucially, we cannot employ Wick's theorem since we no longer have a time-ordered product of operators between the states. It seems we have just exchanged one problem for another!

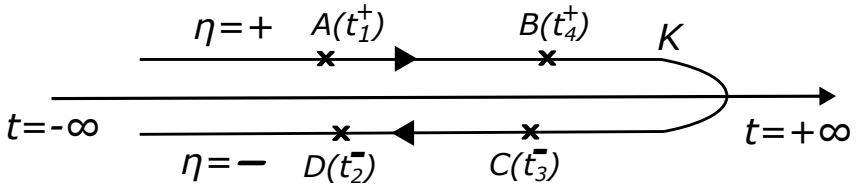


Figure 2.4.: Time ordering on the Keldysh contour. The Keldysh contour, denoted K, runs from $t = -\infty$ to $+\infty$ and then back to $+\infty$. The forward branch going from $-\infty$ to ∞ is labeled by $\eta = +$, and the backward branch running from $+\infty$ to $infty$ by $\eta = -$. Operators on the backward branch always occur *after* those on the forward branch. As an illustration, consider $t_1 < t_2 < t_3 < t_4$. Conventional time ordering on the real axis would yield $\langle TB(t_4)C(t_3)D(t_2)A(t_1)\rangle = \langle B(t_4)C(t_3)D(t_2)A(t_1)\rangle$. Keldysh time ordering orders operators according to their position on the Keldysh contour: $\left\langle \left\{ T_K B(t_4^+)C(t_3^-)D(t_2^-)A(t_1^+)\right\}\right\rangle = \langle D(t_2)C(t_3)B(t_4)A(t_1)\rangle$. The superscripts on the time arguments signify the Keldysh branch that the operators sit on.

Ingeniously, Keldysh (and some others) proposed to order the operators on a contour that goes from $-\infty$ to $+\infty$ (the forward branch), and then back to $-\infty$ (the backward branch), as shown in Figure 2.4 [62, 63]. This contour is now called the Keldysh contour. Time ordering along the Keldysh contour implies: (i) usual time ordering on the forward branch (ii) anti-time ordering on the backward branch (times closer to $-\infty$ are greater than those closer to $+\infty$) and (iii) times on the backward branch are always greater than those on the forward branch.

In Equation (2.64), the usual time-ordered operator product can be placed on the forward branch of the Keldysh contour, while the $S-$matrix, which is evolving backward in time can be placed on the backward branch. Since the latter is on the backward branch it always appears to the left of the usual time-ordered operator product. These objects are hence naturally ordered on the Keldysh contour, allowing us to compactly express Equation (2.64) as:

$$O(\{t_k\}) = \langle 0|\, T_K \left\{ e^{-i\int_{+\infty}^{-\infty} d\bar{t} H_T(\bar{t}^-)} e^{-i\int_{-\infty}^{+\infty} d\bar{t} H_T(\bar{t}^+)} I_T(t_1^+) I_T(t_2^+) \dots \right\} |0\rangle\,, \tag{2.65}$$

where T_K denotes the ordering of times along the Keldysh contour, and the superscripts $\pm$ on the time arguments indicate their insertion in the forward/backward branch of the Keldysh contour. Most importantly, Equation (2.65) now comprises a time-ordered operator product sandwiched between the initial state of the non-interacting theory. We are hence in a position to perturbatively expand the $S-$matrix and employ Wick's theorem to calculate the correlators. This is the technique we will employ throughout this thesis.

Only now, we pay the price that the time argument of the operators could be on either branch of the Keldysh contour. Indeed, a generic operator average in the Keldysh

formalism is expressed as:

$$O(\{t_k^{\eta_k}\}) = \langle 0|\, T_K \left\{ I_T(t_1^{\eta_1}) I_T(t_2^{\eta_2}) \dots e^{-i\sum_{\bar{\eta}=\pm} \bar{\eta} \int_{-\infty}^{+\infty} d\bar{t}\ H_T(\bar{t}^{\bar{\eta}})} \right\} |0\rangle\,, \tag{2.66}$$

where $\eta_k, \bar{\eta} = \pm$ are the Keldysh indices that indicate the position of the operators along the Keldysh contour, where $+/-$ indicates forward/backward branch. If we now perturbatively expand the $S-$matrix or the time evolution operator, we can use Wick's theorem to reduce the correlator to a product of two-point correlation functions or Greens functions.

Keldysh Greens function

In the context of FQHE edges, the focus of this thesis, the most fundamental two-point correlator is that of the bosonic edge modes, given in Equation (2.29). The non-equilibrium Keldysh bosonic Greens function is defined as [26]:

$$\mathcal{G}_j(x,t) = \begin{pmatrix} \mathcal{G}^{++}(x,t) & \mathcal{G}^{+-}(x,t) \\ \mathcal{G}^{-+}(x,t) & \mathcal{G}^{--}(x,t) \end{pmatrix}. \tag{2.67}$$

The Keldysh Greens function is a matrix-valued object, with each component of the matrix giving different possible ordering of the boson operators along the Keldysh contour:

$$\mathcal{G}_j^{\eta_1\eta_2}(x_1 - x_2, t_1 - t_2) = \langle 0|\, T_K \phi_j(x_1, t_1^{\eta_1}) \phi_j(x_2, t_2^{\eta_2})\, |0\rangle - \langle 0|\, \phi_j(0,0)\phi_j(0,0)\, |0\rangle\,, \tag{2.68}$$

where $\eta_1, \eta_2 = \pm$. Thus, the time arguments of the boson operators can lie on the forward or the backward branch, with each order leading to a different Greens function. The different components of the Keldysh Greens function are related to the equilibrium Greens function in the following manner:

- **Both operators lie on the forward branch: $(\eta_1, \eta_2) = (+1, +1)$.**

  On the forward branch, the Keldysh contour always runs in the direction of increasing time. Thus, Keldysh ordering on the forward branch reduces to conventional time ordering

  $$\langle 0|\, T_K \phi_j(x_1, t_1^+) \phi_j(x_2, t_2^+)\, |0\rangle = \langle 0|\, T \phi_j(x_1, t_1) \phi_j(x_2, t_2)\, |0\rangle\,, \tag{2.69}$$

  where T is the time ordering operator, placing smaller times to the right and larger times to the left.

- **Both operators lie on the backward branch: $(\eta_1, \eta_2) = (-1, -1)$.**

On the backward branch, the Keldysh contour always runs in the direction of decreasing time. Hence, there the Keldysh ordering reduces to anti-time ordering

$$\langle 0|\, T_K \phi_j(x_1, t_1^-)\phi_j(x_2, t_2^-)\, |0\rangle = \langle 0|\, \tilde{T}\phi_j(x_1, t_1)\phi_j(x_2, t_2)\, |0\rangle\,, \tag{2.70}$$

where $\tilde{T}$ is the anti-time ordering operator, placing larger times to the right and smaller times to the left.

- **Operators lie on opposite branches: $(\eta_1, \eta_2) = (+1, -1), (-1, +1)$.**

  On the Keldysh contour, the times on the backward branch always occur after all the times on the forward branch. Hence, Keldysh ordering always places the operator on the forward branch to the right, and the operator on the backward branch to the left

$$\langle 0|\, T_K \phi_j(x_1, t_1^-)\phi_j(x_2, t_2^+)\, |0\rangle = \langle 0|\, \phi_j(x_1, t_1)\phi_j(x_2, t_2)\, |0\rangle\,, \tag{2.71}$$

$$\langle 0|\, T_K \phi_j(x_1, t_1^+)\phi_j(x_2, t_2^-)\, |0\rangle = \langle 0|\, \phi_j(x_2, t_2)\phi_j(x_1, t_1)\, |0\rangle\,. \tag{2.72}$$

This complicated effect of the Keldysh time ordering can be neatly incorporated into the Keldysh Greens function, with the following definition:

$$\mathcal{G}_j^{\eta_1\eta_2}(x, t) = \log\left\{\frac{\sinh\left(i\pi T\tau_0\right)}{\sinh\left(\pi T\left[i\tau_0 + \sigma_{\eta_1\eta_2}(t)\left(t - \chi_j x/v\right)\right]\right)}\right\}, \tag{2.73}$$

where

$$\sigma_{\eta_1\eta_2}(t) = \frac{1}{2}\left[(\eta_2 - \eta_1) + \mathrm{sgn}(t)(\eta_1 + \eta_2)\right]. \tag{2.74}$$

It can be checked explicitly that the above function, which takes the times and the Keldysh indices as input, correctly accounts for the Keldysh time ordering of the operators.

2.4. Review of FQHE edge experiments

Using the technical tools developed in the previous sections, here we demonstrate how the transport observables at the edge carry signatures of the topological properties of anyons in the FQHE. We will review the current experimental progress, exposing also the underlying theory, in probing the three key topological properties of anyons: fractional charge, scaling dimension, and braiding phase. This discussion places the original findings of this thesis within the context of contemporary research on anyons in the FQHE.

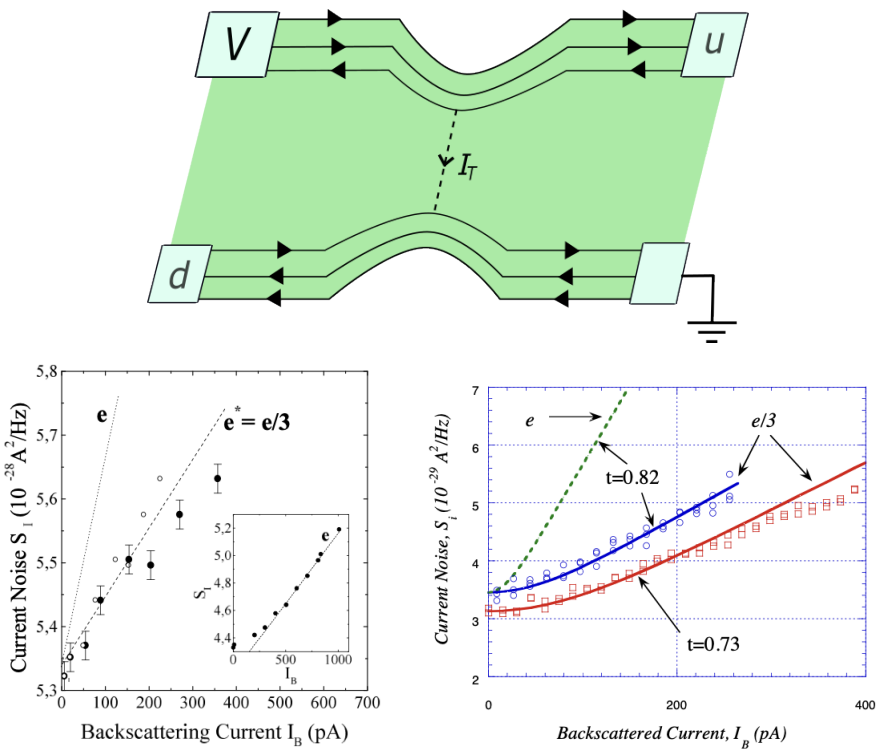


Figure 2.5.: (Top) Schematic of a QPC in FQHE biased with a voltage V on the top edge. This setup is used to measure the charges tunneling at the QPC. (Bottom) Noise vs current data taken from Refs. [30, 31] showing fractional charge $e/3$ tunneling at the QPC.

2.4.1. Fractional charge

We now calculate the average value of the tunneling current operator and its variance. We will show that the ratio of the latter quantities gives the charge of current carriers [29]. This allowed experimental verification of one of the most fundamental assumptions we are making: that current is composed of discrete anyons, and that single anyons can tunnel from one edge to another via a QPC [30, 31].

Consider applying a constant voltage V on the upper edge of the FQHE. as shown in Figure 2.5. From Equation (2.51), this is taken into account by the transformation

$$\phi_j^u(x,t) \longrightarrow \phi_j^u(x,t) + Q_j V t. \tag{2.75}$$

Inducing a potential difference between the two edges breaks the particle-hole symmetry of the tunneling current operator, leading to a non-zero current tunneling onto the lower edge.

We want to access the granularity of the current to probe the anyons. The best thing to do would be to measure the tunneling current as a function of time. If granularity is present, it would manifest as steps in the current vs time plot. The height of these steps should give us the charge of the carriers. However, such a measurement proves to be far out of the reach of contemporary experiments. Experiments are only able to measure time-independent average values where it is more difficult to sense the granularity, but still possible as we show below.

We now proceed to calculate the average of the tunneling current. In the interest of simplicity, we restrict here to a scenario where a single type of anyon tunnels through the QPC. This gets rid of the sum over α in Equations (2.55) and (2.58). The average tunneling current is then expressed in the Keldysh formalism as

$$\langle I_T \rangle = \frac{1}{2} \sum_{\eta} \left\langle \left\{ T_K I_T(t^\eta) e^{-i \int_K dt' H_T(t')} \right\} \right\rangle \tag{2.76}$$

where the superscripts $\eta, \eta' = \pm$ on the time arguments denote Keldysh indices, with $+(-)$ indicating that the times are on the forward (backward) branch of the Keldysh contour. T_K denotes a time-ordering on the Keldysh contour and the subscript K on the integral denotes an integral over the Keldysh contour. We evaluate the average current perturbatively, by expanding the interaction term to the lowest non-trivial order

$$\langle I_T \rangle = -\frac{i}{2} \sum_{\eta\eta'} \eta' \int dt' \left\langle \left\{ T_K I_T(t^\eta) H_T(t'^{\eta'}) \right\} \right\rangle . \tag{2.77}$$

The calculation is presented in full detail in Appendix C and we present the final result here:

$$\langle I_T \rangle = 2 q_{\boldsymbol{g}} |\Gamma_{\boldsymbol{g}}|^2 \tau_0 (2\pi T \tau_0)^{2\delta_{\boldsymbol{g}}-1} \sinh\left(\frac{q_{\boldsymbol{g}} V}{2T}\right) \frac{\left|\Gamma\left(\delta_{\boldsymbol{g}} + i\frac{q_{\boldsymbol{g}} V}{2\pi T}\right)\right|^2}{\Gamma(2\delta_{\boldsymbol{g}})}. \tag{2.78}$$

Notice that the tunneling current depends on the charge $q_{\boldsymbol{g}}$ and scaling dimension $\delta_{\boldsymbol{g}}$ of the tunneling anyons: two of the three important properties quoted in Section 2.2. In principle, a measurement of tunneling current should yield the values of both these quantities. In real experiments, the tunneling amplitude of the QPC is highly non-universal depending on the microscopic details of the QPC and could be a function of V, and hence can vary across different experimental realizations. Moreover, owing to the gaplessness of the bosonic edge modes, their dynamics can be affected by properties not accounted for in our simplistic model. As a consequence, $\delta_{\boldsymbol{g}}$ is renormalized to values higher than the theoretical predictions. These non-universalities of the tunneling current impede determining the charge from average current measurements alone.

However, in a more general context, it was shown by Schottky that already the second moment of the current can sense its granularity [64]. If the current carriers follow a

Poisson distribution in their emission times, the variance of the current or the *shot noise* is directly proportional to the average value of the current. Interestingly, the constant of proportionality yields the charge of the current carriers.

Inspired by this intuition from semi-classical physics, we calculate the variance of the tunneling current operator in the Keldysh formalism

$$\left\langle \delta I_T^2 \right\rangle = \sum_{\eta\eta'} \left\langle \left\{ T_K I_T(t^{\eta}) I_T(t'^{\eta'}) e^{-i\int_K dt H_T(t)} \right\} \right\rangle - \left\langle I_T \right\rangle^2 . \tag{2.79}$$

At the lowest order in the tunneling amplitudes, there is no need to expand the time evolution operator and one can also safely discard the second term which is at least fourth order. To connect to experimentally measurable quantities, we need to Fourier transform the variance. The zero-frequency Fourier transform of the tunneling current variance gives the so-called shot noise:

$$\left\langle S_T \right\rangle = \sum_{\eta\eta'} \int d(t-t') \left\langle \left\{ T_K I_T(t^{\eta}) I_T(t'^{\eta'}) \right\} \right\rangle . \tag{2.80}$$

The detailed calculations are once again presented in Appendix C with the final result taking the form below

$$\left\langle S_T \right\rangle = 4 q_{\boldsymbol{g}}^2 |\Gamma_{\boldsymbol{g}}|^2 \tau_0 (2\pi T \tau_0)^{2\delta_{\boldsymbol{g}}-1} \cosh\left(\frac{q_{\boldsymbol{g}} V}{2T}\right) \frac{\left|\Gamma\left(\delta_{\boldsymbol{g}} + i\frac{q_{\boldsymbol{g}} V}{2\pi T}\right)\right|^2}{\Gamma(2\delta_{\boldsymbol{g}})}. \tag{2.81}$$

For the same reasons discussed in the context of the average tunneling current, even the tunneling noise by itself is highly non-universal and hence does not yield a concrete measurement of universal quantities such as the fractional charge.

However, comparing Equations (2.78) and (2.81) yields something quite exciting. In the limit $q_{\boldsymbol{g}} V \gg T$, as shown originally in Ref. [29], we find these quantities to satisfy the relation

$$\left\langle S_T \right\rangle = 2 q_{\boldsymbol{g}} \left\langle I_T \right\rangle , \tag{2.82}$$

independent of the value of the scaling dimension and the tunneling amplitude; the two major sources of non-universality on quantum Hall QPCs.

Experimentally, the above scheme can be implemented in the setup of Figure 2.5. While the tunneling current and tunneling noise of Equations (2.78) and (2.81) are quantities that can be theoretically analyzed relatively easily, it is not possible to directly access these quantities in experiments. Indeed, experiments typically measure the average current and the current auto-correlation noise at contact d. If the average current at contact d in the absence of the QPC is zero, then the average current at contact d can be shown to be equal to the tunneling current. The current autocorrelation noise however has multiple

contributions. In addition to the tunneling noise, there also exist contributions from the equilibrium thermal noise, and correlations between the tunneling current and equilibrium current on the lower edge. However, it is not difficult to systematically subtract the first contribution in experiments. Moreover, the second contribution is unimportant in the relevant regime of $q_{\boldsymbol{g}}V \gg T$. A measurement of the average current and current autocorrelation noise as a function of the applied voltage hence yields the charge of the particles constituting the currents. Indeed, this approach to measuring charges gave the first evidence of fractional charges in the FQHE as shown in Figure 2.5.

At this point, it is useful to define the so-called *Fano* factor

$$F = \frac{\langle S_T \rangle}{2e \langle I_T \rangle} \tag{2.83}$$

which is typically measured in experiments (where it is understood that experiments measure the average current and current autocorrelation at contact d). The interest in the above dimensionless quantity stems from the fact that it is immune to non-universalities stemming from the tunneling amplitude as this factor simply drops out. Nevertheless, there exist other, less problematic non-universalities such as disorder-induced resonances [44] that are not removed by the Fano factor.

Equation (2.82), exactly obeys the relation derived by Schottky, where charge carriers follow a Poissonian emission statistics. It is hence a strong indication that in the regime $q_{\boldsymbol{g}}V \gg T$, the number of anyons transmitted through a QPC in a given time interval obeys a Poisson distribution, and the emission times from the QPC are distributed uniformly within the latter interval. This observation would be of crucial importance in Chapter 7.

Before closing this section, we want to emphasize the overwhelming evidence supporting fractional charges in the FQHE. DC shot noise gave the first convincing evidence of fractional charges, and remains the standard method to measure charge in contemporary FQHE experiments. Since then fractional charges in FQHE have been seen using several other techniques such as: finite-frequency noise measurements [65], noise due to AC voltage applied on the edges [66], and resonant tunneling of quasiparticles through anti-dots in FQHE [67], among others. These diverse experimental approaches collectively reinforce that fractionally charged quasiparticles are an intrinsic feature of FQHE.

Nevertheless, there remain issues to address in the context of fractional charges. The most convincing agreement between theory and experiment exists only in the Laughlin fractions of the FQHE. In the non-Laughlin fractions, firstly there exist many candidate theories to explain a given FQHE state [24]. Moreover, in the latter states, theory often predicts different charges to tunnel at the QPC. Experimental evidence for these different charges is inconclusive. Early DC shot noise experiments have witnessed a temperature dependence of the Fano factor, and hence the charge tunneling at the QPC, in non-Laughlin FQHE states [49–51, 68–70]. However, recent works have cast doubt on the interpretation of these earlier results [43, 52]. It is therefore necessary to identify

experimentally measurable quantities that can robustly detect multiple charges tunneling simultaneously at the QPC. This issue is addressed in Chapter 3, where we demonstrate that photoassisted shot noise in general Abelian FQHE is sensitive to different charges tunneling simultaneously at the QPC.

Chapter 4 explores another intriguing effect resulting from the fractional charge of anyons. When a fractionally charged anyon encounters a QPC that transmits only electrons, an Andreev reflection-like process occurs. Earlier experiments however strangely observed fractional charges to be transmitted across QPCs in the strong-backscattering regime. While the latter results were attributed to the long propagation length of the anyons, recent experiments have observed the Andreev reflection-like process in the same system. Chapter 4 hence aims to bridge the gap between theory and experiments, providing some insight on both the earlier and recent experiments.

2.4.2. Scaling dimension

If the existence of fractionally charged quasiparticles in the FQHE has been unequivocally established, the understanding of their scaling dimension remains far less certain. Two recent experiments [43, 44] (whose preprints appeared as this thesis was being written) provide contradictory results regarding the scaling dimension. While there exist several theoretical proposals to measure the scaling dimension [71–74], these experiments both have a common theoretical basis pioneered by Refs.[75, 76].

The key idea is to probe the Fano factor of Equation (2.83) in the large temperature regime. As discussed in the paragraph following Equation (2.82), there exist additional contributions to the autocorrelation noise measured in experiments that become important at large temperatures. The general expression of the Fano factor, taking into account the correlations of the tunneling current and edge current, reads [76]:

$$F = \frac{2}{\pi}\frac{q_{\boldsymbol{g}}}{e}\mathrm{Im}\left[\psi\left(\delta_{\boldsymbol{g}} + i\frac{q_{\boldsymbol{g}}V}{2\pi T}\right)\right], \tag{2.84}$$

where ψ is the digamma function. The Fano factor depends on voltage and temperature in a combined way, via the ratio $z = eV/T$. In the small z regime, the Fano factor is dominated by thermal contributions, evolving linearly with z. As z is increased, it eventually asymptotes to the shot noise value of $q_{\boldsymbol{g}}/e$, as expected in the $q_{\boldsymbol{g}}V \gg T$ regime. Interestingly, the transition between these regimes is controlled by $\delta_{\boldsymbol{g}}$ sitting inside the digamma function. The shape of the so-called thermal to shot noise crossover curve depends heavily on the value of $\delta_{\boldsymbol{g}}$. The evolution of F along the crossover varies noticeably in both width and overall shape, depending on the value of $\delta_{\boldsymbol{g}}$. Roughly speaking, the behavior of the Fano factor at large z gives $q_{\boldsymbol{g}}/e$, and at small z, it depends on both $q_{\boldsymbol{g}}$ and $\delta_{\boldsymbol{g}}$. The crossover between the two depends only on $\delta_{\boldsymbol{g}}$.

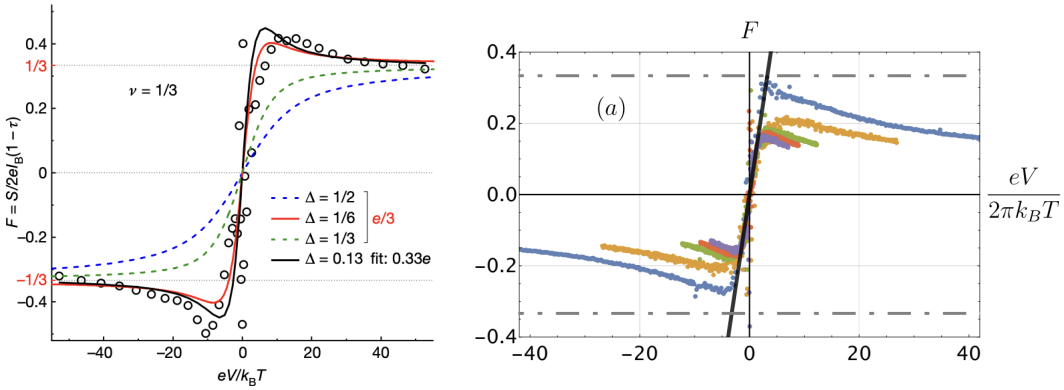


Figure 2.6.: Data from recent experiments measuring the scaling dimension $\delta_{\boldsymbol{g}}$ of quasiparticles in the $\nu = 1/3$ FQHE. (Left) Thermal to shot noise crossover data from Ref. [44] (at a fixed temperature) consistent with $\delta_{\boldsymbol{g}} = 1/3$. (Right) Thermal to shot noise crossover data from Ref. [43]. Each curve corresponds to a different temperature. Ref. [43] fits with theory only the part of data where curves at different temperatures collapse onto each other, finding $\delta_{\boldsymbol{g}} = 1$.

Ref. [44] measured the thermal to shot noise crossover of the Fano factor. They work at a fixed temperature, changing V to manipulate the dimensionless ratio z. Their measurements of the crossover is consistent with the theoretically predicted scaling dimension $\delta_{\boldsymbol{g}} = 1/3$ for quasiparticles in the $\nu = 1/3$ FQHE, as shown in Figure 2.6. Ref. [43] analyze similar measurements, putting together data at several temperatures. Since F depends on the dimensionless ratio z, measurements of F vs z performed at different temperatures should collapse onto each other. Experimentally, this turns out to be the case only for small z as seen in Figure 2.6. Ref. [43] argue that this signals a breakdown of chiral Luttinger liquid theory at higher z (due to effects not taken into account in the simple model). They hence propose to fit with theory only the part of the measurements where curves at different temperatures collapse onto each other. Doing this, they find $\delta_{\boldsymbol{g}} = 1$ for quasiparticles in the $\nu = 1/3$ FQHE, in stark disagreement with Ref. [44]. We also remark that a more recent experiment implementing a Hong-Ou-Mandel collision of fractional voltage pulses in $\nu = 1/3$ FQHE obtain a scaling dimension $\delta_{\boldsymbol{g}} = 2/3$ [45, 77].

These conflicting results highlight the ongoing debate around the measurement of the scaling dimension of anyons in the FQHE, calling for detailed studies in this direction. Hence, in Chapter 5 we study a temperature-difference driven finite-frequency noise in FQHE endowed with a QPC. We find the latter quantity to robustly discriminate anyonic scaling dimensions from non-anyonic ones, in a general Abelian FQHE system.

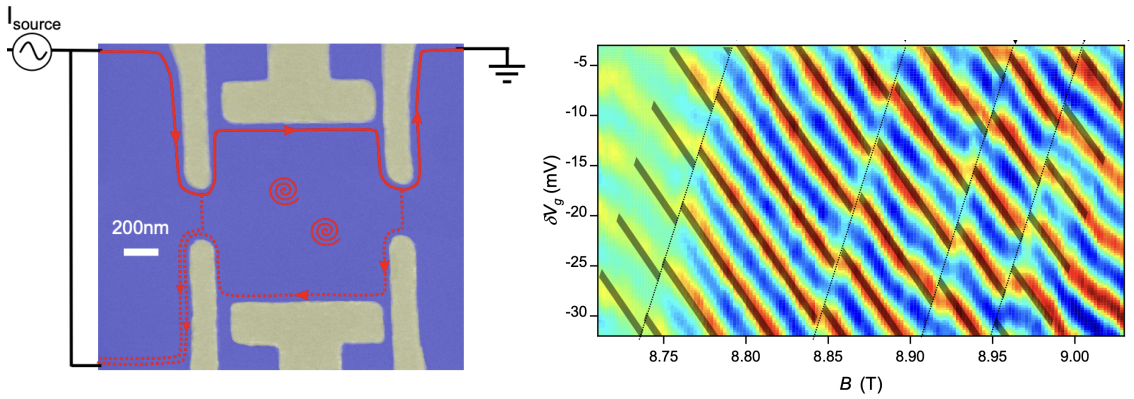


Figure 2.7.: (Left) Schematic figure of the anyonic Fabry-Pérot interferometer. The interference between the two dotted paths is sensitive to the anyons inside island, indicated by vortices. (Right) Varying the magnetic field removes anyons from the island, resulting in quantized phase shifts in the tunneling conductance $\partial \langle I_T \rangle / \partial V$. The phase slips shown here are consistent with $\theta = \pi/3$. Both figures are taken from Ref. [36].

2.4.3. Braiding phase

The language used to describe the different configurations of QPC in Section 2.3.2, that of incoming, reflected, and transmitted currents suggests an interesting analogy with optics. We imagine chiral edge states to act as waveguides carrying anyon beams, and QPCs as (non-linear) beam-splitters splitting the anyon beams into reflected (continue on same edge) and transmitted (tunnel to opposite edge) parts. This inspires one to borrow methods established in the context of classical or quantum optics and apply them to study anyonic exchange statistics. Indeed several approaches to probe anyonic statistics were developed based on Hanbury Brown and Twiss [78–82], Fabry-Perot [35], Hong-Ou-Mandel [77, 83], and Mach-Zehnder [84, 85] interferometry, among others. We describe below two approaches that have yielded remarkable success in measuring anyonic braiding phase.

Fabry-Pérot interferometry

First is the Fabry-Perot interferometer, shown in Figure 2.7. The incoming current on the top edge can take two different paths to reach the measurement apparatus on the lower edge indicated by the dotted lines. In the first path, the current is transmitted to the lower edge through the left QPC. In the second, the current is reflected through the left QPC. It continues on the upper edge and it is then transmitted through the right QPC to the lower edge. Finally, it is reflected again on the left QPC to reach the measurement apparatus. The interference between these two paths of the current is sensitive to what is sitting in the bulk island between the two QPC. By varying the magnetic field or gate voltages, it is possible to add or remove a bulk anyon from the island. This changes

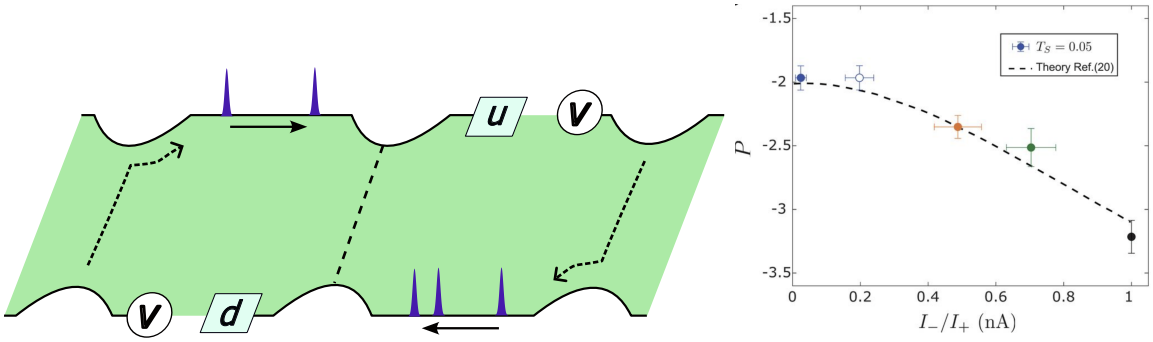


Figure 2.8.: (Left) Schematic of the anyon collider setup. Two source QPCs biased with a voltage send a stream of anyons on the central QPC. The current correlations in the output of the central QPC are sensitive to the braiding phase. (Right) Data from Ref. [34] showing remarkable agreement with theoretical predictions.

the phase gathered in the interference term, showing up as phase slips in the measured tunneling current (or the tunneling conductance $\partial \langle I_T \rangle / \partial V$, as was measured in Ref. [36]) as shown in Figure 2.7. Several groups have by now been successful in measuring anyon braiding phase using this approach in $\nu = 1/3$ [41, 42] and $\nu = 2/5$ FQHE [40].

Anyon collider

The other approach that we summarize now is, appealing to the optics analogy, best described as a random Hong-Ou-Mandel interferometer. Although the nomenclature cosmetically befits this geometry shown in Figure 2.8, the underlying physics is more exotic. The setup consists of three QPCs. The QPCs on the left and right, placed in the weak-backscattering regime are biased with voltage V, satisfying $q_g V \gg T$. This places the QPC in the Poissonian regime, where a beam of anyons obeying Poissonian emission statistics is transmitted on the opposite edges. These anyons travel along the edges and arrive at the central QPC. It is was initially thought that the incoming anyons collide with each other and the current correlations at the output yield a measure of fractional exclusion statistics [33]. The latter is an aspect of anyons not discussed in this thesis. This established the name *anyon collider* for this geometry. Later works have shown that the physics going on here is quite different [86, 87]. Indeed, with a dilute, Poissonian beam of anyons on both edges, the probability of two anyons on opposite edges arriving together at the central QPC is negligible. In fact, this geometry probes the braiding phase of anyons. In contrast to braiding in 2D discussed for example in Section 1.1, the braiding processes on FQHE edges are more abstract. It is due to different time-ordering of anyon operators at a fixed spatial location on the 1D FQHE edges. The anyon braiding thus occurs in $1+1$D, and is hence referred to as time-domain braiding. The physics of the latter processes is described in detail in Chapter 6.

Experiments on this geometry gave the first evidence of anyonic braiding in the $\nu = 1/3$ FQH [34], with later confirmation by several other groups [37–39]. Indeed, the experiments agree remarkably well with the theoretical predictions of Ref. [33] in the context of $\nu = 1/3$. When extended to $\nu = 2/5$, the experiments were in striking disagreement with the theory.

Chapters 6–8 focus on the anyon collider, with particular emphasis on resolving the disagreement between theory and experiment at the filling fraction $\nu = 2/5$. Chapter 6 serves as a pedagogical introduction, explaining the anyon braiding processes that occur within the anyon collider. Chapter 7 extends the theory of the anyon collider to general Abelian FQHE, offering new predictions for the $\nu = 2/3$ FQHE, where experiments are yet to be conducted, and addressing the discrepancy at $\nu = 2/5$. Finally, in Chapter 8, we examine how the finite width of anyons affects the anyon collider. We quantitatively explain the experimental observations at $\nu = 2/5$, resolving the disagreement between theory and experiment at $\nu = 2/5$.

Chapter 3.

Photoassisted shot noise

Fractional charges were first observed via DC shot noise measurements of anyons tunneling at a quantum point contact (QPC) in the fractional quantum Hall effect (FQHE). The latter measurement is now the go-to technique for measuring the charge of anyons. However, as we show in this chapter, in scenarios where different types of charges are expected to tunnel simultaneously at the QPC, determining the individual charges using DC shot noise measurements is challenging.

A promising alternative is the study of shot noise under the influence of periodic AC voltage, called *photo-assisted shot noise* (PASN). In Laughlin FQHE, PASN has been demonstrated as a complementary tool for fractional charge diagnostics. In this chapter, we investigate PASN in non-Laughlin FQHE, where different types of charges are expected to tunnel concurrently at QPCs. We develop a formalism to calculate PASN for a general Abelian quantum Hall system, accommodating multiple bosonic modes on the egdes, and different types of charges tunneling simultaneously at the QPC.

Applied to the specific case of $\nu = 2/3$ FQHE, our analysis reveals PASN as a robust probe for detecting multiple types of charges tunneling at a QPC. Remarkably, PASN remains effective even when the tunneling of one type of charge is significantly less prevalent than the others. We show that even in conditions easily accessible in contemporary experiments, PASN measurements constitute an effective probe of different types of charges tunneling simultaneously at the QPC.

3.1. Preliminaries

This chapter delves into the study of noise driven by AC voltage at a quantum point contact (QPC), known as photo-assisted shot noise (PASN), with the goal of probing fractional charges tunneling through the QPC. Before addressing this theoretically as well as experimentally challenging problem, it is essential to clarify the motivation to do so. In Section 2.4.1, we established that DC shot noise is an effective probe of fractional charges tunneling at a QPC when a unique type of charge tunnels at the QPC. However,

this section will first examine the DC shot noise when different types of charges tunnel simultaneously. We find that, in such cases, DC shot noise is not a reliable tool for probing all the distinct charges involved in the tunneling process.

This observation highlights the need for a more robust method to probe different charges tunneling simultaneously at a QPC. Consequently, we explore PASN in the context of general Abelian FQHE, where different charges are expected to tunnel simultaneously. Before going about this, we will introduce PASN when a single type of charge tunnels at the QPC, demonstrating its complementarity to DC shot noise as a measure of tunneling charges. The latter topic forms the second focus of this section.

3.1.1. Shortcomings of DC shot noise

Let us consider a general Abelian FQHE edge endowed with a QPC. The tunneling Hamiltonian and current operators take the form derived in Section 2.3:

$$H_T(t) = \sum_\alpha \sum_\epsilon \left[\Gamma_{\boldsymbol{g}_\alpha} \psi^{u\dagger}_{\boldsymbol{g}_\alpha}(0,t)\psi^{d}_{\boldsymbol{g}_\alpha}(0,t)\right]^\epsilon, \tag{3.1}$$

$$I_T(t) = \sum_\alpha \sum_\epsilon i\epsilon q_{\boldsymbol{g}_\alpha} \left[\Gamma_{\boldsymbol{g}_\alpha} \psi^{u\dagger}_{\boldsymbol{g}_\alpha}(0,t)\psi^{d}_{\boldsymbol{g}_\alpha}(0,t)\right]^\epsilon, \tag{3.2}$$

where $\psi^{u/d}_{\boldsymbol{g_\alpha}} = e^{i\boldsymbol{g_\alpha}\cdot\boldsymbol{\phi^{u/d}}}$ is the anyon operator with $\boldsymbol{g_\alpha} = (g_{\alpha 1}, \ldots, g_{\alpha N})$ being the anyon vector and $\boldsymbol{\phi^{u/d}} = (\phi_1^{u/d}, \ldots, \phi_N^{u/d})$ is a vector of the bosonic fields. Within the Keldysh formalism, the average value of the tunneling current and its variance, respectively, take the following general forms:

$$\langle I_T(t)\rangle = \left\langle \left\{ T_K I_T(t^-) e^{-i\int_K dt' H_T(t'^{\eta'})} \right\} \right\rangle, \tag{3.3}$$

$$\left\langle \delta I_T^2(t,t')\right\rangle = \left\langle \left\{ T_K \delta I_T(t^-)\delta I_T(t'^+) e^{-i\int_K dt H_T(t)} \right\} \right\rangle, \tag{3.4}$$

where $\delta I_T(t) = I_T(t) - \langle I_T(t)\rangle$. Throughout this chapter, we will work at the lowest order of perturbation in the parameters $\Gamma_{\boldsymbol{g}_\alpha}$. The above quantities then assume a simpler form:

$$\langle I_T(t)\rangle = -i\sum_{\eta'} \eta' \int dt' \left\langle \left\{ T_K I_T(t^-) H_T(t'^{\eta'}) \right\} \right\rangle, \tag{3.5}$$

$$\left\langle \delta I_T^2(t,t')\right\rangle = \left\langle \left\{ T_K \delta I_T(t^-)\delta I_T(t'^+) \right\} \right\rangle. \tag{3.6}$$

Let us start by considering the average current and noise due to a DC voltage, when a unique type of charge tunnels across the QPC. The latter condition amounts to dropping the sums over α in Equation (3.1) and (3.2). Let us consider the upper edge to be driven by a constant voltage V_1. As explained in Section 2.3, this is effected by the transformation

$$\phi_j^u(x,t) \longrightarrow \phi_j^u(x,t) + Q_j V_1 t. \tag{3.7}$$

Following the discussion in Section 2.4.1 and Appendix C, the average current and DC shot noise are given by:

$$\begin{aligned}
\langle I_T \rangle &= 2q_{\boldsymbol{g}} |\Gamma_{\boldsymbol{g}}|^2 \tau_0 (2\pi T \tau_0)^{2\delta_{\boldsymbol{g}}-1} \sinh\left(\frac{q_{\boldsymbol{g}} V_1}{2T}\right) \frac{\left|\Gamma\left(\delta_{\boldsymbol{g}} + i\frac{q_{\boldsymbol{g}} V_1}{2\pi T}\right)\right|^2}{\Gamma(2\delta_{\boldsymbol{g}})}, \\
\langle S_T \rangle &= 4q_{\boldsymbol{g}}^2 |\Gamma_{\boldsymbol{g}}|^2 \tau_0 (2\pi T \tau_0)^{2\delta_{\boldsymbol{g}}-1} \cosh\left(\frac{q_{\boldsymbol{g}} V_1}{2T}\right) \frac{\left|\Gamma\left(\delta_{\boldsymbol{g}} + i\frac{q_{\boldsymbol{g}} V_1}{2\pi T}\right)\right|^2}{\Gamma(2\delta_{\boldsymbol{g}})},
\end{aligned} \tag{3.8}$$

where $\langle S_T \rangle = \int d(t-t') \langle \delta I_T^2(t,t') \rangle$ denotes the shot noise, $\langle I_T \rangle$ denotes the average current tunneling across the QPC, $\Gamma_{\boldsymbol{g}}$ is the tunneling amplitude, $q_{\boldsymbol{g}}$ is the charge of the anyon tunneling across the QPC, $\delta_{\boldsymbol{g}}$ is the scaling dimension of the anyon, T is the temperature of the system, and finally, τ_0 is an ultra-violet cutoff.

In the experimentally accessible large voltage regime, $q_{\boldsymbol{g}} V_1 \gg T$, the shot noise and average tunneling current obey a simple relation, as emphasized in Section 2.4.1

$$\langle S_T \rangle = 2q_{\boldsymbol{g}} \langle I_T \rangle . \tag{3.9}$$

The ratio of the average current and shot noise is called the Fano factor. The latter quantity naturally gets rid of non-universal physics contained primarily in $\Gamma_{\boldsymbol{g}}$ and $\delta_{\boldsymbol{g}}$, allowing an easy extraction of $q_{\boldsymbol{g}}$ if both the current and noise are measured. Experimentally, the noise is measured as a function of the current, with the slope yielding the value of the charge tunneling at the QPC as shown in Figure 2.5.

Let us now calculate the average current and shot noise when different types of charges tunnel simultaneously across the QPC. This amounts to using Equations (3.1) and (3.2) with the sums over different anyons types retained. The calculation is detailed in Appendix C, and the final results are presented here:

$$\begin{aligned}
\langle I_T \rangle &= \sum_\alpha 2q_{\boldsymbol{g}_\alpha} |\Gamma_{\boldsymbol{g}_\alpha}|^2 \tau_0 (2\pi T \tau_0)^{2\delta_{\boldsymbol{g}}-1} \sinh\left(\frac{q_{\boldsymbol{g}_\alpha} V_1}{2T}\right) \frac{\left|\Gamma\left(\delta_{\boldsymbol{g}} + i\frac{q_{\boldsymbol{g}} V_1}{2\pi T}\right)\right|^2}{\Gamma(2\delta_{\boldsymbol{g}})}, \\
\langle S_T \rangle &= \sum_\alpha 4q_{\boldsymbol{g}_\alpha}^2 |\Gamma_{\boldsymbol{g}_\alpha}|^2 \tau_0 (2\pi T \tau_0)^{2\delta_{\boldsymbol{g}}-1} \cosh\left(\frac{q_{\boldsymbol{g}_\alpha} V_1}{2T}\right) \frac{\left|\Gamma\left(\delta_{\boldsymbol{g}} + i\frac{q_{\boldsymbol{g}_\alpha} V_1}{2\pi T}\right)\right|^2}{\Gamma(2\delta_{\boldsymbol{g}})}.
\end{aligned} \tag{3.10}$$

We notice that the average current and noise now comprise a sum over contributions from all the charges tunneling across the QPC. Consequently, we find now in the large voltage limit:

$$\langle S_T \rangle = 2\frac{\sum_\alpha |\Gamma_{\boldsymbol{g}_\alpha}|^2 q_{\boldsymbol{g}_\alpha}^2 q_{\boldsymbol{g}_\alpha}^{2\delta_{\boldsymbol{g}}-1}}{\sum_\alpha |\Gamma_{\boldsymbol{g}_\alpha}|^2 q_{\boldsymbol{g}_\alpha} q_{\boldsymbol{g}_\alpha}^{2\delta_{\boldsymbol{g}}-1}} \langle I_T \rangle \,. \tag{3.11}$$

Here, $|\Gamma_{\boldsymbol{g}_\alpha}|^2$ gives the relative probability of the type$-\alpha$ quasiparticle, and hence charge $q_{\boldsymbol{g}_\alpha}$ tunneling at the QPC. We thus find that the constant of proportionality between current and noise depends on charges of all the anyons in a complicated manner. This renders the DC shot noise an inadequate probe of charges in this scenario. That is, if only a small quantity of different charge tunnels across the QPC, then the difference might not be discernible from experimental errors.

We have assumed that all anyons tunneling at the QPC have the same scaling dimension $\delta_{\boldsymbol{g}}$. This is justified since in the limit $q_{\boldsymbol{g}_\alpha} V_1 \gg T$ that we will consider, the quasiparticles with the lowest scaling dimension provide the dominant contribution. Indeed, it is possible that two quasiparticles have the same scaling dimension but different charges, for example in $\nu = 2/3$ or $\nu = 5/2$.

Consider for example the case of the $\nu = 2/3$ where charges $e/3$ and $2e/3$ are predicted to tunnel simultaneously. The shot noise and average current are then related by

$$\langle S_T \rangle = 2\frac{|\Gamma_{e/3}|^2 (e/3)^{7/3} + |\Gamma_{2e/3}|^2 (2e/3)^{7/3}}{|\Gamma_{e/3}|^2 (e/3)^{4/3} + |\Gamma_{2e/3}|^2 (2e/3)^{4/3}} \langle I_T \rangle \tag{3.12}$$

where we have taken $\delta_{\boldsymbol{g}} = 2/3$ (see Table 3.1).

If in experiments, only $e/3$ charges tunnel through the QPC, the predicted slope of a current-noise plot is $2 \times 1/3 = 0.66$. What if a small quantity, of $2e/3$ charges tunnel simultaneously with the $e/3$ charges? Let us consider that 5% of the tunneling quasiparticles have charge $2e/3$ and the remaining have charge $e/3$. Then the slope predicted by Equation (3.11) is 0.72. Such a deviation is largely indistinguishable from errors characteristic of such experiments. In Ref. [37] for example, the slopes of the data points deviate more than 10% from the theoretically expected values of the fractional charges. Moreover, older experiments probing fractional charges in composite fractions using DC shot noise have observed a temperature dependence of the Fano factor [49, 50, 68–70], with the results being open to interpretations. Indeed, more recent experiments suggest a role of topological or reconstruction-induced neutral modes in the temperature dependence of the Fano factor [52], while others suggest a breakdown of chiral Luttinger liquid theory to explain the same [43].

This calls for an effective probe of charges tunneling in a QPC, when anyons with different charges are predicted to tunnel simultaneously. We hence turn to understanding

the basic notions of photoassisted shot noise (PASN) and how it allows to probe the charges tunneling across the QPC.

3.1.2. Introduction to photoassisted shot noise

In this section, we introduce the concept of photoassisted shot noise (PASN), noise due to current driven by a periodic AC voltage. Photoassisted current and shot noise have proved to be a rich source of information in varied mesoscopic systems such as normal diffusive and ballistic systems [88–90] superconductors [91, 92] and the quantum Hall effect [93–95]. In the fractional quantum Hall effect, it has been shown to provide a complementary diagnosis of the fractional charges tunneling at QPCs [66, 96]. Here, we will outline the theoretical basis of PASN when a unique type of charge tunnels across the QPC, and illustrate that it provides a diagnosis of the charge.

The discussion in Section 3.1, exploring DC shot noise, considers that the voltage V_1 driving the edges is time-independent. We now relax this assumption, and consider a time-dependent periodic voltage drive $V(t) = V_1 + V_2(t)$ applied on the upper edge. $V_2(t)$ has a periodicity $\bar{T}$ such that $\int_0^{\bar{T}} dt V_2(t) = 0$. As shown in Section 2.3, the voltage effects the following transformation of the bosonic fields:

$$\phi_j^u(x,t) \longrightarrow \phi_j^u(x,t) + Q_j \int_{-\infty}^{t} dt'\ V(t'). \tag{3.13}$$

Hence, the anyons tunneling across the QPC, $\psi_{\boldsymbol{g}} = e^{i\boldsymbol{g}\cdot\boldsymbol{\phi}}$ gain a time-dependent phase $e^{i\omega_{\boldsymbol{g}}(t)}$, given by

$$\omega_{\boldsymbol{g}}(t) = q_{\boldsymbol{g}} \int_{-\infty}^{t} dt'\ V(t'). \tag{3.14}$$

For a constant voltage drive, time translation symmetry means that the current correlations carry a dependence only on the difference of the times. In the case of a time-dependent drive, the current correlations also carry a dependence on the sum of the two times at which the currents are measured. But the periodicity implies that such dependence is the same over different periods of the drive. We hence define the photoassisted shot noise as

$$\left\langle \bar{S} \right\rangle = 2 \int d(t-t') \int_0^{\bar{T}} \frac{d(\frac{t+t'}{2})}{\bar{T}}\ \left\langle \delta I_T^2(t,t') \right\rangle . \tag{3.15}$$

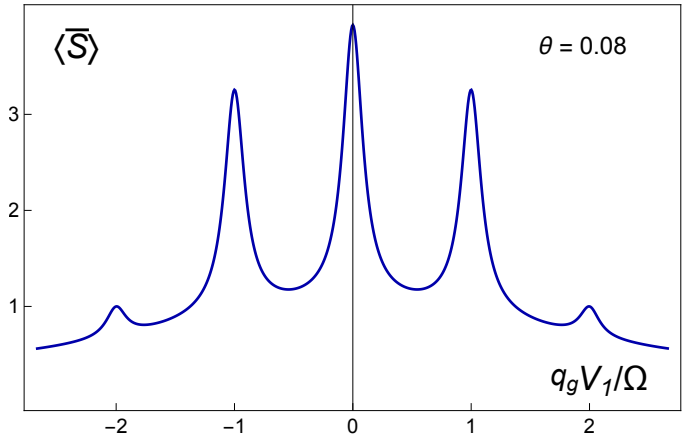


Figure 3.1.: Photo-assisted shot noise shown as a function of $q_{\boldsymbol{g}} V_1/\Omega$. The first two harmonics of the exponentiated sinusoidal drive are included in the sum along with the DC $l = 0$ component. This leads to peaks at $q_{\boldsymbol{g}} V_1/\Omega = l$, for all the l included in the sum. Assuming Ω is known, the distance between subsequent peaks yields the value of $q_{\boldsymbol{g}}$.

The computations, detailed in the forthcoming sections of this chapter, yield the following relation between PASN and DC shot noise of Equation (3.37)

$$\left\langle \bar{S} \right\rangle = \sum_l |p_{\boldsymbol{g}}^{(l)}(q_{\boldsymbol{g}} V_2/\Omega)|^2 \left\langle S_T \right\rangle (q_{\boldsymbol{g}} V_1 - l\Omega)\,, \tag{3.16}$$

where V_2 is the amplitude of $V_2(t)$ and

$$p_{\boldsymbol{g}}^{(l)}\left(\frac{q_{\boldsymbol{g}} V_2}{\Omega}\right) = \frac{1}{\bar{T}} \int_0^{\bar{T}} dt\; e^{-iq_{\boldsymbol{g}} \int_{-\infty}^{t} dt' V_2(t')} e^{il\Omega t}, \tag{3.17}$$

with $\Omega = 2\pi/\bar{T}$ being the frequency of the AC drive. Equation (3.16) admits an interesting interpretation. One can imagine that the anyons emitted to the lower edge through the QPC end up in a superposition of quantum states whose energies are shifted by quantized differences, $l\Omega$, with probability amplitudes $p_{\boldsymbol{g}}^{(l)}$. Equation (3.16) thus presents the PASN as a sum of simultaneous measurements of DC shot noises at shifted DC voltages $V_1 \to V_1 + l\Omega/q_{\boldsymbol{g}}$, weighted by probabilities $|p_{\boldsymbol{g}}^{(l)}|^2$. Thus, the ground state of the periodic voltage-driven system can be thought to exist in a superposition of states with energies $l\Omega$. The transitions to the higher and lower energy states are effected by absorption and emission of photons coming from the AC drive, lending the name photo-assisted shot noise to the AC voltage driven noise. Equation (3.16) is an example of Tien-Gordon relations [97], valid for periodic drives in a wide variety of systems. We will discuss this connection in slightly more detail in Section 3.3.

To illustrate how PASN probes fractional charges, we consider the edge being driven by a sinusoidal voltage. In this case, the amplitudes $p_{\boldsymbol{g}}^{(l)}$ are given by the Bessel function of the first kind. The latter decay quickly with increasing l; it hence suffices to include

the first few terms in the sum of Equation (3.16). We include only $l = 0, \pm 1, \pm 2$, and the resulting PASN is plotted in Figure 3.1 for $\nu = 1/3$ FQHE. Interestingly, the DC shot noise singularity (dip for $\delta_{\boldsymbol{g}} > 1/2$) usually appearing at $V_1 = 0$ now appears at all $V_1 = l\omega/q_{\boldsymbol{g}}$. This is true to the interpretation of PASN being a sum of DC shot noises at shifted voltages and is a signature of photon-assisted transition processes of anyons with charge $q_{\boldsymbol{g}}$. The distance between subsequent peaks gives the value of $q_{\boldsymbol{g}}$, since the drive frequency Ω is known.

Hence PASN serves as a probe of fractional charge, complementary to DC shot noise when a unique charge tunnels at the QPC. It now remains to see if PASN yields additional insights compared to DC shot noise, when different charges tunnel simultaneously across the QPC. The rest of this chapter aims to address the latter question.

3.2. Floquet formalism for Abelian FQHE edges

In the previous section, we understood the basic physical idea of photo-assisted shot noise: when an FQHE edge is driven by a time-dependent voltage, the anyons tunneling through the QPC end up gaining a time-dependent phase, given in Equation (3.14). A Fourier transform of this phase leads to an interpretation of the PASN as a sum of DC shot noises at different quantized energies, weighted by the Fourier coefficients of the phase. The objective of this section is to lay down the mathematical details of the above, culminating in a tunneling current operator which takes into account the possibility of photon-assisted transitions to different energy states.

We consider applying a time-dependent voltage on the upper edge of the QPC. The setup is schematically shown in Figure 3.2. The voltage couples to the current density of the bosonic fields, with the coupling constant given by the (square root of the) conductance Q_j of the bosonic fields as shown in Section 2.3. This results in the bosonic fields gaining a phase:

$$\phi_j^{(u)}(x,t) \to \phi_j^{(u)}(x,t) + Q_j \int_{-\infty}^{t} dt'\ V(t'). \tag{3.18}$$

The voltage can be transferred to the tunneling amplitude by a gauge transformation, leading to a phase gathered by anyons tunneling at the QPC:

$$\Gamma_{\boldsymbol{g}_\alpha} \longrightarrow \Gamma_{\boldsymbol{g}_\alpha} e^{i\omega_{\boldsymbol{g}_\alpha}(t)}. \tag{3.19}$$

This transformation allows us to use the tunneling Hamiltonian and current operators quoted in Equations (3.1) and (3.2), modifying the tunneling amplitude appropriately.

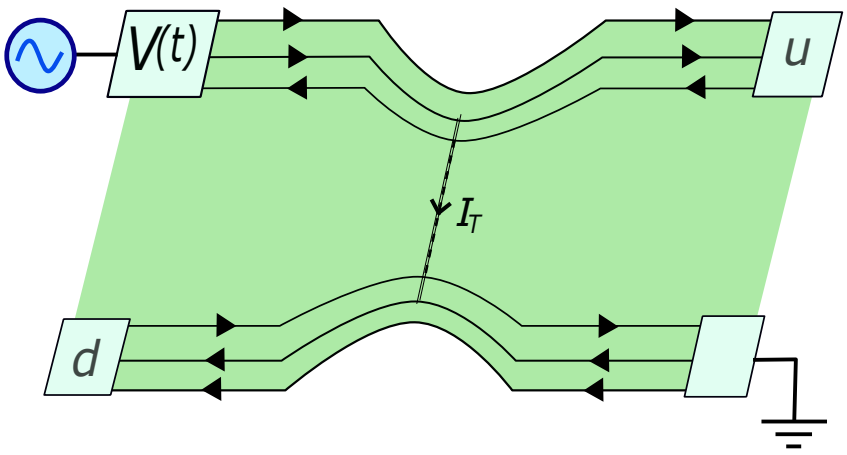


Figure 3.2.: Time dependent voltage drive $V(t) = V_1 + V_2(t)$ is applied on the upper edge of a general Abelian FQHE system, where V_1 is a constant DC voltage, and $V_2(t)$ is a periodic AC voltage with $\int_0^{\bar{T}} dt\ V_2(t) = 0$, where $\bar{T}$ is the period of the AC drive. The current produced by the voltage drive is partitioned at the QPC placed downstream. The resulting tunneling current and its correlations are measured at contact d.

The phase gained by type$-\alpha$ anyons $\psi_{\boldsymbol{g_\alpha}}$ tunneling across the QPC is given by

$$\omega_{\boldsymbol{g}_\alpha}(t) = q_{\boldsymbol{g}_\alpha} \int_{-\infty}^{t} dt'\ V(t'), \tag{3.20}$$

where $q_{\boldsymbol{g}_\alpha}$ is the charge of type$-\alpha$ anyon. We split the time-dependent voltage drive into a constant part V_1, and a periodic time-varying part, $V_2(t)$ of frequency Ω, carrying an explicit time-dependence

$$V(t) = V_1 + V_2(t) \tag{3.21}$$

such that $\int_0^{\bar{T}} dt\ V_2(t) = 0$, where $\bar{T} = 2\pi/\Omega$ is the period of the AC drive.

To proceed further, the phase gained by anyons due to the periodic AC voltage is Fourier decomposed:

$$\exp\left\{\left(-iq_{\boldsymbol{g}_\alpha}\int_{-\infty}^{t} dt'\ V_2(t')\right)\right\} = \sum_l p^{(l)}_{\boldsymbol{g}_\alpha}\left(\frac{q_{\boldsymbol{g}_\alpha}V_2}{\Omega}\right) e^{-il\Omega t}, \tag{3.22}$$

where V_2 denotes the amplitude of the AC drive $V_2(t)$. The Fourier components $p^{(l)}_{\boldsymbol{g}_\alpha}(q_{\boldsymbol{g}_\alpha}V_2/\Omega)$ depend on the shape, amplitude and frequency of the periodic AC voltage applied, and the charges tunneling at the QPC. In what follows, we will suppress the functional dependence of the Fourier components for brevity. The tunneling Hamiltonian and tunneling current

operator can then be expressed as:

$$H_T(t) = \sum_{\alpha} \sum_{\epsilon} \sum_{l} \left[\Gamma_{\boldsymbol{g}_\alpha} p^{(l)*}_{\boldsymbol{g}_\alpha} e^{i(q_{\boldsymbol{g}_\alpha} V_1 + l\Omega)t} \psi^{u\dagger}_{\boldsymbol{g}_\alpha}(0,t) \psi^{d}_{\boldsymbol{g}_\alpha}(0,t) \right]^{\epsilon}, \tag{3.23}$$

$$I_T(t) = \sum_{\alpha} \sum_{\epsilon} \sum_{l} i q_{\boldsymbol{g}_\alpha} \epsilon \left[\Gamma_{\boldsymbol{g}_\alpha} p^{(l)*}_{\boldsymbol{g}_\alpha} e^{i(q_{\boldsymbol{g}_\alpha} V_1 + l\Omega)t} \psi^{u\dagger}_{\boldsymbol{g}_\alpha}(0,t) \psi^{d}_{\boldsymbol{g}_\alpha}(0,t) \right]^{\epsilon}, \tag{3.24}$$

where the sum over ϵ takes care of the Hermitian conjugate processes since $\psi_{\boldsymbol{g}_\alpha} = e^{i\boldsymbol{g}_\alpha \cdot \boldsymbol{\phi}}$. The sum over α runs over different anyon types, while that over l runs over the Fourier components of the phase gained by anyons tunneling through the QPC. These expressions generalize the tunneling operators of Equations (3.1) (3.2), accounting for the phase gained by the tunneling anyons in a transparent manner. As discussed in Section 3.1.2, PASN can be interpreted as the weighted sum of DC shot noises at quantized voltages $V_1 + l\Omega/q_{\boldsymbol{g}_\alpha}$. This possibility is taken into account in the above tunneling operators through the sum over l.

3.3. Photoassisted shot noise: general Abelian FQHE

Using the tunneling operators presented in the preceding section, we now calculate the photo-assisted shot noise in a general Abelian FQHE system. We start by calculating the variance of the tunneling current operator. The latter quantity is expressed within the Keldysh formalism as

$$\left\langle \delta I_T^2(t,t') \right\rangle = \left\langle \left\{ T_K \delta I_T(t^-) \delta I_T(t'^+) e^{-i\int_K dt'' H_T(t'')} \right\} \right\rangle \tag{3.25}$$

where $\delta I_T(t) = I_T(t) - \langle I_T(t) \rangle$. We perturbatively compute the current-correlations at the lowest non-trivial order of the tunneling amplitudes – order $|\Gamma_{\boldsymbol{g}_\alpha}|^2$. We can hence discard the product of average current subtracted from the current correlations whose lowest contribution is at order $|\Gamma_{\boldsymbol{g}_\alpha}|^4$. The lowest-order perturbative current correlations are written as

$$\begin{aligned} \left\langle \delta I_T^2(t,t') \right\rangle &= \sum_{\alpha} \sum_{\epsilon} \sum_{lm} q^2_{\boldsymbol{g}_\alpha} |\Gamma_{\boldsymbol{g}_\alpha}|^2 p^{(l)*}_{\boldsymbol{g}_\alpha} p^{(m)}_{\boldsymbol{g}_\alpha} \\ &\times \exp\left\{ \left\{ i\epsilon \left[q_{\boldsymbol{g}_\alpha} V_1 (t-t') + \Omega(lt - mt') \right] \right\} \right\} \\ \times \left\langle \left\{ T_K \left[\psi^{(u)\dagger}_{\boldsymbol{g}_\alpha}(0,t^-) \psi^{(d)}_{\boldsymbol{g}_\alpha}(0,t^-) \right]^{\epsilon} \left[\psi^{u\dagger}_{\boldsymbol{g}_\alpha}(0,t'^+) \psi^{d}_{\boldsymbol{g}_\alpha}(0,t'^+) \right]^{-\epsilon} \right\} \right\rangle & \end{aligned} \tag{3.26}$$

where the sum over ϵ takes care of the Hermitian conjugate processes, and the sums over l and m run over the Fourier components of the phase gathered by anyons when they tunnel through the QPC. The Keldysh average factorizes into two disjoint parts over the

independent upper and lower bosonic edge modes:

$$\begin{aligned}\left\langle \delta I_T^2(t,t')\right\rangle = \sum_{\alpha}\sum_{\epsilon}\sum_{lm} q_{\boldsymbol{g}_\alpha}^2 |\Gamma_{\boldsymbol{g}_\alpha}|^2 p_{\boldsymbol{g}_\alpha}^{(l)*} p_{\boldsymbol{g}_\alpha}^{(m)} \\ \times \exp\{\{i\epsilon\left[q_{\boldsymbol{g}_\alpha} V_1(t-t') + \Omega(lt-mt')\right]\}\} \\ \times \left\langle \left\{ T_K e^{-i\epsilon \boldsymbol{g_\alpha}.\boldsymbol{\phi^u}(0,t^-)} e^{i\epsilon \boldsymbol{g_\alpha}.\boldsymbol{\phi^u}(0,t'^+)} \right\} \right\rangle \left\langle \left\{ T_K e^{i\epsilon \boldsymbol{g_\alpha}.\boldsymbol{\phi^d}(0,t^-)} e^{-i\epsilon \boldsymbol{g_\alpha}.\boldsymbol{\phi^d}(0,t'^+)} \right\} \right\rangle .\end{aligned} \tag{3.27}$$

The anyon correlation functions are calculated in Appendix B allowing us to express the current-correlations as

$$\begin{aligned}\left\langle \delta I_T^2(t,t')\right\rangle = \sum_{\alpha}\sum_{\epsilon}\sum_{lm} q_{\boldsymbol{g}_\alpha}^2 |\Gamma_{\boldsymbol{g}_\alpha}|^2 p_{\boldsymbol{g}_\alpha}^{(l)*} p_{\boldsymbol{g}_\alpha}^{(m)} \exp\{\left[2\delta_{\boldsymbol{g}_\alpha}\mathcal{G}^{-+}(0,t-t')\right]\} \\ \exp\{\{i\epsilon\left[q_{\boldsymbol{g}_\alpha} V_1(t-t') + \Omega(lt-mt')\right]\}\},\end{aligned} \tag{3.28}$$

where, $\mathcal{G}^{-+}(x,t) \equiv \mathcal{G}(x,t)$, bosonic Greens function as shown in Section 2.3, given by:

$$\mathcal{G}(x,t) = \log\left\{ \frac{\sinh\left(i\pi T_{u/d}\tau_0\right)}{\sinh\left[\pi T_{u/d}\left(i\tau_0 - [t-x]\right)\right]} \right\}. \tag{3.29}$$

As explained in Section 3.1.2, the PASN is defined as the zero-frequency Fourier transform of the current correlations above (over the time difference), averaged over one period of the periodic drive. We make the coordinate transformation $\tau = t - t'$, $u = (t+t')/2$, and employ the latter definition of the PASN:

$$\left\langle \bar{S}\right\rangle = 2\int d\tau \int_0^{\bar{T}} \frac{du}{\bar{T}} \left\langle \delta I_T^2\left(u+\frac{\tau}{2}, u-\frac{\tau}{2}\right)\right\rangle \tag{3.30}$$

From Equations (3.28) and (3.30), we can express the PASN as

$$\begin{aligned}\left\langle \bar{S}\right\rangle = \sum_{\alpha}\sum_{\epsilon}\sum_{lm} 2q_{\boldsymbol{g}_\alpha}^2 |\Gamma_{\boldsymbol{g}_\alpha}|^2 p_{\boldsymbol{g}_\alpha}^{(l)*} p_{\boldsymbol{g}_\alpha}^{(m)} \int_0^{\bar{T}} \frac{du}{\bar{T}} e^{i(l-m)\Omega u} \\ \int d\tau \exp\left\{ \left[2\delta_{\boldsymbol{g}_\alpha}\mathcal{G}(\tau) + i\epsilon\left(\frac{l+m}{2}\Omega + q_{\boldsymbol{g}_\alpha} V_1\right)\tau \right] \right\}\end{aligned} \tag{3.31}$$

Performing the $u-$integral yields a Kronecker delta function δ_{lm}, allowing us to sum over one of the Fourier indices. We also sum over the index ϵ, leaving us with the following expression

$$\left\langle \bar{S}\right\rangle = \sum_{\alpha}\sum_{l} 4\left(q_{\boldsymbol{g}_\alpha}|\Gamma_{\boldsymbol{g}_\alpha} p_{\boldsymbol{g}_\alpha}^{(l)}|\right)^2 \int d\tau \cos\left[\left(l + \frac{q_{\boldsymbol{g}_\alpha} V_1}{\Omega}\right)\Omega\tau\right] e^{2\delta_{\boldsymbol{g}_\alpha}\mathcal{G}(\tau)}. \tag{3.32}$$

We then evaluate the $\tau-$integral, using the finite temperature Greens function of Equation (3.29). Moreover, we define the reduced, dimensionless variables:

$$\begin{aligned} \theta &\equiv \frac{T}{\Omega}, \\ \zeta &\equiv \frac{\nu e V_1}{\Omega}. \end{aligned} \tag{3.33}$$

The quantity ζ (called q in existing literature [98, 99]) counts the charge transported over one period of the AC drive, in units of electrons. We see this explicitly by integrating the equilibrium current over a time-period:

$$\langle Q \rangle = \int_0^{\bar{T}} dt \, \langle I(t) \rangle = \nu \frac{e^2}{2\pi} \int_0^{\bar{T}} dt \; V(t) = \nu \frac{e^2}{2\pi} V_1 \bar{T} = e\zeta, \tag{3.34}$$

where we have used the relation that the current is given by the conductance on the edge times the applied voltage. Finally, the PASN is expressed as:

$$\left\langle \bar{S} \right\rangle = \sum_{\alpha l} 4 q_{\boldsymbol{g}_\alpha}^2 |\Gamma_{\boldsymbol{g}_\alpha} p_{\boldsymbol{g}_\alpha}^{(l)}|^2 \tau_0 \left(2\pi\theta\Omega\tau_0\right)^{2\delta_{\boldsymbol{g}_\alpha}-1} \frac{\cosh\left(\frac{l+\zeta q_{\boldsymbol{g}_\alpha}/\nu}{2\theta}\right)}{\Gamma(2\delta_{\boldsymbol{g}_\alpha})} \left| \Gamma\left(\delta_{\boldsymbol{g}_\alpha} + i\frac{l + \frac{q_{\boldsymbol{g}_\alpha}}{\nu}\zeta}{2\pi\theta}\right)\right|^2, \tag{3.35}$$

where it remains to sum over the Floquet indices.

Tien-Gordon relation of PASN in Abelian FQHE

There exists an interesting relation between transport properties of a device biased with a DC + AC drive, and the same device under a pure DC bias. Such a connection was first noticed by Ref. [97] in the context of normal metal-superconductor junctions. They studied tunneling current in a superconducting diode, driven by a sinusoidal voltage drive $V(t) = V_1 + V_2 \sin(\Omega t)$ which was shown to satisfy the relation:

$$I_{AC+DC}(V_{DC}) = \sum_l J_l^2 \left(\frac{eV_2}{\Omega}\right) I_{DC}\left(eV_1 + l\Omega\right), \tag{3.36}$$

where $J_l(x)$ denotes the Bessel function of the first kind. The current due to an DC + AC drive is shown to be equivalent to a weighted sum of voltage shifted DC currents, with the voltage shifts quantized in the frequency of the drive. Such relations are dubbed Tien-Gordon relations.

Looking for similar relations in the PASN in FQHE, we compare the latter with DC shot noise of (3.10), re-expressed here:

$$\begin{aligned}\langle S_T\rangle &= \sum_\alpha 4q_{\boldsymbol{g}_\alpha}^2|\Gamma_{\boldsymbol{g}_\alpha}|^2\tau_0\left(2\pi T\tau_0\right)^{2\delta_{\boldsymbol{g}_\alpha}-1}\cosh\left(\frac{q_{\boldsymbol{g}_\alpha}V}{2T}\right)\frac{\left|\Gamma\left(\delta_{\boldsymbol{g}_\alpha}+i\frac{q_{\boldsymbol{g}_\alpha}V}{2\pi T}\right)\right|^2}{\Gamma(2\delta_{\boldsymbol{g}})}\\ &\equiv \sum_\alpha S_T^\alpha\left(q_{\boldsymbol{g}_\alpha}V\right),\end{aligned} \tag{3.37}$$

where we have expressed the DC shot noise as the sum of contributions due to tunneling of different anyons.

Comparing Equations (3.35) and (3.37), we find PASN of Abelian FQHE to satisfy a Tien-Gordon-like relation:

$$\left\langle\bar{S}\right\rangle = \sum_\alpha\sum_l |p_{\boldsymbol{g}_\alpha}^{(l)}|^2 S_T^\alpha\left(q_{\boldsymbol{g}_\alpha}V_1+l\Omega\right). \tag{3.38}$$

Hence, as explained in Section 3.1.2, PASN can be understood as the simultaneous measurement of several DC shot noises with shifted voltages $V_1 \longrightarrow V_1 + l\Omega/q_{\boldsymbol{g}_\alpha}$. In this picture, an anyon with charge $q_{\boldsymbol{g}_\alpha}$, when emitted to the lower edge, ends up in a superposition of states with energies shifted by $l\Omega/q_{\boldsymbol{g}_\alpha}$ from the ground state. These shifts result from the absorption or emission of photons from the AC drive of frequency Ω. Each state in the superposition is weighted by the corresponding Floquet coefficients $|p_{\boldsymbol{g}_\alpha}^{(l)}|^2$.

To isolate the purely AC contributions to the PASN, we define an excess noise $\Delta\bar{S}$ by subtracting naturally, the $l=0$ contribution:

$$\Delta\bar{S} = \left\langle\bar{S}\right\rangle - \left\langle\bar{S}\right\rangle_{l=0}. \tag{3.39}$$

3.4. Photoassisted shot noise in $\nu = 2/3$ FQHE

We now apply the formalism developed in the previous sections to a concrete model of the $\nu = 2/3$ FQHE. We investigate PASN when different types of anyons, carrying different charges, tunnel at the QPC. We show that, unlike DC shot noise, PASN can distinguish different charge carriers simultaneously tunneling at the QPC.

$\nu = 2/3$ FQHE is an interesting system to explore such considerations. The canonical model of $\nu = 2/3$ admits anyons with different charges: $2e/3$ and $e/3$. Unlike other filling fractions, these anyons with different charges have the same scaling dimension as shown in Table 3.1. It is thus natural to expect both charges to tunnel simultaneously at the QPC. From the general expression of Equation (3.35), the explicit form of the PASN in

Type (α)	$g_{\alpha 1}$	$g_{\alpha 2}$	$q_{\boldsymbol{g}_\alpha}$	$\delta_{\boldsymbol{g}_\alpha}$
$\boldsymbol{g}_1$	$\sqrt{\frac{2}{3}}$	0	2/3	2/3
$\boldsymbol{g}_2$	$\sqrt{\frac{1}{6}}$	$\sqrt{\frac{1}{2}}$	1/3	2/3
$\boldsymbol{g}_3$	$\sqrt{\frac{1}{6}}$	$-\sqrt{\frac{1}{2}}$	1/3	2/3

Table 3.1.: Anyon quantum numbers, charges and scaling dimensions for the quasiparticles in $\nu = 2/3$ FQHE.

$\nu = 2/3$ is presented below:

$$\begin{aligned}\langle \bar{S} \rangle =& \frac{4\tau_0 \left(2\pi\theta\Omega\tau_0\right)^{2\delta_{\boldsymbol{g}}-1}}{\Gamma(2\delta_{\boldsymbol{g}})} \sum_l \Bigg\{ \\ & \left(\frac{e}{3}\right)^2 |\Gamma_{e/3} p^{(l)}_{e/3}|^2 \cosh\left(\frac{l+e\zeta/2}{2\theta}\right) \left|\Gamma\left(\delta_{\boldsymbol{g}} + i\frac{l+e\zeta/2}{2\pi\theta}\right)\right|^2 \\ & + \left(\frac{2e}{3}\right)^2 |\Gamma_{2e/3} p^{(l)}_{2e/3}|^2 \cosh\left(\frac{l+e\zeta}{2\theta}\right) \left|\Gamma\left(\delta_{\boldsymbol{g}} + i\frac{l+e\zeta}{2\pi\theta}\right)\right|^2 \Bigg\},\end{aligned} \tag{3.40}$$

where we have used $\nu = 2/3$, $q_{\boldsymbol{g_1}} = 2e/3$, $q_{\boldsymbol{g_2}} = q_{\boldsymbol{g_3}} = e/3$, and $\delta_{\boldsymbol{g_1}} = \delta_{\boldsymbol{g_2}} = \delta_{\boldsymbol{g_3}} \equiv \delta_{\boldsymbol{g}}$. We have also made the following change of notation for transparency: $\Gamma_{\boldsymbol{g_1}} \equiv \Gamma_{2e/3}$, $p^{(l)}_{\boldsymbol{g_1}} \equiv p^{(l)}_{2e/3}$, $p^{(l)}_{\boldsymbol{g_2}} = p^{(l)}_{\boldsymbol{g_3}} \equiv p^{(l)}_{e/3}$, and $|\Gamma_{e/3}|^2 \equiv |\Gamma_{\boldsymbol{g_2}}|^2 + |\Gamma_{\boldsymbol{g_3}}|^2$. We also re-express the tunneling amplitudes as $|\Gamma_{e/3}|^2 = \mu_{e/3}|\bar{\Gamma}|^2$ and $|\Gamma_{2e/3}|^2 = \mu_{2e/3}|\bar{\Gamma}|^2$ where $\bar{\Gamma}$ contains the non-universal physics of tunneling at the QPC, while $\mu_{e/3},\ \mu_{2e/3}$ are dimensionless numbers, giving the relative tunneling proportions of the corresponding charges. They satisfy the relation $\mu_{e/3} + \mu_{2e/3} = 1$. For the sake of illustration, we consider the FQHE edges to be driven by a sinusoidal AC drive, on top of a DC component:

$$V(t) = V_1 + V_2 \sin(\Omega t). \tag{3.41}$$

The Floquet coefficients of the phase gathered by the tunneling anyons in this case are given by the Bessel function of the first kind, denoted $J_l(x)$. The excess PASN for $\nu = 2/3$

hence takes the form:

$$\begin{aligned}\Delta\bar{S} =& \frac{4|\bar{\Gamma}|^2\tau_0\left(2\pi\theta\Omega\tau_0\right)^{2\delta_{\boldsymbol{g}}-1}}{\Gamma(2\delta_{\boldsymbol{g}})}\sum_{l\neq 0}\Bigg\{ \\ &\left(1-\mu_{2e/3}\right)\left(\frac{e}{3}\right)^2 J_l^2\left(\frac{eV_2}{3\Omega}\right)\cosh\left(\frac{l+e\zeta/2}{2\theta}\right)\left|\Gamma\left(\delta_{\boldsymbol{g}}+i\frac{l+e\zeta/2}{2\pi\theta}\right)\right|^2 \\ &+\mu_{2e/3}\left(\frac{2e}{3}\right)^2 J_l^2\left(\frac{2eV_2}{3\Omega}\right)\cosh\left(\frac{l+e\zeta}{2\theta}\right)\left|\Gamma\left(\delta_{\boldsymbol{g}}+i\frac{l+e\zeta}{2\pi\theta}\right)\right|^2\Bigg\}.\end{aligned} \tag{3.42}$$

We now study the excess noise as a function of ζ. This connects to earlier experiments, which imposed a sinusoidal drive of fixed frequency and amplitude on the edge, on top of constant DC voltage [66]. The current is partitioned at the QPC, and the resulting noise was measured as a function of the DC voltage.

In Figure 3.3(a) we show $\Delta\bar{S}$ as a function of ζ for $\theta = 0$, using the parameters given in Table 3.1. The Bessel functions decay quickly as l increases in magnitude. It hence suffices to sum over only the first Floquet harmonics ($l = -1, +1$). This approximation nevertheless easily captures the relevant physics of the system. Several interesting features can be observed in the excess PASN. For $\mu_{2e/3} = 0$, corresponding to tunneling only of $e/3$ charges at the QPC, we find $\Delta\bar{S}$ displays dips at $\nu\zeta = \pm 2$. In the opposite regime with $\mu_{e/3} = 1$, where only $2e/3$ charges tunnel, the dips occur at $\nu\zeta = \pm 1$. Hence, tunneling of different charges is characterized by dips in the excess PASN at different values of $\nu\zeta$. The values $\zeta = \pm 1, \pm 2$ at which the dips occur correspond to the Josephson frequency $q_{\boldsymbol{g}_\alpha} V_1$ of the respective tunneling charges. Interestingly, in the intermediate regime where both charges tunnel simultaneously at the QPC, the noise dips at both $\zeta = \pm 1$ and $\zeta = \pm 2$. We show in Figure 3.3(a) the excess noise for $\mu_{2e/3} = 0.05$ that is, 5% of the quasiparticles tunneling at the QPC carry charge $2e/3$, while the remaining carry charge $e/3$. Even for a very small proportion of $2e/3$ charges tunneling, we find robust dips of the excess PASN at $\zeta = \pm 2$, indicating the presence of these charges.

Note that for the same proportion of $e/3$ and $2e/3$ charge tunneling at the QPC, standard DC shot noise calculations predict a charge of $\sim 0.36e$. The latter is indistinguishable from only $e/3$ charges tunneling at the QPC within experimental errors, as discussed in the beginning of this chapter.

In Figure 3.3(b) we plot the quantities discussed above for $\theta = 0.03$. This corresponds to a temperature $T \sim 30mK$ and a AC drive of frequency $\Omega \sim 20GHz$, corresponding to readily accessible set of conditions in contemporary experiments. Here, the curves at $\mu_{2e/3} = 1$ and $\mu_{2e/3} = 0$ still display features akin to the zero temperature scenario with dips at $\zeta = \pm 1$ and $\zeta = \pm 2$ respectively, although somewhat rounded by thermal effects. At $\mu_{2e/3} = 0.05$, the dips at $\zeta = \pm 1$ and $\zeta = \pm 2$ are still clearly visible. Strikingly, the dip at $\zeta = \pm 1$ (corresponding to charges $2e/3$) is the most pronounced; this is understood

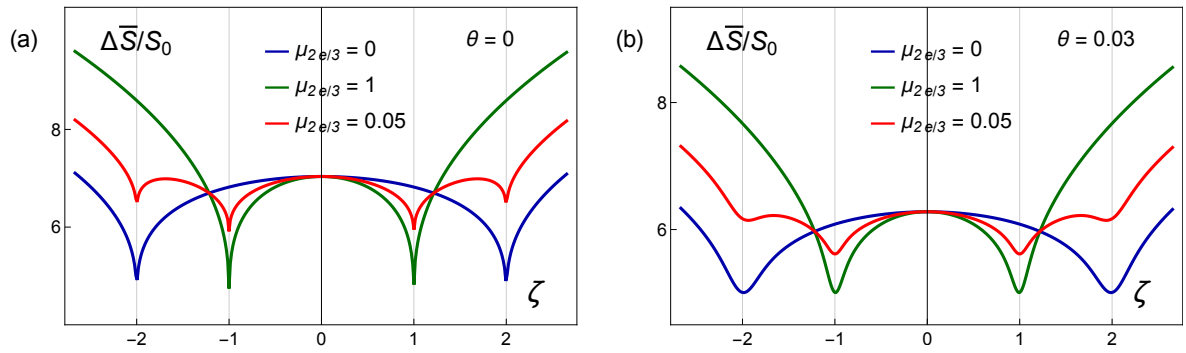


Figure 3.3.: $\Delta\bar{S}$ with only the first harmonics ($l = \pm 1$) as a function of ζ for different combinations of charges tunneling at the QPC. (a) $\theta = 0$, $\Delta\bar{S}$ displays dips at integer values of $\nu\zeta$, with the position of the dips depending on the tunneling charges. When $2e/3$ charges tunnel at the QPC, $\Delta\bar{S}$ displays dips at $\zeta = \pm 1$, while when only $e/3$ charges tunnel, the dips are present at $\zeta = \pm 2$. When there is a small amount of $2e/3$ (5%) tunneling along with mostly $e/3$ (95%), dips are seen at both $\nu\zeta = \pm 1$ and $\zeta = \pm 2$. (b) $\theta = 0.03$ constitutes an easily attainable condition in experiments. Here, the features discussed above are smoothed out by the temperature but persist. The excess PASN is normalized with respect to $S_0 = 4\left|\bar{\Gamma}\right|^2 \tau_0 (\Omega\tau_0)^{2\delta-1} \sum_{q=e/3,2e/3} \mu_q q^2 J_1^2(qV_2/\Omega)/\Gamma(2\delta)$. For both plots, we set $eV_2 = \Omega$.

by looking at Eq. (3.42), where the hyperbolic cosine and Gamma functions depending on ζ are dominant for the greater charge (when $\delta_{\boldsymbol{g}} > 1/2$).

In contrast, DC shot noise measurements for $\mu_{2e/3} = 0.05$ display the opposite behavior: Equation (3.11) predicts a slope of ~ 0.37. The latter is hardly distinguishable from a charge 1/3, and hence $\mu_{e/3} \sim 1$ within experimental errors. While the Fano factor shows only a small quantitative change when the tunneling charge proportion is varied, the PASN gives qualitatively different signals depending on the charges tunneling at the QPC (independent of the proportions), and thus provides an unambiguous detection of the different tunneling charges.

Non-universal scaling dimension

We now consider the validity of our predictions if the scaling dimension of the quasiparticles is changed. It has been shown that sample and geometry-dependent details can renormalize the scaling dimension to a larger value than the theoretical predictions. Moreover, shot noise experiments often fit well with the theory of non-interacting fermions, adapted to fractional charges. This corresponds to taking $\delta_{\boldsymbol{g}_\alpha} = 1$ in our model for all quasiparticles. It is hence important to test the validity of our predictions for scaling dimensions other than the theoretically predicted ones. In Figure 3.4, we plot the excess PASN for $\mu_{e/3} = 0.95$ for different scaling dimensions larger than 2/3. The features discussed so far persist even

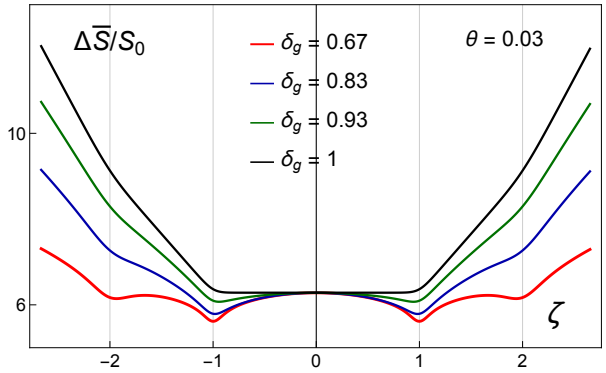


Figure 3.4.: Excess PASN, plotted as a function of ζ for $\mu_{2e/3} = 0.05$, and $\theta = 0.03$ for different scaling dimensions higher than the theoretically predicted one. The PASN shows features at both $\zeta = \pm 1$ and $\zeta = \pm 2$ for all scaling dimensions. The dips at integer values of ζ for $\delta_{\boldsymbol{g}} = 2/3$ dimension slowly morph into slope changes at the same values for $\delta_{\boldsymbol{g}} = 1$. The features at $\zeta = \pm 2$ for $\delta = 1$ are somewhat reduced, bearing similarity to the $\mu_{2e/3} = 1$ case. The excess PASN is normalized with respect to $S_0 = 4\left|\bar{\Gamma}\right|^2 \tau_0 (\Omega\tau_0)^{2\delta-1} \sum_{q=e/3,2e/3} \mu_q q^2 J_1^2(qV_2/\Omega)/\Gamma(2\delta)$. We set $eV_2 = \Omega$

when the scaling dimension gets larger. The dips in the PASN at $\zeta = \pm 1, \ \pm 2$ when $\delta_{\boldsymbol{g}} = 2/3$, slowly morph into slope changes at the same values when $\delta_{\boldsymbol{g}} = 1$. Nevertheless, the PASN is sensitive to both $e/3$ and $2e/3$ charges tunneling at the QPC.QPC.

3.5. Discussion and conclusion

This chapter developed a formalism to study photoassisted shot noise (PASN) in general Abelian quantum Hall edges. The presentation of the PASN in this chapter closely follows the experimental protocol of Ref. [66]. In that experiment, a combination of an AC voltage drive and a DC voltage is applied to the QPC. The resulting shot noise is measured as a function of the DC voltage while holding the AC drive constant. Translating this into our theoretical formalism, we hold the parameters V_2 and Ω constant, while varying V_1. Consequently, we plot the PASN as a function of $\zeta = \nu e V_1/\Omega$, with the understanding that Ω remains fixed while V_1 changes.

Our decision to explore the PASN in this way is motivated by the primary objective of measuring fractional charges. However, the theoretical framework we have developed is versatile and can easily accommodate other scenarios. An interesting direction is the study of minimal excitations, also known as Levitons [98, 99]. Minimal excitations in a general Abelian fractional quantum Hall effect (FQHE) system can be described by eliminating the background DC voltage—resulting in the periodic drive $V(t)$ amplitude dropping to zero at the end of each period. Under this condition, the Floquet coefficients in Equation (3.22) depend on ζ and evolve as we plot the PASN as a function of ζ. It is

worth noting that this approach could also be leveraged to investigate fractional charges by identifying dips in PASN at integer values of ζ [99, 100]. However, this method may be experimentally more challenging – it is far easier to deal with sinusoidal voltage drives as opposed to Lorentzian drives, required to address Levitons.

We chose to focus on the $\nu = 2/3$ FQHE for the sake of clarity. This system is experimentally accessible and allows for a clean separation of the physics of different fractional charges without the added complexity of varying scaling dimensions for different charges. This choice enabled us to illustrate the key physical concepts without unnecessary complications. However, our theoretical framework is broadly applicable to all Abelian fractional quantum Hall states. For states where different charges have different scaling dimensions (such as $\nu = 2/5$), additional considerations are needed—for instance, determining the energy regimes where multiple charges can tunnel simultaneously and the corresponding tunneling amplitudes. Furthermore, extending this formalism to non-Abelian states is straightforward. In a single QPC setup, complications due to fusion multiplicity of non-Abelian anyons are avoided, simplifying the analysis.

In conclusion, we find that PASN is an effective probe of fractional charges tunneling at a QPC in the FQHE. Its sensitivity to different charges tunneling simultaneously at the QPC does not have a parallel in DC noise, which as we have shown, is sensitive to a complicated average of the charges tunneling at the QPC. Using experimentally realistic values of temperature and AC drive frequency, we demonstrate that PASN measurements can provide a comprehensive understanding of the charges tunneling at the QPC. Our conclusions persist even when the scaling dimension is different from the theoretically predicted values. Studying PASN can hence be crucial in experimentally relevant situations of non-Laughlin states where different charges are predicted to tunnel simultaneously at the QPC.

Chapter 4.

Quasiparticle Andreev Reflection

Fractional charges are an intrinsic feature of anyons in the fractional quantum Hall effect (FQHE). In this chapter, we explore the scattering properties of anyons, when they are incident on barriers that do not admit anyons.

Intuition from elastic transport properties of electrons dictates that particles confronted with an opaque barrier are reflected back. This intuition does not extend to anyons. Indeed, anyons can undergo a more exotic process, where they borrow more anyons from the FQHE to form an electron that is transmitted across the barrier (which is opaque only to anyons, but not to electrons). This process is reminiscent of Andreev reflections occuring in normal-metal superconductor junctions.

Experimentally, the above possibility is realized in a two quantum point contact geometry. The first QPC is tuned in the weak-backscattering regime emitting a stream of anyons on the opposite edges. The latter anyons travel along the edge and are incident on a QPC in the strong-backscattering regime. The latter is opaque to anyons but admits electrons. The charge mismatch between the entities tunneling at the two QPCs gives rise to an Andreev-reflection-like phenomenon in the FQHE. The incoming Laughlin quasiparticle triggers the transmission on an electron on the second QPC, and by charge conservation, Laughlin quasiholes are reflected.

The signatures of the Andreev-like reflection processes lie in the current cross- and auto-correlations, which were measured experimentally recently. We provide here a complete calculation of the current correlations, in perfect agreement with recent experiments. Moreover, we shed light on the temperature dependence of this Andreev reflection-like process, providing a possible explanation to earlier paradoxical experiments.

4.1. Preliminaries

Andreev reflection is a phenomenon typically characteristic of superconductors. In a normal metal-superconductor junction biased in the subgap regime, a single electron hitting the junction from the normal metal side cannot be transmitted into the superconductor

due to the superconducting gap [101]. However, a Cooper pair can be transmitted into the superconductor, provided a hole is reflected back into the normal metal. This fundamental process of superconductors called Andreev reflection, has had wide applications in electronic quantum transport [102–108].

Strikingly, a phenomenon akin to Andreev reflection has been proposed in the FQHE, in particular in the Laughlin filling fractions $\nu = 1/m$, with m being an odd integer [109]. The latter system admits a single chiral bosonic field on its edge, hosting fractionally charged anyons with charge $e^* = e/m$. When anyonic quasiparticles are incident on barriers or quantum point contacts, they could display drastically different behavior compared to non-interacting electrons. Electrons incident on quantum point contacts are typically expected to be elastically transmitted or reflected with some probabilities. Electrons thus display behavior analogous to photons incident on a beam splitter, a surprising feature of electrons on ballistic channels, that inspired the field of electron quantum optics [110, 111]. Anyons on FQHE edges however can display distinct behaviors. It has been proposed that the number and even the nature of anyons can change when they are incident on quantum point contacts. Indeed, the latter possibility can occur when the quantum point contact is tuned in a regime that favors the tunneling of quasiparticles different than the incident ones.

The above scenario is realized simply in Laughlin FQHE. The setup is shown schematically in Figure 4.1. We consider an upstream QPC tuned in the weak-backscattering regime and biased with a large voltage V. This leads to the emission of a dilute stream of anyonic quasiparticles with charge e^* on the opposite edge. A second downstream QPC is set in the strong-backscattering regime. Following the discussion in Section 2.3.2, we know that the latter regime admits vacuum between the two edges, hence allowing only electrons to tunnel across the edges. The arrival of an anyon of charge $e^* = e/m$ on the second QPC hence triggers the emission of an electron across the QPC. Charge conservation implies that this process must be accompanied by the correlated reflection of $(m-1)$ quasiholes of charge $-e^*$. The latter process is very similar to the Andreev reflection process in superconductors, lending the name quasiparticle Andreev reflection to the present phenomenon. Note that in stark contrast with electrons, both the number, and the nature of quasiparticles change when anyon is incident on the QPC.

Such a system was first studied experimentally by Ref. [112], who found the charge transmitted across the second QPC to vary as a function of the dilution of the incoming quasiparticle current. Surprisingly, for a highly dilute beam, they found that fractional charges—contrary to electrons—could go across the second QPC, which only electrons are expected to traverse. Later experimental studies have attributed this unexpected result to finite-temperature effects, and possibly to the long propagation path of the quasiparticle beam [113, 114].

Quasiparticle Andreev reflection in the two QPC geometry in the $\nu = 1/3$ FQHE was recently demonstrated in Ref. [114], by measuring current cross- and auto-correlations. The experiment achieved this feat by working at very low temperatures and having a short

propagation length between the two QPCs. These features ensure that the quasiparticles traveling on the edge do not interact strongly with the surrounding environment, or with each other significantly, before hitting the second QPC. Their result of a negative cross-correlation noise was distinguished from anyonic braiding effects [33, 34] arising in similar geometries (see Chapter 7) by measuring cross-correlations as a function of the asymmetry of the input currents, which remained constant.

It should be emphasized that the Andreev-like reflection occurring here is not a consequence of inhomogenous junctions such as a normal metal-superconductor junction. The QPC is not interfaced with a superconductor or even a different filling fraction of the FQHE (see Refs. [115–119]) – the same state exists on either side of the QPC. The Andreev reflection process described here is strictly a consequence of a mismatch between the incident quasiparticles, and the type of quasiparticles that can be transmitted by the QPC.

In the present chapter, the goal is to bridge the gap between theory and experiment in the context of quasiparticle Andreev reflection in FQHE. To this end, we analytically calculate the current cross- and auto-correlations in the two QPC geometry of Figure 4.1. Analytical approaches which use perturbation theory in tunneling operators of the chiral Luttinger model typically represent a daunting task when dealing with more than one QPC. Previous studies dealing with more than one QPC, such as Fabry-Pérot setups [28], either resort to second-order perturbation theory (which is irrelevant for the present problem) or have to use different techniques, such as non-equilibrium bosonization for the anyonic statistics detection scenarios [33, 120]. Here, we present a fully analytical fourth-order perturbative calculation, leading to explicit expressions for the current-current correlations at the outputs.

4.2. System description

The two QPC setup considered in this chapter is shown schematically in Figure 4.1. A Hall bar is placed in the FQHE with a filling factor in the Laughlin series $\nu = 1/m$ (the most practical case being $\nu = 1/3$). The device is endowed with two distinct QPCs which can be individually controlled by voltages applied on corresponding split gates. The first QPC (denoted QPC_L is tuned in the weak backscattering regime, tunneling $e/m \equiv e^*$ quasiparticles, while the second downstream QPC (QPC_R) is operated in the strong-backscattering, tunneling electrons between the edges.

The application of a positive voltage V on the lower arm of QPC_L leads to the emission of a dilute stream of e^* quasiparticles on the edge a. It hence functions as a source of e^* quasiparticles which impinge on the QPC_R, which is tuned to be in the strong-backscattering regime and hence transmits only electrons. The mismatch between the charge e^* of the incoming excitations, and the charge e which can tunnel at QPC_R leads to quasiparticle Andreev reflection. When the arrival of the e^* quasiparticle triggers

an electron tunneling, charge conservation implies that two quasiholes (of charge $-e^*$ each) are reflected at QPC_R (see Figure 4.1). Therefore, the transmitted current I_b measured on contact b, and the reflected current I_a, measured on contact a, contain precious information about the quasiparticle Andreev reflection processes. Of primary interest are the cross-correlations between currents on contacts a and b, $\langle I_a I_b \rangle$, the auto-correlations of the current at contact 3, $\langle I_b I_b \rangle$, and the average output current on contact 3, $\langle I_b \rangle$. In the large voltage/zero temperature regime, these are expected to bear the following relations:

$$\langle I_b I_b \rangle = 2e \left| \langle I_b \rangle \right|, \tag{4.1}$$

$$\langle I_a I_b \rangle = -\frac{4}{3} e \left| \langle I_b \rangle \right|. \tag{4.2}$$

The first of these relations simply expresses that only electron tunneling contributes to $\langle I_b \rangle$. The second relation expresses that for each electron tunneling contributing to $\langle I_b \rangle$, there is necessarily a charge $-2e/3$ which is reflected and which contributes to $\langle I_a \rangle$, leading to a Fano factor of $(-2/3) \times 1$ for the cross-correlation.

It is important to stress the difference between this setup, and a similar setup where both QPCs are placed in the weak backscattering regime, for example in the *anyon collider*[33, 34] introduced towards the end of Chapter 2, and considered in detail in Chapters 7 and 8. When QPC_R is also in the weak-backscattering regime, and thus transmits e^* quasiparticles, it was shown that anyonic statistics plays an essential role in the tunneling current. The dominant contribution comes from interference between the process where the incoming e^* reaches the QPC before a quasiparticle-quasihole pair is excited, and the process where the order of these events is reversed. This process is dubbed *time-domain braiding*, and is explained in detail in Chapter 6. Because of the non-trivial anyonic statistics between two e^* quasiparticles, these interference effects provide the dominant contribution, depending non-perturbatively on the statistical properties of the incoming stream of e^* quasiparticles [86, 121, 122].

In the setup we are considering, since it is electrons that tunnel at QPC_R, the exchange phase between the incoming e^* quasiparticle and an electron (or a hole) is trivially a multiple of π, and there is no contribution related to anyonic statistics. The physics of Andreev reflection is thus different from that of anyonic braiding. This statement is true at the lowest order in perturbation theory of both QPC_L and QPC_R. If we consider higher order perturbation of QPC_L, indeed, the e^* anyons emitted by QPC_L still have a trivial exchange phase with the electrons transmitted through QPC_R. However, it was recently shown that these higher order terms of QPC_L could lead to anyonic exchange of the incoming anyon and the anyons reflected from the second QPC, as opposed to interference between incoming and tunneling anyons [123, 124].

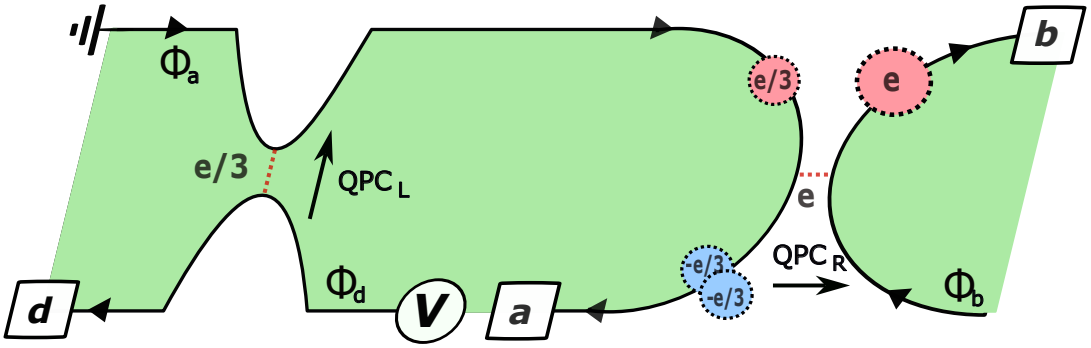


Figure 4.1.: Fractional quantum Hall bar comprising three distinct edges and two quantum point contacts (QPC). The first QPC, tuned in the weak-backscattering regime, is biased with a voltage $V > 0$ on the edge d. This leads to tunneling of e/m quasiparticles on the edge a. These travel along edge a and hit the second upstream QPC, which is tuned in the strong-backscattering regime. The impinging of e/m quasiparticles hence triggers the emission of electrons on the edge b. By charge conservation, charge $e(1-1/m)$ is reflected on edge a. This non-trivial Andreev reflection-like process is depicted in the figure for $m = 3$.

4.3. Theoretical model

In what follows, we focus on providing a complete analytic description of the Andreev reflection physics in the two QPC system of Laughlin FQHE, working at lowest order perturbation theory of both QPCs.

We consider a FQHE bar in the Laughlin filling fraction. There exist three independent bosonic fields on the edges denoted ϕ^d, ϕ^a, ϕ^b that form two quantum point contacts (QPC), denoted QPC_L and QPC_R, as shown in Figure 4.1. The free Hamiltonian of this system is given by

$$H_0 = \frac{v_F}{4\pi} \sum_{k=d,a,b} \int dx \left[\partial_x \phi^k(x)\right]^2, \tag{4.3}$$

where v_F is the propagation velocity of the edges. Each edge carries a coordinate system x. QPC_L operates in the weak-backscattering regime, allowing $e^* = e/m$ quasiparticles to tunnel across it. We apply a constant voltage V on the edge d, causing e^* quasiparticles to tunnel across QPC_L, from edge x to edge a. This process is modeled by the tunneling Hamiltonian

$$H_L(t) = \frac{\Gamma_L}{(2\pi v_F \tau_0)^\nu} \sum_{\epsilon=\pm} O_L^\epsilon(t) e^{-i\epsilon e^* V t}, \tag{4.4}$$

where

$$O_L^{\pm}(t) = e^{\pm i\sqrt{\nu}\left[\phi^d(0,t)-\phi^a(0,t)\right]}, \tag{4.5}$$

Γ_L is the tunneling amplitude of QPC_L, and τ_0 is an ultra-violet cutoff. The e^* quasiparticles then travel along edge a and are incident on QPC_R. We assume $e^*V \gg k_BT$, allowing us to work in the zero-temperature limit (the finite temperature generalization is given in Sec. 4.5). QPC_R operates in the strong backscattering regime, allowing only electrons to tunnel between the two FQHE fluids. The tunneling of electrons across QPC_R is given by

$$H_R(t) = \frac{\Gamma_R}{(2\pi v_F\tau_0)^{1/\nu}} \sum_{\epsilon=\pm} O_R^{\epsilon}(t), \tag{4.6}$$

where

$$O_R^{\pm}(t) = e^{\pm\frac{i}{\sqrt{\nu}}\left[\phi^a(L,t)-\phi^b(L,t)\right]}. \tag{4.7}$$

The tunneling current operator across QPC_R is readily obtained from the tunneling Hamiltonian and reads

$$I_R(t) = ie\frac{\Gamma_R}{(2\pi v_F\tau_0)^{1/\nu}} \sum_{\epsilon=\pm} \epsilon\, O_R^{\epsilon}(t), \tag{4.8}$$

and Γ_R is the tunneling amplitude of QPC_R. The full Hamiltonian of the system is then given by

$$H(t) = H_0 + H_T(t), \tag{4.9}$$

where $H_T(t) = H_L(t) + H_R(t)$. Finally, the current operators on the edges are given by

$$I_j(x,t) = \frac{\sqrt{\nu}ev_F}{2\pi}\partial_x\phi_j(x,t) \equiv \frac{ev_F}{2\pi i}\partial_x\partial_\gamma e^{i\gamma\sqrt{\nu}\phi_j(x,t)}\Big|_{\gamma=0}, \tag{4.10}$$

where we introduced a dummy variable γ , allowing us to express the current as exponentials of the bosonic fields. This trick allows a relatively simpler evaluation of the correlation functions.

4.4. Physical measurables

Ref.[114] provided the first experimental demonstration of Andreev reflection-like physics in the FQHE. They experimentally study the setup shown in Figure 4.1, and measure the cross-correlations of current at contacts a and b, the auto-correlation of current at contact b, and the tunneling current at contact b. In this section, we compute all three of these quantities at zero-temperature.

4.4.1. Cross-correlations

To capture the physics of quasiparticle Andreev reflection, we start by computing the cross-correlation noise of currents on edges a and b. This can be expressed using the Keldysh formalism as

$$S_{ab} = 2\int dt \left\langle T_K \left\{ \delta I_a(x,t^-)\delta I_b(y,0^+) e^{-i\int_K dt H_T(t)} \right\} \right\rangle_C , \tag{4.11}$$

where $\delta I_j = I_j - \langle I_j \rangle$ and we only keep the connected contributions (denoted by the subscript C). Here T_K denotes Keldysh time-ordering. We perform an expansion in the tunneling Hamiltonian up to the lowest non-trivial order $\Gamma_L^2\Gamma_R^2$ yielding

$$S_{ab} = \frac{2\Gamma_L^2\Gamma_R^2}{(2\pi v_F\tau_0)^{2\nu+\frac{2}{\nu}}} \int dt dt_1 \dots dt_4 \sum_{\{\eta_k\}} \eta_1 \dots \eta_4 \; e^{ie^*V(t_3-t_4)} \tag{4.12}$$

$$\begin{aligned} &\Big\langle T_K \Big\{ \frac{e^2 v_F^2}{(2\pi i)^2} \partial_x\partial_{\gamma_1} e^{i\gamma_1\sqrt{\nu}\phi^a(x,t^-)} \partial_y\partial_{\gamma_2} e^{i\gamma_2\sqrt{\nu}\phi^b(y,0^+)} \\ &e^{\frac{i}{\sqrt{\nu}}\left[\phi^a(L,t_1^{\eta_1})-\phi^b(L,t_1^{\eta_1})\right]} e^{-\frac{i}{\sqrt{\nu}}\left[\phi^a(L,t_2^{\eta_2})-\phi^b(L,t_2^{\eta_2})\right]} \\ &e^{-i\sqrt{\nu}\left[\phi^d(0,t_3^{\eta_3})-\phi^a(0,t_3^{\eta_3})\right]} e^{i\sqrt{\nu}\left[\phi^d(0,t_4^{\eta_4})-\phi^a(0,t_4^{\eta_4})\right]} \Big\} \Big\rangle_C \Big|_{\gamma_1,\gamma_2=0}, \end{aligned} \tag{4.13}$$

where $\eta_k = \pm$ indicates the Keldysh contour label, for the k-th time variable. Correlation functions of multiple tunneling operators can be evaluated using the following identity

$$\left\langle T_K \left\{ \prod_{j=1}^{N} e^{i\alpha_j\phi_\mu\left(x_j,t_j^{\eta_j}\right)} \right\} \right\rangle = \exp\left[\sum_{j=1}^{N}\sum_{k=j+1}^{N} \alpha_j\alpha_k \; \mathcal{G}^{\eta_j\eta_k}(x_j-x_k,t_j-t_k) \right], \tag{4.14}$$

where $\mathcal{G}^{\eta_j\eta_k}(x,t)$ is the Keldysh bosonic Greens function given at zero temperature by

$$\mathcal{G}^{\eta_1\eta_2}(x,t) = \log\left(\frac{\tau_0}{\tau_0 + i(t-x/v_F)\sigma_{\eta_1\eta_2}(t)} \right), \tag{4.15}$$

where

$$\sigma_{\eta_1\eta_2}(t) = \frac{1}{2}\left[(\eta_2-\eta_1) + \mathrm{sgn}(t)(\eta_1+\eta_2) \right]. \tag{4.16}$$

Equation (4.14) is non-zero only when $\sum_j \alpha_j = 0$. The latter equation allows us to express S_{ab} as

$$\begin{aligned} S_{ab} = \frac{2e^2 v_F^2}{(2\pi i)^2} \frac{\Gamma_L^2 \Gamma_R^2}{(2\pi v_F \tau_0)^{2\nu+2/\nu}} \int dt dt_1 \dots dt_4 \sum_{\{\eta_k\}} \eta_1 \dots \eta_4 \; e^{ie^* V t_{34}} e^{2\nu \mathcal{G}^{\eta_3\eta_4}(0,t_{34})} e^{\frac{2}{\nu}\mathcal{G}^{\eta_1\eta_2}(0,t_{12})} \\ \times \partial_x \partial_{\gamma_1} \left[e^{-\gamma_1 \mathcal{G}^{-\eta_1}(x-L,t-t_1)} e^{\gamma_1 \mathcal{G}^{-\eta_2}(x-L,t-t_2)} e^{-\gamma_1 \nu \mathcal{G}^{-\eta_3}(x,t-t_3)} e^{\gamma_1 \nu \mathcal{G}^{-\eta_4}(x,t-t_4)} \right]_{\gamma_1=0} \\ \times \partial_y \partial_{\gamma_2} \left[e^{\gamma_2 \mathcal{G}^{+\eta_1}(y-L,-t_1)} e^{-\gamma_2 \mathcal{G}^{+\eta_2}(y-L,-t_2)} \right]_{\gamma_2=0} \\ \left[e^{-\mathcal{G}^{\eta_1\eta_3}(L,t_{13})} e^{\mathcal{G}^{\eta_1\eta_4}(L,t_{14})} e^{\mathcal{G}^{\eta_2\eta_3}(L,t_{23})} e^{-\mathcal{G}^{\eta_2\eta_4}(L,t_{24})} - 1 \right]. \end{aligned} \tag{4.17}$$

The final term in the last line of Equation (4.17) is conveniently rewritten as $K_{1234} - 1$. The -1 contribution removes all the disconnected diagrams up to order $\Gamma_L^2 \Gamma_R^2$, while the term K_{1234} involves two-point correlators of bosonic fields, with each of the two bosonic fields coming from the tunneling operators at different QPCs. This term is given by:

$$K_{1234} = \frac{\exp\left[\mathcal{G}^{\eta_1\eta_4}(L,t_{14}) + \mathcal{G}^{\eta_2\eta_3}(L,t_{23})\right]}{\exp\left[\mathcal{G}^{\eta_1\eta_3}(L,t_{13}) + \mathcal{G}^{\eta_2\eta_4}(L,t_{24})\right]}, \tag{4.18}$$

where we have used the shorthand notation $t_{ij} = t_i - t_j$. Notice that the prefactor of each Green's function in the exponential is equal to 1. This happens since the coefficients $\sqrt{\nu}$ and $1/\sqrt{\nu}$ of the tunneling operators of the left and right QPC respectively (see Equations (4.5) and (4.7)), have a unit product. It is thus a consequence of the trivial exchange phase between the excitations of the two QPC, which allows a simpler analytic treatment.

In the following, we consider the limit of a large separation L between the two QPCs, effectively taking $L \to \infty$. Hence, the tunneling times $t_{1/2}$ at the right QPC are always much greater than the tunneling times $t_{3/4}$ at the left QPC. This allows us to simplify Equation (4.16) and directly write $\sigma_{13}(t_{13}) = \sigma_{23}(t_{23}) = \eta_3$ and $\sigma_{14}(t_{14}) = \sigma_{24}(t_{24}) = \eta_4$. This in turn enables to greatly simplify Equation (4.18) which becomes at zero temperature:

$$K_{1234} = \frac{\left[t_1 - t_3 - \frac{L}{v_F} - i\eta_3\tau_0\right]\left[t_2 - t_4 - \frac{L}{v_F} - i\eta_4\tau_0\right]}{\left[t_1 - t_4 - \frac{L}{v_F} - i\eta_4\tau_0\right]\left[t_2 - t_3 - \frac{L}{v_F} - i\eta_3\tau_0\right]}. \tag{4.19}$$

Moreover, from Equation (4.15), one readily sees that the derivative of the Green's function at zero temperature can be expressed as a delta function in the limit of vanishingly small cutoff

$$\begin{aligned} &\partial_x \mathcal{G}^{\eta_1\eta_2}(x-y, t_1-t_2) \\ &= \begin{cases} +\frac{i\pi}{v_F}\eta_2 \delta\left(t_1 - t_2 - \frac{x-y}{v_F}\right), & x-y > 0 \\ -\frac{i\pi}{v_F}\eta_1 \delta\left(t_1 - t_2 - \frac{x-y}{v_F}\right), & x-y < 0 \end{cases} \end{aligned} \tag{4.20}$$

We ignore in above equation the principal part, which vanishes under the integral. Equations (4.19) and (4.20) allow to greatly simplify the analytic evaluation of the integrals. We first effect the coordinate transformation $t_{1/2} \to t_{1/2} + L/v_F$, further simplifying the expression of Equation (4.19). Then, we employ the delta functions from Equation (4.20) to easily get rid of the integrals over t and t_1 in Equation (4.17). We hence obtain the following expression for S_{ab} containing three more integrals to be evaluated.

$$\begin{aligned} S_{ab} = &\frac{e^2\Gamma_L^2\Gamma_R^2}{2(2\pi v_F\tau_0)^{2\nu+\frac{2}{\nu}}}\int dt_2 dt_3 dt_4 \sum_{\{\eta_k\}} \eta_1\ldots\eta_4 e^{ie^*Vt_{34}} \\ &\times\left[(\eta_2-\eta_1)+\nu(\eta_4-\eta_3)\right] e^{2\nu\mathcal{G}^{\eta_3\eta_4}(0,t_{34})} e^{\frac{2}{\nu}\mathcal{G}^{\eta_1\eta_2}(0,-t_2)} \\ &\times(\eta_1-\eta_2)\left\{\frac{[-t_3-i\eta_3\tau_0]\,[t_2-t_4-i\eta_4\tau_0]}{[-t_4-i\eta_4\tau_0]\,[t_2-t_3-i\eta_3\tau_0]}-1\right\}. \end{aligned} \tag{4.21}$$

Further manipulations and the coordinate transformation $t_3 - t_4 = \tau$, $(t_3+t_4)/2 = \tilde{t}$ allow us to express the cross-correlation as

$$\begin{aligned} S_{ab} = &\frac{e^2\Gamma_L^2\Gamma_R^2}{(2\pi v_F\tau_0)^{2\nu+\frac{2}{\nu}}}\int dt_2 d\tau e^{ie^*V\tau}\sum_{\{\eta_k\}} e^{\frac{2}{\nu}\mathcal{G}^{\eta_1\eta_2}(0,-t_2)} \\ &\times\left[\eta_3\eta_4(1-\eta_1\eta_2)+\nu\frac{\eta_1-\eta_2}{2}(\eta_4-\eta_3)\right] e^{2\nu\mathcal{G}^{\eta_3\eta_4}(0,\tau)} \\ &\times\int d\tilde{t}\frac{-t_2\,[\tau+i(\eta_3-\eta_4)\tau_0]}{\left[-\tilde{t}+\frac{\tau}{2}-i\eta_4\tau_0\right]\left[t_2-\tilde{t}-\frac{\tau}{2}-i\eta_3\tau_0\right]}. \end{aligned} \tag{4.22}$$

The $\tilde{t}$-integral has been evaluated in Appendix E.1 using Cauchy's residue theorem. Using this result and subsequently summing over the Keldysh indices η_2 and η_4, this leads to

$$\begin{aligned} S_{ab} = &\frac{4i\pi e^2\Gamma_L^2\Gamma_R^2}{(2\pi v_F\tau_0)^{2\nu+\frac{2}{\nu}}}\int dt_2 d\tau e^{ie^*V\tau}\sum_{\eta_3} e^{2\nu\mathcal{G}^{\eta_3,-\eta_3}(0,\tau)} \\ &\times\sum_{\eta_1}(\eta_3+\nu\eta_1)\left(\frac{\tau_0}{\tau_0+i\eta_1 t_2}\right)^{2/\nu}\frac{t_2\,(\tau+2i\eta_3\tau_0)}{-t_2+\tau+2i\eta_3\tau_0}. \end{aligned} \tag{4.23}$$

The t_2-integrals have also been evaluated in Appendix E.1. Subsequent trivial manipulations give us, to leading order in the cutoff,

$$\begin{aligned} S_{ab} = &-\frac{4e^2\Gamma_L^2\Gamma_R^2}{v_F^2(2\pi v_F\tau_0)^{2\nu+\frac{2}{\nu}-2}}(1-\nu) \\ &\times\int d\tau\cos(e^*V\tau)\left(\frac{\tau_0}{\tau_0-i\tau}\right)^{2\nu+2/\nu-2}. \end{aligned} \tag{4.24}$$

Finally, the $\tau-$integral can be evaluated using known results [125] to give

$$S_{ab} = -(1-\nu)\frac{2e^2\Gamma_L^2\Gamma_R^2}{v_F^3\Gamma\left(2\nu+\frac{2}{\nu}-2\right)}\left|\frac{e^*V}{2\pi v_F}\right|^{2\nu+\frac{2}{\nu}-3}, \tag{4.25}$$

where the function $\Gamma(x)$ in the denominator denotes the Euler-Gamma function.

4.4.2. Auto-correlations

Now we go on to compute the auto-correlation noise on edge b, which is expressed using the Keldysh formalism as

$$S_{bb} = 2\int dt \left\langle T_K\left\{\delta I_b(x,t^-)\delta I_b(y,0^+)e^{-i\int_K dt H_T(t)}\right\}\right\rangle_C. \tag{4.26}$$

Performing again an expansion in the tunneling Hamiltonian up to order $\Gamma_L^2\Gamma_R^2$ yields

$$\begin{aligned}
S_{bb} = &\frac{2e^2v_F^2\Gamma_L^2\Gamma_R^2}{(2\pi v_F\tau_0)^{2\nu+\frac{2}{\nu}}}\int dtdt_1\dots dt_4\sum_{\{\eta_k\}}\eta_1\dots\eta_4\; e^{ie^*Vt_{34}}\\
&\left\langle T_K\Big\{\frac{1}{(2\pi i)^2}\partial_x\partial_{\gamma_1}e^{i\gamma_1\sqrt{\nu}\phi^b(x,t^-)}\partial_y\partial_{\gamma_2}e^{i\gamma_2\sqrt{\nu}\phi^b(y,0^+)}\right.\\
&e^{-i\sqrt{\nu}\left[\phi^d(0,t_3^{\eta_3})-\phi^a(0,t_3^{\eta_3})\right]}e^{-\frac{i}{\sqrt{\nu}}\left[\phi^a(L,t_2^{\eta_2})-\phi^b(L,t_2^{\eta_2})\right]}\\
&\left.e^{\frac{i}{\sqrt{\nu}}\left[\phi^a(L,t_1^{\eta_1})-\phi^b(L,t_1^{\eta_1})\right]}e^{i\sqrt{\nu}\left[\phi^d(0,t_4^{\eta_4})-\phi^a(0,t_4^{\eta_4})\right]}\Big\}\right\rangle_C\Big|_{\gamma_1,\gamma_2=0},
\end{aligned} \tag{4.27}$$

where we are only interested in the zero-temperature regime at this stage, thus allowing us to discard lower order terms corresponding to purely thermal contributions to the noise.

Proceeding along the same lines as the derivation of the cross-correlations, and employing Equations (4.14) and (4.20) one obtains:

$$\begin{aligned}
S_{bb} = &\frac{e^2\Gamma_L^2\Gamma_R^2}{2(2\pi v_F\tau_0)^{2\nu+\frac{2}{\nu}}}\int dt_2dt_3dt_4\sum_{\{\eta_k\}}\eta_1\dots\eta_4\,(\eta_1-\eta_2)^2\\
&\times e^{ie^*Vt_{34}}e^{2\nu\mathcal{G}^{\eta_3\eta_4}(0,t_{34})}e^{\frac{2}{\nu}\mathcal{G}^{\eta_1\eta_2}(0,-t_2)}\\
&\times\left\{\frac{[-t_3-i\eta_3\tau_0]\,[t_2-t_4-i\eta_4\tau_0]}{[-t_4-i\eta_4\tau_0]\,[t_2-t_3-i\eta_3\tau_0]}-1\right\}.
\end{aligned} \tag{4.28}$$

Comparing Equation (4.28) with Equation (4.21), one finds that the expression for the auto-correlations is the same as the first piece of the cross-correlations, up to a minus sign. Hence, the calculations of the cross-correlations follow through for auto-correlations as

well, giving us finally

$$S_{bb} = \frac{2e^2\Gamma_L^2\Gamma_R^2}{v_F^3\Gamma\left(2\nu+\frac{2}{\nu}-2\right)}\left|\frac{e^*V}{2\pi v_F}\right|^{2\nu+\frac{2}{\nu}-3}. \tag{4.29}$$

4.4.3. Tunneling current

Now we calculate the average tunneling current across QPC_R which is expressed in the Keldysh formalism as

$$\langle I_b(x,t)\rangle = \left\langle T_K\left\{\frac{1}{2}\sum_{\eta_1} I_R(t_1^{\eta_1})\; e^{-i\int_K dt H_T(t)}\right\}\right\rangle \tag{4.30}$$

where $t_1 = t - \frac{x-L}{v_F}$ and the tunneling current operator I_R was defined in Equation (4.8). Expanding in the tunneling Hamiltonian up to third order and retaining only the relevant, non-zero, order $\Gamma_L^2\Gamma_R^2$ terms, one is left with

$$\begin{aligned}\langle I_b(x,t)\rangle = &-\frac{e\Gamma_L^2\Gamma_R^2}{4(2\pi v_F\tau_0)^{2\nu+\frac{2}{\nu}-2}}\int dt_2dt_3dt_4\\ &\times\sum_{\{\eta_k,\epsilon_k\}}\epsilon_1\eta_2\eta_3\eta_4 e^{-ie^*V(\epsilon_3t_3+\epsilon_4t_4)}\\ &\times\langle T_K\left\{O_R^{\epsilon_1}(t_1^{\eta_1})O_R^{\epsilon_2}(t_2^{\eta_2})O_L^{\epsilon_3}(t_3^{\eta_3})O_L^{\epsilon_4}(t_4^{\eta_4})\right\}\rangle_C\,.\end{aligned} \tag{4.31}$$

The ϵ_k indices are then summed over, and the resulting Keldysh correlators are subsequently evaluated using Equation (4.14) giving us

$$\begin{aligned}\langle I_b\rangle = &\, i\frac{e\Gamma_R^2\Gamma_L^2}{(2\pi v_F\tau_0)^{2\nu+2/\nu}}\sum_{\{\eta_k\}}\eta_2\eta_3\eta_4\int dt_2d\tau\sin(e^*V\tau)\\ &\times e^{2\nu\mathcal{G}^{\eta_3\eta_4}(\tau)}e^{\frac{2}{\nu}\mathcal{G}^{\eta_1\eta_2}(-t_2)}\\ &\times\int d\tilde{t}\frac{-t_2\left[\tau+i(\eta_3-\eta_4)\tau_0\right]}{\left[-\tilde{t}+\frac{\tau}{2}-i\eta_4\tau_0\right]\left[t_2-\tilde{t}-\frac{\tau}{2}-i\eta_3\tau_0\right]}.\end{aligned} \tag{4.32}$$

Noting that a proper rescaling of the integrated variables $t_2 \to t_2 + t_1$ and $\tilde{t} \to \tilde{t} + t_1$ allows us to get rid of the external variable t_1, we argue that the tunneling current is constant and does not depend on x, t.

Performing the summation over Keldysh indices η_1 and η_2, the integrals over $\tilde{t}$ and t_2 are then carried out similarly to the previous sections, relying on the results of Appendix

E.1 yielding

$$\langle I_b\rangle = -2i(2\pi)^2\frac{e\Gamma_R^2\Gamma_L^2}{(2\pi v_F\tau_0)^{2\nu+2/\nu}}\tau_0^2 \times\int d\tau\sin(e^*V\tau)\left(\frac{\tau_0}{\tau_0-i\tau}\right)^{2\nu+2/\nu-2}. \tag{4.33}$$

Performing the final $\tau-$integral [125], one is left with

$$\langle I_b\rangle = \frac{e\Gamma_R^2\Gamma_L^2}{v_F^3\Gamma\left(2\nu+\frac{2}{\nu}-2\right)}\left|\frac{e^*V}{2\pi v_F}\right|^{2\nu+2/\nu-3}\mathrm{Sgn}(V). \tag{4.34}$$

4.5. Finite temperature

All the calculations presented in the previous three sections are valid only at zero temperature. In this section, we generalize these results to finite temperatures. We start by noting that the expression of cross-correlations in Equation (4.17), along with the one for the tunneling current in Equation (4.31), both apply to a general temperature, provided that one uses the finite temperature Green's function. Similarly, the expression of Equation (4.27) for the auto-correlations is also valid at finite temperature but it now only describes the *excess* auto-correlations $S_{bb}^{\mathrm{exc}} = S_{bb}(V) - S_{bb}(V=0)$, as we are not interested in the purely thermal contribution.

Substituting then, instead of the zero-temperature Green's function, the finite temperature Keldysh bosonic Greens function

$$\mathcal{G}^{\eta_1\eta_2}(x,\tau) = \log\left(\frac{\sinh(i\pi T\tau_0)}{\sinh\left[\pi T\left(i\tau_0-\sigma_{\eta_1\eta_2}(\tau)(\tau-x/v_F)\right)\right]}\right), \tag{4.35}$$

gives us the corresponding generalization to a finite temperature T.

While the finite temperature extension does not present any formal difficulties, it is still a long and rather tedious calculation. For clarity, we present only the final results here, the main steps of the derivation being presented in Appendix E.2. The tunneling current at finite temperature T is given by

$$\langle I_b\rangle = \frac{e\Gamma_R^2\Gamma_L^2}{\pi v_F^3\Gamma\left(2\nu+\frac{2}{\nu}-2\right)}\left(\frac{T}{v_F}\right)^{2\nu+2/\nu-3}\sinh\left(\frac{e^*V}{2T}\right) \times\left|\Gamma\left(\nu+\frac{1}{\nu}-1+i\frac{e^*V}{2\pi T}\right)\right|^2. \tag{4.36}$$

For $\nu = 1/3$, we obtain for the excess auto-correlations

$$S_{bb}^{\text{exc}} = \frac{4e^2\Gamma_L^2\Gamma_R^2}{\pi^2 v_F^3}\left(\frac{T}{v_F}\right)^{11/3}\sinh\left(\frac{eV}{6T}\right)\frac{\left|\Gamma\left(\frac{7}{3}+i\frac{eV}{6\pi T}\right)\right|^2}{\Gamma\left(\frac{14}{3}\right)}\text{Im}\left[\psi\left(\frac{7}{3}+i\frac{eV}{6\pi T}\right)\right], \quad (4.37)$$

while the cross-correlation can also be calculated similarly yielding

$$\begin{aligned} S_{ab} = -\frac{2}{3}\frac{4e^2\Gamma_L^2\Gamma_R^2}{\pi^2 v_F^3}\left(\frac{T}{v_F}\right)^{11/3}\Bigg\{&\sinh\left(\frac{eV}{6T}\right)\frac{\left|\Gamma\left(\frac{7}{3}+i\frac{eV}{6\pi T}\right)\right|^2}{\Gamma\left(\frac{14}{3}\right)}\text{Im}\left[\psi\left(\frac{7}{3}+i\frac{eV}{6\pi T}\right)\right] \\ &- \frac{1}{8}\frac{\left|\Gamma\left(\frac{1}{3}+i\frac{eV}{6\pi T}\right)\right|^2}{\Gamma\left(\frac{5}{3}\right)}\frac{eV}{6\pi T}\sinh\left(\frac{eV}{6T}\right)\left[\frac{23}{120}+\frac{9}{160}\left(\frac{eV}{3\pi T}\right)^2\right]\Bigg\}, \end{aligned} \quad (4.38)$$

where ψ is the digamma function. One can readily check that in the limit $T \to 0$, these results reproduce the ones obtained in Equations (4.29), (4.25), (4.34).

4.6. Discussion of results

Consolidating the calculations of auto-correlations, cross-correlations, and the tunneling current at zero temperature, we can see that they satisfy the following relations for $\nu = 1/3$

$$\begin{aligned} S_{bb} &= 2e\left|\langle I_b\rangle\right|, \\ S_{ab} &= -\frac{4}{3}e\left|\langle I_b\rangle\right|, \end{aligned} \quad (4.39)$$

which matches the experimental results of Ref. [114]. Equation (4.39) has been plotted as the gray straight lines in Figure 4.2

The $-4/3$ coefficient of the cross-correlation noise generalizes to $-2(m-1)/m$ for an arbitrary Laughlin fraction $\nu = 1/m$. The ratio between the cross- and auto-correlations, equal to $-2/3$ (or more generally $(m-1)/m$) is thus a direct manifestation of the Andreev reflection process, where the transmission of a charge $e \times m/m$ (an electron) is always accompanied of the reflection of a negative charge $e \times (1-m)/m$ ($m-1$ holes of charge $-e/m$).

The analytical results at finite temperature allows us to see how the current and noise are modified when the ratio k_BT/eV is non-zero. This is first illustrated on Figure 4.2, which in addition to the zero-temperature results shows the auto-correlation and cross-correlation noises as a function of the tunneling current $\langle I_b\rangle$ for different values of the temperature T. One can see that the finite temperature leads to a rounding of the noise as function of the current and thus, a lower slope for the noise as a function of the current until $eV \gg k_BT$ where the zero-temperature slope is recovered.

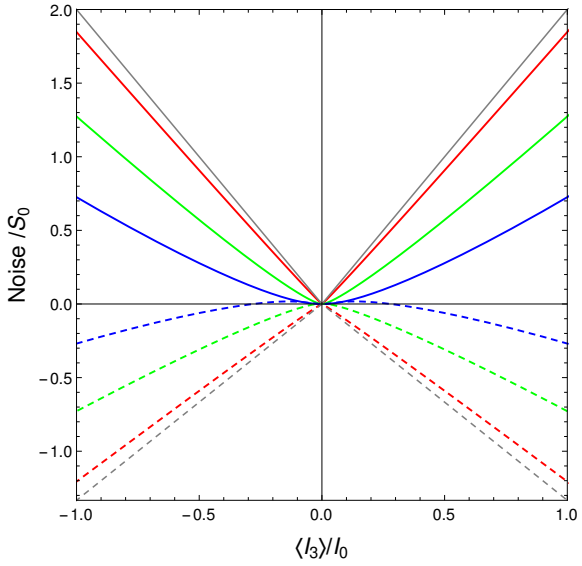


Figure 4.2.: Auto-correlation noise S_{bb}^{exc} (full lines) and cross-correlation noise S_{ab} (dashed lines) plotted as a function of the tunneling current $\langle I_b \rangle$, for different values of the temperature $k_B T = 0$ (gray), 0.1 (red), 0.5 (green), 1 (blue) (arbitrary energy units), with eV varying from -32 to $+32$ in the same units. The zero-temperature case (gray lines) correspond to Equations (4.25), (4.29) and (4.34)), while the finite temperature case correspond to Equations (4.36)-(4.38). The current is normalized by $I_0 = \frac{e\Gamma_R^2\Gamma_L^2}{\pi v_F^3}$, the noise by $S_0 = \frac{4e^2\Gamma_R^2\Gamma_L^2}{\pi^2 v_F^3}$.

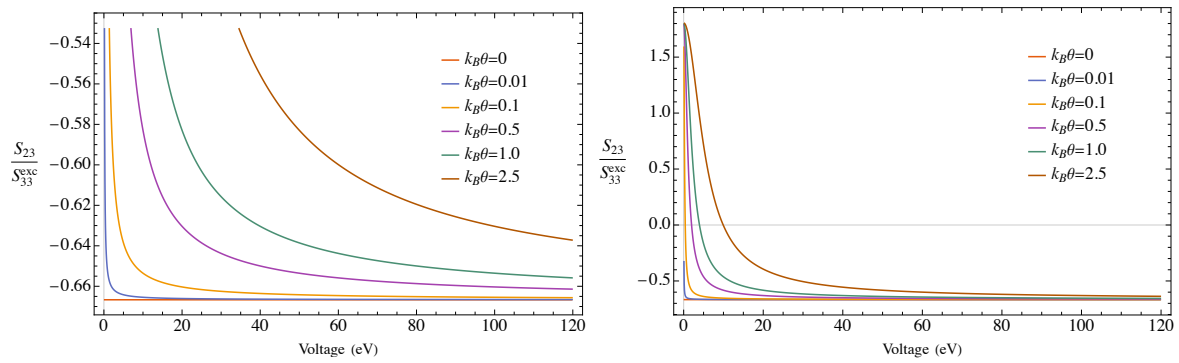


Figure 4.3.: Ratio of cross-correlations to auto-correlations as a function of the voltage eV (in arbitrary energy unit) for different values of k_BT (in the same unit). The ratio asymptotically reaches down to $-2/3$ for $eV \gg k_BT$, in agreement with the zero temperature result. For smaller values of eV/k_BT, the ratio increases and becomes positive for small values of eV/k_BT.

To examine in more detail the impact of temperature on the ratio $S_{ab}/S_{bb}^{\text{exc}}$, Figure 4.3 shows this ratio as a function of voltage at different temperatures. One can see that for large $eV \gg k_BT$, the noise ratio always converges towards the zero-temperature value $S_{ab}/S_{bb}^{\text{exc}} = -2/3$. As eV/k_BT decreases. the ratio increases, and changes sign close to $eV/k_BT = 4$. It reaches a value ~ 1.8 at $eV/k_BT = 0$.

4.7. Comparison with experiments

Figure 4.2 can be compared with the experimental results of Ref. [114] shown in Figure 4.4. The ratios of $eV/(k_BT)$ that we have used in Figure 4.2 (with $k_BT = 0$, 0.1, 0.5 or 1 and eV up to 32 in the same units) are of the same order as the experimental ones, with $T = 15$mK, 35mK and 60mK and V ranging from 0 to $\sim 50\mu V$. The finite-temperature rounding that we observe for the noise as a function of the current is similar to that observed in the experiment, albeit a bit more pronounced in our case.

The non-universality of scaling dimension is a recurrent theme in FQHE edge experiments – the experiment of Ref. [114] is no exception. Indeed, a higher scaling dimension of the anyons and electrons could explain the less pronounced finite-temperature rounding observed in the experiment in comparison to our theory. It is not very difficult to account for scaling dimensions different from the predicted ones within our calculations. In Equation 4.36 for example, in the numerical factor $\nu + 1/\nu - 1$, ν refers to the scaling dimension of anyons tunneling at QPC_L, while $1/\nu$ refers to the scaling dimension of electrons tunneling at QPC_R. For the tunneling current and autocorrelation noise, this factor can be straightforwardly replaced by $\delta_L + \delta_R - 1$, where $\delta_{L/R}$ refer to the modified scaling dimension of quasiparticles tunneling at $QPC_{L/R}$. This already allows easy com-

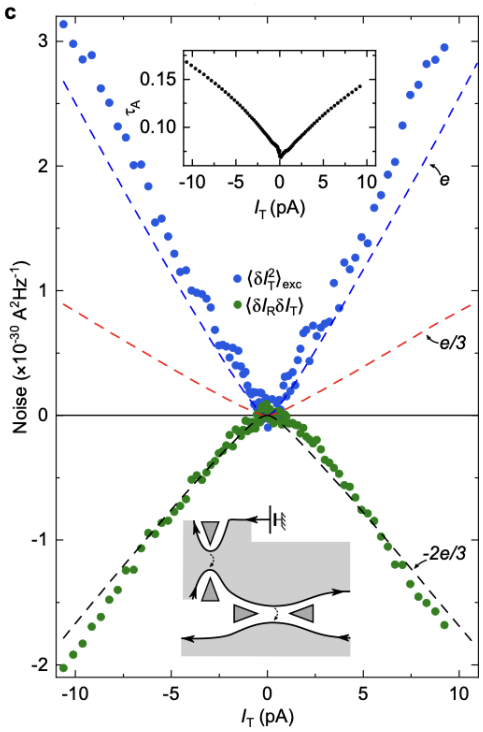


Figure 4.4.: Experimental data of auto- and cross-correlation noise as a function of tunneling current, taken from Ref. [114]. The points in blue, denoted $\langle \delta I_T^2 \rangle$ in the figure, are the auto-correlation noise denoted $\langle I_b I_b \rangle$ in this chapter. Similarly, the points in green, denoted $\langle \delta I_R \delta I_T \rangle$, are the cross-correlation noise, denoted $\langle I_a I_b \rangle$ in this chapter. I_T in the figure denotes the tunneling current through the second QPC, referred to as $\langle I_b \rangle$ in this chapter. The green and blue dashed lines in the figure correspond to our zero-temperature results for auto- and cross-correlation noises as a function of the tunneling current (see grey lines in Figure 4.2. The agreement between zero-temperature theory and experiment (performed at a finite-temperature of 35mK) declines for small $\langle I_b \rangle$, where we are no longer in the $eV \gg k_B T$ regime. Thus finite-temperature effects are important here, leading to a rounding of the noise v/s current curves. This rounding is captured by our finite-temperature results of Equations (4.25), (4.29) and (4.34), although theory predicts a more pronounced rounding compared to that seen in the experiment.

parison with experiments, employing a modified scaling dimension. The evaluation of cross-correlation however uses a finite order expansion of hypergeometric functions, which relies on $\delta_R = 1/\nu$ being an integer (see Equation (E.21) and the discussion at the end of Appendix E.1). However, this only impedes the analytic evaluation of the final integral, which can nevertheless be numerically evaluated relatively easily.

Our theory can also be compared with earlier experiments, which witnessed unexpected results. Ref. [112], which investigated a similar system as Figure 4.1, observed $e/3$ quasiparticles traversing the second QPC, in the strong backscattering regime, by measuring

the current auto-correlations. This is indeed a strange result since there exists vacuum between the two edges forming a QPC in the strong backscattering regime. Anyonic quasiparticles exist only within the FQHE fluid – they cannot traverse vacuum. Our finite temperature results provide a possible explanation for this unexpected behavior. For small eV/k_BT, the ratio $S_{ab}/S_{bb}^{\text{exc}}$ deviates strongly from the expected value, even becoming positive for $eV/k_BT < 4$. We emphasize that the ratio $S_{ab}/S_{bb}^{\text{exc}}$ is interpreted as the ratio of reflected and transmitted charges. It follows that at high temperatures/small voltage, it could look like a charge smaller than that of an electron is transmitted through the second QPC. But it is perfectly compatible with electrons transmitted through the second QPC, once finite temperature effects are taken into account.

4.8. Conclusion

Motivated by recent experiments which demonstrate Andreev-like reflection in the $\nu = 1/3$ FQHE, we have presented an analytical calculation of the output tunneling current, cross-correlation noise, and the auto-correlation noise in the two QPC geometry studied by Ref. [114], following their measurement protocol. We have performed an exact perturbative calculation at order four in the tunneling amplitudes of the two QPCs (two orders of each QPC), beyond the usual second-order calculations for the current and noise at a QPC.

It is clear that tunneling entities on the left and right QPCs, e/m anyons and electrons respectively, braid trivially. This is reflected in their exponents cancelling each other, allowing simpler analytic evaluation of the two-QPC current and noises at lowest order in tunneling amplitude of both QPCs. After the publication of the article related to this chapter [126], another work studying the same geometry appeared [123]. They consider higher-order perturbations (fourth-order and beyond) in the QPC_L. This leads to processes where an incoming $e/3$ quasiparticle could braid non-trivially, of course not with the electrons tunneling at QPC_R, but with an Andreev-reflected $-2e/3$ quasihole. We emphasize that these processes do not occur at the lowest non-trivial order of perturbation considered in this chapter.

We have obtained explicit analytical expressions for the current and noises, both at zero and finite temperature. Our results match that of the experiment of Ref. [114], in particular for the ratio of the cross- and auto-correlation noises, which is a direct manifestation of the Andreev reflection process. Our results also show how finite temperature will modify the noise ratio, which can even become positive for small values of V/T, allowing comparison with both recent and older experiments.

Chapter 5.

Finite-frequency ΔT noise

The scaling dimension of anyons on FQHE edges is an important manifestation of the exotic topological properties of anyons. The latter quantity controls the decay rate of anyon correlations and is currently the subject of intense investigation. However, compared to other properties of anyons, scaling dimension is far more susceptible to non-universal physics of the FQHE edges. This sensitivity has led to significant discrepancies between theory and experiment, even for the simplest Laughlin states. Therefore, identifying reliable probes of the anyon scaling dimension is necessary.

To this end, we explore temperature-driven noise in the FQHE, referred to as ΔT noise. This occurs when two FQHE edges at different temperatures are connected via a quantum point contact (QPC). While the particle-hole symmetry of the QPC results in zero net current, the noise can deviate from equilibrium noise, leading to a measurable *excess* noise.

We calculate the finite-frequency ΔT noise in a general Abelian FQHE system. We show that this noise displays stark differences depending on whether anyons or electrons tunnel across the QPC. For anyon tunneling, the excess ΔT noise is negative over a wide range of frequencies, whereas electron tunneling always produces a positive excess noise. More generally, we find that excess finite-frequency ΔT noise becomes negative only when the scaling dimension of the tunneling particles is less than one—a characteristic feature of anyons. Even when non-universal edge physics alter the scaling dimension, finite-frequency ΔT noise provides a robust method for distinguishing anyon tunneling from non-anyonic quasiparticles tunneling at the QPC.

5.1. Preliminaries

In this chapter, we study the finite-frequency noise due to a temperature gradient between two edges of a QPC in the FQHE. Before going to the original results, it is useful to understand the concepts of finite-frequency noise and zero-frequency temperature-biased noise in their own right.

5.1.1. Finite-frequency noise

Finite-frequency noise turns out to be a subtle quantity to define [127, 128]. In general, current correlations, defined as the variance of current operator $I(t)$, comprise two differently time-ordered quantum averages.

$$\begin{aligned}\tilde{S}_+(t-t') &= \langle \delta I(t)\delta I(t')\rangle \\ \tilde{S}_-(t-t') &= \langle \delta I(t')\delta I(t)\rangle\end{aligned} \tag{5.1}$$

where $\delta I(t) = I(t) - \langle I(t)\rangle$. The two correlators above are not equal since current operators at different times do not commute. When confronted with such a scenario, conventional wisdom from quantum mechanics dictates employing a symmetrized combination of the non-commuting operators to connect to measurable quantities [129]. Finite-frequency noise was hence traditionally defined as the Fourier transform of the symmetrized correlators. Ref. [127] showed that the symmetrization prescription is wrong. The combination of correlators constituting the finite-frequency noise depends rather on the precise measurement apparatus under consideration.

To illustrate the above claim, we define the *emission* and *absorption* noise, respectively.

$$\begin{aligned}S_+(\omega) &= 2\int d\tau\ e^{i\omega\tau}\tilde{S}_+(\tau) \\ S_-(\omega) &= 2\int d\tau\ e^{i\omega\tau}\tilde{S}_-(\tau)\end{aligned} \tag{5.2}$$

The nomenclature is explained as follows. Let us assume that the initial ($|i\rangle$) and final ($|f\rangle$) state of the system is known. A Fermi golden rule calculation yields the emission and absorption noise.

$$\begin{aligned}S_+(\omega) &= 4\pi|\langle f|\,\delta I\,|i\rangle|^2\delta(\omega+\epsilon_f-\epsilon_i) \\ S_-(\omega) &= 4\pi|\langle f|\,\delta I\,|i\rangle|^2\delta(\omega+\epsilon_i-\epsilon_f)\end{aligned} \tag{5.3}$$

where, δI denotes the current operator in the Schrodinger representation, $\epsilon_{i/f}$ is the energy of the initial/final state of the system. Given $\omega > 0$, for $S_+(\omega)$ we have $\epsilon_f < \epsilon_i$, implying emission of energy from the device into the environment, hence the name emission noise. On the contrary, for $S_-(\omega)$ one has $\epsilon_i < \epsilon_f$ which means that energy from the environment is absorbed by the device, granting it the name absorption noise.

With the above definitions, we give a concrete example of finite-frequency noise measurement. Ref. [127] proposes the measurement of finite-frequency noise of a mesoscopic device, for example, a QPC in a quantum Hall system, by coupling it inductively to an LC circuit. The latter functions as a detector of the current correlations. The LC detector is characterized by the charge Q stored in the capacitor, which can be easily measured in experiments. Inductive coupling between the mesoscopic device and the LC circuit

implies that $Q(t)$ can be modeled as a harmonic oscillator, linearly coupled to the rate of change of current in the mesoscopic circuit

$$\frac{d^2Q(t)}{dt^2} = -\Omega^2 Q(t) - \alpha \frac{dI(t)}{dt}. \tag{5.4}$$

Here, Ω is the resonant frequency of the LC circuit, α is the inductive coupling between the LC circuit and the mesoscopic device, and $I(t)$ denotes the current operator on the mesoscopic device that we are probing. Given the direct connection between the charge $Q(t)$, and the time derivative of the current $I(t)$, correlations of $Q(t)$ yield a measurement of the finite-frequency noise due to the currents $I(t)$ in the mesoscopic device. As calculated explicitly in Ref. [127]

$$\left\langle \delta Q^2(0) \right\rangle = \kappa \left[S_+(\Omega) \left(N_\Omega + 1 \right) - S_-(\Omega) N_\Omega \right] \tag{5.5}$$

where $\delta Q(t) = Q(t) - \langle Q(t) \rangle$, κ is coupling constant of the mesoscopic device and the detector, and N_ω denotes a Bose-Einstein distribution associated with the quantized harmonic oscillator modes of the LC circuit. The resonance frequency of the LC circuit sets the frequency at which the noise is measured.

As suggested before, the combination of finite-frequency correlators measured via an LC circuit is far from symmetric and is defined directly by the detector. We emphasize however that the combination of emission and absorption noise appearing in Equation (5.5) is specific to the particular measurement apparatus under consideration [130]. Theoretically, it is hence simpler to address the emission and absorption noises separately, allowing us to adapt easily to any measurement scheme.

For future convenience, the emission and absorption noise are expressed within the Keldysh formalism as

$$\begin{aligned} S_+(\omega) &= 2 \int d(t-t') \; e^{i\omega(t-t')} \left\langle \left\{ T_K \delta I(t^+) \delta I(t'^-) e^{-i \int_K dt'' H_T(t'')} \right\} \right\rangle \\ S_-(\omega) &= 2 \int d(t-t') \; e^{i\omega(t-t')} \left\langle \left\{ T_K \delta I(t^-) \delta I(t'^+) e^{-i \int_K dt'' H_T(t'')} \right\} \right\rangle \end{aligned} \tag{5.6}$$

where $H_T(t)$ denotes the interaction Hamiltonian. The choice of Keldysh indices enforces the time ordering of the emission and absorption noise as defined in Equations (5.1) and (5.2). Since these are related by $S_+(\omega) = S_-(-\omega)$, it suffices to calculate just one of the quantities.

We note before closing this section that finite-frequency noise has given deep insight into mesoscopic systems, beyond zero-frequency noise [131–135]. In the context of FQHE, among other things, it has yielded a complementary diagnosis of the fractional charge of anyons [65].

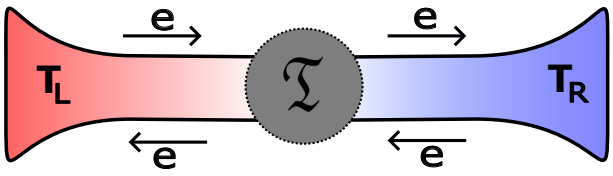


Figure 5.1.: Schematic device geometry to measure ΔT noise in a Fermi liquid system. The above device hosts two Fermi leads on the left and right, held at temperatures T_L and T_R respectively. The leads meet at a junction characterized by a constant transparency $\mathfrak{T}$. The absence of a potential difference and the junction being particle-hole symmetric entails a net-zero current of electrons across the junction. However, partitioning of the electron currents at the junction leads to a non-zero ΔT noise, that is driven by the temperature gradient, on top of the thermal noise

5.1.2. Zero-frequency ΔT noise in Fermi liquids

Shot noise is typically generated by partitioning of an incoming current. A non-zero voltage gives rise to a non-zero charge current, whose fluctuations (caused by partitioning) are related to the shot noise. It was recently realized that a non-zero excess shot noise (over the thermal noise) of the charge current can exist even when the average incoming current is zero [136–138]. In this case, instead of a voltage difference creating a non-equilibrium state, a temperature gradient across a junction between two particle reservoirs drives the system out of equilibrium. In systems with particle-hole symmetry, this setup results in zero net charge current while still producing non-zero charge noise.

To illustrate this, let us consider two Fermi leads, connected by a junction of transmission $\mathfrak{T}$, as shown in Figure 5.1. We assume that the voltage bias between the two leads is zero, but they are both held at different temperatures. The zero-frequency noise measured at the left or right lead is given by standard scattering theory calculations [26]:

$$S = \frac{e^2}{\pi}\int d\epsilon \Big\{\mathfrak{T}\left[f_R(\epsilon)(1-f_R(\epsilon)) + f_L(\epsilon)(1-f_L(\epsilon))\right] + \mathfrak{T}(1-\mathfrak{T})\left(f_R(\epsilon)-f_L(\epsilon)\right)^2\Big\}, \tag{5.7}$$

where

$$f_{L/R}(\epsilon) = \frac{1}{1+e^{\frac{E}{T_{L/R}}}} \tag{5.8}$$

is the Fermi function on the left/right lead, and $T_{L/R}$ denotes the temperature on the left/right lead. Taking both the leads to be at the same potential, we set it to zero without loss of generality. In Equation (5.7), we distinguish two contributions. The first

line gives the thermal noise present in both the leads. On the other hand, the second line represents a purely non-equilibrium contribution to the noise. Indeed, if one turns off the temperature difference, setting $T_L = T_R$, the latter contribution vanishes while the thermal contribution persists. This temperature-difference driven contribution to the noise, which is clearly different from the equilibrium thermal noise, is dubbed ΔT noise.

While Fermi statistics of the electrons in the leads is readily accounted for in the above discussion, interactions between electrons is left out. Several theoretical works have later shown that ΔT noise carries signatures of interactions between the particles carrying the current and also their statistics [72, 139–145]. In the fractional quantum Hall effect, Ref. [71] calculated the zero-frequency ΔT noise at a QPC for Laughlin states. The latter works finds that when anyons tunnel at the QPC, the ΔT contributions to the noise are negative – an overall reduced noise compared to the equilibrium scenario. This striking result is in contrast to the ΔT noise when electrons tunnel at the QPC, which remains positive. Hence, ΔT noise was shown to robustly distinguish anyons tunneling at the QPC, from electrons in the context of Laughlin states.

However, the ability of the zero-frequency ΔT noise in distinguishing anyons from electrons is restricted to Laughlin fractions with $\nu < 1/2$. In Ref. [71], it can be seen that for $\nu > 1/2$, the excess ΔT noise is positive for tunneling of both electrons and anyons. It is hence necessary to look for observables that can robustly distinguish anyons from electrons even in non-Laughlin filling fractions. Moreover, it has been shown that the behavior of ΔT noise depends on the scaling dimension $\delta_{\boldsymbol{g}}$ [145], and not on the filling fraction ν – two distinct physical quantities. For Laughlin fractions however, the two are numerically equivalent, $\delta_{\boldsymbol{g}_\alpha} = \nu$. The latter relation is no longer valid for non-Laughlin fractions. Studying ΔT noise in non-Laughlin fractions, as done in this chapter, thus allows to easily pin down the physical quantities responsible for the behavior of ΔT noise.

5.2. ΔT emission noise in FQHE

In the remainder of this chapter, we put together the two concepts discussed in the previous sections. We calculate the ΔT finite-frequency noise, or rather the ΔT emission noise, at a QPC biased with a temperature gradient. As explained in the previous section, zero-frequency ΔT noise contains important information about anyons in FQHE. But its utility is restricted to Laughlin states with $\nu < 1/2$. For $\nu > 1/2$, zero-frequency ΔT is unable to robustly distinguish electrons from anyons. This motivates us to study finite-frequency ΔT noise, for a general Abelian FQHE state. Indeed, we will find the finite-frequency noise to robustly distinguish anyons from electrons in a general Abelian FQHE.

We consider here a quantum point contact in an arbitrary Abelian FQHE, where the two edges are held at different temperatures. The setup is shown schematically in Figure

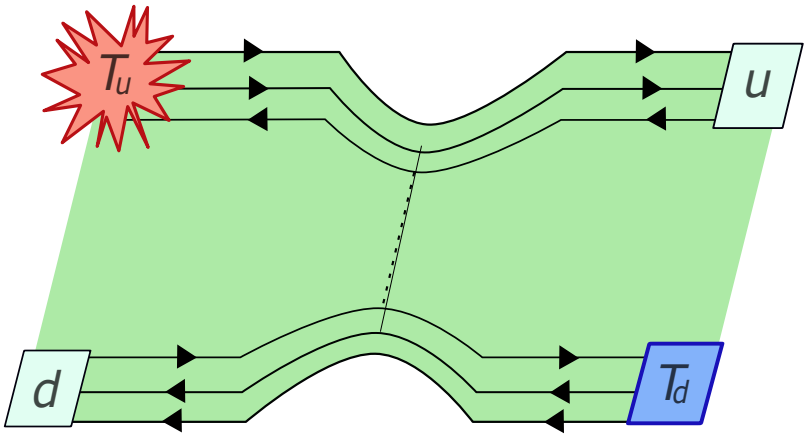


Figure 5.2.: A general Abelian FQHE system containing multiple co-propagating bosonic modes, endowed with a QPC. The upper/lower edge is held at a temperature $T_{u/d}$. The QPC allows for tunneling of anyonic quasiparticles or electrons between the upper and lower edges. The resulting correlations in the current fluctuations are measured at contacts u and d.

5.2. The tunneling current operator at the QPC takes the form shown in Section 2.3:

$$I_T(t) = \sum_{\alpha} \sum_{\epsilon} i\epsilon q_{\boldsymbol{g}_\alpha} \left[\Gamma_{\boldsymbol{g}_\alpha} \psi^{u\dagger}_{\boldsymbol{g}_\alpha}(0,t)\psi^{d}_{\boldsymbol{g}_\alpha}(0,t)\right]^{\epsilon}, \tag{5.9}$$

where the upper/lower edge is characterized by temperature $T_{u/d}$, $\psi^{u/d}_{\boldsymbol{g}_\alpha}(0,t) = e^{i\boldsymbol{g}_\alpha\cdot\boldsymbol{\phi}^{u/d}}$ denotes an anyon operator on the upper/lower edge, and $\Gamma_{\boldsymbol{g}_\alpha}$ denotes the tunneling amplitude associated with the tunneling of type$-\alpha$ anyon. Now we define the finite-frequency emission noise of the system as:

$$S_+(\omega, T_u, T_d) = \int d(t-t')\; e^{i\omega(t-t')} \left\langle \left\{ T_K \delta I(t^+)\delta I(t'^-) e^{-i\int_K dt'' H_T(t'')} \right\} \right\rangle, \tag{5.10}$$

where $H_T(t)$ denotes the tunneling Hamiltonian of the QPC. As discussed in Section 5.1, the choice of the Keldysh indices ensures that for the frequency $\omega > 0$, energy is emitted from the device under consideration into a detector. At lowest order in perturbation theory (two orders in $\Gamma_{\boldsymbol{g}_\alpha}$), we can drop the time evolution operator as the tunneling current operators already contribute two $\Gamma_{\boldsymbol{g}_\alpha}$. Using the current expression from Equation

(5.9), we write

$$\begin{aligned} S_+(\omega, T_u, T_d) = &- \sum_{\alpha\beta} q_{\boldsymbol{g}_\alpha} q_{\boldsymbol{g}_\beta} \sum_{\epsilon\epsilon'} \epsilon\epsilon' \int d(t-t')\ e^{i\omega(t-t')} \\ \times &\left\langle \left\{ T_K \left[\Gamma_{\boldsymbol{g}_\alpha} \psi^{u\dagger}_{\boldsymbol{g}_\alpha}(0,t^-) \psi^{d}_{\boldsymbol{g}_\alpha}(0,t^-) \right]^{\epsilon} \left[\Gamma_{\boldsymbol{g}_\beta} \psi^{u\dagger}_{\boldsymbol{g}_\beta}(0,t'^+) \psi^{d}_{\boldsymbol{g}_\beta}(0,t'^+) \right]^{\epsilon'} \right\} \right\rangle . \end{aligned} \tag{5.11}$$

Recalling that the quasiparticle operators are given by $\psi^{u/d}_{\boldsymbol{g}_\alpha} = e^{i\boldsymbol{g}_\alpha \cdot \boldsymbol{\phi}^{u/d}}$, and using the independence of the upper and lower edges, we have:

$$\begin{aligned} S_+(\omega, T_u, T_d) = &- \sum_{\alpha\beta} q_{\boldsymbol{g}_\alpha} q_{\boldsymbol{g}_\beta} \sum_{\epsilon\epsilon'} \epsilon\epsilon' \Gamma^{\epsilon}_{\boldsymbol{g}_\alpha} \Gamma^{\epsilon'}_{\boldsymbol{g}_\beta} \int d(t-t')\ e^{i\omega(t-t')} \\ \times &\prod_j \left\langle \left\{ T_K e^{-i\epsilon g_{\alpha j} \phi^u_j(0,t^-)} e^{-i\epsilon' g_{\beta j} \phi^u_j(0,t'^+)} \right\} \right\rangle \left\langle \left\{ T_K e^{i\epsilon g_{\alpha j} \phi^d_j(0,t^-)} e^{i\epsilon' g_{\beta j} \phi^d_j(0,t'^+)} \right\} \right\rangle \end{aligned} \tag{5.12}$$

From the details in Appendix B, the above correlation functions are non-vanishing only when $\epsilon' = -\epsilon$ and $\alpha = \beta$. The non-zero correlator of exponentiated bosonic fields is hence given by

$$\left\langle \left\{ T_K e^{-i\epsilon g_{\alpha j} \phi^{u/d}_j(0,t^-)} e^{-i\epsilon' g_{\alpha j} \phi^{u/d}_j(0,t'^+)} \right\} \right\rangle = \exp\left\{ g^2_{\alpha j} \mathcal{G}^{u/d\eta_1\eta_2}_j(0, t-t') \right\} \tag{5.13}$$

Here, $\mathcal{G}^{\eta_1\eta_2}_{u/d,j}(x,t)$ is the Keldysh bosonic Greens function of the $j-$th bosonic mode on the upper/lower edge. At finite temperature, the latter reads

$$\mathcal{G}^{u/d\eta_1\eta_2}_j(x,t) = \log \left\{ \frac{\sinh\left(i\pi T_{u/d}\tau_0\right)}{\sinh\left[\pi T_{u/d}\left(i\tau_0 - \sigma_{\eta_1\eta_2}(t)[t - \chi_j x]\right)\right]} \right\}, \tag{5.14}$$

where χ_j is the chirality of the $j-$th bosonic mode, and

$$\sigma_{\eta_1\eta_2}(t) = \frac{1}{2}\left[(\eta_2 - \eta_1) + \mathrm{sgn}(t)(\eta_1 + \eta_2)\right] \tag{5.15}$$

imposes the appropriate Keldysh ordering of the Greens functions. Using the above expression of the correlation functions, we write

$$\begin{aligned} S_+(\omega, T_u, T_d) = &\sum_{\alpha} \sum_{\epsilon\epsilon'} \left(q_{\boldsymbol{g}_\alpha} |\Gamma_{\boldsymbol{g}_\alpha}|\right)^2 \int d(t-t')\ e^{i\omega(t-t')} \\ \times &\prod_j \exp\left[g^2_{\alpha j} \mathcal{G}^{u+-}_j(t-t')\right] \exp\left[g^2_{\alpha j} \mathcal{G}^{d+-}_j(t-t')\right] . \end{aligned} \tag{5.16}$$

Now, taking the product over j as a sum over j into the exponentials, and recalling that $\sum_j g_{\alpha j} = \delta_{\boldsymbol{g}_\alpha}$, the scaling dimension of $\psi_{\boldsymbol{g}_\alpha}$, we find:

$$\begin{aligned} S_+(\omega, T_u, T_d) = \sum_\alpha \left(q_{\boldsymbol{g}_\alpha}|\Gamma_{\boldsymbol{g}_\alpha}|\right)^2 \int d\tau\ e^{i\omega(t-t')} \\ \times \exp\left[\delta_{\boldsymbol{g}_\alpha}\mathcal{G}^{u+-}(t-t') + \delta_{\boldsymbol{g}_\alpha}\mathcal{G}^{d+-}(t-t')\right]. \end{aligned} \tag{5.17}$$

Making the transformation $\tau = t - t'$, and plugging in the expression of the bosonic thermal Greens function from Equation (5.14), we are left with the following integral to evaluate:

$$\begin{aligned} S_+(\omega, T_u, T_d) = \sum_\alpha \left(q_{\boldsymbol{g}_\alpha}|\Gamma_{\boldsymbol{g}_\alpha}|\right)^2 \int d\tau\ e^{i\omega\tau} \\ \times \left[\frac{\sinh(i\pi T_u\tau_0)}{\sinh(\pi T_u(i\tau_0+\tau))}\right]^{\delta_{\boldsymbol{g}_\alpha}} \left[\frac{\sinh(i\pi T_d\tau_0)}{\sinh(\pi T_d(i\tau_0+\tau))}\right]^{\delta_{\boldsymbol{g}_\alpha}}. \end{aligned} \tag{5.18}$$

5.2.1. Expansion in the temperature gradient

Unfortunately, Equation (5.18) is not analytically tractable in its full form since the temperature on the upper and lower edges are different. The full numerical treatment of this problem, comparing the fractional quantum Hall system with Fermi liquids, is detailed by the author of this thesis in Ref. [146], but not included in the thesis. While these details are interesting in their own right, they are not directly related to the physics of scaling dimension that we focus on in this chapter.

Here, we treat this integral perturbatively in the small temperature gradient limit. Starting from $T_{u/d} = \bar{T} \pm \frac{\Delta T}{2}$ where $\Delta T \ll \bar{T}$, we expand the exponentiated Greens function perturbatively up to second order in $\Delta T/2$:

$$S_+(\omega, T_u, T_d) = \sum_\alpha S_0^{(\alpha)}(\omega, \bar{T}) \left[1 + \left(\frac{\Delta T}{2\bar{T}}\right)^2 C_2^{(\alpha)}(\omega, \bar{T})\right], \tag{5.19}$$

where

$$S_0^{(\alpha)}(\omega, \bar{T}) = \left(q_{\boldsymbol{g}_\alpha}\Gamma_{\boldsymbol{g}_\alpha}\right)^2 \int d\tau e^{i\omega\tau} \left[\frac{\sinh\left(i\pi\bar{T}\tau_0\right)}{\sinh\left(\pi\bar{T}(i\tau_0+\tau)\right)}\right]^{2\delta_{\boldsymbol{g}_\alpha}} \tag{5.20}$$

and

$$C_2^{(\alpha)}(\omega,\bar{T}) = \frac{1}{S_0^{(\alpha)}(\bar{T},\omega)}\left(q_{\boldsymbol{g}_\alpha}\Gamma_{\boldsymbol{g}_\alpha}\right)^2\int d\tau\; e^{i\omega\tau}\left[\frac{\sinh\left(i\pi\bar{T}\tau_0\right)}{\sinh\left(\pi\bar{T}(i\tau_0+\tau)\right)}\right]^{2\delta_{\boldsymbol{g}_\alpha}} \left[\frac{\delta_{\boldsymbol{g}_\alpha}(\pi(i\tau_0+\tau))^2}{\sinh\big(\pi\bar{T}(i\tau_0+\tau)\big)} - \frac{\delta_{\boldsymbol{g}_\alpha}(i\pi\tau_0)^2}{\sinh\big(i\pi\tau_0\bar{T}\big)}\right] \tag{5.21}$$

Here, $\sum_\alpha S_0^{(\alpha)}(\omega,\bar{T})$ is just the equilibrium thermal noise. Integrals of both Equations (5.20) and (5.21) can be evaluated analytically. The details of the calculation are summarized in Appendix D. First, we find the expression for $S_0^{(\alpha)}(\omega,\bar{T})$ to be

$$S_0^{(\alpha)}(\omega,\bar{T}) = \left(q_{\boldsymbol{g}_\alpha}\Gamma_{\boldsymbol{g}_\alpha}\right)^2\tau_0\left[2\pi\tau_0\bar{T}\right]^{2\delta_{\boldsymbol{g}_\alpha}-1}e^{-\frac{\omega}{2T}}\frac{\left|\Gamma\left(\delta_{\boldsymbol{g}_\alpha}+\frac{i\omega}{2\pi\bar{T}}\right)\right|^2}{\Gamma(2\delta_{\boldsymbol{g}_\alpha})}, \tag{5.22}$$

giving us the equilibrium thermal noise at temperature $\bar{T}$. The more interesting result is $C_2^{(\alpha)}$ which reads:

$$C_2^{(\alpha)}\left(\frac{\omega}{2\pi\bar{T}}\right) = \delta_{\boldsymbol{g}_\alpha}\left[-1+\frac{\left|\delta_{\boldsymbol{g}_\alpha}+\frac{i\omega}{2\pi\bar{T}}\right|^2}{2\delta_{\boldsymbol{g}_\alpha}(2\delta_{\boldsymbol{g}_\alpha}+1)}\left(\pi^2+4\pi\mathrm{Im}\left[\psi\left(\delta_{\boldsymbol{g}_\alpha}+1+\frac{i\omega}{2\pi\bar{T}}\right)\right]\right.\right. \\ \left.\left. +4\left\{\mathrm{Im}\left[\psi\left(\delta_{\boldsymbol{g}_\alpha}+1+\frac{i\omega}{2\pi\bar{T}}\right)\right]\right\}^2-2\mathrm{Re}\left[\psi'\left(\delta_{\boldsymbol{g}_\alpha}+1+\frac{i\omega}{2\pi\bar{T}}\right)\right]\right)\right] \tag{5.23}$$

where ψ is the digamma function and the prime indicates a derivative. Physically, $C_2^{(\alpha)}$ is proportional to the excess noise divided by the thermal noise measured at the average temperature $\bar{T}$, for the anyon of type$-\alpha$.

Interestingly, it turns out that $C_2^{(\alpha)}(\omega,\bar{T})$ does not depend separately on frequency and temperature, but rather in a combined way, being a function of the ratio $\theta = \omega/2\pi\bar{T}$. Indeed, since ω and T are the only relevant energy scales in the problem we consider, it is natural that any dimensionless quantity depends on their ratio.

In what follows, we will study the quantity $C_2^{(\alpha)}$ in detail for Laughlin fractions, as well as non-Laughlin fractions $\nu = 2/5$ and $2/3$. In the Laughlin fractions, we have a unique quasiparticle tunneling through the QPC, characterized by scaling dimension $\delta_{\boldsymbol{g}}$. We are hence free to drop the sum over α in Equation (5.19), and the superscripts or subscripts (α) in Equations (5.19) to (5.23). In contrast, the non-Laughlin fractions of $\nu = 2/5$ and $2/3$ consist of different anyons indexed by α. It turns out however that all the anyons in both these systems have the same scaling dimension $\delta_{\boldsymbol{g}}$. Hence, we are also

FQHE states	Scaling Dimension ($\delta_{\boldsymbol{g}}$)	
	Anyons	Electrons
Laughlin ($\nu = 1/m$)	ν	$1/\nu$
$\nu = 2/5$	$3/5$	$5/3$
$\nu = 2/3$	$2/3$	$3/2$

Table 5.1.: Scaling dimension of anyons and electrons tunneling at the QPC, in the weak- and strong-backscattering regime respectively; m denotes an odd integer.

free to drop the sum over α for these systems, giving us:

$$S_+(\omega, T_u, T_d) = S_0(\omega, \bar{T}) \left[1 + \left(\frac{\Delta T}{2\bar{T}}\right)^2 C_2(\omega, \bar{T})\right] \tag{5.24}$$

where

$$C_2\left(\frac{\omega}{2\pi\bar{T}}\right) = \delta_{\boldsymbol{g}} \left[-1 + \frac{\left|\delta_{\boldsymbol{g}} + \frac{i\omega}{2\pi\bar{T}}\right|^2}{2\delta_{\boldsymbol{g}}(2\delta_{\boldsymbol{g}}+1)} \left(\pi^2 + 4\pi \mathrm{Im}\left[\psi\left(\delta_{\boldsymbol{g}} + 1 + \frac{i\omega}{2\pi\bar{T}}\right)\right] + 4\left\{\mathrm{Im}\left[\psi\left(\delta_{\boldsymbol{g}} + 1 + \frac{i\omega}{2\pi\bar{T}}\right)\right]\right\}^2 - 2\mathrm{Re}\left[\psi'\left(\delta_{\boldsymbol{g}} + 1 + \frac{i\omega}{2\pi\bar{T}}\right)\right]\right)\right] \tag{5.25}$$

5.3. ΔT emission noise probes scaling dimension

In this section, we show that the finite-frequency C_2 coefficient calculated in the previous section robustly discriminates anyonic scaling dimension (typically $\delta_{\boldsymbol{g}} < 1$) from non-anyonic ones (typically $\delta_{\boldsymbol{g}} > 1$) in a general Abelian FQHE. We first start by addressing Laughlin fractions. The motivations to study finite-frequency C_2 for non-Laughlin fractions of FQHE are explained as we go along.

5.3.1. Laughlin fractions

We start by studying the behavior of the C_2 coefficient for Laughlin fractions of the FQHE. There are two interesting regimes to explore in this context: the weak- and the strong-backscattering regime. As explained in Section 2.3.2, weak-backscattering regime involves bringing the two edges close while still having the FQHE between the edges. This regime admits tunneling of anyonic quasiparticles across the edges. The opposite strong-backscattering regime consists of breaking the FQHE liquid in two, leaving a

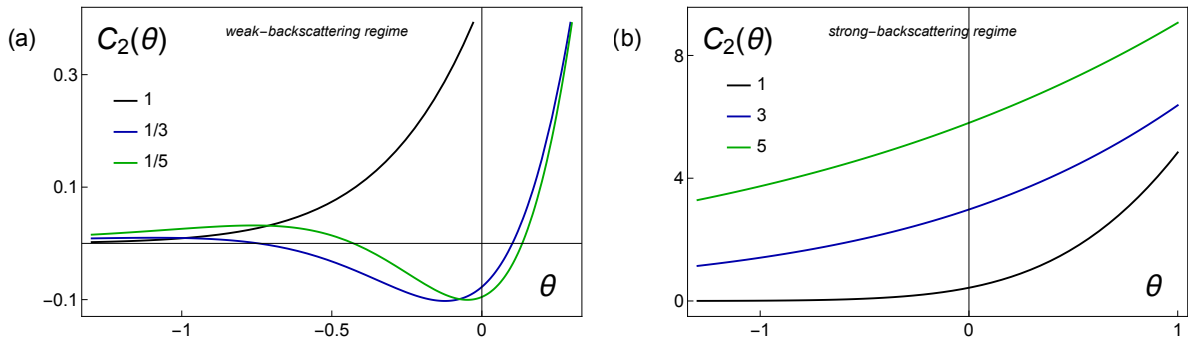


Figure 5.3.: C_2 coefficient as a function of $\theta = \omega/2\pi\bar{T}$ for different states in the Laughlin series ($\nu = 1,\ 1/3,\ 1/5$). (a) Weak-backscattering regime, quasiparticles tunnel across the QPC with scaling dimensions $\delta_{\boldsymbol{g}_\alpha} = 1,\ 1/3,\ 1/5$, for $\nu = 1,\ 1/3,\ 1/5$ respectively. $\delta_{\boldsymbol{g}} = 1$ corresponds to tunneling of electrons in integer QHE. The other values correspond to tunneling of anyonic quasiparticles in Laughlin filling fractions $\nu = 1/3,\ 1/5$, respectively. For tunneling of Laughlin anyonic quasiparticles, we find that the C_2 coefficient is negative across a wide range of θ. On the contrary, for tunneling of electrons, C_2 always stays positive. (b) Strong-backscattering regime, electrons tunnel across the QPC with scaling dimensions $\delta_{\boldsymbol{g}_\alpha} = 1,\ 3,\ 5$, for $\nu = 1,\ 1/3,\ 1/5$ respectively. The first corresponds to tunneling of electrons in integer QHE, while the latter two correspond to tunneling of electrons in the strong-backscattering regime of the FQHE. It is noteworthy that unlike the anyon tunneling, tunneling of electrons has a behavior quite similar to the trivial integer QHE case.

vacuum between the edges. Hence, only electrons can tunnel between the edges. We study below the behavior of C_2 in both these regimes.

It is to be noted that while the weak- and the strong-backscattering regime are physically quite different, mathematically they are described on the same footing. Indeed, one can use Equation (5.25) to analyze both these regimes, with the difference between the two regimes lying solely in the values of the scaling dimension $\delta_{\boldsymbol{g}}$. Anyon tunneling in the weak-backscattering regime typically involves $\delta_{\boldsymbol{g}} < 1$, while electrons in the strong-backscattering regime usually exhibit $\delta_{\boldsymbol{g}} > 1$. This discussion holds true even for the non-Laughlin fractions.

In the weak-backscattering regime the tunneling Hamiltonian is composed of anyonic operators on both edges. The scaling dimension is then given by $\delta_{\boldsymbol{g}} = \nu$, where $\nu = 1/(2n+1)$, $n \in \mathbf{Z}$ for Laughlin fractions. We plot in Figure 5.3(a) the behavior of C_2 for different Laughlin FQHE with QPC in the weak backscattering regime. There is a clear distinction between the behavior for the Laughlin fractions and that for the integer quantum Hall case. While for $\delta_{\boldsymbol{g}} = 1$ the C_2 coefficient increases monotonically, for Laughlin fractions in the weak-backscattering regime, it displays a dip, crossing into negative values for frequencies close to zero for the Laughlin fractions. In all cases, the C_2

coefficient grows as a power-law at high frequency. Nevertheless, the contribution to the emission noise is washed out by the exponential decay of the equilibrium thermal noise. We also note that C_2 intercepts the $y-$axis, corresponding to the zero-frequency noise, at negative values.

In the strong backscattering regime, electrons tunnel across the edges. The scaling dimension in the Laughlin fractions is then given by $\delta_{\boldsymbol{g}} = 1/\nu$. Here, we find that the curves for Laughlin FQH show a strong resemblance to the $\delta_{\boldsymbol{g}} = 1$ curve, monotonically increasing as a function of $\omega/\bar{T}$ and no dips to negative values as shown in Figure 5.3(b).

5.3.2. Comparison with zero-frequency ΔT noise

In the previous subsection we studied the finite frequency C_2 for anyon and electron tunneling across the QPC in Laughlin fractions. We found that when anyons tunnel across the QPC, C_2 is negative across a range of frequencies, including at zero frequency. In contrast, it is positive when electrons tunnel through the QPC. The question now is whether finite-frequency ΔT noise brings in additional insights compared to zero-frequency ΔT noise? If not, one lacks motivation to pursue the experimentally as well as theoretically more challenging finite-frequency noise.

It can be shown our calculations are consistent with the zero-frequency ΔT noise prediction of Ref. [71]. Setting $\theta = 0$ in Equation (5.25), the zero-frequency ΔT noise for a general Abelian FQHE reads:

$$C_2(\theta = 0) = \delta_{\boldsymbol{g}} \left\{ -1 + \frac{\delta_{\boldsymbol{g}}}{2\delta_{\boldsymbol{g}} + 1} \left[\frac{\pi^2}{2} - \psi'(\delta_{\boldsymbol{g}} + 1) \right] \right\}. \tag{5.26}$$

We emphasize that the above result describes the ΔT noise due to tunneling of an anyon with scaling dimension $\delta_{\boldsymbol{g}}$ in an arbitrary Abelian FQHE. In contrast to Ref. [71], it is not restricted to Laughlin fractions. We plot $C_2(\theta = 0)$ as a function of the scaling dimension $\delta_{\boldsymbol{g}}$ in Figure 5.4 for the weak- and strong-backscattering regimes. In the strong-backscattering regime, where electrons tunnel across the QPC, C_2 is always positive. The weak-backscattering regime, where anyons tunnel across the QPC, displays a different behavior. For $\delta_{\boldsymbol{g}} < 1/2$, C_2 is negative in the weak-backscattering regime, distinguishing anyons from electrons.

We note here that the condition $\delta_{\boldsymbol{g}} < 1/2$, is satisfied only for Laughlin fractions. For Laughlin FQHE, the scaling dimension of anyons is numerically equivalent to the filling fraction ($\nu = 1/3,\ 1/5,\ 1/7\ldots$). The finite-frequency noise hence might not provide more information about the scaling dimension compared to the zero-frequency noise for Laughlin fractions.

In non-Laughlin fractions such as $\nu = 2/3,\ 2/5$, the anyonic quasiparticles are characterized by scaling dimension $1/2 < \delta_{\boldsymbol{g}} < 1$. For $\delta_{\boldsymbol{g}} > 1/2$, Figure 5.4 shows that anyon

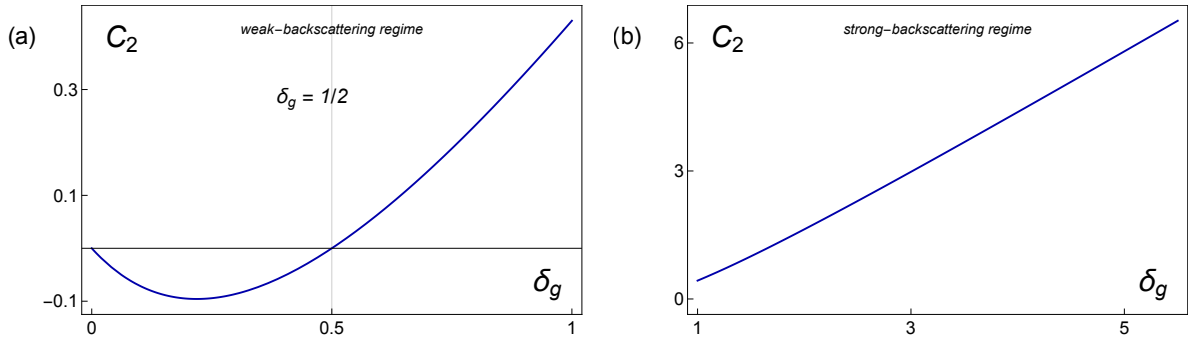


Figure 5.4.: Zero-frequency ΔT noise of Equation (5.26) as a function of scaling dimension $\delta_{\boldsymbol{g}}$. In the strong backscattering regime, C_2 is always positive. In the weak-backscattering regime, C_2 achieves negative values for $\delta_{\boldsymbol{g}} < 1/2$, distinguishing anyons from electrons. However, when $\delta_{\boldsymbol{g}} > 1/2$ C_2 is positive even in the weak-backscattering regime.

tunneling yields a positive value of C_2. For these values of $\delta_{\boldsymbol{g}}$, zero-frequency ΔT noise is unable to distinguish anyons from electrons in a general Abelian FQHE, especially when $\delta_{\boldsymbol{g}} > 1/2$. This constitutes a strong motivation to study finite-frequency ΔT noise.

5.3.3. Non-Laughlin fractions

We now shift our attention to the non-Laughlin fractions. Specifically, we will consider the cases of $\nu = 2/3$ and $\nu = 2/5$ where experiments are actively being pursued.

- $\boldsymbol{\nu = 2/3}$**:** $e/3$ quasiparticles are observed to tunnel at the QPC with $\delta_{\boldsymbol{g}} = 2/3$
- $\boldsymbol{\nu = 2/5}$**:** $e/5$ quasiparticles are observed to tunnel at the QPC with $\delta_{\boldsymbol{g}} = 3/5$

We show the behavior of C_2 for the above values of scaling dimension in Figure 5.5. We see here a behavior similar to the weak-backscattering regime of Laughlin FQHE, with the C_2 being negative across a wide range of θ, and blowing up for large, positive θ. Interestingly, in contrast with Laughlin fractions, the zero-frequency value of C_2 is positive. As discussed before, for all $\delta_{\boldsymbol{g}} > 1/2$, the zero-frequency value of C_2 is positive. While zero-frequency C_2 is a good indicator of anyonic behavior for Laughlin fractions, a proper diagnosis of anyonic behavior even in non-Laughlin fractions requires studying the finite-frequency behavior of C_2.

We complete this section by looking at the C_2 when electrons tunnel across the QPC in the non-Laughlin fractions.

- $\boldsymbol{\nu = 2/3}$**:** electron tunneling at QPC with $\delta_{\boldsymbol{g}} = 3/2$
- $\boldsymbol{\nu = 2/5}$**:** electron tunneling at QPC with $\delta_{\boldsymbol{g}} = 5/3$

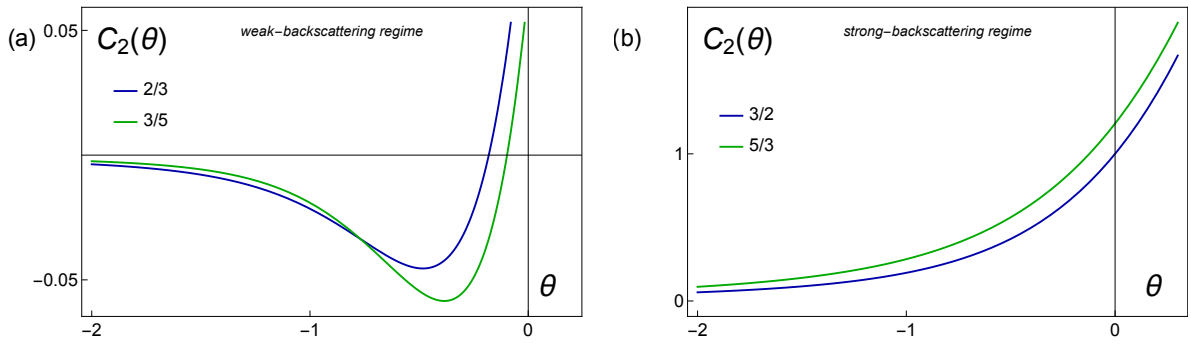


Figure 5.5.: (a) C_2 as a function of θ for $\delta_{\boldsymbol{g}} = 2/3$, for $e/3$ quasiparticles in $\nu = 2/3$ FQHE and $\delta_{\boldsymbol{g}} = 3/5$, for $e/5$ quasiparticles in $\nu = 2/5$ FQHE. (b) C_2 as a function of θ for $\delta_{\boldsymbol{g}} = 3/2$, for electrons in $\nu = 2/3$ FQHE and $\delta_{\boldsymbol{g}} = 5/3$, for electrons in $\nu = 2/5$ FQHE. When anyonic quasiparticles tunnel across the QPC, the C_2 coefficient becomes negative across values of θ in contrast to the scenario of electron tunneling, where C_2 always remains positive.

Similar to electron tunneling in Laughlin fractions, we see here again a clear lack of negativity of the C_2.

From the studies of anyon and electron tunneling in Laughlin as well as non-Laughlin fractions, we note a clear trend. The C_2 coefficient is negative over a large range of θ for all $\delta_{\boldsymbol{g}} < 1$, while it is absolutely positive for all $\delta_{\boldsymbol{g}} > 1$.

5.3.4. Non-chiral Luttinger liquids

While our calculations started from tunneling Hamiltonian of chiral Luttinger liquids in the FQHE, the results extend straightforwardly to QPC in arbitrary Luttinger liquid systems driven by a temperature gradient. The only difference in C_2 of Equation (5.25) would be in the scaling dimension $\delta_{\boldsymbol{g}}$. The latter depends on the details of the specific system under consideration. Importantly, non-chiral Luttinger liquids are characterized by $\delta_{\boldsymbol{g}} > 1$ (see supplemental material of Ref. [71]).

5.3.5. Consolidating the results

In Figure 5.6, we plot C_2 as a function of θ (on the $x-$axis), and $\delta_{\boldsymbol{g}}$ (on the $y-$axis). It is clear the C_2 is never negative for any $\delta_{\boldsymbol{g}} \geq 1$, while it can be negative over a wide interval of θ when $\delta_{\boldsymbol{g}} < 1$. Since anyons in the FQHE are characterized by $\delta_{\boldsymbol{g}} < 1$ our results concretely tie a negative C_2 to anyonic behavior, in contrast with conventional Luttinger liquid physics, as non-chiral Luttinger liquids are typically associated with $\delta_{\boldsymbol{g}} > 1$.

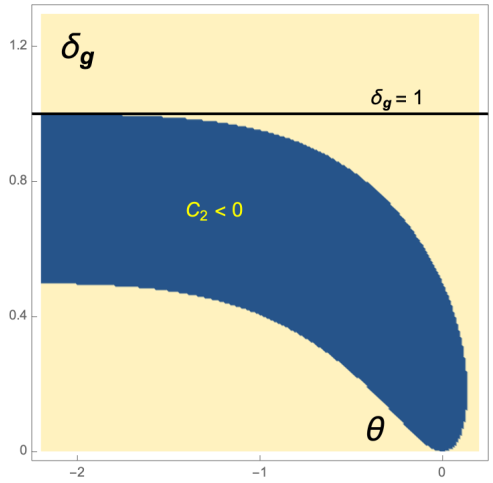


Figure 5.6.: Density plot of C_2 as a function of θ on the $x-$axis and δ_g on the $y-$axis. Blue corresponds to $C_2 < 0$, while yellow signifies $C_2 \geq 0$. While C_2 is negative in a wide interval of θ for all $\delta_g < 1$, it is always non-negative for all $\delta_g \geq 1$.

5.4. Discussion and conclusion

This chapter explored the finite frequency noise driven by a temperature difference, in quantum point contacts of general Abelian FQHE. While the full excess noise requires numerical evaluation, the regime of a small temperature difference allows perturbative expansion in the temperature gradient. The perturbative expansion in ΔT relies on the temperature gradient between the edges being small enough. Consider for example $\Delta T = 5mK$ and $\bar{T} = 45mK$, which corresponds to routinely used temperatures in FQHE noise measurements. In this case, the higher-order terms in the ΔT expansion are at least 81 times smaller than the quadratic contribution, and can hence be safely discarded.

However, it must be noted that creating a temperature difference between FQHE edges is a challenging experimental feat, compared for example to a potential difference. While various techniques exist to generate a temperature gradient [147, 148], systems featuring counter-propagating charge and neutral modes offer a relatively straightforward approach [59]. When a source current is injected into a charge mode propagating away from the quantum point contact (QPC) and collected at a downstream drain as shown in Figure 5.7, the equilibration process heats up the entire edge. Since the neutral mode propagates towards the QPC, a temperature bias is created even at the location of the QPC.

Moving to the main results of this chapter, we focused on the lowest-order, temperature-driven, non-equilibrium contribution to the noise, dubbed C_2. The dimensionless quantity C_2 is shown to robustly discriminate between tunneling of anyons and electrons across a QPC in general Abelian FQHE. C_2 takes negative values over a wide frequency range for anyon tunneling, while it remains strictly positive for electron tunneling. Extending our analysis to arbitrary Luttinger liquid systems, we find that $C_2(\theta)$ becomes negative

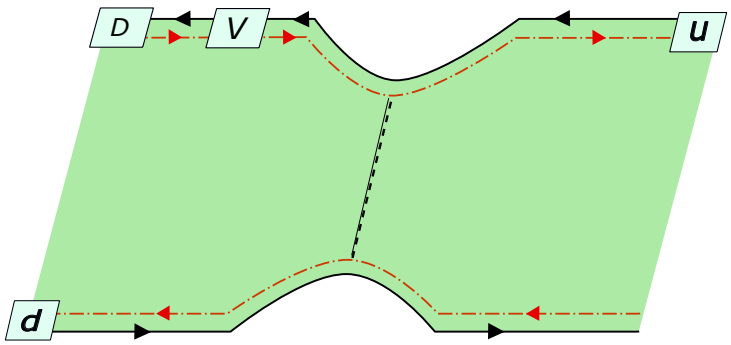


Figure 5.7.: Inducing temperature difference between edges to a counter-propagating voltage, inspired by Ref. [59]. We consider FQHE states with counter-propagating neutral modes such as $\nu = 2/3$. A voltage is applied on the upper edge. The charge mode propagates away from the QPC, and is drained at contact D. Due to intra-edge equilibration, the voltage nevertheless heats up the neutral mode propagating towards the QPC. The lower edge remains unheated, thus achieving a temperature gradient between the upper and lower edges. The resulting ΔT noise can be measured at contacts u and d.

only when the scaling dimension δ_g of the tunneling entities satisfies $0 < \delta_g < 1$, a characteristic feature of anyons on FQHE edges. This behavior contrasts with $C_2(\theta = 0)$, the zero-frequency component, which distinguishes anyons from electrons only when $\delta_g < 1/2$. As a result, zero-frequency noise is useful only for Laughlin FQHE states, where anyons exhibit $\delta_g < 1/2$. However, with finite-frequency noise, $C_2(\theta)$ turns negative across a range of frequencies for all $0 < \delta_g < 1$ underscoring its utility for any Abelian FQHE. Note that this is also potentially important for Laughlin fractions, where although theory predicts $\delta_g < 1/2$, several recent experiments are consistent with $\delta_g > 1/2$ [43, 149].

The scaling dimension δ_g of anyons tunneling across a QPC in FQHE has been a source of confusion for many decades now. Although $\delta_g < 1$ is theoretically predicted for anyonic quasiparticles, experiments are routinely consistent with $\delta_g = 1$ [150]. Moreover, experiments measuring the scaling dimension of anyons in the $\nu = 1/3$ Laughlin fraction using voltage biased shot noises have observed conflicting scaling dimensions: $\delta_g = 1/3$ [44], 2/3[149], and 1 [43]. Indeed, it has been suggested that the chiral Luttinger liquid model is too simplistic. Since the latter theory is gapless, additional effects such as Coulomb interactions at the location of the QPC or edge-reconstruction, modify the dynamics of the edge [151]. Moreover, the tunneling amplitudes of the QPC could evolve non-trivially with the applied voltage. These effects could result in the scaling dimension achieving a value higher than the theoretical predictions.

To conclude this chapter, several recent experiments have attempted to measure δ_g with conflicting results [44, 149, 152]. Finite-frequency ΔT noise is thus well-placed, offering additional perspectives on measuring the scaling dimension of anyons in FQHE. Indeed, temperature-biased noise measurements are less "invasive" compared to voltage biased noise measurements, which could change the tunneling amplitudes of the QPC. At

the very least, finite-frequency ΔT noise is sensitive to anyonic scaling dimensions, even when it has been renormalized to higher values, as long as $\delta_{\boldsymbol{g}} < 1$.

Chapter 6.

Time-Domain Braiding

Starting from this chapter, we will delve into the most exotic and defining aspect of anyons: the fractional exchange or braiding phase. While braiding typically involves moving one anyon around another in 2D space, fractional quantum Hall edges equipped with quantum point contacts (QPCs) offer a more abstract method for this process. QPCs in the weak-backscattering regime bring together two edges of the FQHE, with a small region of the FQHE system lying between the edges. This setup allows anyons approaching the QPC (from an unspecified source) to braid with anyon-antianyon virtual excitations generated at the QPC. Unlike conventional anyon braiding in 2D space this process is more abstract. Conventional anyon braiding is not feasible in a 1D system like the FQHE edges. Instead, as discussed in this chapter, the time-ordering of incoming anyon relative to the anyon-antianyon pairs generated at the QPC effectively introduces a second dimension, allowing for braiding in $1 + 1$D.

This chapter primarily serves as a pedagogical introduction to the idea of time-domain braiding, originally developed by Refs. [86, 121] in the past decade. We start with a heuristic discussion of time-domain braiding processes. We illustrate how the equilibrium thermal noise of FQHE edges can be interpreted in terms of the spontaneous creation of virtual anyon-antianyon pairs at the QPC. We then explain how this thermal noise is modified by the arrival of an anyon at the QPC, highlighting the impact of the incoming anyon braiding with the virtual anyons generated at the QPC.

Having understood the key physical concepts, we generalize the discussion of time-domain braiding to general Abelian FQHE. Using the tunneling current as a concrete physical observable, we show how time-domain braiding generalizes to more complex situations where each FQHE edge carries multiple bosonic modes, and the QPCs allow tunneling of different types of anyons. This generalization sets the stage for the next chapters where we investigate realistic setups probing time-domain braiding processes, ultimately allowing us to measure the anyon braiding phase.

6.1. Heuristic discussion

In this section, we consider an FQHE system endowed with a QPC as shown in Figure 6.1. For the sake of conceptual clarity, we consider Laughlin fractions of the FQHE in this section such that only a single type of anyon tunnels across the QPC, and each edge of the FQHE is characterized by a single bosonic mode. The QPC brings the opposite edges of the FQHE close together, enabling anyon-antianyon pairs created in the bulk to tunnel to opposite edges. This spontaneous tunneling of anyon-antianyon pairs to opposite edges is described by the tunneling Hamiltonian discussed in Section 2.3:

$$\begin{aligned} H_T(t) &= \Gamma_{\boldsymbol{g}} \left(e^{i\boldsymbol{g}.\boldsymbol{\phi^u}(0,t) - i\boldsymbol{g}.\boldsymbol{\phi^d}(0,t)} + e^{-i\boldsymbol{g}.\boldsymbol{\phi^u}(0,t) + i\boldsymbol{g}.\boldsymbol{\phi^d}(0,t)} \right) \\ &\equiv \Gamma_{\boldsymbol{g}} \left[\psi^u_{\boldsymbol{g}}(0,t)\psi^{d\dagger}_{\boldsymbol{g}}(0,t) + \psi^d_{\boldsymbol{g}}(0,t)\psi^{u\dagger}_{\boldsymbol{g}}(0,t) \right] \\ &\equiv \mathcal{T}^\dagger(t) + \mathcal{T}(t), \end{aligned} \tag{6.1}$$

where $\Gamma_{\boldsymbol{g}}$ is the tunneling amplitude, $\boldsymbol{\phi^{u/d}} = (\phi^{u/d})$ is bosonic mode on the FQHE edge u/d, $\boldsymbol{g} = (\sqrt{\nu})$ is the vector indicating of the weight of each bosonic mode in the anyon operator. The notation introduced by the second and third lines of the above equation allows brevity in the forthcoming discussion. The tunneling current operator at the QPC can similarly be expressed as

$$I_T(t) = iq_{\boldsymbol{g}} \left(\mathcal{T}^\dagger - \mathcal{T} \right) \tag{6.2}$$

where $q_{\boldsymbol{g}}$ is the charge of the anyon.

Let us now calculate the noise on the edges due to the tunneling processes or anyon-antianyon creation events at the QPC. This quantity is expressed within the Keldysh formalism as

$$S = \int d(t_1 - t_2) \left\langle 0 \right| T_K \; \delta I_T(t_1^-) \delta I_T(t_2^+) e^{-i \int_K dt' H_T(t')} \left| 0 \right\rangle , \tag{6.3}$$

where $|0\rangle$ denotes the ground state of the bosonic edge theory, $\delta I_T = I_T - \langle I_T \rangle$, T_K denotes time ordering on the Keldysh contour, and subscript K on the integral denotes integration along the Keldysh contour. Without spending time on these details, at the lowest order in perturbation theory, the noise can be expressed as

$$S_0 = q_{\boldsymbol{g}}^2 \int d(t_1 - t_2) \left[\left\langle 0 \right| \mathcal{T}(t_2)\mathcal{T}^\dagger(t_1) \left| 0 \right\rangle + \left\langle 0 \right| \mathcal{T}^\dagger(t_2)\mathcal{T}(t_1) \left| 0 \right\rangle \right] , \tag{6.4}$$

where Keldysh time order has been imposed on the correlators, allowing us to get rid of the time-ordering symbol. The subscript 0 in S_0 indicates that the noise has been calculated on the ground state with no excitations.

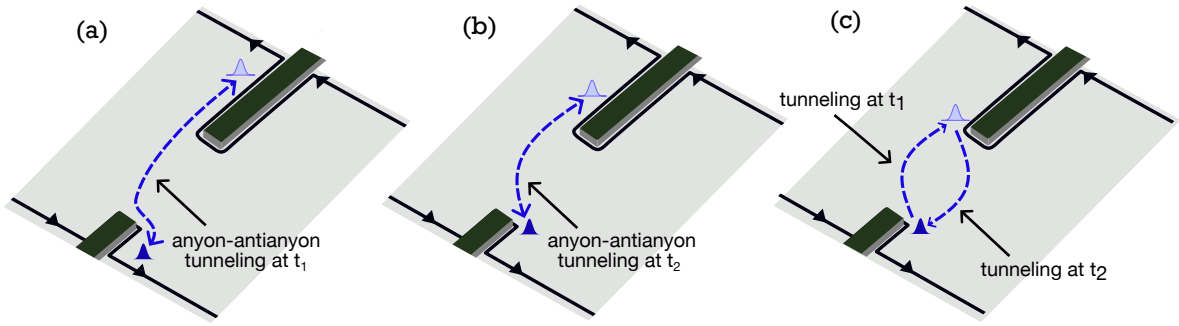


Figure 6.1.: Quantum point contacts bring two edges of the FQHE close, allowing tunneling of anyon-antianyon pairs from bulk into the edges. (a, b) Tunneling of anyon-antianyon pairs from bulk to the edges, where an anyon tunnels to the lower edge and an antianyon to the upper edge at the same time t_1/t_2 for process in $(a)/(b)$. (c) The overlap of the latter two processes. The anyons effectively jump between the edges at times t_1 and t_2, forming a loop as shown in the figure.

Akin to the noise above, all edge observables at the lowest order in perturbation theory involve the correlator $\langle 0|\,\mathcal{T}(t_2)\mathcal{T}^\dagger(t_1)\,|0\rangle$ (and its complex conjugate). It is hence prudent to understand this correlator in detail.

The above correlator can be interpreted as the overlap of two processes: $\mathcal{T}^\dagger(t_1)\,|0\rangle$ and $\mathcal{T}^\dagger(t_2)\,|0\rangle$. The process $\mathcal{T}^\dagger(t_1)\,|0\rangle$ denotes a pair creation event, where an anyon tunnels to the lower edge, and an antianyon to the upper edge, both at time t_1 as shown in Figure 6.1(a). The process $\mathcal{T}^\dagger(t_2)\,|0\rangle$ indicates a similar pair creation event, but at time t_2 as shown in Figure 6.1(b). The overlap between these two processes, forms a *loop in the time domain*, as shown in Figure 6.1(c).

Thus, the thermal noise in the quantum Hall edges

$$S_0 \sim \int d(t_1 - t_2) \left[\frac{\sinh(\pi T \tau_0)}{\sinh(\pi T(i\tau_0 - (t_1 - t_2)))}\right]^{2\delta_g} \tag{6.5}$$

obtained by evaluating the correlators in Equation (6.4) can be understood to be the consequence of time-domain loops formed by virtual anyon-antianyon pairs generated at the QPC, where T denotes the temperature of the system. As evidenced by the above expression, the overlap of the processes forming the time-domain loops is appreciable when $|t_1 - t_2| < 1/T$, and decays exponentially otherwise.

What happens to the noise if an anyon is incident on the QPC? We consider injecting an anyon on the upper edge (from an unspecified source), taken to reach the QPC at time

t_0. This modifies the quantum state of the bosonic edge theory. The state of the edge theory, with one anyon propagating on the upper edge, and reaching the QPC at time t_0 is written by augmenting the ground state with a single anyon operator:

$$|\varphi\rangle = \psi_{\boldsymbol{g}}^{u\dagger}(0,t_0)\,|0\rangle\,. \tag{6.6}$$

To understand the impact of the incoming anyon on observables such as current or noise, the averages must now be calculated on the above state. The noise due to one incoming anyon on the QPC can hence be expressed as:

$$\begin{aligned} S_1 = q_{\boldsymbol{g}}^2 \int d(t_1-t_2)\Big[&\langle 0|\,\psi_{\boldsymbol{g}}^{u}(0,t_0)\mathcal{T}(t_2)\mathcal{T}^\dagger(t_1)\psi_{\boldsymbol{g}}^{u\dagger}(0,t_0)\,|0\rangle \\ &+ \langle 0|\,\psi_{\boldsymbol{g}}^{u}(0,t_0)\mathcal{T}^\dagger(t_2)\mathcal{T}(t_1)\psi_{\boldsymbol{g}}^{u\dagger}(0,t_0)\,|0\rangle\Big] \\ &\equiv \int d(t_1-t_2)\left(\mathcal{B}+\mathcal{B}^\dagger\right). \end{aligned} \tag{6.7}$$

We emphasize the presence of the incoming anyon in the above expressions, indicated by the subscript 1 in S_1.

The first correlator in Equation (6.7) can again be interpreted as the overlap of two processes: $\mathcal{T}^\dagger(t_1)\psi_{\boldsymbol{g}}^{u\dagger}(0,t_0)\,|0\rangle$ and $\mathcal{T}^\dagger(t_2)\psi_{\boldsymbol{g}}^{u\dagger}(0,t_0)\,|0\rangle$. We argue that if the incoming anyon satisfies $t_0 \in [t_1,t_2]$, it braids with the anyon-antianyon pairs generated at the QPC.

Let us think of the composite processes occurring in the correlator to see if the above claim is sensible. Assume $t_1 < t_0 < t_2$ is satisfied. Then moving in the direction of increasing time, first at time t_1, an anyon-antianyon pair is created at the QPC with the anyon tunneling to the lower edge, and the antianyon to the upper edge. Subsequently, at time t_0, the anyon injected on the upper edge arrives as the QPC and continues propagating on the edge. At a yet later time t_2, another anyon-antianyon pair is generated at the QPC, with the anyon now tunneling to the upper edge, and the antianyon to the lower edge, thus annihilating the pairs created before. Within this composite process, the anyon injected on the upper edge goes through the braiding loop formed by the virtual anyon-antianyon pairs.

Hence, the time-domain braiding of incoming anyons with virtual anyon-antianyon pairs can be understood as the overlap of two different time-ordered processes:

1. Anyon arrives at the QPC after a pair creation event has occurred: $t_1 < t_0$. This process is written as $\mathcal{T}^\dagger(t_1)\psi_{\boldsymbol{g}}^{u\dagger}(t_0)\,|0\rangle$, and shown in Figure 6.2(a).

2. Anyon arrives at the QPC before a pair creation event has ocurred: $t_0 < t_2$. This process is written as $\mathcal{T}^\dagger(t_2)\psi_{\boldsymbol{g}}^{u\dagger}(t_0)\,|0\rangle$ and shown in Figure 6.2(b).

The overlap between these processes illustrated in Figure 6.2 leads to an explicit braiding of the anyons in the time domain, where the incoming anyon goes through the braiding loop formed by the tunneling anyons. On the other hand, if the time ordering $t_1 < t_0 < t_2$

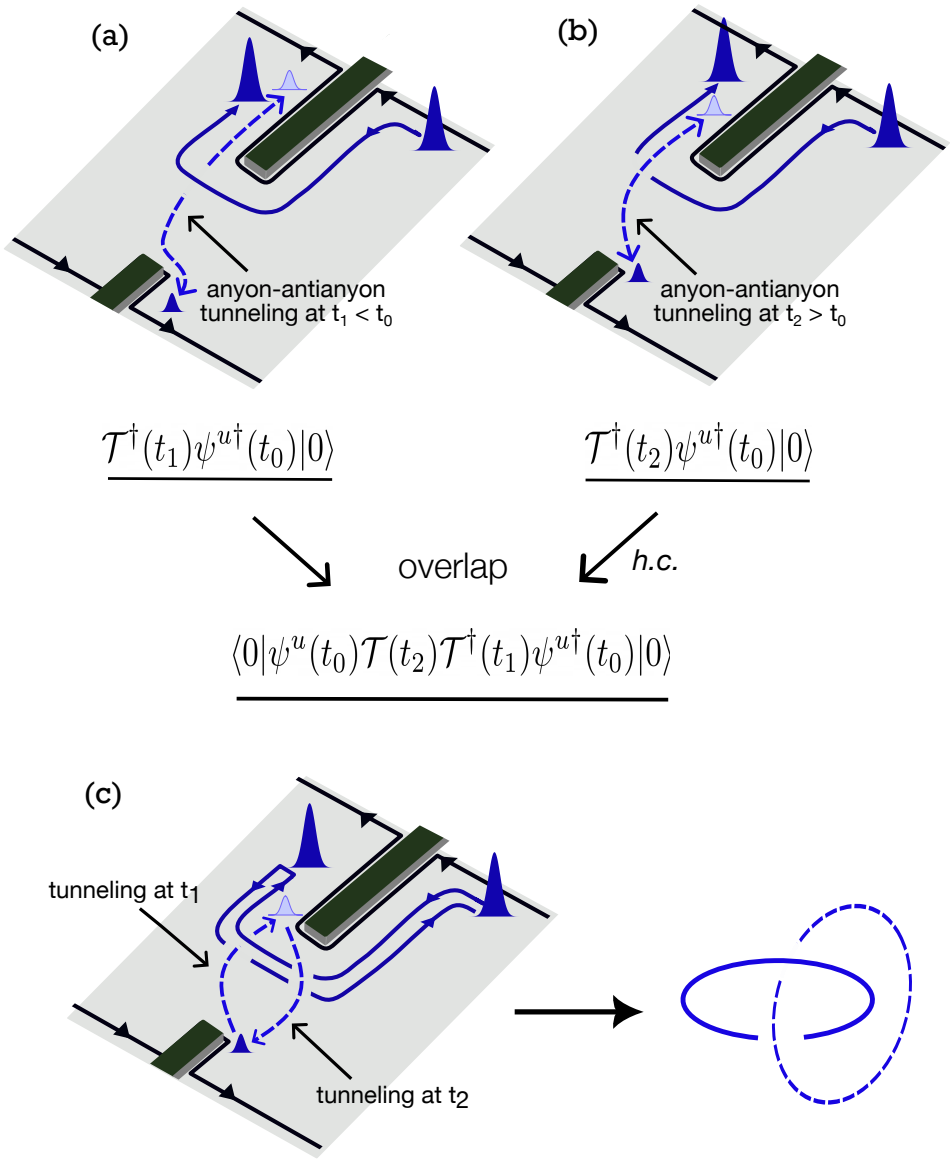


Figure 6.2.: Incoming anyon (path in solid blue line) braiding in the time-domain with anyon-antianyon pairs (path in dashed blue line) generated at the QPC. Dark blue excitations are anyons while pale blue excitation is antianyon. The incoming anyon travels along the upper edge and arrives at the QPC at time t_0. (a) Anyon-antianyon pair tunnels to the edges at time $t_1 < t_0$, before the incoming anyon passes the QPC. This is indicated by the dashed line going under the solid line. (b) Anyon-antianyon pair tunnels to the edges at time $t_2 > t_0$, after the incoming anyon passes the QPC. This is indicated by the dashed line going over the solid line. (c) The overlap of the latter two processes leads to a braiding loop of the incoming anyon with the anyon-antianyon pairs tunneling at the QPC. The parts of the loops traveling backward come from the second process which has been hermitian conjugated.

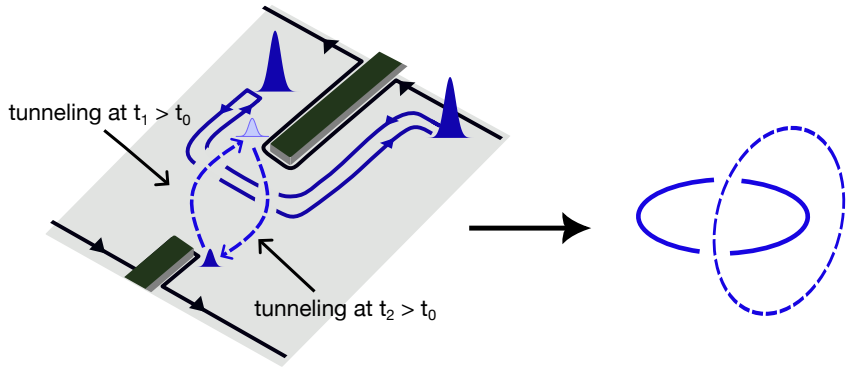


Figure 6.3.: Incoming anyon travels on the upper edge, arriving at the QPC at time t_0. Anyon-antianyon pairs are generated at the QPC at times t_1 and t_2, where $t_1, t_2 > t_0$. Since both tunneling events occur after the incoming anyon has passed through the QPC, the latter does not go through the loops formed by the tunneling anyons. Hence, there is no non-trivial braiding phase associated with this process.

(or $t_2 < t_0 < t_1$) is not satisfied, the incoming anyon does not go through the braiding loop formed by the tunneling anyons, as shown in Figure 6.3. As a result, there is no non-trivial fractional phase associated with these processes.

Mathematically, the time-domain processes described above can be seen quite simply. Consider the correlator $\mathcal{B}$ in Equation (6.7), expressed explicitly here for the sake of clarity:

$$\mathcal{B} = \langle 0| \psi^u_{\boldsymbol{g}}(0,t_0)\psi^d_{\boldsymbol{g}}(0,t_2)\psi^{u\dagger}_{\boldsymbol{g}}(0,t_2)\psi^u_{\boldsymbol{g}}(0,t_1)\psi^{d\dagger}_{\boldsymbol{g}}(0,t_1)\psi^{u\dagger}_{\boldsymbol{g}}(0,t_0)\,|0\rangle\,. \tag{6.8}$$

The injected anyon operators (those to the extreme left and right) can be annihilated by exchanging them across the tunneling terms of the QPC (the four anyon operators in the center). Doing this, we find:

$$\mathcal{B} = e^{i\pi\lambda_{\boldsymbol{gg}}[\mathrm{sgn}(t_1-t_0)-\mathrm{sgn}(t_2-t_0)]}\,\langle 0|\,\mathcal{T}(t_2)\mathcal{T}^\dagger(t_1)\,|0\rangle\,, \tag{6.9}$$

where $\lambda_{\boldsymbol{gg}} = \boldsymbol{g}.\boldsymbol{g}$ gives the exchange phase of the anyons. In the above equation, we have employed the Baker-Campbell-Hausdorff identities, and the commutation relation of the bosonic fields:

$$\left[\phi^{u/d}_j(x,t), \phi^{u/d}_k(x',t')\right] = i\chi_j\pi\delta_{jk}\mathrm{Sgn}(X_j - X'_k), \tag{6.10}$$

where $X_j = v_j t - \chi_j x$. The exponential phase factor in Equation (6.9) becomes $e^{\pm 2i\pi\lambda_{\boldsymbol{gg}}}$ for $t_1 < t_0 < t_2$ or $t_2 < t_0 < t_1$, giving the braiding phase of injected anyon with the virtual anyons created at the QPC. On the other hand, the phase factor is trivial if t_0

does not satisfy the latter conditions, as expected from the discussion in the preceding paragraphs.

Time-domain braiding of the injected anyon with the virtual anyons produces an excess noise ΔS over the equilibrium noise S_0, defined as:

$$\Delta S = S_1 - S_0. \tag{6.11}$$

Following simple calculations which we skip here, the excess noise can be shown to take the form

$$\Delta S \sim \int d(t_1 - t_2) \left\{ \cos\left(\pi \lambda_{\boldsymbol{gg}} \left[\mathrm{sgn}(t_1 - t_0) - \mathrm{sgn}(t_2 - t_0)\right]\right) - 1 \right\} \left[\frac{\sinh\left(\pi T \tau_0\right)}{\sinh\left(\pi T (i\tau_0 - (t_1 - t_2))\right)} \right]^{2\delta_{\boldsymbol{g}}}. \tag{6.12}$$

From the above expression, we make two important observations. In the absence of time-domain braiding processes, that is $t_0 \notin [t_1, t_2]$, the excess noise is zero. This is not surprising since in the absence of braiding, no extra noise is created by the propagation of the anyon alone.

Importantly, time-domain braiding processes exist only for anyons. For fermions and bosons we have $\lambda_{\boldsymbol{gg}} = 0$ or 1. The cosine returns a unit value, yielding a zero excess noise. This indicates the absence of any non-trivial process apart from creation of particle-hole pairs, leading to the equilibrium noise. For fermions and bosons, the time domain braiding loops between incoming and tunneling particles are trivially unlinked from each other [11, 121].

It is important to note the distinction between braiding of anyons as conventionally understood, and the time-domain braiding processes described here. Speaking of anyon braiding in 2D space, we think of having explicit control over the movement of anyons – they can be thought to be trapped within potential wells that are under experimental control. Thus, the dynamics of anyons are not important in this context. In contrast, the time-domain braiding processes described here depend explicitly on the dynamics of the tunneling anyons. While the anyon injected on the edge was assumed to be under control with a specified time of arrival at the QPC (will be relaxed in the next chapter), one has no control whatsoever on the tunneling processes at the QPC – it depends on the correlation function at the QPC. The anyon pair creation events are spontaneous, occurring at all times at the QPC. Hence the incoming anyon may or may not pass a braiding loop, and in full generality one has both braiding ($t_0 \in [t_1, t_2]$) and non-braiding ($t_0 \notin [t_1, t_2]$) processes simultaneously occurring at the QPC.

6.2. Tunneling current: single anyon in general Abelian FQHE

The previous section heuristically discussed the time-domain braiding process, with an emphasis on clarifying the physical idea. In this section, the aim is to illustrate time-domain braiding with rigorous calculations of FQHE edge theory. Moreover, we show how time-domain braiding naturally generalizes to arbitrary Abelian FQHE, which admits multiple bosonic modes on the edge, different types of anyons, and all of which are expected to simultaneously tunnel at QPCs.

Before jumping into the calculations, it is worth understanding the idea behind the generalization. Generalization of time-domain braiding to arbitrary Abelian FQHE relies on the physics depicted in Figure 6.4 for a two bosonic mode edge theory. In general Abelian FQHE, both the incoming and the tunneling anyons are composed of excitations on all the bosonic modes. The different bosonic modes, and their excitations are indicated by red and blue colors in Figure 6.4. All the excitations composing the incoming anyon travel towards the QPC, reaching there at time t_0. As discussed in Section 6.1, the pair creation events at the QPC could have two possibilities. (i) The anyon-antianyon pair, now composed of excitations on all the bosonic modes, tunnels to the edge before the incoming anyon has passed the QPC, as shown in Figure 6.4(a). (ii) The anyon-antianyon pair, tunnels to the edge after the incoming anyon has passed the QPC, as shown in Figure 6.4(b). The overlap of these processes, shown in Figure 6.4(c) forms a braiding loop in time: where the full incoming anyon (both red and blue excitations) goes through the loops formed by the full anyon-antianyon pairs (again, both red and blue excitations). However, since the red and blue bosonic modes are independent of one another, their braiding loops decouple. The total braiding phase is hence the product of the phase resulting from the braiding of red excitations and the phase from the blue excitations.

The key complexity in generalizing time-domain braiding to arbitrary FQHE lies in the fact that a generic anyon now comprises excitations across all bosonic modes. Nevertheless, as long as the bosons remain independent, the total braiding phase is simply the product of the braiding phases of the excitations on individual bosonic modes.

It is now time to dive into the mathematics. Our theoretical investigation will focus on the tunneling current at the quantum point contact (QPC), a tangible physical observable. We will demonstrate how it responds to the time-domain braiding of anyons, revealing the underlying physics.

The system we consider is the same as that depicted in Figure 6.4: general Abelian FQHE bar, endowed with a QPC. Each edge comprises N bosonic modes. The free

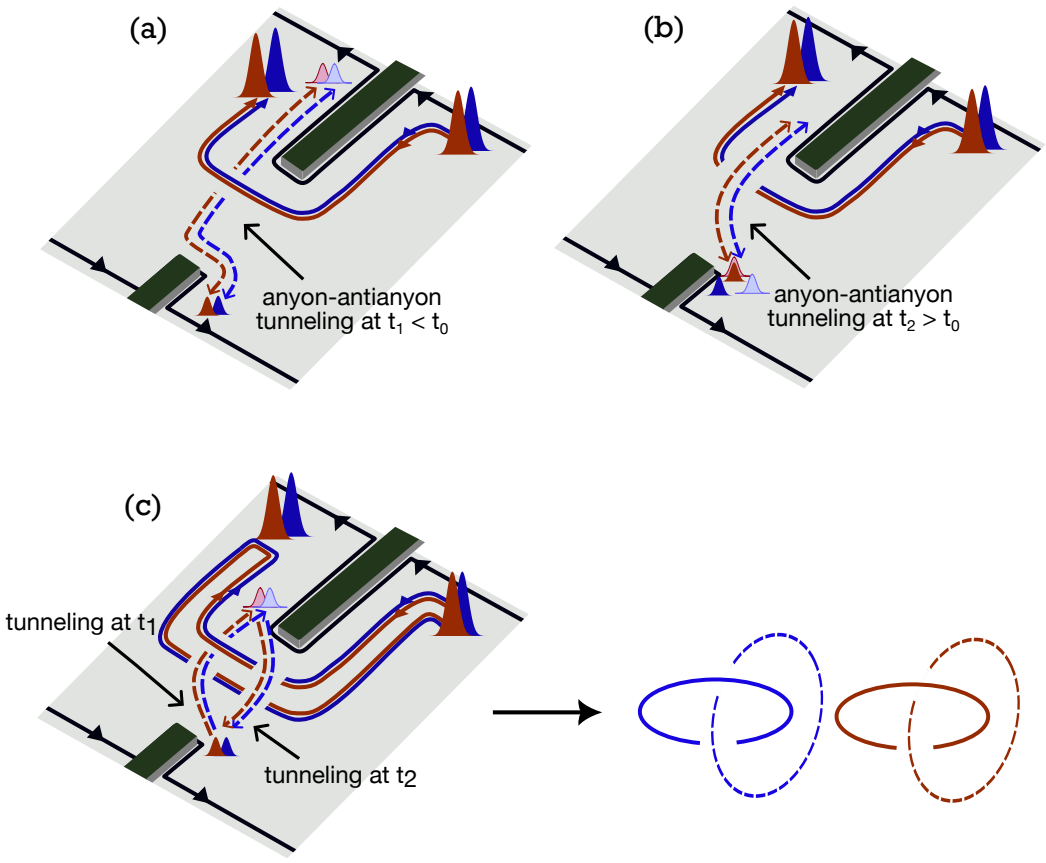


Figure 6.4.: Time-domain braiding of anyons in FQHE with two independent bosonic modes on each edge. The different bosonic modes are indicated in red and blue. A generic anyon is composed of excitations on both bosonic mode, indicated in dark red or blue (anyons) and pale red or blue (antianyons). The incoming anyon, indicated by large dark red and blue excitations travels along the upper edge, following the solid red and blue lines, arriving at the QPC at time t_0. Anyon-antianyon pairs (small excitations) tunnel at the QPC, with paths in dashed red and blue lines. (a) Anyon-antianyon pairs, now comprising excitations on both bosonic modes, tunnel at time $t_1 < t_0$, before the incoming anyon has arrived at the QPC. (b) Anyon-antianyon pairs, tunnel at time $t_2 > t_0$, after the incoming anyon has arrived at the QPC. (c) Overlap between the latter two processes leads to a braiding loop of the full incoming anyon (both red and blue excitations) with the full tunneling anyon pairs (again, both red and blue excitations). However, the red and blue bosonic modes are independent, and hence their braiding loops decouple. The full braiding phase is a product of the braiding phases of excitations on individual bosonic modes.

Hamiltonian describing this system is:

$$H_0 = \sum_{j=1}^{N} \frac{v_j}{4\pi} \int dx \left[(\partial_x \phi_j^u(x,t))^2 + (\partial_x \phi_j^d(x,t))^2 \right] \tag{6.13}$$

where v_j is the propagation velocity of the $j-$th bosonic mode, and the boson fields obey commutation relations

$$\left[\phi_j^{u/d}(x,t), \phi_m^{u/d}(x',t') \right] = i\chi_j \pi \delta_{jm} \text{Sign}(X_j - X'_m), \tag{6.14}$$

where χ_j denotes the chirality of the $j-$th bosonic mode, and $X_j = v_j t - \chi_j x$.

The QPC, located at $x = 0$, is thought to admit tunneling of anyons between the edges. As a general Abelian FQHE admits different anyons that are all expected to tunnel simultaneously at the QPC, the tunneling Hamiltonian comprises a sum over several anyon-antianyon pair creation terms, as discussed in Section 2.3:

$$H_T(t) = \sum_{\alpha} \Gamma_{\boldsymbol{g}_\alpha} \left(e^{i\boldsymbol{g_\alpha}.\boldsymbol{\phi^u}(0,t) - i\boldsymbol{g_\alpha}.\boldsymbol{\phi^d}(0,t)} + e^{-i\boldsymbol{g_\alpha}.\boldsymbol{\phi^u}(0,t) + i\boldsymbol{g_\alpha}.\boldsymbol{\phi^d}(0,t)} \right), \tag{6.15}$$

where sum over α runs over the different anyons, $\Gamma_{\boldsymbol{g}_\alpha}$ denotes the tunneling amplitude of type$-\alpha$ anyon, $\boldsymbol{g_\alpha} = (g_{\alpha 1}, \ldots, g_{\alpha N})$ denotes the anyon vector of type$-\alpha$ anyons, and $\boldsymbol{\phi^{u/d}} = (\phi_1^{u/d}, \ldots, \phi_N^{u/d})$. Similarly, the tunneling current operator is given by

$$I_T(t) = \sum_{\alpha} i q_{\boldsymbol{g}_\alpha} \Gamma_{\boldsymbol{g}_\alpha} \left(e^{i\boldsymbol{g_\alpha}.\boldsymbol{\phi^u}(0,t) - i\boldsymbol{g_\alpha}.\boldsymbol{\phi^d}(0,t)} - e^{-i\boldsymbol{g_\alpha}.\boldsymbol{\phi^u}(0,t) + i\boldsymbol{g_\alpha}.\boldsymbol{\phi^d}(0,t)} \right). \tag{6.16}$$

Given the particle-hole symmetry of these terms, it is obvious that the average tunneling current calculated on the ground state of the edge theory would be zero. Let us hence consider that a single anyon is injected on the upper edge. Importantly, since the edge admits different anyons, we assume that the injected anyon carries a probability amplitude of each anyon type. The state with such an anyon on the upper edge is expressed as:

$$|\varphi\rangle \equiv \sum_{\beta} p_{\boldsymbol{g_\beta}} e^{-i\boldsymbol{g_\beta}.\boldsymbol{\phi^u}(-\mathcal{L}, -\mathcal{T})} |0\rangle \tag{6.17}$$

where $p_{\boldsymbol{g_\beta}}$ is the probability amplitude that the anyon arriving at the QPC is of type$-\beta$. The anyon is assumed to have been injected on the upper edge, at position $-\mathcal{L}$ far to the left of the QPC, and at time $-\mathcal{T}$ far in the past. It is important to note here that while we do not specify a source here, known sources of anyons (such as an upstream QPC) cannot create a state where the different anyon types are in a superposition. Rather, the source state is a density matrix in the anyon type space with only the diagonal carrying non-zero values $|p_{\boldsymbol{g_\beta}|^2}$, and all the non-diagonal elements being zero. For the sake of notational convenience in the forthcoming calculations, we specify the incoming state as in Equation (6.17), but the off-diagonal overlaps will always taken to be zero.

A generic anyon $\psi_{\boldsymbol{g_\alpha}} = e^{i\sum_j g_{\alpha j}\phi_j}$ in any Abelian FQHE comprises excitations over all the bosonic modes of the theory, as indicated by the sum in the exponential. These bosonic modes may have different propagation velocities v_j or even different chiralities χ_j. At the moment of injection $-\mathcal{T}$, we assume that the excitations $e^{ig_{\alpha j}\phi_j}$ on the $j-$th bosonic mode are bound together at spatial location $-\mathcal{L}$ to form the anyon $\psi_{\boldsymbol{g_\alpha}}$. However, after this moment the individual excitations propagate independently, depending on the properties of the respective bosonic mode. Most importantly, excitations on $\chi_j = +1$ bosons propagate towards the QPC, while those on $\chi_j = -1$ bosons propagate away from the QPC. The excitations propagating towards the QPC arrive at the location of the QPC ($x = 0$) at a time $t_0 = -\mathcal{T} + \mathcal{L}/v_j$. Although in full generality the bosonic modes can have different velocities, leading to different arrival times for excitations on different bosonic modes, this would not change our discussion as long as the time delay between excitations arriving at the QPC is negligible compared to the thermal timescale ($|\frac{\mathcal{L}}{v_i} - \frac{\mathcal{L}}{v_j}| \ll 1/T$). On the other hand, it should be clear that the excitations propagating away from the QPC never reach the QPC. We will show explicitly that there is no braiding contribution related to the latter excitations.

To start calculating the average tunneling current, we express it in the Keldysh formalism as:

$$\langle I_T(t_1)\rangle = \frac{1}{2}\langle\varphi|\sum_{\eta_1} I_T(t_1^{\eta_1})\; e^{-i\int_K dt_2 H_T(t_2)}\,|\varphi\rangle \tag{6.18}$$

where the average is taken over the state containing one anyon. The expression is normalized with $\langle\varphi|\varphi\rangle$. At lowest order in the tunneling amplitudes $\Gamma_{\boldsymbol{g}_\alpha}$, we can express the average tunneling current as

$$\begin{aligned}\langle I(t_1)\rangle = \sum_\alpha \frac{q_{\boldsymbol{g}_\alpha}|\Gamma_{\boldsymbol{g}_\alpha}|^2}{2}\sum_\beta P_{\boldsymbol{g_\beta}}\sum_\epsilon \epsilon \sum_{\eta_1\eta_2}\eta' \int dt_2 \\ \langle 0|\,T_K\; e^{i\boldsymbol{g_\beta}\cdot\boldsymbol{\phi^u}(-\mathcal{L},-\mathcal{T}^-)} e^{i\epsilon\boldsymbol{g_\alpha}\cdot\boldsymbol{\phi^u}(0,t_1^{\eta_1})} e^{-i\epsilon\boldsymbol{g_\alpha}\cdot\boldsymbol{\phi^d}(0,t_1^{\eta_1})} \\ e^{i\epsilon\boldsymbol{g_\alpha}\cdot\boldsymbol{\phi^d}(0,t_2^{\eta_2})} e^{-i\epsilon\boldsymbol{g_\alpha}\cdot\boldsymbol{\phi^u}(0,t_2^{\eta_2})} e^{-i\boldsymbol{g_\beta}\cdot\boldsymbol{\phi^u}(-\mathcal{L},-\mathcal{T}^+)}\,|0\rangle\,,\end{aligned} \tag{6.19}$$

where $P_{\boldsymbol{g_\beta}} = |p_{\boldsymbol{g_\beta}}|^2$. The injected anyons have been taken into the Keldysh time-ordering such that the original ordering is respected, in order to use Wick's theorem. Given the proliferation of sums in the above expression, it is instructive to break it down. The sum over η_1, η_2 runs over the Keldysh indices of the tunneling times of anyons in the QPC. The sum over ϵ takes care of Hermitian conjugate processes at the QPC. The sum on α runs over all the types of anyons that are generated at the QPC, while the sum over β, γ runs over the types of anyons injected on the edge.

Since the upper and lower edges are independent, we can separate the bosonic correlator in the above expression into two correlators, one over each edge:

$$\begin{aligned}\langle I_T(t_1)\rangle = \sum_\alpha \frac{q_{\boldsymbol{g}_\alpha}|\Gamma_{\boldsymbol{g}_\alpha}|^2}{2}\sum_\beta P_{\boldsymbol{g}_{\boldsymbol{\beta}}}\sum_\epsilon \epsilon \sum_{\eta_1\eta_2}\eta_2\int dt_2 \\ \prod_{j=1}^{N}\langle 0|\, T_K\; e^{ig_{\beta j}\phi_j^u(-\mathcal{L},-\mathcal{T}^-)}e^{i\epsilon g_{\alpha j}\phi_j^u(0,t_1^{\eta_1})}e^{-i\epsilon g_{\alpha j}\phi_j^u(0,t_2^{\eta_2})}e^{-ig_{\beta j}\phi_j^u(-\mathcal{L},-\mathcal{T}^+)}\,|0\rangle \\ \times\langle 0|\, T_K\; e^{-i\epsilon g_{\alpha j}\phi_j^d(0,t_1^{\eta_1})}e^{i\epsilon g_{\alpha j}\phi_j^d(0,t_2^{\eta_2})}\,|0\rangle\,,\end{aligned} \tag{6.20}$$

where we have also written out the individual bosonic fields explicitly. In the above expression, it is understood that the averages are over ground states of the respective bosonic fields. These correlation functions can be evaluated using the identity:

$$\left\langle T_K\left\{\prod_{s=1}^{n} e^{a_s\phi_j^{u/d}\left(x_s,t_s^{\eta_s}\right)}\right\}\right\rangle = \exp\left[\sum_{s=1}^{n}\sum_{p=s+1}^{n} a_s a_p\; \mathcal{G}_j^{\eta_s\eta_p}(x_s-x_p,t_s-t_p)\right], \tag{6.21}$$

which is non-zero only when $\sum_s a_s = 0$. $\mathcal{G}_j^{\eta_1\eta_2}(x,t)$ denotes the Keldysh bosonic Greens function of the $j-$th bosonic mode, given at finite temperature by:

$$\mathcal{G}^{\eta_1\eta_2}(x,\tau) = \log\left(\frac{\sinh(i\pi T\tau_0)}{\sinh\left[\pi T\left(i\tau_0-\sigma_{\eta_1\eta_2}(\tau)(\tau-\chi_j x/v_j)\right)\right]}\right), \tag{6.22}$$

where

$$\sigma_{\eta_1\eta_2}(t) = \frac{1}{2}\left[(\eta_2-\eta_1)+\mathrm{sgn}(t)(\eta_1+\eta_2)\right]. \tag{6.23}$$

Evaluating the correlators in Equation (6.20) using above identities, we immediately find that for the upper edge correlators to be non-vanishing, $\beta=\gamma$ is imposed, getting rid of one of the sums. This means that the overlap of the time-ordered processes is non-vanishing only when the incoming anyons are the same in the bra and ket of the augmented state. Hence, we can further express the average tunneling current in terms of the Greens functions as:

$$\begin{aligned}\langle I(t_1)\rangle = \sum_\alpha \frac{q_{\boldsymbol{g}_\alpha}|\Gamma_{\boldsymbol{g}_\alpha}|^2}{2}\sum_\epsilon \epsilon \sum_{\eta_1\eta_2}\eta_2\int dt_2 \\ \prod_{j=1}^{N} e^{2g_{\alpha j}^2\mathcal{G}_j^{\eta_1\eta_2}(0,t_1-t_2)}\sum_\beta P_{\boldsymbol{g}_{\boldsymbol{\beta}}}\left[\frac{e^{g_{\alpha j}g_{\beta j}\mathcal{G}_j^{\eta_1+}(\mathcal{L},\; t_1+\mathcal{T})}}{e^{g_{\alpha j}g_{\beta j}\mathcal{G}_j^{-\eta_1}(-\mathcal{L},-t_1-\mathcal{T})}}\frac{e^{g_{\alpha j}g_{\beta j}\mathcal{G}_j^{-\eta_2}(-\mathcal{L},-t_2-\mathcal{T})}}{e^{g_{\alpha j}g_{\beta j}\mathcal{G}_j^{\eta_2+}(\mathcal{L},\; t_2+\mathcal{T})}}\right]^{\epsilon}.\end{aligned} \tag{6.24}$$

We note that the first term on the second line of Equation (6.24) is related to a two-point correlation function where both anyon operators come from the QPC tunneling Hamiltonian. It is thus a term that describes the local dynamics of the QPC. On the other

hand, the Greens functions within the square brackets are related to two-point functions where one of the anyons comes from the QPC tunneling Hamiltonian, while the other anyon is the one we inject on the edge. There should hence be no doubt that any physics where the injected anyon interacts non-trivially with the tunneling anyons lies in this term.

To continue with the calculation, we assume that the anyon is injected in the distant past, that is, $\mathcal{T} \to \infty$. Then, from Equation (6.23), it is clear that $\sigma_{\eta_1+}(t_1+\mathcal{T}) = \sigma_{\eta_2+}(t_2+\mathcal{T}) = \sigma_{-\eta_1}(-t_1-\mathcal{T}) = \sigma_{-\eta_2}(-t_2-\mathcal{T}) = 1$. We note here that the preceding assumption is avoided by employing a four-branch contour, discussed in Appendix F, instead of the standard two-branch Keldysh contour discussed in Section 2.3.5. Nevertheless, it is reassuring that the two approaches give the same results which reads:

$$\begin{aligned}\langle I(t)\rangle = \sum_{\alpha} \frac{q_{\boldsymbol{g}_\alpha}|\Gamma_{\boldsymbol{g}_\alpha}|^2}{2} \sum_{\beta} P_{\boldsymbol{g}\boldsymbol{\beta}} \sum_{\epsilon} \epsilon \sum_{\eta_1\eta_2} \eta_2 \int dt_2 \\ \prod_{j=1}^{N} e^{2g_{\alpha j}^2 \mathcal{G}_j^{\eta_1\eta_2}(0,t_1-t_2)} \sum_{\beta} P_{\boldsymbol{g}\boldsymbol{\beta}} \left[\frac{e^{g_{\alpha j}g_{\beta j}\mathcal{G}_j(\mathcal{L},\ t_1+\mathcal{T})}}{e^{g_{\alpha j}g_{\beta j}\mathcal{G}_j(-\mathcal{L},-t_1-\mathcal{T})}} \frac{e^{g_{\alpha j}g_{\beta j}\mathcal{G}_j(-\mathcal{L},-t_2-\mathcal{T})}}{e^{g_{\alpha j}g_{\beta j}\mathcal{G}_j(\mathcal{L},\ t_2+\mathcal{T})}} \right]^{\epsilon}\end{aligned} \tag{6.25}$$

where $\mathcal{G}_j(x,t) \equiv \mathcal{G}_j^{-+}(x,t)$. It is now useful to separate the bosonic modes with different chiralities. Of the N bosonic modes, let M have a chirality $\chi_j = +1$, and the remaining have $\chi_j = -1$. As seen in Equation (6.22) the chirality decides the combination of spatial and temporal arguments that enters the Greens function. We hence find:

$$\begin{aligned}\langle I_T(t_1)\rangle = \sum_{\alpha} \frac{q_{\boldsymbol{g}_\alpha}|\Gamma_{\boldsymbol{g}_\alpha}|^2}{2} \sum_{\epsilon} \epsilon \sum_{\eta_1\eta_2} \eta_2 \int dt_2 \\ \times \sum_{\beta} P_{\boldsymbol{g}\boldsymbol{\beta}} \prod_{j=1}^{M} e^{2g_{\alpha j}^2 \mathcal{G}_j^{\eta_1\eta_2}(t_1-t_2)} \left[\frac{e^{g_{\alpha j}g_{\beta j}\mathcal{G}_j(t_1+\mathcal{T}-\mathcal{L}/v_j)}}{e^{g_{\alpha j}g_{\beta j}\mathcal{G}_j(-t_1-\mathcal{T}+\mathcal{L}/v_j)}} \frac{e^{g_{\alpha j}g_{\beta j}\mathcal{G}_j(-t_2-\mathcal{T}+\mathcal{L}/v_j)}}{e^{g_{\alpha j}g_{\beta j}\mathcal{G}_j(t_2+\mathcal{T}-\mathcal{L}/v_j)}} \right]^{\epsilon} \\ \times \prod_{j=M+1}^{N} e^{2g_{\alpha j}^2 \mathcal{G}_j^{\eta_1\eta_2}(t_1-t_2)} \left[\frac{e^{g_{\alpha j}g_{\beta j}\mathcal{G}_j(t_1+\mathcal{T}+\mathcal{L}/v_j)}}{e^{g_{\alpha j}g_{\beta j}\mathcal{G}_j(-t_1-\mathcal{T}-\mathcal{L}/v_j)}} \frac{e^{g_{\alpha j}g_{\beta j}\mathcal{G}_j(-t_2-\mathcal{T}-\mathcal{L}/v_j)}}{e^{g_{\alpha j}g_{\beta j}\mathcal{G}_j(\ t_2+\mathcal{T}+\mathcal{L}/v_j)}} \right]^{\epsilon},\end{aligned} \tag{6.26}$$

where without loss of generality, the second line contains Greens functions of all bosonic modes with $\chi_j = +1$ whose excitations propagate towards the QPC, and the third line, those with $\chi_j = -1$ whose excitations propagate away from the QPC.

The ratio of the Greens functions appearing inside the square brackets in the above equation assumes a simple value in the limit $\tau_0 \to 0$. This value can be extracted with a

careful treatment of the branch cut. Using Equation (6.22), we find:

$$\begin{aligned}
&\frac{e^{g_{\alpha j}g_{\beta j}\mathcal{G}_j^u(-z)}}{e^{g_{\alpha j}g_{\beta j}\mathcal{G}_j^u(+z)}} \\
&= \left[\frac{\sinh(i\pi T\tau_0)}{\sinh(\pi T(i\tau_0+z))}\right]^{g_{\alpha j}g_{\beta j}} \left[\frac{\sinh(\pi T(i\tau_0-z))}{\sinh(i\pi T\tau_0)}\right]^{g_{\alpha j}g_{\beta j}} \\
&= \left[\frac{\mathrm{sgn}(z)\,\sinh(i\pi T\tau_0)}{\sinh(\pi T(|z|+i\tau_0\mathrm{sgn}(z)))}\right]^{g_{\alpha j}g_{\beta j}} \left[\frac{\sinh(\pi T(|z|-i\tau_0\mathrm{sgn}(z)))}{-\mathrm{sgn}(z)\,\sinh(i\pi T\tau_0)}\right]^{g_{\alpha j}g_{\beta j}} \\
&\xrightarrow{\tau_0\to 0} [i\mathrm{sgn}(z)]^{g_{\alpha j}g_{\beta j}}\,[-i\mathrm{sgn}(z)]^{-g_{\alpha j}g_{\beta j}} \\
&= e^{i\pi g_{\alpha j}g_{\beta j}\mathrm{sgn}(z)}
\end{aligned} \tag{6.27}$$

Employing the above result in the tunneling current, and summing over the Keldysh indices of the QPC tunneling times, we obtain:

$$\begin{aligned}
\langle I_T(t_1)\rangle = \sum_\alpha q_{\boldsymbol{g}_\alpha}|\Gamma_{\boldsymbol{g}_\alpha}|^2 \sum_\epsilon \epsilon \int_{-\infty}^{t_1} dt_2 \left(e^{2\delta_{\boldsymbol{g}_\alpha}\mathcal{G}(t_1-t_2)} - e^{2\delta_{\boldsymbol{g}_\alpha}\mathcal{G}(t'-t)}\right) \\
\times \sum_\beta P_{\boldsymbol{g}_\beta} \prod_{j=1}^{M} e^{-i\pi\epsilon g_{\alpha j}g_{\beta j}[\mathrm{sgn}(t_1+\mathcal{T}-\mathcal{L}/v_j)-\mathrm{sgn}(t_2+\mathcal{T}-\mathcal{L}/v_j)]} \\
\times \prod_{j=M+1}^{N} e^{-i\pi\epsilon g_{\alpha j}g_{\beta j}[\mathrm{sgn}(t_1+\mathcal{T}+\mathcal{L}/v_j)-\mathrm{sgn}(t_2+\mathcal{T}+\mathcal{L}/v_j)]}
\end{aligned} \tag{6.28}$$

Recall that we work in the limit $\mathcal{T},\mathcal{L}\to\infty$, such that $-\mathcal{T}+\mathcal{L}/v_j = t_0$, the arrival time of the ($\chi_j = +1$) anyon excitations on the QPC. This means the exponential in the second line above can assume non-trivial values depending on the interplay between the times t_1, t_2, and t_0, yielding the braiding phase of the incoming anyon with the tunneling ones. On the other hand, the factor $\mathcal{T}+\mathcal{L}/v_j$ is always very large and positive in the limit we consider. Hence, two sign functions in the exponential on the third line always cancel each other out, irrespective of the times t_1, t_2 and the third line always yields 1. This should not be surprising since the third line corresponds to the braiding phase of excitations that propagate away from the QPC – they never arrive at the QPC and hence do not braid with the anyon pairs generated there. We can hence express the average tunneling current as:

$$\begin{aligned}
\langle I_T(t_1)\rangle = \sum_\alpha q_{\boldsymbol{g}_\alpha}|\Gamma_{\boldsymbol{g}_\alpha}|^2 \sum_\epsilon \epsilon \int_{-\infty}^{t_1} dt_2 \left(e^{2\delta_{\boldsymbol{g}_\alpha}\mathcal{G}(t_1-t_2)} - e^{2\delta_{\boldsymbol{g}_\alpha}\mathcal{G}(t'-t)}\right) \\
\times \sum_\beta P_{\boldsymbol{g}_\beta} e^{-i\pi\epsilon\boldsymbol{g}_\alpha\cdot\boldsymbol{g}_\beta[\mathrm{sgn}(t-t_0)-\mathrm{sgn}(t'-t_0)]},
\end{aligned} \tag{6.29}$$

where it is now implied that the dot product $\boldsymbol{g_\alpha}.\boldsymbol{g_\beta}$ now runs only over the bosonic modes that propagate towards the QPC. It thus gives a partial braiding statistics of the incoming anyon with those generated at the QPC. Only the excitations propagating towards the QPC braid with the excitations generated at the QPC, on the corresponding bosonic modes. Of course, for fully chiral systems, the dot product contains all bosonic modes on the edge, giving the full braiding statistics of the incoming anyons with the anyons tunneling at the QPC, $\lambda_{\boldsymbol{g_\alpha} \boldsymbol{g_\beta}}$. Thus, we will henceforth always refer to the braiding phase $\lambda_{\boldsymbol{g_\alpha} \boldsymbol{g_\beta}}$ with the above caveat in mind.

Importantly, Equation (6.29) involves two crucial summations: one over α, representing all possible types of anyon pairs generated at the QPC, and another over β, representing the type of the injected anyon. The braiding of these different anyon types is illustrated in Figure 6.5 where two distinct types of anyons are symbolized by a *shuriken* (star) and a *kunai* (blade). The incoming anyon, indexed by α can be either a shuriken or a kunai; the tunneling anyons indexed by β can also take either form.

The overall braiding phase is a weighted sum over all the different possible braidings shown in Figure 6.5. The weights are determined by the probability P_β that indicates whether the incoming anyon is a shuriken or a kunai. Similarly, the tunneling amplitudes $|\Gamma_{\boldsymbol{g_\alpha}}|^2$ contain the relative probability of type$-\alpha$ anyon tunneling at the QPC, telling us whether a shuriken or a kunai tunnels at the QPC. Crucially, as explained in Figure 6.4 and the preceding paragraph, the excitations of the incoming anyon (of any type) on a given bosonic mode, braids with the excitations of tunneling anyon-antianyon (of any type) on the same bosonic mode. In other words, red incoming excitations braid only with red tunneling excitations, and the same holds for the blue excitations

Finally, summing over ϵ, we arrive at the following expression for the tunneling current:

$$\begin{aligned}\langle I_T(t_1)\rangle = \sum_{\alpha\beta} 2q_{\boldsymbol{g_\alpha}} |\Gamma_{\boldsymbol{g_\alpha}}|^2 P_{\boldsymbol{g_\beta}} \sin\left(2\pi \boldsymbol{g_\alpha}.\boldsymbol{g_\beta}\right) \theta(t_1 - t_0) \\ \int_{-\infty}^{t_1} dt_2 i\theta(t_0 - t_2) \left(e^{2\delta_{\boldsymbol{g_\alpha}} \mathcal{G}(t_1 - t_2)} - e^{2\delta_{\boldsymbol{g_\alpha}} \mathcal{G}(t_2 - t_1)}\right).\end{aligned} \tag{6.30}$$

To explain the above expression, first, the θ function outside the integral implies that the current is non-zero only after the quasiparticle has arrived at the QPC, and that inside the integral is due to causality on the chiral edge – the incoming quasiparticle influences the current at all times before it has passed the QPC. We also note the prefactor: $\sin\left(2\pi \boldsymbol{g_\alpha}.\boldsymbol{g_\beta}\right)$, which indicates direct dependence of the tunneling current on the braiding phase between the incoming anyon, and the ones generated at the QPC, due to time-domain braiding processes. For a given value of t_2 (the integration variable), the current is non-zero only for $t_2 < t_0 < t_1$. Hence the latter condition is automatically imposed on the arrival time t_0, to observe signatures of time-domain braiding processes.

It can be shown that the integral in the above equation always returns a positive value. Hence, the sign of the tunneling current is fully determined by the value of the

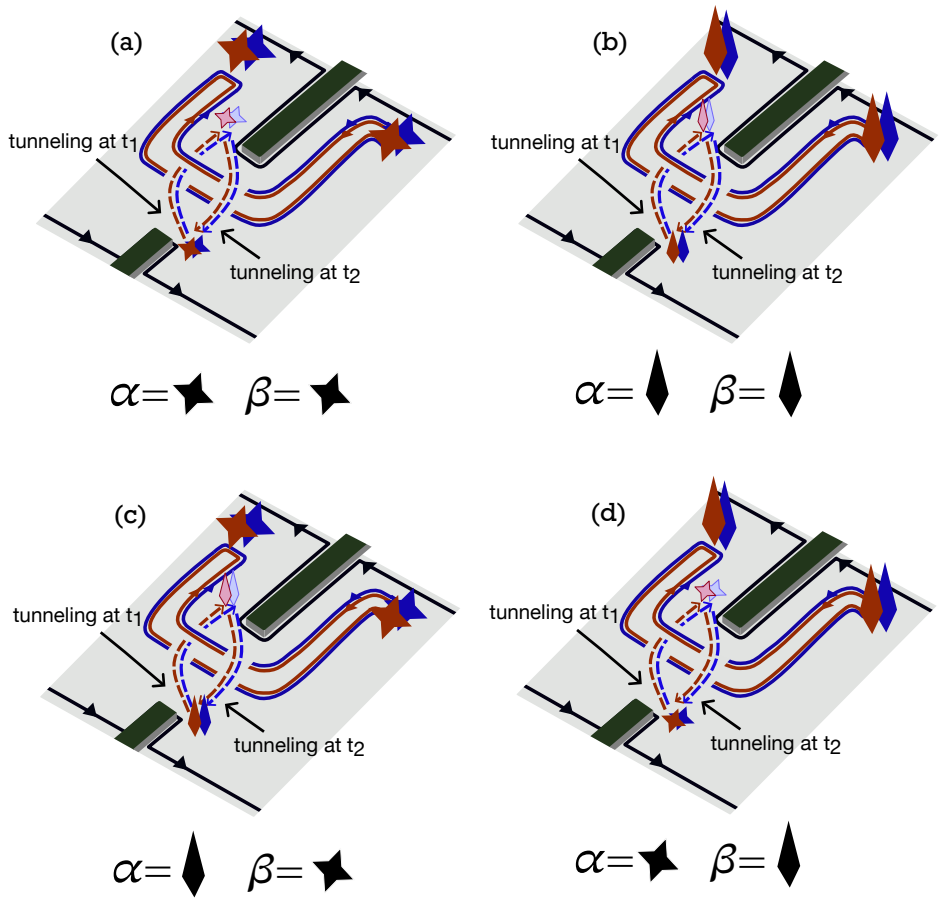


Figure 6.5.: Incoming anyons (large, dark red and dark blue) braid with tunneling pairs of anyons (small, dark red and dark blue) and antianyons (small, pale red and pale blue). The incoming anyon, indexed by α can be of two types symbolized by *shuriken* (star-like) and *kunai* (blade-like). The tunneling anyons can also be of either type. The sums over α and β in Equation (6.29) run over all types, leading to the four different braiding processes shown above. The overall braiding phase would be a weighted sum of the braiding phases from the above processes. Crucially, since red and blue bosonic modes are independent, the red incoming excitations braid only with the red tunneling excitations; the same holds for blue excitations.

braiding phase. Clearly, for $\boldsymbol{g_\alpha}.\boldsymbol{g_\beta} < 1/2$, we have a positive tunneling current, while for $\boldsymbol{g_\alpha}.\boldsymbol{g_\beta} > 1/2$ we predict a negative tunneling current. The latter is counter-intuitive since what we have here is an anyon traveling on the upper edge and hitting the QPC. Naively one expects it to either tunnel to the lower edge or continue on the same edge without tunneling. Neither of these situations can lead to a net negative current. Hence, our conventional intuition breaks down when considering anyons, where time-domain braiding processes, and not trivial tunneling processes, provide the dominant contribution.

Nevertheless, we will see in Chapter 7 that experiments probing time-domain braiding processes do not see a negative tunneling current, in contradiction with theoretical predictions. Solving this issue to arrive at an agreement between theory and experiment is one of the goals of this thesis.

Chapter 7.

Generalized Abelian Anyon Collider

The anyon collider experiment marked the first experimental demonstration of anyon braiding phase in the $\nu = 1/3$ Laughlin FQHE. The setup, proposed by Ref. [33], comprises two dilute streams of anyons meeting at a quantum point contact. Initially, it was thought that anyons in the two stream collide and spatially exclude each other, with the bunching or anti-bunching of anyons being intermediate between fermions and bosons. However, further analysis revealed that it is rather the time-domain braiding processes discussed in Chapter 6 that occurs in this setup. The anyons in the incoming streams braid with the anyon-antianyon pairs generated at the QPC where the two beams meet. Signatures of these braiding processes manifest in various physical observables, including the cross-correlations of the output currents from the QPC.

While the experiment agrees incredibly well with theory at $\nu = 1/3$, the same experiment at $\nu = 2/5$ has a strong disagreement with theoretical predictions. The latter predictions are based on interpolation of the results of Ref. [33], which does not account for the complexities of non-Laughlin filling fractions. In this chapter, we generalize the theory of the anyon collider to an arbitrary Abelian FQHE state comprising many bosonic modes on the edge, and different types of anyons tunneling at the QPC. The multiple bosonic modes may be co-propagating (as in $\nu = 2/5$) or counter-propagating (as in $\nu = 2/3$).

We apply our theory to two FQHE systems: $\nu = 2/3$ and $\nu = 2/5$. In the $\nu = 2/3$ system, we provide explicit predictions for different scenarios of anyon braiding, in anticipation of future experiments. On the other hand, given the existing experimental results in $\nu = 2/5$, the objective here is to reconcile theory and experiment. Our model comprising multiple bosonic modes on each edge, and different types of anyons tunneling at the QPCs, allows us to move forward in this direction. We can now investigate the consequences of non-trivial effects on the edge such as inter-mode interactions and tunneling of different types of anyons. This investigation yields crucial insights on how the physics of the anyon collider is shaped by these non-trivial ingredients, leading to a more complete understanding of anyon braiding phase in non-Laughlin FQHE systems.

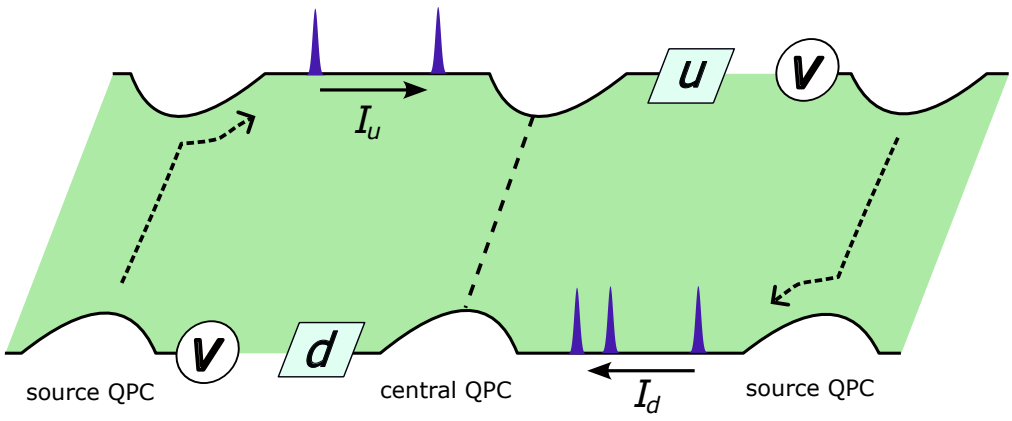


Figure 7.1.: Schematic of the anyon collider setup. The geometry comprises three QPCs. The two QPCs on the left and the right are called *source* QPCs. They are both biased with a voltage V. A Poissonian stream of anyons (in blue) is emitted by the source QPCs, leading to currents $I_{u/d}$ on the upper/lower edges. The anyon streams travel downstream and hit the so-called *central* QPC. The resulting average current and current correlations are measured at contacts u and d.

7.1. Upstream QPC as anyon sources: the anyon collider

In the previous chapter, we considered a single anyon, coming from an unspecified source, hitting a QPC. This gives rise to anyon braiding in the time domain, which can be potentially observed with transport measurements. However, sources that can send single anyons in a controlled manner are beyond the reach of contemporary experiments. Keeping the latter point in mind, we want to think about realistic sources of anyons. As discussed in Section 2.4.1, QPCs in the weak backscattering regime biased with a voltage V on one edge, emit a stream of anyons on the opposite edge. Ref. [33] hence proposed using upstream QPCs in the weak-backscattering regime, biased with a large voltage as a source of anyons. These anyons would then travel on the chiral edges, and hit another QPC placed downstream as shown in Figure 7.1.

The QPCs to the left and right in Figure 7.1 are called source QPCs. They are operated in the weak-backscattering regime, emitting a dilute, random stream of anyons on the opposite edges. The stream of anyons leads to an average current I_u/I_d on edge u/d. The anyon streams travel along the edges, to reach the *central* QPC, where the incoming anyons braid in the time domain with the anyon-antianyon pairs tunneling at the central QPC, as described in Chapter 6.

With an upstream QPC as the source of anyons, it is not possible to control the number of anyons arriving at the central QPC, and also the times at which they arrive

there. The tunneling of anyons due to a voltage bias is a random, uncorrelated process. This is reflected in the proportionality between the average current and its fluctuations, as shown in Equation (2.82). The latter indicates that the number of anyons emitted in a given time interval follows a Poisson distribution, while the emission times of the anyons are uniformly distributed within the latter interval.

In this section, we will calculate the tunneling current generated at the central QPC by an incoming random stream of anyons, following the approaches outlined in Refs. [33, 120]. This calculation is crucial, as it introduces the non-perturbative treatment of incoming anyons introduced in Ref. [120].

7.1.1. Theoretical framework

Ref. [33] focuses exclusively on the Laughlin FQHE, which is characterized by a single bosonic edge mode and a unique anyonic quasiparticle tunneling across both the source and central QPCs. Similarly, in this section, we confine our analysis to the Laughlin case, laying the groundwork for generalization to arbitrary Abelian FQHE in the subsequent sections.

Source QPC

In this section, we turn off the source QPC on the right for simplicity. We imagine that the source QPC on the left sends a dilute stream of anyons along the upper edge of the system. In the large voltage regime, $q_{\boldsymbol{g}}V \gg T$, as discussed in Section 2.4.1, each anyon emission event is uncorrelated and can be thought to be a Poisson process. Hence, the number of anyons emitted in a given time interval obeys a Poisson distribution, and the emission times are distributed uniformly within the latter time interval.

We theoretically model the anyons incoming from the source QPC using an $N-$anyon state, with given emission times $-\mathcal{T}_k$ of the $k-$the anyon. The number of anyons N is taken to follow a Poisson distribution while emission times $\mathcal{T}_k$ are assumed to be uniformly distributed. Nevertheless, we begin from a specific realization of this probability distribution, with the averages to be taken at a later stage. Our starting point is hence the following state where anyons emitted by the source QPC are modeled by augmenting the ground state of the edge theory with N anyon operators:

$$|\varphi\rangle = \prod_{k=1}^{N} \psi_{\boldsymbol{g}}^{u\dagger}(-\mathcal{L}, -\mathcal{T}_k)\,|0\rangle \tag{7.1}$$

where $|0\rangle$ denotes the ground state of the edge theory and $\psi_{\boldsymbol{g}}^{u/d\dagger} = e^{-i\boldsymbol{g}.\boldsymbol{\phi}^{\boldsymbol{u/d}}}$ denotes anyon operators, with $\boldsymbol{g} = (\sqrt{\nu})$ and $\boldsymbol{\phi}^{\boldsymbol{u/d}} = (\phi^{u/d})$ for Laughlin filling fractions of the FQHE. The left source QPC is located at $-\mathcal{L}$, indicating the spatial location at which the anyons

are injected on the upper edge, $-\mathcal{T}_k$ is the time at which the $k-$th anyon is injected on the edge at the location of the source QPC, and N is the total number of anyons emitted by the source QPC. The total number of anyons emitted by the source QPC in a given time interval follows a Poisson distribution, whose Poisson parameter is given the average number current $I_u/q_{\boldsymbol{g}}$, where $q_{\boldsymbol{g}}$ is the charge of the anyons. The latter statement is the same as saying that the emission of anyons on the edge is a random, uncorrelated process. It then follows that the injection times $\mathcal{T}_k$ are uniformly distributed in the time interval over which the anyons are emitted. Moreover, the average temporal spacing between subsequent anyons is given by $t_s = q_{\boldsymbol{g}}/I_u$. The physical consequences of the incoming anyons are thus captured by calculating averages over the augmented state of Equation 7.1 instead of the ground state.

It is important to note that this approach does not involve a microscopic treatment of the source QPCs. Instead, the physics of the source QPCs is reduced to the emission of anyons along the edges, as reflected in Equation (7.1), where the ground state is augmented with incoming anyonic excitations. However, a more detailed, non-perturbative treatment of the source QPCs is possible under certain approximations, as shown in Refs. [87, 122]. This ultimately yields the same results as those derived in this section.

Central QPC

The central QPC is located at $x = 0$. The $k-$th anyon coming from the source QPC reaches the central QPC at time $t_k = -\mathcal{T}_k + \mathcal{L}/v$, where v is the propagation velocity of the chiral bosonic mode. Anyon-antianyon pairs are spontaneously created at the central QPC, due to the proximity of the upper and lower edges, allowing tunneling of anyon pairs from the bulk onto the edges. These processes are described by the tunneling Hamiltonian

$$H_T(t) = \Gamma_{\boldsymbol{g}} \left(e^{i\boldsymbol{g}.\boldsymbol{\phi}^{\boldsymbol{u}}(0,t) - i\boldsymbol{g}.\boldsymbol{\phi}^{\boldsymbol{d}}(0,t)} + \text{H.c.} \right), \tag{7.2}$$

and the current produced on the lower edge due to these tunneling processes are described by the tunneling current operator

$$I_T(t) = i q_{\boldsymbol{g}} \Gamma_{\boldsymbol{g}} \left(e^{i\boldsymbol{g}.\boldsymbol{\phi}^{\boldsymbol{u}}(0,t) - i\boldsymbol{g}.\boldsymbol{\phi}^{\boldsymbol{d}}(0,t)} - \text{H.c.} \right). \tag{7.3}$$

These operators are special cases of those introduced in Section 2.3. To study the impact of the incoming anyons on for example the tunneling current, we must calculate moments of the latter quantity, not averaged on the ground state of the edge theory, but on the $N-$anyon state defined in Equation (7.1).

7.1.2. Tunneling current due to N anyons

At equilibrium, in the absence of any drive on the edge, the average tunneling current is zero – this follows from the particle-hole symmetry of Equations (7.2) and (7.3). Sending anyons on the upper edge constitutes a non-equilibrium drive that breaks particle-hole symmetry, and leads to a net current across the QPC. Let us calculate the average tunneling current due to an arbitrary realization of N anyons incident on the central QPC at times $\{t_1, t_2 \ldots, t_N\}$. For this, we use the Keldysh formalism, and the tunneling current operator in Equation (7.3) is averaged over the $N-$anyon state given in Equation (7.1)

$$\langle I(t,\{t_k\})\rangle_N = \frac{1}{2}\langle\varphi|\sum_\eta I_T(t^\eta)\; e^{-i\int_K dt' H_T(t')}\,|\varphi\rangle\,, \tag{7.4}$$

where the subscript N on the average value of the current indicates that the current is due to a specific realization of N anyons hitting the central QPC. Also, the expression is normalized by $\langle\varphi|\varphi\rangle$.

Notice that the current, in full generality, depends on t_k, the arrival times of the anyons at the central QPC. Writing out the current explicitly, at lowest order in perturbation theory of the central QPC, we are left with the following Keldysh correlation function of bosonic vertex operators to evaluate:

$$\begin{aligned}\langle I(t,\{t_k\})\rangle_N = \frac{q_{\boldsymbol{g}}|\Gamma_{\boldsymbol{g}}|^2}{2}\sum_\epsilon \epsilon\sum_{\eta\eta'}\eta'\int dt'\\ \prod_{k=1}^{N}\prod_{m=1}^{N}\Big\langle\Big\{T_K\; e^{i\sqrt{\nu}\phi^u(-\mathcal{L},-\mathcal{T}_k^-)}e^{i\epsilon\sqrt{\nu}\phi^u(0,t^\eta)}e^{-i\epsilon\sqrt{\nu}\phi^d(0,t^\eta)}\\ e^{i\epsilon\sqrt{\nu}\phi^d(0,t'^{\eta'})}e^{-i\epsilon\sqrt{\nu}\phi^u(0,t'^{\eta'})}e^{-i\sqrt{\nu}\phi^u(-\mathcal{L},-\mathcal{T}_m^+)}\Big\}\Big\rangle.\end{aligned} \tag{7.5}$$

The evaluation of the above correlation function proceeds very similarly to that of the correlation function with a single anyon on the upper edge, calculated in Section 6.2. We follow Equations (6.19) to (6.29) with one additional observation: the normalization of the current with $\langle\varphi|\varphi\rangle$ gets rid of all the two-point functions where both operators are one of the incoming anyons. With this, we find the following result for the current due to N incoming anyons:

$$\langle I(t,\{t_k\})\rangle_N = \frac{q_{\boldsymbol{g}}|\Gamma_{\boldsymbol{g}}|^2}{2}\sum_\epsilon\epsilon\sum_{\eta\eta'}\eta'\int_{-\infty}^{\infty}dt' e^{2\delta_{\boldsymbol{g}}\mathcal{G}^{\eta\eta'}(t-t')}\prod_{k=1}^{N}e^{i\epsilon\pi\nu(\mathrm{sgn}(t-t_k)-\mathrm{sgn}(t'-t_k))}. \tag{7.6}$$

In the above equation, we find a time-domain braiding phase contribution due to each incoming anyon (provided $t_k \in [t', t]$). Let us now sum over ϵ and the Keldysh indices.

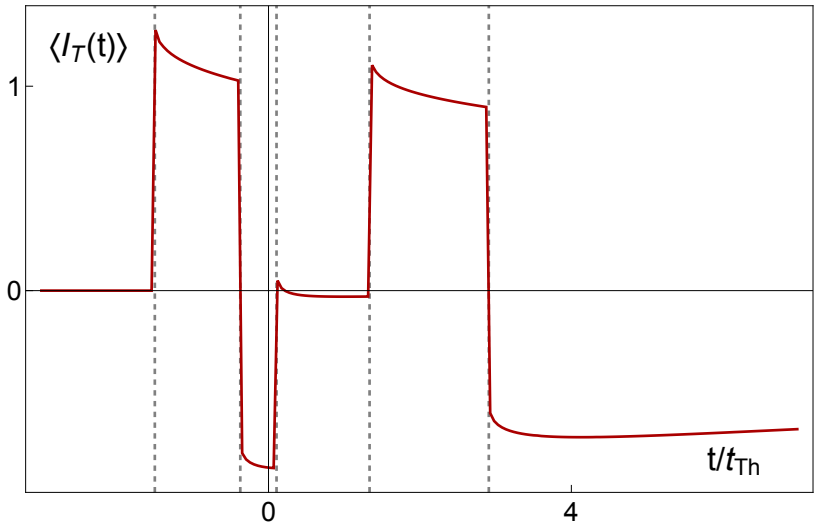


Figure 7.2.: Time-dependent tunneling current for an arbitrary realization of 5 anyons in the $\nu = 1/3$ arriving at the central QPC at times uniformly distributed times within the time interval shown in this figure. The arrival times of the anyons at the central QPC are indicated by dashed vertical lines. When the first anyon arrives at the central QPC, the system feels the phase $e^{2i\pi/3}$ and the current increases abruptly, producing a net positive current. The current then decays slowly with time. When the second anyon arrives at the central QPC before the current due to the first anyon has decayed completely, the system feels the phase due to two anyons, $e^{4i\pi/3}$, producing a net negative current, which then also decays slowly. The above argument can be repeated for all the subsequent anyons arriving at the central QPC. The current thus depends non-perturbatively on all the incoming anyons.

This gives us the following expression for the current due to N anyons:

$$\langle I(t,\{t_k\})\rangle_N = 2iq_{\boldsymbol{g}}|\Gamma_{\boldsymbol{g}}|^2 \int_{-\infty}^{t} dt' \left(e^{2\delta_{\boldsymbol{g}}\mathcal{G}(t-t')} - e^{2\delta_{\boldsymbol{g}}\mathcal{G}(t'-t)}\right) \sin\left(2\pi\nu\sum_{k=1}^{N}\left[\theta(t-t_k)-\theta(t'-t_k)\right]\right) \tag{7.7}$$

This expression generalizes the single anyon current of Equation (6.30). The $N-$anyon current is shown in Figure 7.2 for an arbitrary realization of 5 anyons hitting the QPC in the $\nu = 1/3$ FQHE. The arrival times at the central QPC t_k are uniformly distributed within the time interval considered in the figure.

When the first anyon hits the central QPC, the system feels a braiding phase $e^{2\pi i/3}$ of the incoming anyon with anyon-antianyon pairs tunneling at the central QPC. This produces a net tunneling current, that decays slowly in time, as a power law of exponent $2\delta_{\boldsymbol{g}}$. The timescale of the decay is set by the thermal timescale $t_{\rm Th} = 1/T$. If another

anyon arrives at the QPC before the current has fully decayed, the system now feels an effective phase $e^{4\pi i/3}$, of two incoming anyons braiding with the anyon-antianyon pairs. This produces a negative current, as can be seen in Figure 7.2. The system hence retains a memory of anyons that have already passed the QPC, with the memory lasting up to the thermal timescale. The above argument can be repeated for all the incoming anyons, and the effective braiding phase seen at the QPC is a result of the interplay between the slow decrease of the current and the number of incoming anyons. Thus, in the low-temperature limit that we work in, the current depends non-perturbatively on all the incoming anyons.

We emphasize that the above discussion holds only for anyons carrying a fractional braiding phase and importantly, a scaling dimension less than 1. Indeed, the current is zero if $\nu \in \mathbf{Z}$ in Equation (7.7) which is the case for electrons. In this case, one has to regularize the theta functions, leading to delta-peaked currents exactly when the electron arrives at the QPC [77, 153]. However, it is now an apt moment to remark that anyons do not inherently demand a non-perturbative treatment. For example, even if the braiding phase is fractional but the scaling dimension $\delta_{\boldsymbol{g}} \geq 1$, the current due to each anyon decays quickly. The same statement applies in the large temperature limit, where $t_s \sim t_{Th}$. In this case, despite a small scaling dimension, the current decays quickly as the Greens function decay exponentially. In these scenarios, there is no "memory" of the past anyons of the kind seen in Figure 7.2, and hence they can be treated well with perturbative approaches [78, 86]. Having said that, in this thesis we will nevertheless only be concerned with anyons in the low-temperature limit, and $\delta_{\boldsymbol{g}} < 1$.

7.1.3. Poisson-averaged tunneling current

Going back to the low-temperature limit of anyons, we note that the timescale at which individual anyons arrive at the QPC is far out of reach of contemporary experiments. Indeed the experiments measure an average current, over timescales much larger than t_s, leading to a time-independent value in contrast to the time-dependent current shown in Figure 7.2. Thus, we average over the arrival times of the anyons at the QPC t_k in Equation (7.6). Since the latter times are uniformly distributed, the time-averaged tunneling current reads:

$$\langle I(t)\rangle_N = \frac{q_{\boldsymbol{g}}|\Gamma_{\boldsymbol{g}}|^2}{2}\sum_{\epsilon}\epsilon\sum_{\eta\eta'}\eta'\int_{-\infty}^{\infty}dt' e^{2\delta_{\boldsymbol{g}}\mathcal{G}^{\eta\eta'}(t-t')}\left(e^{i\epsilon\pi\nu}\right)^N. \tag{7.8}$$

Clearly, this current is independent of the arrival times of the anyons, and cares only about the number of anyons arriving at the QPC. Of course, as emphasized several times before, the latter obeys a Poisson distribution. The probability of N anyons arriving at

the QPC in the time interval $(t-t')$ is given by:

$$P(N) = \frac{1}{N!}\left[\frac{I_u}{q_{\boldsymbol{g}}}|t-t'|\right]^N e^{-\frac{I_u}{q_{\boldsymbol{g}}}(t-t')} \tag{7.9}$$

where $I_u/q_{\boldsymbol{g}}$ is the average number current of anyons in a time interval. Using this distribution, we average over the number N, giving us the following expression for the tunneling current:

$$\begin{aligned}\langle I_T(t)\rangle = q_{\boldsymbol{g}}|\Gamma_{\boldsymbol{g}}|^2 \sum_{\epsilon} \epsilon \int_{-\infty}^{t} dt' \left(e^{2\delta_{\boldsymbol{g}}\mathcal{G}(t-t')} - e^{2\delta_{\boldsymbol{g}}\mathcal{G}(t'-t)}\right) \\ \sum_{N=0}^{\infty} \frac{1}{N!}\left[\frac{I_u}{q_{\boldsymbol{g}}}(t-t')\right]^N e^{-\frac{I_u}{q_{\boldsymbol{g}}}(t-t')} \left(e^{2i\epsilon\pi\nu}\right)^N .\end{aligned} \tag{7.10}$$

Here, $I_u(t-t')/q_{\boldsymbol{g}}$ gives the number of anyons incident at the central QPC in the time interval $[t', t]$. In the above expression, we have restored time independence since the number of anyons incident on the QPC per unit time is a constant. Hence, we are free to perform the transformation $\tau = t - t'$. We also evaluate the sum over N, giving us the manifestly time-independent average tunneling current at the central QPC due to a Poissonian stream of anyons sent by a source QPC:

$$\langle I_T\rangle = q_{\boldsymbol{g}}|\Gamma_{\boldsymbol{g}}|^2 \sum_{\epsilon} \epsilon \int_0^{\infty} d\tau \left(e^{2\delta_{\boldsymbol{g}}\mathcal{G}(-\tau)} - e^{2\delta_{\boldsymbol{g}}\mathcal{G}(\tau)}\right) e^{-\frac{I_u}{q_{\boldsymbol{g}}}\tau\left(1-e^{2i\epsilon\pi\nu}\right)} \tag{7.11}$$

Now, summing over ϵ, we have the following expression for the current

$$\langle I_T\rangle = 2iq_{\boldsymbol{g}}|\Gamma_{\boldsymbol{g}}|^2 \int_0^{\infty} d\tau \frac{\sin\left[\frac{I_u}{q_{\boldsymbol{g}}}\tau\sin(2\pi\nu)\right]}{\exp\left[\frac{I_u}{q_{\boldsymbol{g}}}\tau\left(1-\cos(2\pi\nu)\right)\right]} \left(e^{2\delta_{\boldsymbol{g}}\mathcal{G}(-\tau)} - e^{2\delta_{\boldsymbol{g}}\mathcal{G}(\tau)}\right) \tag{7.12}$$

obtained in Equation (7) of Ref. [33].

7.2. Generalizing the anyon collider

The previous section laid down the theory of the anyon collider for Laughlin fractions. The latter states are characterized by a single bosonic mode on the edges, and a unique anyon tunneling across the QPCs. We now seek a generalization of the theory to address a general Abelian quantum Hall system, where each edge comprises multiple bosonic modes, and different anyons tunnel simultaneously across both, the source and the central QPCs. Indeed, such a generalization is necessary to address non-Laughlin fractions of the FQHE such as $\nu = 2/3$ and $\nu = 2/5$. It is well known that FQHE edge experiments are plagued

with non-universal physics including intra-edge interactions and edge reconstruction. A generalization of the anyon collider theory would allow us to study the impact of such edge effects on the observables of the anyon collider, enabling better comparison with experiments.

To address the anyon collider in an arbitrary Abelian FQHE, we recall the general idea of the latter states discussed in Section 2.2. This can be encapsulated in the following three points:

1. Each FQHE edge carries multiple bosonic modes, which may be co-propagating or counter-propagating.
2. All the anyons admitted on the edge are the exponential of a linear combination of all the bosonic modes on the edge: $\psi_{\boldsymbol{g_\alpha}} = e^{i\boldsymbol{g_\alpha}\cdot\boldsymbol{\phi}}$.
3. All the anyons admitted on the FQHE edge can tunnel across the QPCs.

In this section, we will hence put together the idea of Poisson averages with the three points above.

7.2.1. Theoretical framework

Source QPC

For simplicity, we begin by turning off the source QPC on the right, as in the previous discussion. Similar to the Laughlin case, we will not treat the source QPCs microscopically. Instead, we assume that the source QPC emits a stream of anyons along the upper edge, as described earlier. However, unlike before, the source QPC now allows the tunneling of all anyon types present on the edge. Each emission event hence involves a sum over all possible anyon types, with each type weighted by its probability amplitude of emission. Thus, an $N-$anyon state can be expressed as:

$$|\varphi\rangle \equiv \prod_{k=1}^{N} \sum_{\beta} p_{\boldsymbol{g_\beta}} \psi^{u\dagger}_{\boldsymbol{g_\beta}}(-\mathcal{L}, -\mathcal{T}_k) \, |0\rangle \, , \tag{7.13}$$

where, $\psi^{u/d}_{\boldsymbol{g_\beta}} \sim e^{-i\boldsymbol{g_\beta}\cdot\boldsymbol{\phi^{u/d}}}$ is the anyon operator of type$-\beta$, and $p_{\boldsymbol{g_\beta}}$ is the probability amplitude that type$-\beta$ anyon is emitted in a given emission event. Moreover, $\boldsymbol{g_\beta} = (g_{\beta 1}, \ldots, g_{\beta N})$ and $\boldsymbol{\phi^{u/d}} = \left(\phi_1^{u/d}, \ldots, \phi_N^{u/d}\right)$. The other notations as the same as in Section 7.1.1. The state generalizes the state of Equation (7.13) to address multiple types of anyons.

We repeat the caveat mentioned in Section 6.2: an upstream source QPC cannot create an incoming state where the different anyon types are in a superposition. Rather,

the incoming state is a density matrix in the anyon type space with only the diagonal carrying non-zero values $|p_{\boldsymbol{g_\beta}|^2}$, and all the non-diagonal elements being zero. For the sake of notational convenience in the forthcoming calculations, we specify the incoming state as in Equation (6.17), but the off-diagonal overlaps will always taken to be zero.

When an anyon is emitted on the edge, the excitation on the $j-$th bosonic mode travels at a velocity v_j. The excitation on the $j-$th bosonic mode of the $k-$th anyon emitted on the upper edge hence reaches the central QPC, located at $x = 0$, at a time $t_{k,j} = -\mathcal{T}_k + \mathcal{L}/v_j$. However, as discussed in Chapter 6, as long as $\mathcal{L}(1/v_i - 1/v_j) \ll t_{\rm Th}$, we can assume that all the excitations arrive simultaneously at the central QPC at a time t_k, that is $-\mathcal{T}_k + \mathcal{L}/v_j = t_k$ for all j.

Central QPC

As before, the central QPC allows tunneling of anyon-antianyon pairs from the bulk on to the edges. But now, in the general Abelian FQHE edge, different anyon-antianyon pairs are allowed to tunnel on to the edges. This is taken into account in the tunneling Hamiltonian by a sum over all anyons admitted by the FQHE edge theory as shown in Section 2.3:

$$H_T(t) = \sum_\alpha \Gamma_{\boldsymbol{g}_\alpha} \left(e^{i\boldsymbol{g_\alpha}.\boldsymbol{\phi^u}(0,t) - i\boldsymbol{g_\alpha}.\boldsymbol{\phi^d}(0,t)} + H.c. \right). \tag{7.14}$$

Similarly, the tunneling current operator is expressed as

$$I_T(t) = \sum_\alpha i q_{\boldsymbol{g}_\alpha} \Gamma_{\boldsymbol{g}_\alpha} \left(e^{i\boldsymbol{g_\alpha}.\boldsymbol{\phi^u}(0,t) - i\boldsymbol{g_\alpha}.\boldsymbol{\phi^d}(0,t)} - H.c. \right), \tag{7.15}$$

where $q_{\boldsymbol{g}_\alpha}$ is the charge of the type$-\alpha$ anyon. These expressions are the same as those introduced in Section 2.3.

We would once again like to calculate moments of the tunneling current operator. Taking into account the effect of the incoming anyons, we calculate the average tunneling current due to N incoming anyons in the next section by averaging the current operator over the $N-$anyon state in Equation (7.13).

7.2.2. Tunneling current

The calculation of the average tunneling current proceeds as before. Let us start with the current due to a given realization of $N-$anyons hitting the central QPC at times $\{t_1, \ldots, t_N\}$. Using the Keldysh formalism, the average tunneling current can be expressed

as:

$$\langle I_T(t,\{t_k\})\rangle_N = \frac{1}{2}\langle\varphi|\sum_\eta I_T(t^\eta)\; e^{-i\int_K dt' H_T(t')}\,|\varphi\rangle\,. \tag{7.16}$$

where the average is normalized by $\langle\varphi|\varphi\rangle$. At lowest order in perturbation theory, using Equations (7.13) to (7.15), we express the average tunneling current as below

$$\begin{aligned}\langle I(t,\{t_k\})\rangle_N = \prod_{k,m=1}^{N}\sum_\beta P_{\boldsymbol{g_\beta}}\sum_\alpha \frac{q_{\boldsymbol{g}_\alpha}|\Gamma_{\boldsymbol{g}_\alpha}|^2}{2}\sum_\epsilon \epsilon\sum_{\eta\eta'}\eta'\int dt' \\ \Big\langle\Big\{T_K\; e^{i\boldsymbol{g_\beta}\cdot\boldsymbol{\phi^u}(-\mathcal{L},-\mathcal{T}_k^-)}e^{i\epsilon\boldsymbol{g_\alpha}\cdot\boldsymbol{\phi^u}(0,t^\eta)}e^{-i\epsilon\boldsymbol{g_\alpha}\cdot\boldsymbol{\phi^d}(0,t^\eta)} \\ e^{i\epsilon\boldsymbol{g_\alpha}\cdot\boldsymbol{\phi^d}(0,t'^{\eta'})}e^{-i\epsilon\boldsymbol{g_\alpha}\cdot\boldsymbol{\phi^u}(0,t'^{\eta'})}e^{-i\boldsymbol{g_\beta}\cdot\boldsymbol{\phi^u}(-\mathcal{L},-\mathcal{T}_m^+)}\Big\}\Big\rangle,\end{aligned} \tag{7.17}$$

where $|p_{\boldsymbol{g_\beta}}|^2 = P_{\boldsymbol{g_\beta}}$. This expression puts together the ideas of Equations (6.19) and (7.5), giving the current due to time-domain braiding of N anyons in an arbitrary Abelian FQHE. Given the proliferation of sums in the above expression, we break it down. The sum over η,η' runs over the Keldysh indices of the tunneling times of anyons in the central QPC. The sum over ϵ takes care of Hermitian conjugate processes at the central QPC. The sum on α runs over all the types of anyons that can tunnel across the central QPC, and the sum over β,γ run over all the types of anyons that can be emitted by the source QPC.

Let us now proceed to evaluate the correlation function above. We will again follow Equations (6.19) to (6.29) to this end. As in Section 7.1.3, the normalization factor $\langle\varphi|\varphi\rangle$ cancels out the two-point functions associated with only the incoming anyons. Moreover, from Equation (6.21), for the above correlator to be non-vanishing $\beta=\gamma$ is imposed. This gets rid of one of the sums in Equation (7.17). We further sum over the Keldysh indices, giving us:

$$\begin{aligned}\langle I(t,\{t_k\})\rangle_N = \sum_\alpha q_{\boldsymbol{g}_\alpha}|\Gamma_{\boldsymbol{g}_\alpha}|^2\sum_\epsilon \epsilon\int_{-\infty}^{t} dt'\left(e^{2\delta_{\boldsymbol{g}_\alpha}\mathcal{G}(t-t')}-e^{2\delta_{\boldsymbol{g}_\alpha}\mathcal{G}(t'-t)}\right) \\ \prod_{k=1}^{N}\sum_\beta P_{\boldsymbol{g_\beta}}e^{i\epsilon\pi\boldsymbol{g_\alpha}\cdot\boldsymbol{g_\beta}(\mathrm{sgn}(t-t_k)-\mathrm{sgn}(t'-t_k))},\end{aligned} \tag{7.18}$$

where $P_{\boldsymbol{g_\beta}} = |p_{\boldsymbol{g_\beta}}|^2$ is the probability that a type$-\beta$ anyon arrives at the central QPC in a given event, such that $\sum_\beta P_\beta = 1$. As remarked before, since the source QPC emits many types of anyons, $P_{\boldsymbol{g_\beta}}$ obeys a multinomial distribution. This expression generalizes Eqaution (7.6), taking into account the latter ingredient.

The second line of Equation (7.18) contains the braiding phases of the incoming anyons with the anyon-antianyon pairs tunneling at the central QPC. Here, $\boldsymbol{g_\alpha}$ denotes the anyons

tunneling at the central QPC while $\boldsymbol{g_\beta}$ denotes the incoming ones, with $\boldsymbol{g_\alpha}.\boldsymbol{g_\beta}$ giving their braiding phase. Note that there exists a sum over β, weighted by the probability that a type$-\beta$ anyon arrives at the QPC in a given event, and also a sum over α (on the first line) accounting for different anyons tunneling at the central QPC. This expression hence captures the braiding phase due to different incoming anyons with all the anyons tunneling at the central QPC, as shown in Figure 6.5 and the paragraphs around it.

We now want to perform a Poissonian average over the number of arriving anyons as done in Section 7.1.3. Let γ_u be the mean number of anyons hitting the QPC per unit time, or the number current. However, since we now have different incoming anyons with different charges and different numbers, relating the number current to the charge current I_u is slightly more complicated. Let $I_{u\beta}$ be the average charge current due to type$-\beta$ anyons. These currents satisfy $I_u = \sum_\beta I_{u\beta}$, where I_u is the total charge current on the edge. Of course, since P_β is the probability that a type$-\beta$ anyon is emitted by the source, one can write $I_{u\beta} = P_\beta I_u$. Now, since we know the charge of each type of anyon, the number current of type$-\beta$ anyon is given by $I_{u\beta}/q_{\boldsymbol{g_\beta}}$. Hence, the total number current γ_u can be be related to the incoming charge currents by $\gamma_u = \sum_\beta I_{u\beta}/q_{\boldsymbol{g_\beta}} = I_u \sum_\beta P_\beta/q_{\boldsymbol{g_\beta}}$. Keeping this relation in mind, let us stick to the notation γ_u for the number current of the incoming anyons.

Akin to the procedure in Equation (7.10), the Poisson averaged tunneling current can be expressed as:

$$\begin{aligned}\langle I_T(t)\rangle = &\sum_\alpha q_{\boldsymbol{g}_\alpha}|\Gamma_{\boldsymbol{g}_\alpha}|^2 \sum_\epsilon \epsilon \int_{-\infty}^{t} dt' \left(e^{2\delta_{\boldsymbol{g}_\alpha}\mathcal{G}(t-t')} - e^{2\delta_{\boldsymbol{g}_\alpha}\mathcal{G}(t'-t)}\right) \\ &\sum_{N=0}^{\infty} \frac{1}{N!}\left(\gamma_u(t-t')\right)^N e^{-\gamma_u(t-t')} \left(\sum_\beta P_{\boldsymbol{g_\beta}} e^{2i\epsilon\pi \boldsymbol{g_\alpha}.\boldsymbol{g_\beta}}\right)^N,\end{aligned} \tag{7.19}$$

directly generalizing Equation (7.10) to arbitrary FQHE systems. We now evaluate the sum over N. Moreover, as time-translation invariance has been restored, we make the transformation $\tau = t - t'$, giving us

$$\begin{aligned}\langle I_T\rangle = &\sum_\alpha q_{\boldsymbol{g}_\alpha}|\Gamma_{\boldsymbol{g}_\alpha}|^2 \sum_\epsilon \epsilon \int_{0}^{\infty} dt' \left(e^{2\delta_{\boldsymbol{g}_\alpha}\mathcal{G}(-\tau)} - e^{2\delta_{\boldsymbol{g}_\alpha}\mathcal{G}(\tau)}\right) \\ &\exp\left[-\gamma_u(t-t')\left(1 - \sum_\beta P_{\boldsymbol{g_\beta}} e^{2i\epsilon\pi \boldsymbol{g_\alpha}.\boldsymbol{g_\beta}}\right)\right].\end{aligned} \tag{7.20}$$

We emphasize that this expression is a direct generalization of Equation (7.11). Indeed, the only difference lies in the sums over α and β, and the mutual braiding phase of the type$-\beta$ incoming anyons with type$-\alpha$ tunneling anyons.

So far, we have calculated the tunneling current due to anyons on the upper edge, coming from the left source QPC. Let us turn on the right source QPC, which now sends

anyons also on the lower edge. The state containing anyons both on the upper, and the lower edge can be expressed as:

$$|\varphi\rangle \equiv \prod_{k=1}^{N_u} \sum_{\beta} p_{\boldsymbol{g_\beta}} \psi^{u\dagger}_{\boldsymbol{g_\beta}}(-\mathcal{L}^u, -\mathcal{T}^u_k) \prod_{m=1}^{N_d} \sum_{\sigma} p_{\boldsymbol{g_\sigma}} \psi^{u\dagger}_{\boldsymbol{g_\sigma}}(\mathcal{L}^d, -\mathcal{T}^d_m) \, |0\rangle \,, \tag{7.21}$$

where $-\mathcal{L}^{u/d}$ is the position of the left/right source QPC, $-\mathcal{T}^{u/d}_k$ is the emission time of anyon on the upper/lower edge at the location of the left/right source QPC, $N_{u/d}$ is the number of anyons emitted on the upper/lower edge.

Carrying out the same steps as before, we obtain the following expression for the average tunneling current due to the incoming anyons on both, the upper and lower edges:

$$\begin{aligned} \langle I_T \rangle = \sum_{\alpha} q_{\boldsymbol{g}_\alpha} |\Gamma_{\boldsymbol{g}_\alpha}|^2 \sum_{\epsilon} \epsilon \int_0^\infty dt' \left(e^{2\delta_{\boldsymbol{g}_\alpha} \mathcal{G}(-\tau)} - e^{2\delta_{\boldsymbol{g}_\alpha} \mathcal{G}(\tau)} \right) \\ \exp\left[-\gamma_u (t-t') \left(1 - \sum_{\beta} P_{\boldsymbol{g_\beta}} e^{2i\epsilon\pi \boldsymbol{g_\alpha}.\boldsymbol{g_\beta}} \right) \right] \\ \exp\left[-\gamma_d (t-t') \left(1 - \sum_{\beta} P_{\boldsymbol{g_\beta}} e^{-2i\epsilon\pi \boldsymbol{g_\alpha}.\boldsymbol{g_\beta}} \right) \right], \end{aligned} \tag{7.22}$$

where $\gamma_{u/d}$ denotes the average number current of anyons on the upper/lower edges. Notice the difference in the signs of the braiding phases due to anyons arriving on the upper or lower edge. While the sign difference follows from the mathematics, the physical reason is also clear. The sign difference arises because the sense of the braiding loop formed by the anyons tunneling at the central QPC is opposite for the incoming anyons on opposite edges. If the braiding loop looks clockwise to an anyon arriving from the left, it will naturally look clockwise to an anyon arriving from the right.

Making now the transformation $\gamma_\pm = \gamma_u \pm \gamma_d$, and summing over ϵ, the average tunneling current reads:

$$\begin{aligned} \langle I_T \rangle = \sum_{\alpha} 4i |\Gamma_{\boldsymbol{g_\alpha}}|^2 q_{\boldsymbol{g}_\alpha} \int_0^\infty d\tau \frac{\sin\left[\gamma_- \tau \sum_\beta P_\beta \sin\left(2\pi \boldsymbol{g_\alpha}.\boldsymbol{g_\beta}\right) \right]}{\exp\left[\gamma_+ \tau \sum_\beta P_\beta \left(1 - \cos\left(2\pi \boldsymbol{g_\alpha}.\boldsymbol{g_\beta}\right)\right) \right]} \\ \times \left[e^{2\delta_{\boldsymbol{g}_\alpha} \mathcal{G}(-\tau)} - e^{2\delta_{\boldsymbol{g}_\alpha} \mathcal{G}(\tau)} \right] \end{aligned} \tag{7.23}$$

and we use the zero temperature Greens function

$$\mathcal{G}(t) = \log\left(\frac{\tau_0}{\tau_0 + it} \right) \tag{7.24}$$

to reduce the difference of the Greens functions to $2i\tau^{-2\delta_{\boldsymbol{g}_\alpha}}\tau_0^{2\delta_{\boldsymbol{g}_\alpha}}\sin\left(\pi\delta_{\boldsymbol{g}_\alpha}\right)$ and calculate the resulting integral [125], giving us

$$\langle I_T\rangle = -\sum_\alpha c_\alpha \sin\left(\pi\delta_{\boldsymbol{g}_\alpha}\right)\mathrm{Im}\left[\left(\mathcal{C}_{\boldsymbol{g}_\alpha}+ix\mathcal{S}_{\boldsymbol{g}_\alpha}\right)^{2\delta_{\boldsymbol{g}_\alpha}-1}\right] \tag{7.25}$$

where

$$\begin{aligned} x &= \gamma_-/\gamma_+ \\ c_\alpha &= 8|\Gamma_{\boldsymbol{g}_\alpha}|^2 q_{\boldsymbol{g}_\alpha}\tau_0^{2\delta_{\boldsymbol{g}_\alpha}}\Gamma(1-2\delta_{\boldsymbol{g}_\alpha})\gamma_+^{2\delta_{\boldsymbol{g}_\alpha}-1} \\ \mathcal{C}_{\boldsymbol{g}_\alpha} &= \sum_\beta P_\beta\left[1-\cos\left(2\pi\boldsymbol{g}_\alpha.\boldsymbol{g}_\beta\right)\right] \\ \mathcal{S}_{\boldsymbol{g}_\alpha} &= \sum_\beta P_\beta\sin\left(2\pi\boldsymbol{g}_\alpha.\boldsymbol{g}_\beta\right) \end{aligned} \tag{7.26}$$

We have introduced here the asymmetry of the incoming currents $x=\gamma_-/\gamma_+$, discussed in detail in Section 7.2.3. It is justified to use the zero-temperature Greens function, instead of the finite-temperature one since we assume the thermal timescale $t_{\mathrm{Th}}=1/T$ to be much larger than the other timescales such as the average temporal spacing $t_s=q_{\boldsymbol{g}_\alpha}/I_+$ between subsequent anyons. This assumption is consistent with experimental conditions [34, 37–39] and amounts to working in the zero-temperature limit. Finite-temperature does introduce some corrections [37] which we do not worry about here. While finite-temperature poses no formal difficulties, taking the zero-temperature limit simplifies the expressions significantly in exchange for no great physical changes.

7.2.3. Asymmetry of incoming currents

In the previous subsection, we introduced a quantity $x=\gamma_-/\gamma_+$, which parametrizes the asymmetry of the incoming number currents γ_u and γ_d. This parameter has enormous utility in experiments, and hence deserves attention.

Let us briefly return to our favorite toy example of single anyons on the edge. Only now, consider a single anyon on both, the upper and lower edge. They travel along the respective edges and are incident on the QPC at times t_{u0} and t_{d0} respectively. Following the calculations of Section 6.2, the tunneling current due to the two incoming anyons can

be expressed as

$$\begin{aligned}\langle I_T(t)\rangle = \sum_\alpha q_{\boldsymbol{g}_\alpha}|\Gamma_{\boldsymbol{g}_\alpha}|^2 \int_{-\infty}^{t} dt' \left(e^{2\delta_{\boldsymbol{g}_\alpha}\mathcal{G}(t-t')} - e^{2\delta_{\boldsymbol{g}_\alpha}\mathcal{G}(t'-t)}\right) \\ \sum_\beta P_{\boldsymbol{g}_\beta} \sin\Big\{2\pi \boldsymbol{g}_\alpha.\boldsymbol{g}_\beta\left[\theta(t-t_{0u}) - \theta(t'-t_{0u})\right] \\ -2\pi \boldsymbol{g}_\alpha.\boldsymbol{g}_\beta\left[\theta(t-t_{0d}) - \theta(t'-t_{0d})\right]\Big\},\end{aligned} \tag{7.27}$$

where, the first/second line inside the sine denotes the braiding contributions from the anyon on the upper/lower edge. It is clear that the anyons on opposite edges contribute opposite braiding phases, canceling each other out. Indeed, if $t_{u0} = t_{d0}$, the tunneling current is exactly zero since the time-domain braiding phase of the upper edge anyon is fully canceled by that due to the lower edge anyon. If the anyons arrive with a time-delay (that is smaller than the thermal timescale), there is a similar cancellation. Assume $t_{u0} < t_{d0}$ without loss of generality. The anyon on the upper thus first arrives at the QPC, and braids in the time-domain with anyon pairs generated at the QPC. This produces a slowly decaying current seen, for example, in Figure 7.2. Now when the lower edge anyon arrives at the QPC, it too braids with the anyon pairs at the QPC. But it produces an opposite braiding phase, that cancels the braiding of the upper edge anyon, and the current then quickly decays to zero. The key takeaway is that anyons on opposite edges negate each other's braiding effects.

Having understood the toy model of single anyons, let us return to the collider. Here, we have two source QPCs, sending a stream of anyons on both edges. The average number of anyons per unit time on the upper/lower edge is given by $\gamma_{u/d}$. As previously discussed, the anyons on the opposite edges cancel out each other's braiding phases. Hence, the net braiding at the central QPC depends on the numbers $\gamma_{u/d}$ of the anyons on both edges. Indeed, $\gamma_{u/d}$ are under direct experimental control. The number current of anyons can be increased/decreased by increasing/decreasing the voltage applied on the respective source QPCs. There exist two extreme possibilities: $\gamma_d = 0$ (without loss of generality) or $x = 1$ leading to the maximum net braiding at the central QPC, and $\gamma_u = \gamma_d$ or $x = 0$, leading to maximum cancellation of the braiding processes. Experiments can probe all quantities measured at the central QPC, as a function of the current asymmetry x. It is hence possible to measure how these quantities evolve as a function of the "net braiding", allowing more robust fits with theoretical predictions.

7.3. Non-equilibrium bosonization

A mathematically elegant way to account for the incoming anyons, is to impose appropriate initial conditions on the bosonic fields. This method of *non-equilibrium bosonization* accounts for anyon excitations created on top of the ground state of the bosonic fields (by

an unspecified source) in a non-perturbative manner [120]. This method was introduced by Ref. [120] for Laughlin edges, and we extend it here to arbitrary Abelian edges.

7.3.1. Definition

The equilibrium bosonic fields are augmented with solitonic excitations to capture the effect of incoming anyons

$$\bar{\phi}_j^{u/d}(t) = \phi_j^{u/d}(t) + 2\pi \sum_{k=1}^{N} g_{\beta j}\theta(t - t_k^{u/d}) \tag{7.28}$$

where $\theta(x)$ is the Heaviside step function, $t_k^{u/d}$ are the arrival times of the quasiparticles on the upper/lower edge at the central QPC, and $\bar{\phi}_j^{u/d}$ denotes the $j-$th bosonic field with added solitonic excitations. With this modification of the bosonic fields, one can simply calculate quantum averages on the ground state of the edge theory, as opposed to using the augmented states of Equations (7.1) or (7.13). On the other hand, we consider the quasiparticle arrival times $t_k^{u/d}$ to follow a classical probability distribution. The latter decouples from the quantum average of the equilibrium bosonic field. Let us illustrate this with an example. We calculate a correlation function of anyons on the upper edge, carrying a stream of anyonic excitations coming from a source QPC. This is given by

$$\begin{aligned} &\left\langle e^{ig_{\alpha j}\bar{\phi}_j^u(0,t^\eta)} e^{-ig_{\alpha j}\bar{\phi}_j^u(0,t'^{\eta'})} \right\rangle = \langle 0| \, e^{ig_{\alpha j}\phi_j(0,t^\eta)} e^{-ig_{\alpha j}\phi_j(0,t'^{\eta'})} \, |0\rangle \\ &\times \left\langle \exp\left\{ i2\pi \sum_{k=1}^{N} g_{\alpha j} g_{\beta j} \left(\theta(t - t_k^u) - \theta(t' - t_k^u)\right) \right\} \right\rangle_{\text{n-eq}} . \end{aligned} \tag{7.29}$$

The first line denotes the quantum average of bosonic vertex operators on the ground state of the edge modes, giving the usual Greens function. The second line contains the non-equilibrium average, indicated with the subscript n-eq, which captures the properties of the anyons incoming from the unspecified source. Note that this correlator does not care about the Keldysh time ordering of the equilibrium bosonic fields, as the ties t_k are taken to obey a classical distribution. In general we do not know the exact times t_k. When the source is an upstream QPC in the weak-backscattering regime, as stressed in Section 7.1, these times obey a uniform distribution, while the number N obeys a Poisson distribution. We now show how to evaluate this correlation function.

The classical, *non-equilibrium* average comprises several components. First, the number of anyons N emitted by the source QPC obeys a Poisson distribution. The Poisson parameter of the latter distribution, giving the number of anyons emitted per unit time, is denoted γ_u. The arrival times of the anyons at the central QPC, given by t_k are uniformly distributed within the time interval $[t', t]$ (as emphasized before if the arrival

times lie outside the latter interval, the anyons do not contribute to transport observables at the QPC). Next, we assume that the source can emit all types of anyons admitted on the respective quantum Hall edge. Hence, associated with each anyon arrival, there is probability distribution giving the type of anyon arriving there. The probability of the anyon being type$-\beta$ is $P_\beta \in [0,1]$ such that $\sum_\beta P_\beta = 1$. Hence, one can think that there is a multinomial distribution associated with each anyon arrival event.

A moment's thought will reveal that the above process is equivalent to distinct Poisson processes corresponding to each anyon type, where the Poisson parameter is $P_\beta \gamma_u$ for type$-\beta$ anyon arriving at the QPC [154]. To calculate the non-equilibrium correlator, we use the latter formulation since it allows simpler expressions. The non-equilibrium correlation function then reads:

$$\begin{aligned}\left\langle \exp\left\{ i2\pi \sum_k g_{\alpha j} g_{\beta j} \left(\theta(t - t_k^u) - \theta(t' - t_k^u)\right)\right\}\right\rangle_{\text{n-eq}} \\ = \prod_\beta \sum_{N_\beta=0}^{\infty} e^{-P_\beta \gamma_u |t-t'|} \frac{(P_\beta \gamma_u |t-t'|)^{N_\beta}}{N_\beta!} e^{2\pi i g_{\alpha j} g_{\beta j} N_\beta}.\end{aligned} \tag{7.30}$$

Where we have assumed there are N_β number of type$-\beta$ anyons arriving at the central QPC. The product over β takes care of the different types of anyons arriving at the central QPC. While this expression might look different, it is in fact fully equivalent to Equation (7.17). Indeed, reducing the latter to a product of two-point functions and examining it in the limit of vanishing cutoff leads to this realization. Continuing with the present calculation, we evaluate the sum in Equation (7.30) to find:

$$\begin{aligned}\left\langle \exp\left\{ i2\pi \sum_k g_{\alpha j} g_{\beta j} \left(\theta(t - t_k^u) - \theta(t' - t_k^u)\right)\right\}\right\rangle_{\text{n-eq}} \\ = \exp\left[\gamma_u (t-t') \left(1 - \sum_\beta P_\beta e^{2\pi i g_{\alpha j} g_{\beta j}}\right)\right],\end{aligned} \tag{7.31}$$

where we have used that $\sum_\beta P_\beta = 1$. From this, it is not difficult to see that

$$\begin{aligned}\left\langle e^{i\boldsymbol{g_\alpha}\cdot\bar{\boldsymbol{\phi}}^{\boldsymbol{u}}(0,t^\eta)} e^{-i\boldsymbol{g_\alpha}\cdot\bar{\boldsymbol{\phi}}^{\boldsymbol{u}}(0,t'^{\eta'})}\right\rangle \left\langle e^{-i\boldsymbol{g_\alpha}\cdot\bar{\boldsymbol{\phi}}^{\boldsymbol{d}}(0,t^\eta)} e^{i\boldsymbol{g_\alpha}\cdot\bar{\boldsymbol{\phi}}^{\boldsymbol{d}}(0,t'^{\eta'})}\right\rangle \\ = e^{2\delta_{\boldsymbol{g}_\alpha}\mathcal{G}(t-t')} \times \exp\left[-\gamma_u (t-t') \left(1 - \sum_\beta P_\beta e^{2\pi i \boldsymbol{g_\alpha}\cdot\boldsymbol{g_\beta}}\right)\right] \\ \times \exp\left[-\gamma_d (t-t') \left(1 - \sum_\beta P_\beta e^{-2\pi i \boldsymbol{g_\alpha}\cdot\boldsymbol{g_\beta}}\right)\right]\end{aligned} \tag{7.32}$$

leading naturally to the integrand in Equation (7.22) (modulo Keldysh indices and the Hermitian conjugate). Hence, it is possible to avoid the formalism of prepared states and simply augment the bosonic fields with appropriate solitons and calculate the averages as defined in this section.

7.3.2. Tunneling noise

To illustrate the utility of non-equilibrium bosonization, we calculate the tunneling noise at the central QPC using this method. We start with the general expression of tunneling noise using the Keldysh formalism:

$$\langle S_T \rangle = \int dt' \sum_{\eta\eta'} \left\langle \left\{ T_K \delta I_T(t^\eta) \delta I_T(t'^{\eta'}) e^{-i\int_K dt H_T(t)} \right\} \right\rangle , \tag{7.33}$$

where $\delta I_T(t) = I_T(t) - \langle I_T \rangle$. To lowest order in the tunneling amplitudes of the central QPC, this reads

$$\begin{aligned} \langle S_T \rangle = \sum_\alpha |\Gamma_{\boldsymbol{g_\alpha}}|^2 q_{\boldsymbol{g}_\alpha}^2 \sum_\epsilon \sum_{\eta\eta'} \int dt' \\ \left\langle \left\{ T_K \left[e^{-i\boldsymbol{g_\alpha}\cdot\bar{\boldsymbol{\phi}}^{\boldsymbol{u}}(0,t^\eta)} e^{i\boldsymbol{g_\alpha}\cdot\bar{\boldsymbol{\phi}}^{\boldsymbol{d}}(0,t^\eta)} \right]^\epsilon \left[e^{-i\boldsymbol{g_\alpha}\cdot\bar{\boldsymbol{\phi}}^{\boldsymbol{u}}(0,t'^{\eta'})} e^{i\boldsymbol{g_\alpha}\cdot\bar{\boldsymbol{\phi}}^{\boldsymbol{d}}(0,t'^{\eta'})} \right]^{-\epsilon} \right\} \right\rangle \end{aligned} \tag{7.34}$$

where the bar on the bosonic fields denotes the existence of non-equilibrium anyonic solitons on the bosonic field. We now separate the correlation function of the bosonic fields on the upper and lower edges:

$$\begin{aligned} \langle S_T \rangle = \sum_\alpha |\Gamma_{\boldsymbol{g_\alpha}}|^2 q_{\boldsymbol{g}_\alpha}^2 \sum_\epsilon \sum_{\eta\eta'} \int dt' \prod_j \left\langle \left\{ T_K e^{-i\epsilon g_{\alpha j} \bar{\phi}_j^u(0,t^\eta)} e^{i\epsilon g_{\alpha j} \bar{\phi}_j^u(0,t'^{\eta'})} \right\} \right\rangle \\ \times \left\langle \left\{ T_K e^{i\epsilon g_{\alpha j} \bar{\phi}_j^d(0,t^\eta)} e^{-i\epsilon g_{\alpha j} \bar{\phi}_j^d(0,t'^{\eta'})} \right\} \right\rangle . \end{aligned} \tag{7.35}$$

Separating further the equilibrium correlators from the non-equilibrium solitonic correlators, we can write

$$\begin{aligned} \langle S_T \rangle = \sum_\alpha |\Gamma_{\boldsymbol{g_\alpha}}|^2 q_{\boldsymbol{g}_\alpha}^2 \sum_\epsilon \sum_{\eta\eta'} \int dt' \prod_j \left\langle \left\{ T_K e^{-i\epsilon g_{\alpha j} \phi_j^u(0,t^\eta)} e^{i\epsilon g_{\alpha j} \phi_j^u(0,t'^{\eta'})} \right\} \right\rangle \\ \left\langle \left\{ T_K e^{i\epsilon g_{\alpha j} \phi_j^d(0,t^\eta)} e^{-i\epsilon g_{\alpha j} \phi_j^d(0,t'^{\eta'})} \right\} \right\rangle \\ \left\langle e^{-2\pi i\epsilon \sum_k g_{\alpha j} g_{\beta j} \left(\theta(t-t_k^u) - \theta(t'-t_k^u)\right)} \right\rangle_{\text{n-eq}} \left\langle e^{2\pi i\epsilon \sum_k g_{\alpha j} g_{\beta j} \left(\theta(t-t_k^d) - \theta(t'-t_k^d)\right)} \right\rangle_{\text{n-eq}} \end{aligned} \tag{7.36}$$

Then we use the non-equilibrium average defined in Equation (7.30), to express the tunneling noise as

$$\begin{aligned}\langle S_T\rangle = \sum_{\alpha} |\Gamma_{\boldsymbol{g_\alpha}}|^2 q_{\boldsymbol{g}_\alpha}^2 \sum_{\epsilon}\sum_{\eta\eta'}\int_{-\infty}^{\infty} dt' e^{2\delta_{\boldsymbol{g_\alpha}}\mathcal{G}(\sigma_{\eta\eta'}(t-t'))} \\ \exp\left[-\gamma_u(t-t')\left(1-\sum_{\beta}P_\beta e^{2\pi i\epsilon \boldsymbol{g_\alpha}.\boldsymbol{g_\beta}}\right)\right] \\ \exp\left[-\gamma_d(t-t')\left(1-\sum_{\beta}P_\beta e^{-2\pi i\epsilon \boldsymbol{g_\alpha}.\boldsymbol{g_\beta}}\right)\right]\end{aligned} \tag{7.37}$$

yielding an expression similar to the one obtained for current from the augmented state calculations. Summing over ϵ and the Keldysh indices, we can conveniently express the tunneling noise as

$$\langle S_T\rangle = \sum_{\alpha} 4|\Gamma_{\boldsymbol{g_\alpha}}|^2 q_{\boldsymbol{g}_\alpha}^2 \int_0^{\infty} d\tau \frac{\cos\left[\gamma_-\tau\sum_\beta P_\beta \sin\left(2\pi \boldsymbol{g_\alpha}.\boldsymbol{g_\beta}\right)\right]}{\exp\left[\gamma_+\tau\sum_\beta P_\beta\left(1-\cos\left(2\pi \boldsymbol{g_\alpha}.\boldsymbol{g_\beta}\right)\right)\right]}\left[e^{2\delta_{\boldsymbol{g}_\alpha}\mathcal{G}(\tau)}+e^{2\delta_{\boldsymbol{g}_\alpha}\mathcal{G}(-\tau)}\right], \tag{7.38}$$

where we have again made the transformations $\gamma_\pm = \gamma_u \pm \gamma_d$, and $\tau = t - t'$. The sum of the Greens functions at zero temperature is reduced to $2\tau^{-2\delta_{\boldsymbol{g}_\alpha}}\tau_0^{2\delta_{\boldsymbol{g}_\alpha}}\cos\left(\pi\delta_{\boldsymbol{g}_\alpha}\right)$ and calculating the integral yields

$$\langle S_T\rangle = \sum_{\alpha} c_\alpha q_{\boldsymbol{g}_\alpha}\cos\left(\pi\delta_{\boldsymbol{g}_\alpha}\right)\mathrm{Re}\left[\left(\mathcal{C}_{\boldsymbol{g_\alpha}}+ix\mathcal{S}_{\boldsymbol{g_\alpha}}\right)^{2\delta_{\boldsymbol{g}_\alpha}-1}\right] \tag{7.39}$$

with the quantities $x, c_\alpha, \mathcal{C}_{\boldsymbol{g_\alpha}}, \mathcal{S}_{\boldsymbol{g_\alpha}}$ defined in Equation (7.26).

7.4. Cross-correlations and generalized Fano factor

A convenient quantity to experimentally measure is the cross-correlation of currents coming out of the two arms of the central QPC. Let $\tilde{I}_u/\tilde{I}_d$ be the output current of the central QPC on the upper/lower edge. The presence of the central QPC allows a non-zero tunneling current I_T, from the upper to the lower edge. We hence have $\tilde{I}_u = I_u - I_T$ and $\tilde{I}_d = I_d + I_T$. Hence the correlation between the currents $\tilde{I}_u$ and $\tilde{I}_d$ is:

$$\left\langle \delta\tilde{I}_u \delta\tilde{I}_d\right\rangle = -\langle S_T\rangle + \langle \delta I_T \delta I_u\rangle - \langle \delta I_T \delta I_d\rangle . \tag{7.40}$$

The first term on the RHS is the tunneling noise, calculated in the preceding section, caused by the partitioning at the central QPC. The next two terms give the *injection*

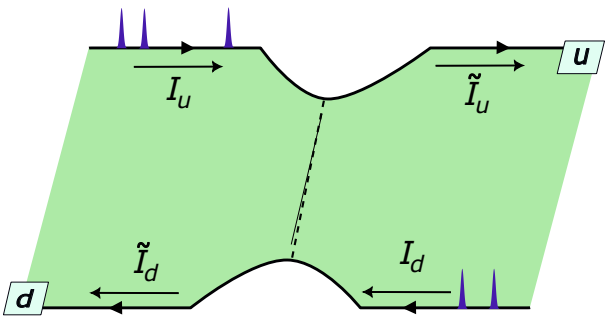


Figure 7.3.: Schematic showing input and output currents of the central QPC in the collider. Source QPCs are not shown.

noise, which is due to the fluctuations in the incoming current. The latter is related to the tunneling current $\langle I_T \rangle$ via a *fluctuation-dissipation* relation

$$\langle \delta I_T \delta I_{u0} \rangle - \langle \delta I_T \delta I_{d0} \rangle = \sum_\beta q_{\boldsymbol{g\beta}} \left[(\gamma_u P_\beta) \frac{\partial}{\partial (\gamma_u P_\beta)} - (\gamma_d P_\beta) \frac{\partial}{\partial (\gamma_d P_\beta)} \right] \langle I_T \rangle \,, \tag{7.41}$$

shown explicitly in Appendix G. This relation allows us to express the cross-correlation in terms of the tunneling noise and derivatives of the tunneling current:

$$\left\langle \delta \tilde{I}_u \delta \tilde{I}_d \right\rangle = - \langle S_T \rangle + \sum_\beta q_{\boldsymbol{g\beta}} \left[(\gamma_u P_\beta) \frac{\partial}{\partial (\gamma_u P_\beta)} - (\gamma_d P_\beta) \frac{\partial}{\partial (\gamma_d P_\beta)} \right] \langle I_T \rangle \tag{7.42}$$

As is usual in FQHE edge experiments, any single quantity is riddled with non-universal factors. These are represented in our equations by the tunneling amplitudes. A natural way to get rid of these non-universalities is to study a ratio of two quantities measured at the same QPC. Indeed, this was the objective of studying the Fano factor to measure the fractional charges, addressed in Section 2.4.1. Building on the proposal of Ref.[33] we define here a generalized Fano factor, dividing the cross-correlations by the differential transmission of the QPC – the derivative of the tunneling current with respect to the incoming current – leading to the following definition of the so called $P-$value:

$$P(x) = \frac{\langle \delta I_u \delta I_d \rangle}{\langle q \rangle \, \gamma_+ \frac{\partial \langle I_T \rangle}{\partial \gamma_-}\big|_{\gamma_-=0}} \tag{7.43}$$

where $x = \gamma_+/\gamma_-$, and $\langle q \rangle = \sum_\alpha P_{\boldsymbol{g\alpha}} q_\alpha$ is the average charge of all the anyon-antianyon pairs tunneling at the central QPC. In contrast to the proposal of Ref. [33], the $P-$value defined above accommodates multiple bosonic modes on the edges, and multiple types of quasiparticles tunneling simultaneously at the QPC. Nevertheless, it coincides with the generalized Fano factor of Ref. [33] when there exists a single bosonic mode on the edge, and a unique anyon tunnels across all the QPCs. The generalized Fano factor can be written out explicitly as

$$
\begin{aligned}
P(x) = &-\frac{\sum_\alpha c_\alpha q_{\boldsymbol{g}_\alpha} \cos\left(\pi\delta_{\boldsymbol{g}_\alpha}\right) \mathrm{Re}\,\xi_{\boldsymbol{g}_\alpha}^{2\delta_{\boldsymbol{g}_\alpha}-1}}{\sum_\alpha c_\alpha (2\delta_{\boldsymbol{g}_\alpha}-1)\sin\left(\pi\delta_{\boldsymbol{g}_\alpha}\right)\langle q\rangle\, \mathcal{S}_{\boldsymbol{g}_\alpha}\mathcal{C}_{\boldsymbol{g}_\alpha}^{2\delta_{\boldsymbol{g}_\alpha}-2}} \\
&+\frac{\sum_\alpha c_\alpha (2\delta_{\boldsymbol{g}_\alpha}-1)\sin\left(\pi\delta_{\boldsymbol{g}_\alpha}\right)\left[\mathcal{S}_{\boldsymbol{g}_\alpha}^{(q)}\,\mathrm{Re}\,\xi_{\boldsymbol{g}_\alpha}^{2\delta_{\boldsymbol{g}_\alpha}-2} + x\mathcal{C}_{\boldsymbol{g}_\alpha}^{(q)}\,\mathrm{Im}\,\xi_{\boldsymbol{g}_\alpha}^{2\delta_{\boldsymbol{g}_\alpha}-2}\right]}{\sum_\alpha c_\alpha (2\delta_{\boldsymbol{g}_\alpha}-1)\sin\left(\pi\delta_{\boldsymbol{g}_\alpha}\right)\langle q\rangle\, \mathcal{S}_{\boldsymbol{g}_\alpha}\mathcal{C}_{\boldsymbol{g}_\alpha}^{2\delta_{\boldsymbol{g}_\alpha}-2}}
\end{aligned}
\tag{7.44}
$$

where we are using the notation defined Equation (7.26), and we have introduced more notation for compactness:

$$
\begin{aligned}
\xi_{\boldsymbol{g}_\alpha} &= \mathcal{C}_{\boldsymbol{g}_\alpha} + i\mathcal{S}_{\boldsymbol{g}_\alpha} \\
\mathcal{C}_{\boldsymbol{g}_\alpha}^{(q)} &= \sum_\beta P_\beta q_{\boldsymbol{g}_\beta}\left[1-\cos\left(2\pi\boldsymbol{g}_\alpha.\boldsymbol{g}_\beta\right)\right] \\
\mathcal{S}_{\boldsymbol{g}_\alpha}^{(q)} &= \sum_\beta P_\beta q_{\boldsymbol{g}_\beta}\sin\left(2\pi\boldsymbol{g}_\alpha.\boldsymbol{g}_\beta\right).
\end{aligned}
\tag{7.45}
$$

This quantity gets rid of non-universal tunneling amplitudes contained in c_α (see Equation (7.26)) when all tunneling anyons have equal scaling dimension. The $P-$value carries an explicit dependence on the exchange phase of incoming and tunneling anyons, $\boldsymbol{g}_\alpha.\boldsymbol{g}_\beta$. Hence, a measurement of this generalized Fano factor can be used to extract the exchange phases. Note that the Fano factor also depends on the scaling dimension $\delta_{\boldsymbol{g}_\alpha}$, which also carries some non-universality. However, it has been shown that this effect is quantitatively less important (see Ref.[37] and also Section 7.7.2).

Specializing to the case of single bosonic mode along the edge, and unique anyon tunneling at all the QPCs (amounts to setting $\Gamma_{\boldsymbol{g}_\alpha}, P_{\boldsymbol{\beta}} = 0$ for $\alpha,\beta \neq 1$) we arrive at the following expression for the Fano factor:

$$
\begin{aligned}
P(x) = \mathrm{Re}\left[1+i\frac{x}{\tan\left(\pi\lambda_{\boldsymbol{gg}}\right)}\right]^{2\delta_{\boldsymbol{g}}-2} &+ x\tan\left(\pi\lambda_{\boldsymbol{gg}}\right)\mathrm{Im}\left[1+i\frac{x}{\tan\left(\pi\lambda_{\boldsymbol{gg}}\right)}\right]^{2\delta_{\boldsymbol{g}}-2} \\
&+\frac{1}{2\delta-1}\frac{\tan\left(\pi\lambda_{\boldsymbol{gg}}\right)}{\tan\left(\pi\delta_{\boldsymbol{g}}\right)}\mathrm{Re}\left[1+i\frac{x}{\tan\left(\pi\lambda_{\boldsymbol{gg}}\right)}\right]^{2\delta_{\boldsymbol{g}}-1},
\end{aligned}
\tag{7.46}
$$

which for $x=0$, takes the simple value:

$$
P(x=0) = \frac{1}{2\delta_{\boldsymbol{g}}-1}\frac{\tan\left(\pi\lambda_{\boldsymbol{gg}}\right)}{\tan\left(\pi\delta_{\boldsymbol{g}}\right)},
\tag{7.47}
$$

recovering the results of Ref.[33].

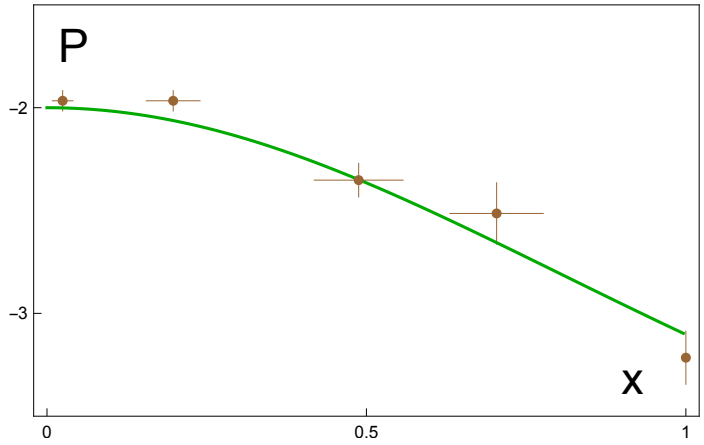


Figure 7.4.: Theoretical predictions of the $P-$value as a function of current asymmetry for $\nu = 1/3$ (green curve) from Ref. [33] compared with experimental data from Ref.[37] (brown points), showing an excellent agreement.

7.5. Experimental status

The anyon collider experiment, first implemented in 2020, provided the inaugural experimental evidence for anyonic exchange statistics in the $\nu = 1/3$ FQHE [34]. Since then, this experiment has been successfully reproduced several times, both in the simpler $\nu = 1/3$ system and the more complex $\nu = 2/5$ system [37–39]. In these experiments, the generalized Fano factor, as defined in Equation (7.43), was measured as a function of current asymmetry to extract the braiding phase. Below, we discuss the current experimental status for both these filling fractions and highlight the challenges that need to addressed by theory.

7.5.1. $\nu = 1/3$

In the simplest FQHE system of $\nu = 1/3$ with a single edge mode, the theoretical predictions of Ref.[33] agree perfectly with the experimental measurements [34, 37–39], as shown in Figure 7.4. The initial interpretation of this setup was based on fractional exclusion of anyons coming from the source QPCs colliding at the central QPC. However, it was later shown that the Poissonian emission statistics of the source QPCs (in the weak-backscattering regime) implies that such collisions are very rare. As emphasized in this thesis, it has been explicitly shown that the anyon collider experiment probes time-domain braiding processes due to braiding of incoming anyons from the source QPC, with those tunneling at the central QPC [86, 121, 122].

It is important to note that the predictions of Ref. [33] are geared towards simple Laughlin fractions such as the $\nu = 1/3$ state, where a single bosonic mode propagates

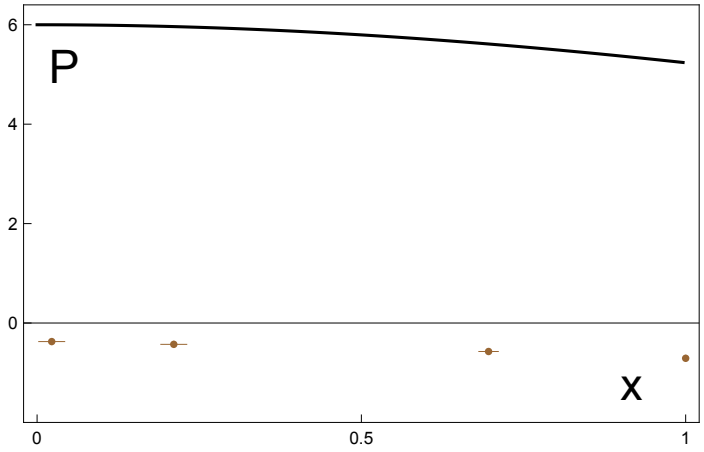


Figure 7.5.: Theoretical predictions of the $P-$value of Equation (7.46) adapted to $\nu = 2/5$ (black curve), compared with experimental data of Ref. [37] (brown points). There is a strong disagreement between theory and experiment, even with the sign of the $P-$value.

along the quantum Hall edge, and a unique anyon tunnels at the QPC. A complete theory of the anyon collider for an arbitrary Abelian quantum Hall system, comprising multiple bosonic modes on the edge, and different types of anyons tunneling at the QPC was absent in Ref. [33].

7.5.2. $\nu = 2/5$

The same experiment at $\nu = 2/5$ [37–39] was in spectacular disagreement with the theoretical prediction of Ref. [33]. Although the latter did not lay down an explicit theory of general Abelian quantum Hall systems, it is possible to adapt the parameters of braiding phase and scaling dimension to address non-Laughlin fractions. This amounts to taking $\lambda_{\boldsymbol{gg}} = 3/5$ and $\delta_{\boldsymbol{g}} = 3/5$ in Equation (7.46). Doing this, one finds a strong disagreement between theory and experiment: theory predicts a large, positive Fano factor (close to 6) while experiments measure a small, negative Fano factor (close to -1) as shown in Figure 7.5 .

This disagreement directly relates to the tunneling current physics discussed towards end of Chapter 6. In the 2/5 FQHE, $e/5$ anyons have an exchange phase of $3\pi/5$, which, using Equation (7.46), predicts a negative tunneling current at the QPC. While this result can be theoretically explained through time-domain braiding processes, experiments consistently observe a positive tunneling current, leading to a sign mismatch in the predicted $P-$value. Resolving this discrepancy between theory and experiment at $\nu = 2/5$ is essential for a deeper understanding of anyons.

In the following, we apply the theory developed in the previous sections to two experimentally significant non-Laughlin FQHE systems: $\nu = 2/3$ and $\nu = 2/5$. For the $\nu = 2/5$ system, our focus is to reconcile theoretical predictions with experimental results, while for the $\nu = 2/3$ system, we provide explicit predictions in anticipation of future experiments.

7.6. $\nu = 2/3$: predictions from the generalized model

So far, we have discussed anyon braiding in the $\nu = 1/3$ and $\nu = 2/5$ fractional quantum Hall states, both of which are fully chiral with all bosonic edge modes propagating in the same direction. However, the $\nu = 2/3$ state features counter-propagating charge and neutral modes, and hence offers a richer perspective on anyon braiding. In this state, a generic anyon consists of excitations on both these modes. When an anyon is emitted at the source QPCs, its charge and neutral components separate and propagate in opposite directions. This separation allows for the independent study of the braiding of charge and neutral excitations.

Notably, a similar edge structure with counter-propagating charge and neutral (non-Abelian) modes is predicted in the anti-Pfaffian and particle-hole Pfaffian candidate states of $\nu = 5/2$. Understanding braiding in the $\nu = 2/3$ state could therefore provide valuable insights into these more complex systems. Although anyon collider experiments have thus far only been performed on the $\nu = 1/3$ and $\nu = 2/5$ states, no technical obstacles are preventing similar studies in the $\nu = 2/3$ state. Indeed, our interest in $\nu = 2/3$ is driven by preliminary, unpublished experimental results [149].

We consider here the canonical model of $\nu = 2/3$ FQHE, comprising two counter-propagating bosonic modes. A downstream charged mode and an upstream neutral mode [155]. This edge structure is captured by the inputs $N = 2$, $\boldsymbol{Q} = (\sqrt{2/3}, 0)$ and $\boldsymbol{\chi} = (+1, -1)$, giving the number, conductance, and chiralities of the bosonic modes respectively, as described in Section 2.2. The resulting electron and anyon vectors are listed in Table 7.1, which are related to the operators by $\psi_{\boldsymbol{e_\alpha}} = e^{i\boldsymbol{e_\alpha}\cdot\boldsymbol{\phi}}$ and $\psi_{\boldsymbol{g_\alpha}} = e^{i\boldsymbol{g_\alpha}\cdot\boldsymbol{\phi}}$, respectively. Interestingly, for $\nu = 2/3$ we find three anyons of the same scaling dimension: two carrying charge $e/3$, and the third carrying charge $2e/3$. From Table 7.1 we see that $e/3$ anyons are composed of charged and neutral excitations. When an $e/3$ quasiparticle is emitted at the source QPC, the charged excitation propagates in one direction, and the neutral excitation propagates in the opposite direction. Although the anyon when emitted at the source QPC is whole, the neutral and charge excitations of the quasiparticle separate and propagate in opposite directions, making it possible to consider the braiding of charged and neutral excitations separately.

Type (α)	$e_{\alpha 1}$	$e_{\alpha 2}$	$\delta_{\boldsymbol{e_\alpha}}$
$\boldsymbol{e}_1$	$\sqrt{\frac{3}{2}}$	$\sqrt{\frac{1}{2}}$	2
$\boldsymbol{e}_2$	$\sqrt{\frac{3}{2}}$	$-\sqrt{\frac{1}{2}}$	2

Type (α)	$g_{\alpha 1}$	$g_{\alpha 2}$	$q_{\boldsymbol{g}_\alpha}$	$\delta_{\boldsymbol{g}_\alpha}$
$\boldsymbol{g}_1$	$\sqrt{\frac{1}{6}}$	$\sqrt{\frac{1}{2}}$	1/3	2/3
$\boldsymbol{g}_2$	$\sqrt{\frac{1}{6}}$	$-\sqrt{\frac{1}{2}}$	1/3	2/3
$\boldsymbol{g}_3$	$\sqrt{\frac{2}{3}}$	0	2/3	2/3

Table 7.1.: Electron operators (left) and quasiparticle operators (right) for $\nu = 2/3$ FQHE with $\boldsymbol{Q} = (\sqrt{2/3}, 0)$ and $\boldsymbol{\chi} = (+1, -1)$.

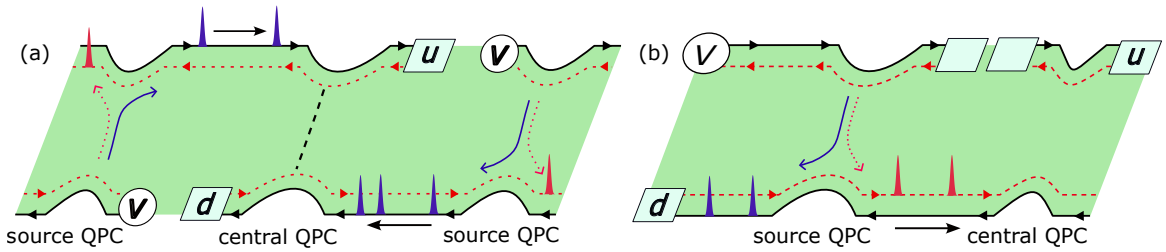


Figure 7.6.: Braiding of anyons in $\nu = 2/3$ FQHE. $\nu = 2/3$ edge comprises counter-propagating charge (black, solid) and neutral (red, dashed) modes. (a) Charged mode flows towards the central QPC. Both source QPCs are biased with a voltage V, sending charged part of the anyons to the central QPC. The tunneling current and current correlations are measured as discussed before. (b) Neutral mode flows towards the central QPC. Here, a single source QPC is biased with a voltage V, sending a stream of neutral anyons to the central QPC. The resulting current auto-correlations are measured at contact d

7.6.1. Charged mode braiding

To study the braiding of charged excitations, we consider the scenario shown in Figure 7.6(a) where the charged excitations emitted at the source QPCs flow towards the central QPC. On the other hand, the neutral excitations flow away from the central QPC. As discussed in Section 6.2, in this case, the braiding phase of the incoming anyon with the anyons generated in the central QPC comprises only the excitations flowing towards the central QPC. When only the charged excitations reach the QPC, we have: $\lambda_{\boldsymbol{g_\alpha g_\beta}} = g_{\alpha 1} g_{\beta 1}$ (where 1 is the index of the charged bosonic mode). Keeping this in mind, the mutual braiding statistics of different anyons is given as: $\lambda_{\boldsymbol{g_1 g_1}} = \lambda_{\boldsymbol{g_2 g_2}} = \lambda_{\boldsymbol{g_1 g_2}} = 1/6$, $\lambda_{\boldsymbol{g_3 g_1}} = \lambda_{\boldsymbol{g_3 g_2}} = 1/3$, and $\lambda_{\boldsymbol{g_3 g_3}} = 2/3$ (see Table 7.1). However, although there are no incoming neutral excitations, neutral anyonic excitations are nevertheless generated at the central QPC. Thus the dynamics at the central QPC comprises both the charge and neutral modes, thus leaving the scaling dimensions unchanged: $\delta_{\boldsymbol{g_1}} = \delta_{\boldsymbol{g_2}} = \delta_{\boldsymbol{g_3}} = 2/3$.

Figure 7.7 shows the generalized Fano factor for charge mode braiding in $\nu = 2/3$. Since we have different types of incoming and tunneling anyons, we consider three distinct possibilities.

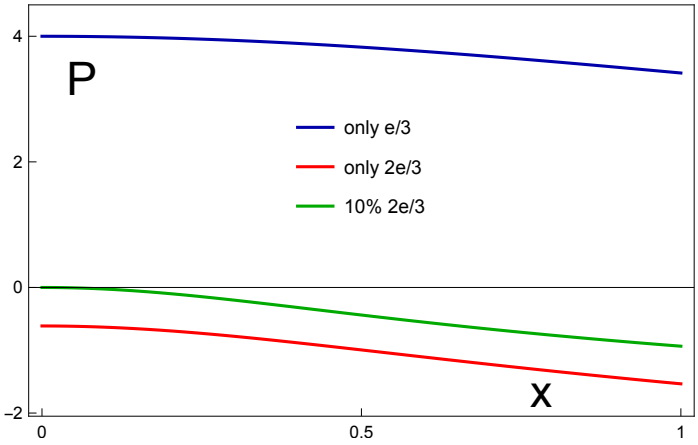


Figure 7.7.: Generalized Fano factor as a function of current asymmetry for $\nu = 2/3$. We consider three possible scenarios: tunneling of only $2e/3$ quasiparticles, only $e/3$ quasiparticles, and a mix of the two with 10% of the tunneling entities being $2e/3$.

First, when both the incoming and tunneling anyons are the ones with charge $2e/3$, we find a positive $P-$value, akin to that found for $\nu = 2/5$ in Section 7.5.2. There, the reason was an exchange phase $\lambda_{gg} = 3/5 > 1/2$, leading to a prediction of a negative tunneling current, thus flipping the sign of the $P-$value. We have a similar situation here with $\lambda_{g_3 g_3} = 2/3$ which explains the prediction of a positive $P-$value.

Secondly, we consider the incoming and tunneling anyons to be ones with charge $e/3$. This scenario predicts a zero cross-correlations for $x = 0$, and as x is increased, the $P-$value increases in magnitude. This presents an interesting scenario to explore experimentally, as, despite a non-equilibrium drive, the anyonic exchange phase and scaling dimension conspire to produce a zero cross-correlation noise at $x = 0$, reminiscent of fermionic behavior [33, 34].

Lastly, we explore the scenario where all types of anyons tunnel simultaneously at the source and central QPCs. Specifically, we consider 10% of all tunneling entities to be $2e/3$ quasiparticles, with the rest being $e/3$ quasiparticles. This choice is motivated by DC shot noise measurements in $\nu = 2/3$ which predominantly measure a $e/3$ charge. Nevertheless, as explained in Chapter 3, these measurements can be insensitive to a small proportion of $2e/3$ charges tunneling simultaneously with the $e/3$ charges. In this case, we have a finite cross-correlation even at $x = 0$, and the magnitude of the $P-$value still increases with x, similar to the behavior observed for $\nu = 1/3$ and $2/5$.

7.6.2. Neutral mode braiding

Now we examine the braiding of neutral excitations. Since the $2e/3$ anyons do not consist of neutral excitations, we are free to drop this anyon in the forthcoming discussion. With

inputs from preliminary experimental efforts, we consider the geometry shown in Figure 7.6(b) with a single source QPC, where neutral excitations propagate towards the second QPC, while charge excitations propagate away from it.

At the second QPC, both charge and neutral excitations are generated, and the incoming neutral excitations braid with tunneling ones, creating *charge noise* in the process. This noise can be measured in contacts u and d, to probe the braiding of neutral modes.

In this setup, it is experimentally easier to access the auto-correlation noise on say, contact u, as opposed to cross-correlation noise considered before. In the low-temperature limit, the autocorrelation noise is the same as the tunneling noise $\langle S_T \rangle$ (the correlation of the edge and tunneling *charge* currents are zero in this system). Adapting Equation (7.39) to the present situation with a single QPC, we set $x = 1$, and $\gamma_+ = \gamma_N$, where γ_N denotes the number current of incoming neutral excitations

$$\langle S_T \rangle = \sum_{\alpha} c_\alpha q_{\boldsymbol{g}_\alpha} \cos\left(\pi \delta_{\boldsymbol{g}_\alpha}\right) \mathrm{Re}\left[\left(\mathcal{C}_{\boldsymbol{g}_\alpha} + i\mathcal{S}_{\boldsymbol{g}_\alpha}\right)^{2\delta_{\boldsymbol{g}_\alpha}-1}\right]. \tag{7.48}$$

Since neutral excitations typically do not produce a non-zero charge current at the QPC, we apply a small voltage at the edge, to achieve a non-zero tunneling current at the QPC. We hence want to calculate the tunneling current at the QPC, due to incoming neutral excitations from one side, and small bias voltage on the other. We start from the following expression

$$\langle I_T \rangle = \sum_{\epsilon\alpha\eta\eta'} \epsilon\eta' |\Gamma_{\boldsymbol{g}_\alpha}|^2 q_{\boldsymbol{g}_\alpha} \int_{-\infty}^{\infty} dt' e^{i\epsilon q_{\boldsymbol{g}_\alpha} V(t-t')} e^{-\gamma_N |t-t'| \left(1 - \sum_\beta P_\beta e^{-2i\pi \epsilon \boldsymbol{g}_\alpha \cdot \boldsymbol{g}_\beta}\right)} e^{2\delta_{\boldsymbol{g}_\alpha} \mathcal{G}^{\eta\eta'}(t-t')} \tag{7.49}$$

where the first term inside the integral is due to the voltage bias, and the second term is due to the neutral excitations. Summing over ϵ and the Keldysh indices, we find

$$\langle I_T \rangle = \sum_{\alpha} 4i |\Gamma_{\boldsymbol{g}_\alpha}|^2 q_{\boldsymbol{g}_\alpha} \int_0^{\infty} d\tau e^{-\gamma_N \mathcal{C}_{\boldsymbol{g}_\alpha}} \sin\left[\left(V q_{\boldsymbol{g}_\alpha} + \gamma_N \mathcal{S}_{\boldsymbol{g}_\alpha}\right)\tau\right] \left[e^{2\delta_{\boldsymbol{g}_\alpha}\mathcal{G}(t)} - e^{2\delta_{\boldsymbol{g}_\alpha}\mathcal{G}(-t)}\right] \tag{7.50}$$

where the notations are defined in Equation (7.26), After performing the integral, we obtain

$$\langle I_T \rangle = \sum_{\alpha} c_\alpha \sin\left(\pi \delta_{\boldsymbol{g}_\alpha}\right) \mathrm{Im}\left\{\left[\mathcal{C}_{\boldsymbol{g}_\alpha} + i\left(q_{\boldsymbol{g}_\alpha} V/\gamma_N + \mathcal{S}_{\boldsymbol{g}_\alpha}\right)\right]^{2\delta_{\boldsymbol{g}_\alpha}-1}\right\}. \tag{7.51}$$

With these, we define a new generalized Fano factor relevant for braiding of neutral excitations

$$P' = \frac{\langle S_T \rangle}{\langle q \rangle \, \gamma_N \frac{\partial \langle I_T \rangle}{\partial I_{in}}\big|_{V=0}} \tag{7.52}$$

where $I_{in} = \nu G_0 V$. We find the following expression for the P' factor

$$P' = \frac{\sum_\alpha c_\alpha q_{\boldsymbol{g}_\alpha} \cos\left(\pi\delta_{\boldsymbol{g}_\alpha}\right) \mathrm{Re}\left[\left(\mathcal{C}_{\boldsymbol{g}_\alpha} + i\mathcal{S}_{\boldsymbol{g}_\alpha}\right)^{2\delta_{\boldsymbol{g}_\alpha}-1}\right]}{\frac{\langle q \rangle}{\nu} \sum_\alpha c_\alpha \sin\left(\pi\delta_{\boldsymbol{g}_\alpha}\right)\left(1-2\delta_{\boldsymbol{g}_\alpha}\right) \mathrm{Re}\left[\left(\mathcal{C}_{\boldsymbol{g}_\alpha} + i\mathcal{S}_{\boldsymbol{g}_\alpha}\right)^{2\delta_{\boldsymbol{g}_\alpha}-2}\right]} \tag{7.53}$$

For braiding of neutral excitations, again $\lambda_{\boldsymbol{g_\alpha g_\beta}} = g_{\alpha 2} g_{\beta 2}$ (where 2 is the index of the neutral bosonic mode). We can then calculate from Table 7.1, $\lambda_{\boldsymbol{g_1 g_1}} = \lambda_{\boldsymbol{g_2 g_2}} = \lambda_{\boldsymbol{g_1 g_2}} = \pm 1/2$, and hence $\mathcal{S}_{\boldsymbol{g}_1} = \mathcal{S}_{\boldsymbol{g}_2} = 0$, and $\mathcal{C}_{\boldsymbol{g}_1} = \mathcal{C}_{\boldsymbol{g}_2} = 2$. Moreover, since the $2e/3$ charge quasiparticle drops out, $\langle q \rangle = q_{\boldsymbol{g}_1} = q_{\boldsymbol{g}_2} = e/3$, and of course $\delta_{\boldsymbol{g}_1} = \delta_{\boldsymbol{g}_2} = 2/3$. With these simplifications, we have

$$P' = \frac{2\cos\left(2\pi/3\right) 2^{4/3-1}}{\left(1-4/3\right)\sin\left(4\pi/3\right) 2^{4/3-2}} \approx 6.93 \tag{7.54}$$

In the single source geometry considered here, we do not have the current asymmetry as a parameter, reducing our predictions to a single number. This raises concerns about comparing our theoretical results with experimental data, since this number could be modified by non-universal edge physics such as interactions, leading to a non-universal scaling dimension, or edge reconstruction, among many other potential sources. Consequently, there is considerable scope for further investigation in this system.

7.7. $\nu = 2/5$: attempts to bridge theory and experiment

As explained in Section 7.5.2, there is a notable discrepancy between theory and experiment at $\nu = 2/5$. Theory predicts a large, positive $P-$value, while experiments measure small, negative $P-$value. This disagreement arises from the sign of the tunneling current: $e/5$ anyons in $\nu = 2/5$ are expected to have an exchange phase $3\pi/5$. For exchange phases greater than $\pi/2$, theory predicts a negative tunneling current. However, experiments unambiguously observe a positive tunneling current – a characteristic of anyons with exchange phase less than $\pi/2$. This discrepancy suggests that there is some mechanism within the system that effectively reduces the exchange phase seen at the central QPC to a value less than $\pi/2$, resulting in the observed positive tunneling current.

The relatively complex edge structure of $\nu = 2/5$ presents several potential mechanisms for this phase reduction, including different edge structures, simultaneous tunneling of different types of anyons and intra-edge interactions. The generalized theory of the anyon collider developed in Section 7.2 is well-suited to explore how these non-trivial edge effects influence the observable quantities of the collider, most importantly, the exchange phase and the $P-$value from which the former can be extracted in experiments.

7.7.1. Various edge models

We consider here different edge structures of the 2/5 FQHE defined by the inputs N, the number of bosonic modes on each edge, $\boldsymbol{Q}$ the charge vector that gives the conductance of the bosonic modes, and $\boldsymbol{\chi}$, the chirality vector that gives the chirality of each bosonic mode, as described in Section 2.2. The choice of these parameters will be motivated by experimental observations. We are free to choose these parameters with the crucial constraint that for an FQHE system of filling fraction ν, the above parameters must satisfy

$$\sum_{j=1}^{N} \chi_j Q_j^2 = \nu \tag{7.55}$$

This means that the conductance of the edge is given by the filling fraction of the bulk, a topologically quantized quantity.

We start with the canonical edge structure of the $\nu = 2/5$ FQHE, comprising two edge modes ($N = 2$), one each of conductance $G_0/3$ and $G_0/15$. This edge structure is inspired by Wen's picture of 2/5 FQHE [24] (see Figure 1.5). It is understood as a 1/3 FQHE whose quasiparticles form another Laughlin quantum Hall system of filling fraction 1/15, on top of the 1/3 FQHE as illustrated in Figure 1.5. Such a composite edge is described by the phenomenological inputs: $N = 2$, $\boldsymbol{Q} = (\sqrt{1/3}, \sqrt{1/15})$ and $\boldsymbol{\chi} = (1, +1)$. The conductance of the bosonic modes given by the latter charge vector are consistent with the conductance plateaus seen in experiments [37, 38].

With these inputs, we can use Equations (2.34) and (2.36) to find the lowest scaling dimension electron and anyon operators listed in Table 7.2(a). The numbers listed in 7.2(a) (and all other tables) are related to the electron operator by $\psi_{\boldsymbol{e_\alpha}} = e^{i\boldsymbol{e_\alpha}\cdot\boldsymbol{\phi}}$ and to the anyon operators by $\psi_{\boldsymbol{g_\alpha}} = e^{i\boldsymbol{g_\alpha}\cdot\boldsymbol{\phi}}$. The electron operators, using Equation (2.35), give the $K-$matrix

$$K = \begin{pmatrix} 3 & 2 \\ 2 & 3 \end{pmatrix} \tag{7.56}$$

and exchange statistics $\lambda_{\boldsymbol{g_1 g_1}} = \lambda_{\boldsymbol{g_1 g_2}} = \lambda_{\boldsymbol{g_2 g_2}} = 3/5$, where we remind the reader that $\lambda_{\boldsymbol{g_\alpha g_\beta}} = \boldsymbol{g_\alpha}\cdot\boldsymbol{g_\beta} = K^{-1}_{\alpha\beta}$.

An equally reasonable model is inspired by the spin unpolarized Halperin (m, m, n) state [46]. This admits an edge structure of two co-propagating bosonic modes of conductance $G_0/5$ each, which is described with the inputs $\boldsymbol{Q} = (\sqrt{1/5}, \sqrt{1/5})$ and $\boldsymbol{\chi} = (+1, +1)$, leading to the electron and anyon operators in Table 7.2(b). It is easy to see that these lead to the same $K-$matrix in Equation (7.56), and the same exchange statistics $\lambda_{\boldsymbol{g_1 g_1}} = \lambda_{\boldsymbol{g_1 g_2}} = \lambda_{\boldsymbol{g_2 g_2}} = 3/5$.

Another edge model is due to the possibility of disorder-induced tunneling between the bosonic modes [156]. Starting from the model of Table 7.2(a), inter-mode tunneling between the two charged bosonic modes can lead to an edge structure with a charge mode of conductance $2G_0/5$ and a co-propagating neutral mode. This edge structure is described by the inputs $\boldsymbol{Q} = (\sqrt{2/5}, 0)$ and $\boldsymbol{\chi} = (+1, +1)$. This model leads to the lowest scaling dimension electron and anyon operators listed in Table 7.2(c). We find yet again that this model leads to the same $K-$matrix of Equation (7.56) and the same exchange statistics of the anyons.

The three edge models described in this section, all with 2 co-propagating bosonic modes, lead to the same $K-$matrix, exchange statistics, and scaling dimensions of the anyonic quasiparticles. That is, holding N and $\boldsymbol{\chi}$ constant, and changing $\boldsymbol{Q}$, such that Equation (2.32) is respected, only rotates the vectors $\boldsymbol{g}_\alpha$, leaving the observables $\boldsymbol{g}_\alpha \cdot \boldsymbol{g}_\beta$ and $\delta_{\boldsymbol{g}_\alpha}$ invariant. All the models considered here give an exchange statistics $3\pi/5$ and scaling dimension $3/5$. The resulting $P-$value is compared with the experimental data in Figure 7.8(a). These predictions are of course the same as the one in Figure 7.5, severely disagreeing with the experiments.

7.7.2. $2e/5$ anyons

The theoretical model of 2/5 FQHE admits an anyon of charge $2e/5$, which has a lower scaling dimension than the $e/5$ quasiparticles, as shown in Table 7.3. Despite the emphasis throughout this thesis on the dominance of lowest scaling dimension operators, we ignore the $2e/5$ anyon simply because it is not observed in standard experimental conditions. Shot noise measurements in standard experimental conditions ascertain a charge $e/5$ tunneling at the QPCs. As discussed in Chapter 3, this type of measurement can be insensitive to small quantity of $2e/5$ charge tunneling along with the $e/5$ quasiparticles. Moreover, experiments have indeed observed tunneling of $2e/5$ anyons, albeit in relatively stringent experimental conditions [49, 69]. This motivates us to study the influence simultaneous tunneling of $e/5$ and a small proportion of $2e/5$ quasiparticles on the $P-$value.

In going about this, we immediately face a problem. The scaling dimension of the $2e/5$ quasiparticle is different from that of the $e/5$ quasiparticles, and the $P-$value of Equation (7.44) is not well suited to consider simultaneous tunneling of quasiparticles with different scaling dimensions. In this case, the tunneling amplitudes and input currents of

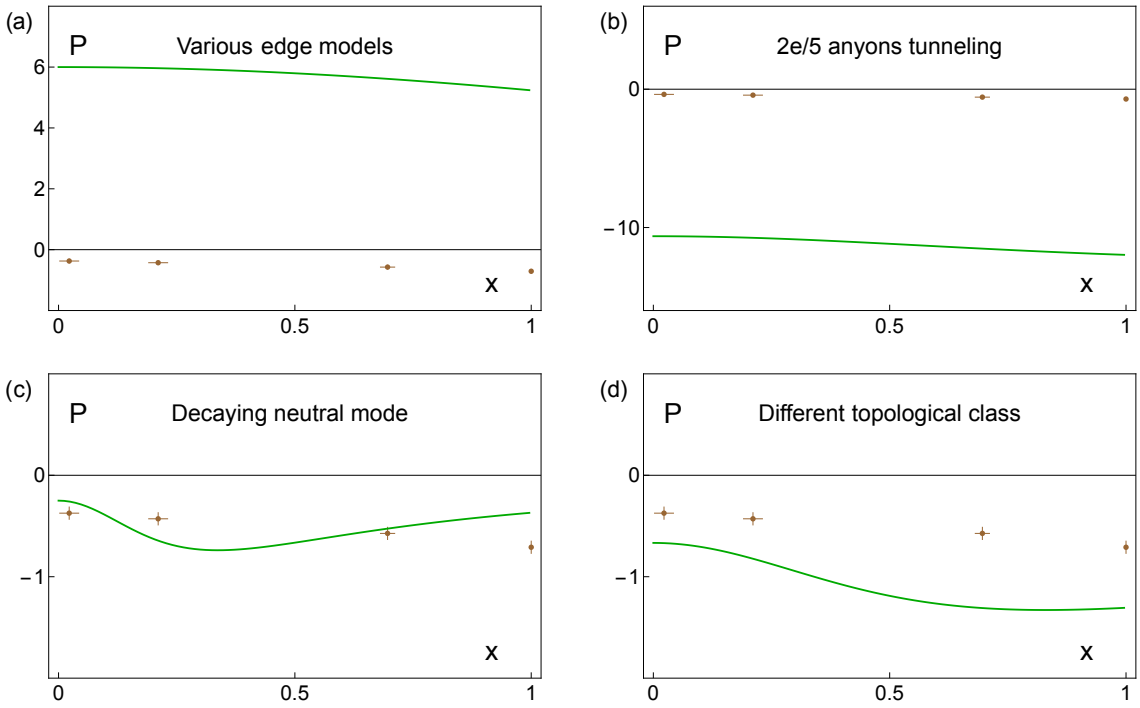


Figure 7.8.: We show here all the attempts to resolve the conflict between theory and experiment of the anyon collider at $\nu = 2/5$. The generalized Fano factor or $P-$value is plotted as a function of the current asymmetry, with the experimental data in brown and theoretical predictions in green.

(a) considers several edge models with two co-propagating edge modes [$N = 2$, $\boldsymbol{\chi} = (+1, +1)$], and different charge vectors: $\boldsymbol{Q} = (\sqrt{1/3}, \sqrt{1/15}), (\sqrt{1/5}, \sqrt{1/5}), (\sqrt{2/5}, 0)$. These edge models all host anyons with the same exchange statistics of $3\pi/5$, leading to severe disagreement with experimental data.

(b) considers simultaneous tunneling of $2e/5(20\%)$ and $e/5(80\%)$ anyons. The sign of the theoretical predictions agree with the data, but there is still a huge quantitative disagreement.

(c) considers an edge model with charge vector $\boldsymbol{Q} = (\sqrt{2/5}, 0)$ carrying a neutral bosonic mode. We consider that the neutral mode decays. Although theory and experiment agree well for small x, the agreement strongly departs for $x > 0.3$.

(d) considers an edge model with $\boldsymbol{Q} = (\sqrt{1/3}, \sqrt{1/15})$, but takes operators with higher scaling dimensions (in contrast to (a)). This model achieves a relatively better agreement with the experimental data but lacks formal justification.

Electron Operators

Type (α)	$e_{\alpha 1}$	$e_{\alpha 2}$	$\delta_{\boldsymbol{e}_\alpha}$
$\boldsymbol{e}_1$	$-\frac{2}{\sqrt{3}}$	$-\sqrt{\frac{5}{3}}$	3
$\boldsymbol{e}_2$	$-\sqrt{3}$	0	3

Anyon Operators

Type (α)	$g_{\alpha 1}$	$g_{\alpha 2}$	$q_{\boldsymbol{g}_\alpha}$	$\delta_{\boldsymbol{g}_\alpha}$
$\boldsymbol{g}_1$	0	$\sqrt{\frac{3}{5}}$	1/5	3/5
$\boldsymbol{g}_2$	$\sqrt{\frac{1}{3}}$	$-\frac{2}{\sqrt{15}}$	1/5	3/5

(a) $\boldsymbol{Q} = (\sqrt{1/3}, \sqrt{1/15})$ and $\boldsymbol{\chi} = (+1, +1)$

Type (α)	$e_{\alpha 1}$	$e_{\alpha 2}$	$\delta_{\boldsymbol{e}_\alpha}$
$\boldsymbol{e}_1$	$\frac{1-\sqrt{5}}{2}$	$-\frac{1+\sqrt{5}}{2}$	3
$\boldsymbol{e}_2$	$-\frac{1+\sqrt{5}}{2}$	$\frac{1-\sqrt{5}}{2}$	3

Type (α)	$g_{\alpha 1}$	$g_{\alpha 2}$	$q_{\boldsymbol{g}_\alpha}$	$\delta_{\boldsymbol{g}_\alpha}$
$\boldsymbol{g}_1$	$\frac{\sqrt{5}-5}{10}$	$\frac{\sqrt{5}+5}{10}$	1/5	3/5
$\boldsymbol{g}_2$	$\frac{\sqrt{5}+5}{10}$	$-\frac{2}{\sqrt{5}+5}$	1/5	3/5

(b) $\boldsymbol{Q} = (\sqrt{1/5}, \sqrt{1/5})$ and $\boldsymbol{\chi} = (+1, +1)$

Type (α)	$e_{\alpha 1}$	$e_{\alpha 2}$	$\delta_{\boldsymbol{e}_\alpha}$
$\boldsymbol{e}_1$	$-\sqrt{\frac{5}{2}}$	$\sqrt{\frac{1}{2}}$	3
$\boldsymbol{e}_2$	$-\sqrt{\frac{5}{2}}$	$-\sqrt{\frac{1}{2}}$	3

Type (α)	$g_{\alpha 1}$	$g_{\alpha 2}$	$q_{\boldsymbol{g}_\alpha}$	$\delta_{\boldsymbol{g}_\alpha}$
$\boldsymbol{g}_1$	$\sqrt{\frac{1}{10}}$	$\sqrt{\frac{1}{2}}$	1/5	3/5
$\boldsymbol{g}_2$	$\sqrt{\frac{1}{10}}$	$-\sqrt{\frac{1}{2}}$	1/5	3/5

(c) $\boldsymbol{Q} = (\sqrt{2/5}, 0)$ and $\boldsymbol{\chi} = (+1, +1)$

Table 7.2.: Electron and quasiparticle operators for different edge models of $\nu = 2/5$ FQHE. We obtain different sets of electron and anyon operators for each choice of $\boldsymbol{Q}$ and $\boldsymbol{\chi}$, indicated in the subcaptions.

Type (α)	$g_{\alpha 1}$	$g_{\alpha 2}$	$q_{\boldsymbol{g}_\alpha}$	$\delta_{\boldsymbol{g}_\alpha}$
$\boldsymbol{g}_1$	0	$\sqrt{\frac{3}{5}}$	1/5	3/5
$\boldsymbol{g}_2$	$\sqrt{\frac{1}{3}}$	$-\frac{2}{\sqrt{15}}$	1/5	3/5
$\boldsymbol{g}_3$	$\sqrt{\frac{1}{3}}$	$\frac{1}{\sqrt{15}}$	2/5	2/5

Table 7.3.: Anyon operators for $\nu = 2/5$ FQHE with $\boldsymbol{Q} = (\sqrt{1/3}, \sqrt{1/15})$ and $\boldsymbol{\chi} = (+1, +1)$, including the experimentally unobserved charge $2e/5$ quasiparticle.

the quasiparticles do not drop out of the equation, leading to a non-universal dependence of the $P-$value on these quantities. We circumvent this difficulty by considering the $2e/5$ quasiparticles to have a scaling dimension 3/5. While this assumption is *ad hoc* by all means, the non-universality of scaling dimensions has been well established. Moreover, it can be seen explicitly that the error introduced by changing scaling dimensions is minimal.

Indeed, at $x = 0$, for scaling dimensions 2/5 and 3/5 the $P-$values are exactly equal. The difference increases with the current asymmetry, and reaches a maximum of $\sim 6\%$ for $x = 1$.

In Figure 7.8(b), the $P-$value predictions for 20% tunneling of $2e/5$ quasiparticles simultaneously with the 80% $e/5$ quasiparticles, is compared with the experimental observations. Clearly, the theoretical predictions are nowhere close to the experimental data. However, it is interesting that the sign of the $P-$value predictions now agree with the data. Recall that the sign mismatch was due to the exchange statistics of $e/5$ anyons $\pi\lambda_{\boldsymbol{g_1}.\boldsymbol{g_1}} = \pi\lambda_{\boldsymbol{g_2}.\boldsymbol{g_2}} = \pi\lambda_{\boldsymbol{g_1}.\boldsymbol{g_2}} = 3\pi/5$ being greater than $\pi/2$, leading to a negative tunneling current. $2e/5$ anyons on the other hand are characterized by a self-exchange phase $\pi\lambda_{\boldsymbol{g_3}.\boldsymbol{g_3}} = 2\pi/5$, and a mutual exchange phase with the $e/5$ anyons $\pi\lambda_{\boldsymbol{g_1}.\boldsymbol{g_3}} = \pi\lambda_{\boldsymbol{g_2}.\boldsymbol{g_3}} = \pi/5$. The latter are both less than $\pi/2$, giving a positive tunneling current. Hence, as the proportion of $2e/5$ anyons increases, the net tunneling current becomes positive. It might be tempting to increase further the proportion of $2e/5$ anyons, to achieve agreement with the experiments. But one must keep in mind that DC shot noise experiments still measure a charge very close to $e/5$, which heavily constrains the maximum proportion of $2e/5$ anyons – 20% is already quite generous.

7.7.3. Killing the neutral mode

We focus now on the edge model of Table 7.2(c), which contains a charge mode of conductance $2G_0/5$, and a co-propagating neutral mode. It has been argued in the literature that neutral bosonic modes can be fully quenched at *high* temperatures that can be as low as 50mK [68, 69] – not far from the temperatures used in the anyon collider experiments [34, 37–39]. In this regime, the neutral mode becomes non-dynamical: its Green function vanishes and there is no propagation of excitations on the neutral mode.

Hence, only the charge excitations emitted on the source QPCs reach the central QPC and braid with the charge excitations tunneling there tunneling there. The braiding only of the charges excitations results in a reduced braiding phase seen at the central QPC:

$$\lambda_{\boldsymbol{g_\alpha}\boldsymbol{g_\beta}} \equiv \boldsymbol{g_\alpha}.\boldsymbol{g_\beta} = g_{\alpha 1}g_{\beta 1} + \cancel{g_{\alpha 2}g_{\beta 2}} = g_{\alpha 1}g_{\beta 1} \tag{7.57}$$

Since the neutral mode is non-dynamical, there are no pair creation events at the central QPC that contain the neutral mode. Hence, the neutral mode contribution to the scaling dimension also drops out:

$$\delta_{\boldsymbol{g}_\alpha} = \sum_{j=1,2} g_{\alpha j}^2 = g_{\alpha 1}^2 + \cancel{g_{\alpha 2}^2} = g_{\alpha 1}^2 \tag{7.58}$$

Hence, we are left with the parameters: $\lambda_{\boldsymbol{g_1}\boldsymbol{g_1}} = \lambda_{\boldsymbol{g_2}\boldsymbol{g_2}} = \lambda_{\boldsymbol{g_1}\boldsymbol{g_2}} = \delta_{\boldsymbol{g_1}} = \delta_{\boldsymbol{g_2}} = 1/10$. The $P-$value with a non-dynamical neutral mode is compared with the experimental data in Figure 7.8(c)

Type (α)	$e_{\alpha 1}$	$e_{\alpha 2}$	$\delta_{\boldsymbol{e_\alpha}}$
$\boldsymbol{e}_1$	$\frac{\sqrt{5}-5}{2\sqrt{3}}$	$-\frac{\sqrt{5}+5}{2\sqrt{3}}$	5
$\boldsymbol{e}_2$	$\frac{\sqrt{5}+5}{2\sqrt{3}}$	$-\frac{\sqrt{5}-5}{2\sqrt{3}}$	5

Type (α)	$g_{\alpha 1}$	$g_{\alpha 2}$	$q_{\boldsymbol{g}_\alpha}$	$\delta_{\boldsymbol{g}_\alpha}$
$\boldsymbol{g}_1$	$\sqrt{\frac{3-\sqrt{5}}{30}}$	$\sqrt{\frac{3+\sqrt{5}}{30}}$	1/5	1/5
$\boldsymbol{g}_2$	$\sqrt{\frac{3+\sqrt{5}}{30}}$	$\frac{\sqrt{5}-5}{10\sqrt{3}}$	1/5	1/5

Table 7.4.: Higher scaling dimension electron operators (left) and quasiparticle operators (right) for $\nu = 2/5$ FQHE with $\boldsymbol{Q} = (\sqrt{1/3}, \sqrt{1/15})$ and $\boldsymbol{\chi} = (+1, +1)$.

Although this model agrees well with experiments at small current asymmetry, it quickly diverges from the data as the asymmetry increases. The experimental data decreases monotonically with current asymmetry, while the predictions of $P-$value for the model with decaying neutral mode initially decreases but starts increasing around $x = 0.3$.

7.7.4. Different topological class

So far, we have been solving Equation (2.34) to obtain all possible electron operators on the edge, choosing the operators with the lowest scaling dimension, and using these to calculate the anyon operators. The second step above is based on the renormalization group arguments, that contributions from the lowest scaling dimension operators dominate at low energies. Let us now relax this assumption to consider higher scaling dimension electron operators. This implies considering a different topological class of the FQHE, described by different bulk wavefunction and $K-$matrix. The next lowest scaling dimension electron operators for the edge theory with $\boldsymbol{Q} = (\sqrt{1/3}, \sqrt{1/15})$ and $\boldsymbol{\chi} = (+1, +1)$ are listed in Table 7.4. This model is described by the $K-$matrix:

$$K = \begin{pmatrix} 5 & 0 \\ 0 & 5 \end{pmatrix} \tag{7.59}$$

and admits $\lambda_{\boldsymbol{g_1 g_1}} = \lambda_{\boldsymbol{g_2 g_2}} = \delta_{\boldsymbol{g_1}} = \delta_{\boldsymbol{g_2}} = 1/5$ and $\lambda_{\boldsymbol{g_1 g_2}} = 0$. This theoretical model yields a relatively close agreement with the experimental data, as shown in Figure 7.8(d).

While this agreement is encouraging, the use of higher scaling dimension operators has no formal justification. Hence we are left with a largely unsatisfactory resolution of the problem we set out to solve.

7.7.5. Interactions

We consider now that the bosonic modes on each edge interact with each other. Since our primary concern is to resolve the discrepancy between theory and experiment at $\nu = 2/5$, we restrict ourselves in this section to systems with only two co-propagating bosonic modes on the edge. Let us add now to the action, a density-density interaction term between the bosonic modes on the same edge. The action then reads

$$\begin{aligned} S = \frac{1}{4\pi}\int dxdt\big[\partial_t\phi_1\partial_x\phi_1 - v_1(\partial_x\phi_1)^2 + \partial_t\phi_2\partial_x\phi_2 - v_2(\partial_x\phi_2)^2 - 2U\partial_x\phi_1\partial_x\phi_2 \\ + \epsilon^{\mu\nu}A_\mu(Q_1\partial_\nu\phi_1 + Q_2\partial_\nu\phi_2)\big] \end{aligned} \tag{7.60}$$

where U is the strength of the density-density interaction of the two bosonic modes. The last term denotes coupling to the electromagnetic field A_μ, with the indices μ, ν running over x and t, $\epsilon^{tx} = -\epsilon^{xt} = 1$, and Einstein summation convention is implied. Importantly, Q_i give the coupling of bosonic field ϕ_i to the electromagnetic field. We recall that conductance of the edge is topologically quantized and hence the coupling constants Q_i obey the constraint:

$$Q_1^2 + Q_2^2 = \nu. \tag{7.61}$$

Interactions render the action non-diagonal in the basis of the original bosonic modes. We hence rotate to the new basis via the transformation:

$$\begin{aligned} \phi_1 &= \cos\gamma\ \tilde{\phi}_1 - \sin\gamma\ \tilde{\phi}_2 \\ \phi_2 &= \sin\gamma\ \tilde{\phi}_1 + \cos\gamma\ \tilde{\phi}_2, \end{aligned} \tag{7.62}$$

where,

$$\tan 2\gamma = \frac{2U}{v_2 - v_1}. \tag{7.63}$$

This transformation diagonalizes the action

$$\begin{aligned} S = \frac{1}{4\pi}\int dxdt\big[\partial_t\tilde{\phi}_1\partial_x\tilde{\phi}_1 - v_1(\partial_x\tilde{\phi}_1)^2 + \partial_t\tilde{\phi}_2\partial_x\tilde{\phi}_2 - v_2(\partial_x\tilde{\phi}_2)^2 \\ + \epsilon^{\mu\nu}A_\mu(\tilde{Q}_1\partial_\nu\tilde{\phi}_1 + \tilde{Q}_2\partial_\nu\tilde{\phi}_2)\big], \end{aligned} \tag{7.64}$$

where we emphasize that the diagonalized bosonic fields $\tilde{\phi}_j$ couple to the electromagnetic field via new coupling constants $\tilde{Q}_j$. These are related to the original coupling constants Q_i by

$$\begin{aligned} \tilde{Q}_1 &= Q_1\cos\gamma + Q_2\sin\gamma \\ \tilde{Q}_2 &= -Q_1\sin\gamma + Q_2\cos\gamma, \end{aligned} \tag{7.65}$$

and hence trivially satisfy the relation $\tilde{Q}_1^2 + \tilde{Q}_2^2 = Q_1^2 + Q_2^2 = \nu$. That is, interactions have the effect of rotating the vector $\boldsymbol{Q}$, which corresponds to different edge models of the same bulk FQHE liquid. As we saw in Section 7.7.1, although these models describe different behavior on the edge, the quasiparticles in all these models have the same exchange statistics and scaling dimension. Hence, interactions rotate the original anyon operators and distribute them differently across the bosonic modes. But interactions do not change the braiding statistics of the incoming anyon with those tunneling at the QPC, in the context of the anyon collider.

The above conclusion can change if all the bosonic modes on which the quasiparticle exists are not partitioned at the central QPC of the collider. It is possible to imagine a situation where the outer mode (conductance 1/3) of the $\nu = 2/5$ is fully reflected and only the inner mode (conductance 1/15) is back-scattered weakly. In this case, intra-edge interactions can rotate the quasiparticles among the two bosonic modes just as discussed before. However since only the inner mode is partitioned at the QPC, the braiding statistics of the part on the inner mode could be different than the original one. Nevertheless, intra-edge interactions are expected to be highly non-universal and sample-dependent. The physics described in this paragraph, if true, is expected to lead to non-universal results across different realizations of the experiment. It is encouraging that this is not the case with different groups obtaining largely similar results [34, 37–39], potentially ruling out the mechanism discussed in this paragraph.

7.8. Conclusion

This chapter introduced the anyon collider as an experimentally accessible setup to probe the time-domain braiding processes of anyons. The primary goal was to develop a comprehensive theory for the anyon collider that applies to general Abelian FQHE systems, incorporating multiple bosonic modes on each edge and the simultaneous tunneling of different anyons at the QPCs.

Using this generalized theory, we focused on two specific states: $\nu = 2/3$, where no experiments have yet been conducted, and $\nu = 2/5$, where experimental results conflict significantly with theoretical predictions.

For the $\nu = 2/3$ state, we provided detailed theoretical predictions based on our model. Since the edge of this state features counter-propagating charge and neutral modes, we considered two distinct scenarios. In the first, the charge mode propagates towards the central QPC while the neutral mode moves away from it. In the second, the neutral mode approaches the QPC while the charge mode moves in the opposite direction. Our theory successfully addresses both scenarios, offering insights into potential experimental outcomes.

In the $\nu = 2/5$ states the focus was to exploit the generality of our model to address the disagreement between theory and experiment. We considered several different possible edge models of the $\nu = 2/5$ FQHE, simultaneous tunneling of different anyons, quenched neutral modes, different topological classes of the 2/5 FQHE, and intra-edge interactions. None of these additional ingredients allowed a simple and satisfactory reconciliation of theory and experiment.

Chapter 8.

Finite width anyons

In the previous chapter, we introduced the anyon collider geometry as a powerful tool for probing the time-domain braiding of anyons. This setup led to the first experimental confirmation of anyons in the $\nu = 1/3$ fractional quantum Hall effect (FQHE), with results closely matching the theoretical predictions from Ref. [33]. However, at $\nu = 2/5$ the same experiment revealed a striking disagreement with existing theory.

To address this discrepancy, we extended the theory of the anyon collider to encompass general Abelian FQHE. We explored various edge phenomena such as intra-edge interactions, edge reconstruction, and different models of the $\nu = 2/5$ FQHE. Despite these efforts, none provided a satisfactory explanation for the mismatch between theory and experiment.

In this chapter, we consider an aspect of anyon physics that has been overlooked so far: the finite width of anyons. While physical objects typically have a finite width, this feature is often neglected when the width is small compared to other length scales in the system. However, for anyons, we show that even when their width is orders of magnitude smaller than the relevant length scales, it crucially influences braiding signatures.

We begin by calculating the tunneling current of a single finite-width anyon incident on a quantum point contact (QPC), providing a clear understanding of how anyon width impacts physical observables in a simplified setting. Having understood the key idea, we extend the theory of the anyon collider, accounting now for the finite width of the incoming anyons. With this, we are able to show that the finite width of anyons causes a decrease in the effective braiding phase of the time domain braiding processes occurring in the anyon collider. This insight leads us to a satisfactory resolution of the problem identified in the previous chapter.

We further establish a direct relation between the width of the anyons and the transparency of the source QPCs, hence relating the width of the anyons to an experimentally controllable quantity. We find the width of the anyons for which an agreement is found with experiments at $\nu = 2/5$ FQHE is compatible with values of QPC transparency used in experiments. Exploring this connection further, we compare theory and experiment at

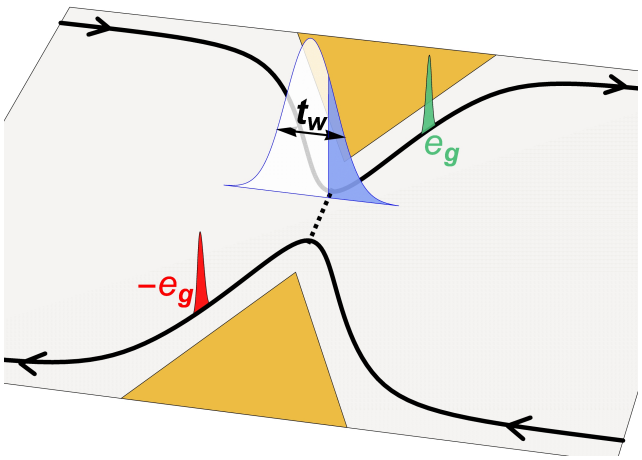


Figure 8.1.: A single finite width anyon (blue-white) traveling on the upper edge to hit the QPC. It braids with the anyon-antianyon pairs (red-green) created at the QPC. The incoming anyon, due to its width, may be only partially enclosed in time-domain braiding loops formed by the anyon-antianyon pairs tunneling at the QPC (indicated by the blue part in the figure).

$\nu = 1/3$, varying the QPC transparency, and find a strong agreement, placing our theory on a firm quantitative footing.

8.1. Tunneling current due to a single anyon

In this section, we calculate the tunneling current due to a single finite-width anyon incident on the quantum point contact, as shown in Figure 8.1. For simplicity, we assume a single type of anyon tunneling across the QPC. The tunneling Hamiltonian at the QPC is given by

$$H_T(t) = \Gamma \left(e^{i\boldsymbol{g_1}\cdot\boldsymbol{\phi^u}(0,t) - i\boldsymbol{g_1}\cdot\boldsymbol{\phi^d}(0,t)} + \text{H.c.} \right) \tag{8.1}$$

where $\boldsymbol{g_1} = (g_{11}, \ldots, g_{1N})$ is the anyon vector giving the combination of bosonic fields $\boldsymbol{\phi^{u/d}} = (\phi_1^{u/d}, \ldots, \phi_N^{u/d})$ that form the anyon operators. The tunneling current operator from the upper edge to the lower edge is

$$I_T(t) = iq_{\boldsymbol{g_1}}\Gamma \left(e^{i\boldsymbol{g_1}\cdot\boldsymbol{\phi^u}(0,t) - i\boldsymbol{g_1}\cdot\boldsymbol{\phi^d}(0,t)} - \text{H.c.} \right) \tag{8.2}$$

where $q_{\boldsymbol{g_1}}$ is the charge of the anyon labeled by the quasiparticle vector $\boldsymbol{g_1}$. These operators are special cases of the operators discussed in Section 2.3 when a unique type of anyon tunnels across the QPC.

We consider that a single anyon travels on the upper edge, reaching the QPC at time t_0. This process is modeled by augmenting the bosonic field $\boldsymbol{\phi^u}$ with a solitonic excitation

$$\bar{\phi}_i^u = \phi_i^u + 2\pi g_{2i}\left[\frac{1}{\pi}\tan^{-1}\left(\frac{t-t_0}{t_w}\right)+\frac{1}{2}\right] \tag{8.3}$$

where $\bar{\phi}_j$ denotes a bosonic field augmented with solitons. For the sake of generality, we assume that a different type of anyon, given by the anyon vector $\boldsymbol{g_2}$ travels on the upper edge and is incident on the QPC, which tunnels anyons of type $\boldsymbol{g_1}$. The above equation is a generalization of Equation (7.28): the Heaviside theta function has now been regularized (smeared out), and the anyons traveling on the edge now possess a finite width t_w. The form of the regularization chosen implies a Lorentzian shape of the anyonic quasiparticles, and it is straightforward to consider other shapes of the anyons.

The tunneling current in the QPC due to this anyon can be expressed, to leading order in perturbation theory, within the Keldysh formalism as

$$\langle I_T(t)\rangle = -\frac{i}{2}\int dt' \sum_{\eta\eta'}\eta'\left\langle\left\{T_K I_T(t^\eta)H_T(t'^{\eta'})\right\}\right\rangle \tag{8.4}$$

where η,η' denote the Keldysh contour labels, and T_K denotes time ordering on the Keldysh contour. We plug in the tunneling Hamiltonian and tunneling current operators

$$\begin{gathered}\langle I_T(t)\rangle = \frac{q_{\boldsymbol{g_1}}\Gamma^2}{2}\int dt' \sum_\epsilon \epsilon \sum_{\eta\eta'}\eta' \\ \left\langle\left\{T_K\left[e^{i\boldsymbol{g_1}.\bar{\boldsymbol{\phi}}^u(t^\eta)-i\boldsymbol{g_1}.\bar{\boldsymbol{\phi}}^d(t^\eta)}\right]^\epsilon\left[e^{i\boldsymbol{g_1}.\bar{\boldsymbol{\phi}}^u(t'^{\eta'})-i\boldsymbol{g_1}.\bar{\boldsymbol{\phi}}^d(t'^{\eta'})}\right]^{-\epsilon}\right\}\right\rangle\end{gathered} \tag{8.5}$$

where the sum over ϵ exists to account for both terms in Eqs. (8.1) and (8.2). We further expand this, separating the equilibrium bosonic fields from the solitonic anyon excitation, giving us:

$$\begin{gathered}\langle I_T(t)\rangle = \frac{q_{\boldsymbol{g_1}}\Gamma^2}{2}\int dt' \sum_\epsilon \epsilon \sum_{\eta\eta'}\eta' \\ \prod_j\left\langle\left\{T_K e^{i\epsilon g_{1j}\phi_j^u(t^\eta)}e^{-i\epsilon g_{1j}\phi_j^u(t'^{\eta'})}\right\}\right\rangle\left\langle\left\{T_K e^{-i\epsilon g_{1j}\phi_j^d(t^\eta)}e^{i\epsilon g_{1j}\phi_j^d(t'^{\eta'})}\right\}\right\rangle \\ \exp\left\{2\epsilon g_{1j}g_{2j}\left[\tan^{-1}\left(\frac{t-t_0}{t_w}\right)-\tan^{-1}\left(\frac{t'-t_0}{t_w}\right)\right]\right\}\end{gathered} \tag{8.6}$$

The bosonic correlators are evaluated using the results of Appendix B. Subsequently, summing over ϵ, we get:

$$\begin{aligned}\langle I_T(t)\rangle = 2iq_{\boldsymbol{g_1}}\Gamma^2 \int dt' \sum_{\eta\eta'} \eta' e^{2\delta_{\boldsymbol{g_1}}\mathcal{G}^{\eta\eta'}(t-t')} \\ \sin\left\{2\sum_j g_{1j}g_{2j}\left[\tan^{-1}\left(\frac{t-t_0}{t_w}\right)-\tan^{-1}\left(\frac{t'-t_0}{t_w}\right)\right]\right\},\end{aligned} \tag{8.7}$$

where $\delta_{\boldsymbol{g_1}} = \sum_j g_{1j}^2$ is the scaling dimension of the anyon described by the anyon vector $\boldsymbol{g_1}$. The bosonic Greens function is given by:

$$\mathcal{G}^{\eta_1\eta_2}(x,\tau) = \log\left(\frac{\sinh(i\pi T\tau_0)}{\sinh\left[\pi T\left(i\tau_0 - \sigma_{\eta_1\eta_2}(\tau)(\tau-\chi_j x/v_j)\right)\right]}\right), \tag{8.8}$$

where

$$\sigma_{\eta_1\eta_2}(t) = \frac{1}{2}\left[(\eta_2-\eta_1)+\mathrm{sgn}(t)(\eta_1+\eta_2)\right]. \tag{8.9}$$

Summing now over the Keldysh indices and using the, the current takes the form

$$\begin{aligned}\langle I_T(t)\rangle = 2iq_{\boldsymbol{g_1}}\Gamma^2 \int_{-\infty}^{t} dt' \left(e^{2\delta_{\boldsymbol{g_1}}\mathcal{G}(t-t')} - e^{2\delta_{\boldsymbol{g_1}}\mathcal{G}(t'-t)}\right) \\ \sin\left\{2\sum_j g_{1j}g_{2j}\left[\tan^{-1}\left(\frac{t-t_0}{t_w}\right)-\tan^{-1}\left(\frac{t'-t_0}{t_w}\right)\right]\right\}\end{aligned} \tag{8.10}$$

where the summation inside the sine includes only the bosonic modes flowing towards the QPC, as explained in Section (6.2). Keeping the latter in mind, we can write for fully chiral edges

$$\begin{aligned}\langle I_T(t)\rangle = 2iq_{\boldsymbol{g_1}}\Gamma^2 \int_{-\infty}^{t} dt' \left(e^{2\delta_{\boldsymbol{g_1}}\mathcal{G}(t-t')} - e^{2\delta_{\boldsymbol{g_1}}\mathcal{G}(t'-t)}\right) \\ \sin\left\{2\lambda_{\boldsymbol{g_1 g_2}}\left[\tan^{-1}\left(\frac{t-t_0}{t_w}\right)-\tan^{-1}\left(\frac{t'-t_0}{t_w}\right)\right]\right\}\end{aligned} \tag{8.11}$$

where $\lambda_{\boldsymbol{g_1 g_2}} = \boldsymbol{g_1}.\boldsymbol{g_2}$ is related to the braiding phase of the incoming anyon with those tunneling at the QPC. We would like to emphasize that while the scaling dimension concerns only the anyons tunneling at the QPC, the exchange phases are a property of both the incoming anyons and those tunneling at the QPC, as indicated by the subscripts. With this in mind, we take $\delta_{\boldsymbol{g_1}} \equiv \delta$ and $\lambda_{\boldsymbol{g_1 g_2}} \equiv \lambda$ for conciseness in what follows in this section.

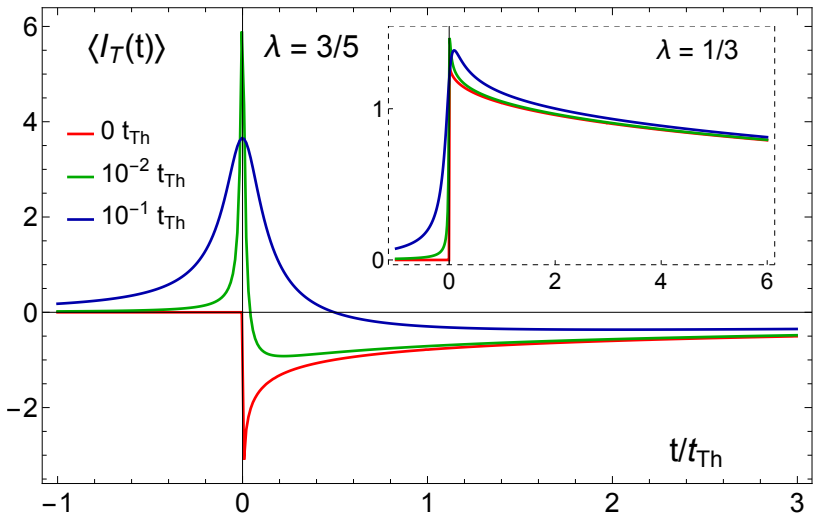


Figure 8.2.: Tunneling current at the QPC, in units of $I_0 = \Gamma^2 T(\pi T\tau_0)^{2\delta-1}$, due to a single incoming anyon as a function of time (Equation(8.11)) for $\lambda = \delta = 3/5$, and for different anyon widths ($t_w = 0, 0.01, 0.1$ in units of $t_{Th} = \hbar/k_B T$). The center of the anyon hits the QPC at $t = 0$. As the width is increased the current shifts from negative to positive values. Inset: same figure for $\lambda = \delta = 1/3$, showing that the effect of the anyon width is not significant for $\lambda < 1/2$.

From the expression of current in Equation (8.11), we find that due to the finite width of the incoming anyon, its braiding phase with the anyon-antianyon pairs tunneling at the QPC (given by the sine term in Equation (8.11)) is smeared out in time. The braiding phase contributes only partially to the current at a given time, which significantly affects the tunneling current as illustrated in Fig. 8.2. For $t_w \to 0$, the sine in Equation (8.11) reduces to $\theta(t - t_0)\theta(t_0 - t')\sin(2\pi\lambda)$, where θ is the Heaviside step function, and the current then reduces to a slowly decaying function of time, with a characteristic timescale set by the temperature, $t_{\rm Th} = 1/T$ [77].

We show the tunneling current as a function of time for $\lambda = 3/5$ in Fig. 8.2 for different values of the width t_w of the incoming anyon. This value of λ, together with the $\delta = 3/5$ we use here, corresponds to the canonical models of anyons in the 2/5 FQHE [24]. For $t_w = 0$, the tunneling current is strictly negative, as $\sin(2\pi \times 3/5) < 0$. As soon as the anyon has a finite width, the current becomes positive, on a time interval around t_0 which becomes wider as t_w is increased.

This behavior is in complete contrast to that at $\lambda = 1/3$ (which corresponds to the Laughlin $\nu = 1/3$ case). Here, the current due to an anyon of zero width is positive. However, endowing the anyon with a finite width does not significantly impact the current, as shown in the inset of Fig. 8.2, for $\delta = 1/3$.

Importantly, even if δ is adjusted, the qualitative behavior of the currents remains largely unchanged. As long as $\lambda > 1/2$, the current due to zero-width anyons is negative.

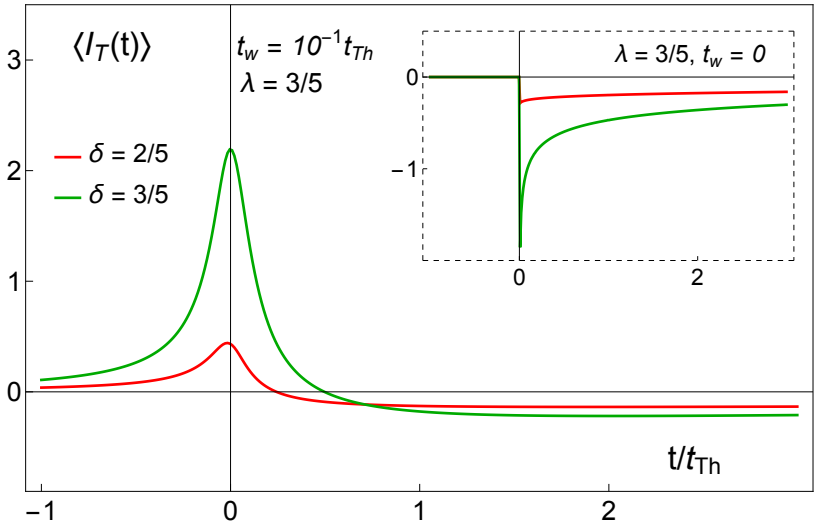


Figure 8.3.: Tunneling current at the QPC, in units of $I_0 = \Gamma^2 T(\pi T\tau_0)^{2\delta-1}$, due to a single incoming anyon as a function of time (Equation (8.11)) for $\lambda = 3/5$ shown for different anyonic scaling dimensions ($\delta = 2/5,\ 3/5$). The center of the anyon hits the QPC at $t = 0$. Inset: Current for anyons with $t_w = 0$ is negative for all scaling dimensions. Main plot: current for $t_w = 10^{-1}t_{Th}$, where the current now becomes positive close to $t = 0$ for all scaling dimensions. Changing the scaling dimension shifts the value of t at which the current recovers negative values, without affecting the qualitative behavior.

The current becomes positive for small times if the anyons have a finite width, regaining a negative value as t increases. Changing δ modifies the power-law decrease of the Green functions in Equation (8.11), which mainly moves the value of t at which the current regains a negative value, without changing the overall behavior of the current, as shown in Figure 8.3.

Let us quickly summarize the findings of this section. When a single zero-width anyon with $\lambda > 1/2$ is incident on a QPC, theory predicts a negative tunneling current. We show here that the finite width of anyons could dramatically alter this prediction, resulting in a positive tunneling current even when $\lambda > 1/2$. This prediction is true independent of the value of scaling dimension δ. This finding is quite interesting because of the issue we faced in Chapter 7. We saw in Section 7.5 that there is a strong disagreement between theory and experiment at $\nu = 2/5$ FQHE – the disagreement was traced back precisely to a difference in the sign of the tunneling current predicted by theory and that measured in experiments. In the latter system, indeed, the charge $e/5$ anyons are characterized by an exchange phase $\lambda = 3/5 > 1/2$. Given the change in sign of tunneling current due to single finite width anyon detailed in this section, it seems judicious to incorporate the finite width of anyons in the theory of the anyon collider, in the hope that the above discrepancy is resolved. This will be the subject of the next section.

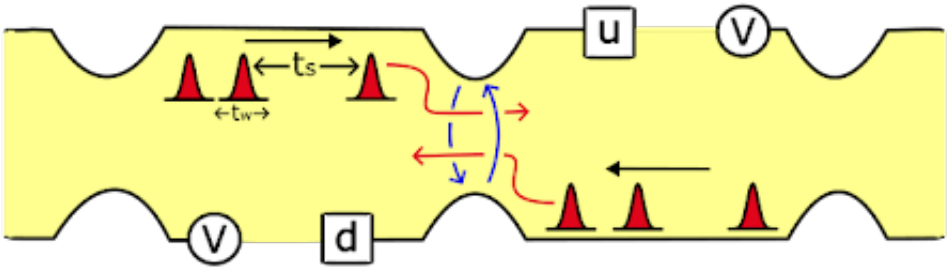


Figure 8.4.: Finite-width anyons in the theory of the anyon collider. The anyons emitted by the source QPCs are take to have a finite width t_w, and the average separation between successive anyons is denoted t_s. The anyons incoming from the source QPCs braid in the time domain with anyons tunneling at the central QPC.

8.2. Finite width anyons in the anyon collider

We now consider the case of a Poissonian stream of finite-width anyons incident on the QPC, leading to an average current $I_{u/d}$ on the upper/lower edge. This corresponds to the anyon collider considered in the previous chapter, where upstream QPCs in the weak-backscattering regime are used as the sources of the anyon streams, as shown in Figure 8.4. The stream of N incoming finite-width anyons can be modeled by augmenting the bosonic fields with N regularized solitonic excitations

$$\bar{\phi}_i^{u/d} = \phi_i^{u/d} + 2g_{2i} \sum_{k=0}^{N} \left[\tan^{-1}\left(\frac{t - t_k^{u/d}}{t_w} \right) + \frac{\pi}{2} \right], \tag{8.12}$$

where $t_k^{u/d}$ denotes the time at which the $k-$th anyon on the u/d edge hits the QPC. The number of anyons N obeys a Poisson distribution, and the arrival times t_k are uniformly distributed. This expression generalizes Equation (7.28), now taking into account the finite width of the incoming anyons.

It is now an opportune moment to discuss the relevant time scales in this problem. In the single anyon case, there were two time scales characterizing the system: the thermal time $t_{\mathrm{Th}} = 1/T$ and, t_w, the temporal width of the anyon. A stream of anyons introduces another important time scale: the average temporal spacing between successive anyons, given by the inverse of the incoming current on the QPC, $t_s = q_{\boldsymbol{g_2}}/I_+$, where $I_\pm = I_u \pm I_d$. In what follows, we will stick to the limit $t_w \ll t_s$, which allow us to treat each anyon

independently, and perform Poisson averaging as done in Section 7.3. Moreover, we emphasize that it is despite this assumption that the finite width of anyons crucially influences transport observables. We will show that even when $t_w \ll t_s \ll t_{\mathrm{Th}}$, but $t_w \neq 0$, transport observables like tunneling current change significantly, compared to $t_w = 0$.

8.2.1. Non-equilibrium correlator of finite-width anyons

In this section, we derive the non-equilibrium correlation function of the finite-width anyons. Let us start from a concrete physical quantity, the tunneling current at the central QPC due to a Poissonian stream of finite-width anyons. This quantity will naturally lead to the non-equilibrium correlator, once we separate the solitonic excitations from the bosonic field. The average tunneling current is defined within the Keldysh formalism as

$$\langle I_T(t)\rangle = -\frac{i}{2}\int dt' \sum_{\eta\eta'} \eta' \left\langle \left\{ T_K I_T(t^\eta) H_T(t'^{\eta'}) \right\} \right\rangle . \tag{8.13}$$

Substituting in the tunneling Hamiltonian and current operators of Equations (8.1) and (8.2), where now the bosonic fields have been augmented with the solitonic excitations, we write:

$$\begin{aligned} \langle I_T(t)\rangle = \frac{q_{\boldsymbol{g_1}}\Gamma^2}{2}\int dt' \sum_{\epsilon} \epsilon \sum_{\eta\eta'} \eta' \\ \left\langle \left\{ T_K \left[e^{i\boldsymbol{g_1}\cdot\bar{\boldsymbol{\phi}}^u(t^\eta) - i\boldsymbol{g_1}\cdot\bar{\boldsymbol{\phi}}^d(t^\eta)} \right]^\epsilon \left[e^{i\boldsymbol{g_1}\cdot\bar{\boldsymbol{\phi}}^u(t'^{\eta'}) - i\boldsymbol{g_1}\cdot\bar{\boldsymbol{\phi}}^d(t'^{\eta'})} \right]^{-\epsilon} \right\} \right\rangle \end{aligned} \tag{8.14}$$

Following the discussion of Section 7.3, we seperate the correlators into two parts: a quantum average of the bosonic fields and a classical average of the solitonic excitations:

$$\begin{aligned} \langle I_T(t)\rangle = \frac{q_{\boldsymbol{g_1}}\Gamma^2}{2}\int dt' \sum_{\epsilon}\sum_{\eta\eta'} \epsilon\eta' \left\langle \left\{ T_K e^{i\epsilon\boldsymbol{g_1}\cdot\boldsymbol{\phi}^u(t^\eta)} e^{-i\epsilon\boldsymbol{g_1}\cdot\boldsymbol{\phi}^u(t'^{\eta'})} \right\} \right\rangle \\ \times \left\langle \left\{ T_K e^{-i\epsilon\boldsymbol{g_1}\cdot\boldsymbol{\phi}^d(t^\eta)} e^{i\epsilon\boldsymbol{g_1}\cdot\boldsymbol{\phi}^d(t'^{\eta'})} \right\} \right\rangle \\ \times \left\langle \exp\left\{ \sum_j 2i\epsilon g_{1j} g_{2j} \sum_{k=0}^{N} \left[\tan^{-1}\left(\frac{t-t_k^u}{t_w}\right) - \tan^{-1}\left(\frac{t'-t_k^u}{t_w}\right) \right] \right\} \right\rangle_{\text{n-eq}} \\ \times \left\langle \exp\left\{ -\sum_j 2i\epsilon g_{1j} g_{2j} \sum_{k=0}^{N} \left[\tan^{-1}\left(\frac{t-t_k^d}{t_w}\right) - \tan^{-1}\left(\frac{t'-t_k^d}{t_w}\right) \right] \right\} \right\rangle_{\text{n-eq}} . \end{aligned} \tag{8.15}$$

Here, the first two lines contain the equilibrium bosonic correlators, while the third and fourth line comprise the non-equilibrium classical average of finite width anyons.

The evaluation of the non-equilibrium correlator follows similar lines as the discussion of Section 7.3 but is a bit subtle. Let us quickly recall the notion of Poissonian average in Section 7.3. The idea was that we average over the arrival times of the incoming anyons (which follow a uniform distribution) since experiments measure currents over timescales where many anyons have arrived at the QPC. We hence only care about the number of anyons arriving at the QPC, within the time interval $[t', t]$, the tunneling times of anyons at the central QPC. Those anyons arriving within the latter time interval lead to a non-trivial braiding phase at the QPC. However, the number of anyons arriving at the central QPC is not fixed when the anyons are sent by an upstream source QPC. We hence perform a Poissonian average over the number of anyons arriving at the QPC, and the Poisson parameter is given by the number current of anyons coming from the source QPC.

We will follow the same philosophy for finite width anyons, except that there is a caveat. Since the anyons now have a finite width, they can start influencing the transport observables at the central QPC, even before their center arrives at the QPC. This is seen in the single particle current in Figure 8.2. There, the center of the anyon is taken to arrive at the QPC at time $t = 0$. For zero-width anyons, the current is exactly zero until $t = 0$ when the anyon arrives at the QPC, producing a non-zero current. However, for finite-width anyons, the current is non-zero even for times $t < 0$. It is hence required to account for the influence of anyons on the QPC even before their center hits the QPC. We achieve this by considering that anyons influence the correlations functions if they arrive in a larger time interval: $[t' - ct_w, t + ct_w]$, where c is a dimensionless number, that depends on the shape of anyons [153]. For rectangular anyons, for example, $c = 1/2$, while for Lorentzian anyons, $c \to \infty$. In full generality, one should take $c \to \infty$. This will be done at a later stage to avoid artificial divergences.

The phase at the QPC, due to braiding of a stream of finite-width anyons and anyon-antianyon pairs tunneling at the QPC, is determined by an integral over the arrival time of the incoming anyons. This integral is weighted by the probability of the anyon's center reaching the QPC at a specific time. In the limit $t_w \ll t_s$, the latter probability distribution can be assumed to be uniform. Hence, we can express the non-equilibrium correlator of finite-width anyons as:

$$\begin{aligned}\left\langle \exp\left\{ \pm \sum_j 2i\epsilon g_{1j} g_{2j} \sum_{k=0}^{N} \left[\tan^{-1}\left(\frac{t - t_k^{u/d}}{t_w}\right) - \tan^{-1}\left(\frac{t' - t_k^{u/d}}{t_w}\right)\right]\right\}\right\rangle_{\text{n-eq}} \\ = \sum_{N=0}^{\infty} \frac{\left(\frac{I_{u/d}|t-t'+2ct_w|}{q_{\boldsymbol{g_2}}}\right)^N}{N!} e^{-\frac{I_{u/d}|t-t'+2ct_w|}{q_{\boldsymbol{g_2}}}} \\ \times \left\{ \int_{t'-ct_w}^{t+ct_w} dt_0 \frac{1}{|t-t'+2ct_w|} e^{\pm 2i\epsilon\lambda_{\boldsymbol{g_1 g_2}}\left[\tan^{-1}\left(\frac{t-t_0}{t_w}\right) - \tan^{-1}\left(\frac{t'-t_0}{t_w}\right)\right]} \right\}^N \end{aligned} \tag{8.16}$$

Here, $I_{u/d}/q_{\boldsymbol{g_2}}$ gives the average number of anyons arriving at the QPC in the time interval $[t'-ct_w, t+ct_w]$. The quantities inside the sum on the second line above give the Poisson probability of N anyons arriving at the QPC in the time interval $(t-t'+2ct_w)$. The factor $1/(t-t'+2ct_w)$ inside the integral in the third line gives the (uniform) probability of the center of the anyon arriving at the QPC at a given time t_0. This expression generalizes the non-equilibrium correlator definition in Equation (7.30) to address finite-width anyons.

Let us now evaluate the Poisson sum over the number of anyons N, which gives us

$$\begin{aligned}\left\langle \exp\left\{ \pm \sum_j 2i\epsilon g_{1j} g_{2j} \sum_{k=0}^{N} \left[\tan^{-1}\left(\frac{t-t_k^{u/d}}{t_w}\right) - \tan^{-1}\left(\frac{t'-t_k^{u/d}}{t_w}\right)\right]\right\}\right\rangle_{\text{n-eq}} \\ = \exp\left\{ -\frac{I_{u/d}}{q_{\boldsymbol{g_2}}} \int_{t'-ct_w}^{t+ct_w} dt_0 \left\{ 1 - e^{\pm 2i\epsilon\lambda_{\boldsymbol{g_1 g_2}}\left[\tan^{-1}\left(\frac{t-t_0}{t_w}\right)-\tan^{-1}\left(\frac{t'-t_0}{t_w}\right)\right]}\right\}\right\}\end{aligned} \tag{8.17}$$

where the factor $\exp\{-I_{u/d}|t-t'+2ct_w|/q_{\boldsymbol{g_2}}\}$ coming from the Poisson average has been taken inside the integral. We can now take the limit $c \to \infty$ without introducing any divergences. This yields the following expression for the non-equilibrium correlator of finite-width anyons.

$$\begin{aligned}\left\langle \exp\left\{ \pm \sum_j 2i\epsilon g_{1j} g_{2j} \sum_{k=0}^{N} \left[\tan^{-1}\left(\frac{t-t_k^{u/d}}{t_w}\right) - \tan^{-1}\left(\frac{t'-t_k^{u/d}}{t_w}\right)\right]\right\}\right\rangle_{\text{n-eq}} \\ = \exp\left\{ -\frac{I_{u/d}}{q_{\boldsymbol{g_2}}} \int_{-\infty}^{\infty} dt_0 \left\{ 1 - e^{\pm 2i\epsilon\lambda_{\boldsymbol{g_1 g_2}}\left[\tan^{-1}\left(\frac{t-t_0}{t_w}\right)-\tan^{-1}\left(\frac{t'-t_0}{t_w}\right)\right]}\right\}\right\}\end{aligned} \tag{8.18}$$

This expression generalizes the result shown in Equation (7.31). With this final expression, we proceed to calculate the relevant physical observables of the anyon collider, which now take into account the effect of the finite width of anyons.

8.2.2. Tunneling current due to finite-width anyons

We proceed with the calculation of the tunneling current by substituting the results of Equation (8.18) into the tunneling current in Equation (8.15), giving us the following

expression for the tunneling current

$$\begin{aligned}\langle I_T(t)\rangle &= \frac{q_{\boldsymbol{g_1}}\Gamma^2}{2}\int_{-\infty}^{t} dt' \sum_{\epsilon}\epsilon\left[e^{2\delta_{\boldsymbol{g_1}}\mathcal{G}(t-t')} - e^{2\delta_{\boldsymbol{g_1}}\mathcal{G}(t'-t)}\right] \\ &\times \exp\left\{-\frac{I_+}{q_{\boldsymbol{g_2}}}\int_{-\infty}^{\infty} dt_0\left[1-\cos\left(2\lambda_{\boldsymbol{g_1 g_2}}\left(\tan^{-1}\left(\frac{t-t_0}{t_w}\right)-\tan^{-1}\left(\frac{t'-t_0}{t_w}\right)\right)\right)\right]\right\} \\ &\times \exp\left\{i\epsilon x\frac{I_+}{q_{\boldsymbol{g_2}}}\int_{-\infty}^{\infty} dt_0\left[\sin\left(2\lambda_{\boldsymbol{g_1 g_2}}\left(\tan^{-1}\left(\frac{t-t_0}{t_w}\right)-\tan^{-1}\left(\frac{t'-t_0}{t_w}\right)\right)\right)\right]\right\},\end{aligned} \tag{8.19}$$

where we have made the variable change $I_u \pm I_d = I_\pm$, $x = I_-/I_+$ and summed over the Keldysh indices. We now make two coordinate transformations. In the integral on the first line, we employ the transformation $t - t' \to t$, and in the integrals inside the exponentials, we use $u = t_0/t_s$, where $t_s = q_{\boldsymbol{g_2}}/I_+$. For brevity, we will henceforth take $\lambda_{\boldsymbol{g_1 g_2}} \equiv \lambda$, $\delta_{\boldsymbol{g_1}} \equiv \delta$, and finally, we sum over ϵ to obtain the following expression for the tunneling current:

$$\langle I_T\rangle = 2iq_{\boldsymbol{g_1}}\Gamma^2\int_0^{\infty} dt\ \frac{\sin\left[x\,\mathrm{Im}f(t,\lambda,\tau_w)\right]}{\exp\left[\mathrm{Re}f(t,\lambda,\tau_w)\right]}\left(e^{2\delta\mathcal{G}(t)} - e^{2\delta\mathcal{G}(-t)}\right). \tag{8.20}$$

Here, $f(t,\lambda,\tau_w)$ is the phase due to braiding of finite width anyons with the anyon-antianyon pairs tunneling at the central QPC, and is given by

$$f(t,\lambda,\tau_w) = \int_{-\infty}^{\infty} du\left\{1-\exp\left(-2i\lambda\left[\tan^{-1}\left(\frac{t/t_s-u}{\tau_w}\right)+\tan^{-1}\left(\frac{u}{\tau_w}\right)\right]\right)\right\}. \tag{8.21}$$

In the above expression, we have defined the scaled width of anyons, $\tau_w = t_w/t_s$, a dimensionless number which turns out to be an important quantity, and is discussed in detail in Section 8.3. We emphasize that Equation (8.20) generalized the zero-width anyon current of Equation (7.22), with Equation (8.21) giving the phase accumulated due to braiding of the Poissonian stream of finite-width anyons with anyon-antianyon pairs at the QPC. This is readily seen by taking $t_w \to 0$, giving $f(t,\lambda,\tau_w) \to t/t_s(1-e^{-2i\pi\lambda})$, which is the phase due to a stream of zero-width anyons [33]. The finite width phase now takes into account various factors such as the shape of the anyons, and the influence of anyons at the QPC even before their center hits the QPC. The behavior of this quantity, described in Section 8.2.4, will turn out to have crucial consequences on the observables of the collider, especially the tunneling current.

8.2.3. Tunneling noise, cross-correlation noise, and $P-$value

Here, we briefly show the expressions of all the relevant physical quantities measured in the anyon collider. The tunneling noise is defined at the lowest order in the Keldysh

formalism as

$$\langle S_T \rangle = \int dt' \sum_{\eta\eta'} \left\langle \left\{ T_K \delta I_T(t^{\eta}) \delta I_T(t'^{\eta'}) \right\} \right\rangle \tag{8.22}$$

The evaluation of this quantity follows the same lines as that of the tunneling current. We quote only the final result here, which reads:

$$\langle S_T \rangle = 2q_{\boldsymbol{g_1}}^2 \Gamma^2 \int_0^{\infty} dt \; \frac{\cos\left[x \, \mathrm{Im} f(t,\lambda,\tau_w)\right]}{\exp\left[\mathrm{Re} f(t,\lambda,\tau_w)\right]} \left(e^{2\delta_{\boldsymbol{g_1}} \mathcal{G}(t)} + e^{2\delta_{\boldsymbol{g_1}} \mathcal{G}(-t)} \right) \tag{8.23}$$

From Chapter 7, we know that the cross-correlation of currents at contacts u and d (see Figure 8.4) obeys a fluctuation-dissipation relation, relating the latter to the tunneling noise and tunneling current in a relatively straightforward manner [33]. The equation below is the same as Equation (7.42) specialized to the case of unique anyons tunneling through each QPC

$$\langle \delta I_u \delta I_d \rangle = - \langle S_T \rangle + q_{\boldsymbol{g}_1} I_- \frac{\partial \langle I_T \rangle}{\partial I_+} + q_{\boldsymbol{g}_1} I_+ \frac{\partial \langle I_T \rangle}{\partial I_-}. \tag{8.24}$$

The derivative of the tunneling current due to finite-width anyons are calculated easily:

$$\begin{aligned} \frac{\partial \langle I_T \rangle}{\partial I_+} = 2iq_{\boldsymbol{g_1}} \Gamma^2 \int_0^{\infty} dt \; & \frac{\sin\left[x \, \mathrm{Im} f(t,\lambda,\tau_w)\right]}{\exp\left[\mathrm{Re} f(t,\lambda,\tau_w)\right]} \\ & \left[-\frac{\mathrm{Re} f(t,\lambda,\tau_w)}{q_{\boldsymbol{g_2}}} \right] \left(e^{2\delta_{\boldsymbol{g_1}} \mathcal{G}(t)} - e^{2\delta_{\boldsymbol{g_1}} \mathcal{G}(-t)} \right), \end{aligned} \tag{8.25}$$

$$\frac{\partial \langle I_T \rangle}{\partial I_-} = 2iq_{\boldsymbol{g_1}} \Gamma^2 \int_0^{\infty} dt \; \frac{\cos\left[x \, \mathrm{Im} f(t,\lambda,\tau_w)\right]}{\exp\left[\mathrm{Re} f(t,\lambda,\tau_w)\right]} \left[\frac{\mathrm{Im} f(t,\lambda,\tau_w)}{q_{\boldsymbol{g_2}}} \right] \left(e^{2\delta_{\boldsymbol{g_1}} \mathcal{G}(t)} - e^{2\delta_{\boldsymbol{g_1}} \mathcal{G}(-t)} \right). \tag{8.26}$$

The generalized Fano factor or $P-$value explored in detail in Chapter 7 for $\nu = 2/5$ and $2/3$ and measured in recent experiments to extract the braiding phase [34, 37–39] is defined as

$$P(x) = \frac{\left\langle \delta \tilde{I}_u \delta \tilde{I}_d \right\rangle}{q_{\boldsymbol{g_1}} I_+ \frac{\partial \langle I_T \rangle}{\partial I_-}\big|_{I_-=0}} \tag{8.27}$$

where $\tilde{I}_{u/d}$ are currents measured at contact u/d. We note that the quantities in Equations (8.20), (8.23), (8.25) and (8.26) that enter the $P-$value, do not admit analytic evaluation when anyons have a finite width. For Lorentzian-shaped anyons, analytic evaluation is possible in the special case of $\lambda_{\boldsymbol{g_1 g_2}} = n\pi$, which corresponds to a trivial braiding phase. In general, the more interesting scenario of fractional braiding phase demands a numerical

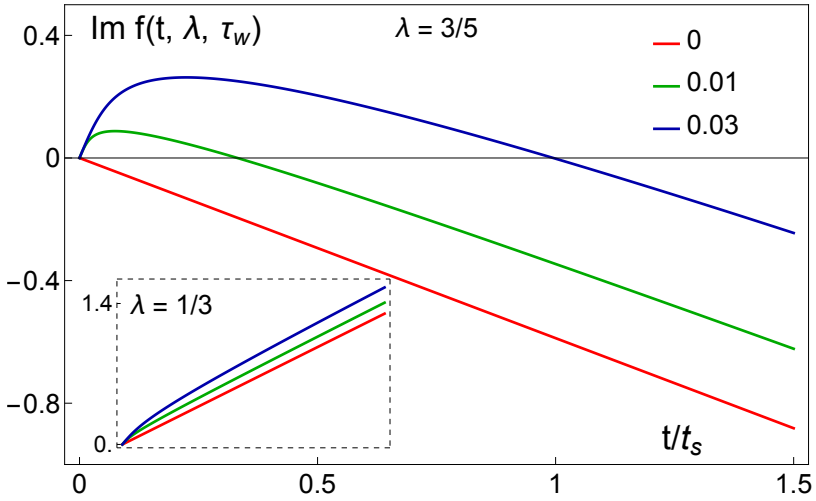


Figure 8.5.: Imaginary part of the finite-width phase as a function of time for $\lambda = 3/5$, for scaled width $\tau_w = 0, 0.01, 0.03$. It is $\sin(2\pi * 3/5)(t/t_s)$ for $\tau_w = 0$, but becomes positive close to $t = 0$ when τ_w is finite. Inset: same curves for $\lambda = 1/3$, showing that for $\lambda < 1/2$ a finite width does not significantly change the phase.

evaluation of these quantities as done here, or approximations that do not capture the physics detailed here [153].

8.2.4. Behavior of finite-width phase

Notice the real and imaginary parts of the finite width phase $f(t, \lambda, \tau_w)$ entering all the quantities in Equations (8.20), (8.23), (8.25), and (8.26). As emphasized at the end of Section 8.2.2, the latter quantity gives the phase due to braiding of the incoming finite-width anyons with the anyon-antianyon pairs tunneling at the central QPC. This quantity directly influences the behavior of all transport observables in the anyon collider. It is hence crucial to understand how this quantity behaves when anyons have a finite width.

We plot the imaginary part of the finite-width phase $f(t, \lambda, \tau_w)$ as a function of time in Figure 8.5, for $\lambda = 3/5$ and different values of the scaled width τ_w. For $\tau_w = 0$, the imaginary part of the phase is simply linear in t, with a negative slope equal to $\sin(2\pi\lambda)$. As soon as the anyons have a finite width, we find a dramatic change occurring close to $t = 0$: $\mathrm{Im} f(t, \lambda, \tau_w)$ is initially positive, and takes a finite amount of time (set by τ_w) to become negative and eventually recover the same negative slope. This behavior is reminiscent of the behavior of the current due to a single anyon shown in Figure 8.2.

The inset of Figure 8.5 shows the imaginary part of the phase for $\lambda = 1/3$. There, we see a linear behavior with a positive slope for $\tau_w = 0$, which is only marginally affected when τ_w is non-zero.

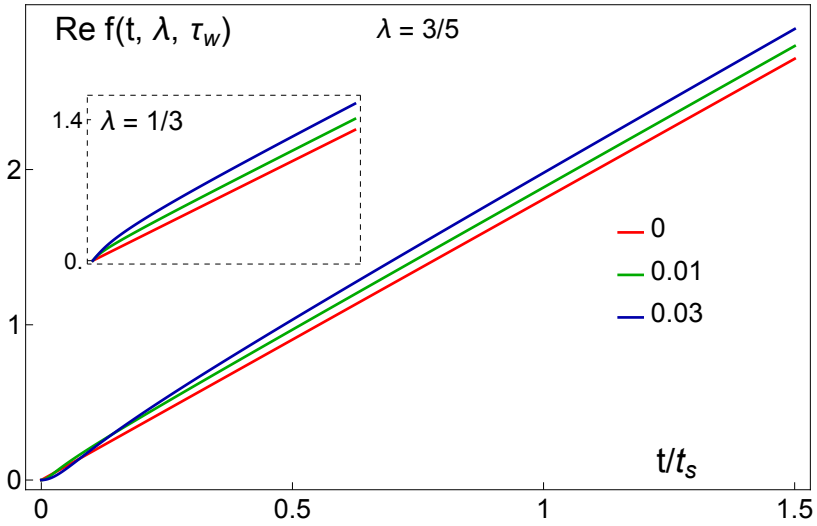


Figure 8.6.: Real part of the finite-width phase as a function of time for $\lambda = 3/5$, for scaled width $\tau_w = 0, 0.01, 0.03$. For $\tau_w = 0$, the phase is $(1 - \cos(2\pi * 3/5))(t/t_s)$, deviating very slightly from the latter ever for $\tau_w \neq 0$. Finite width of anyon does not significantly impact the real part of the phase for $\lambda = 3/5$ Inset: same curves for $\lambda = 1/3$, displaying similar behavior as described above.

The real part of the phase, which also enters Equations (8.20), (8.23), (8.25) and (8.26), mostly contributes to the integral at short times. This is because the exponential containing the real part of the phase decays quickly, within a few t_s. However, it does not vary significantly with τ_w for any λ, as shown in Figure 8.6.

The main takeaway of this section: finite width of anyons changes the effective braiding phase close to $t = 0$ when $\lambda > 1/2$. Close to $t = 0$, the effective exchange phase is similar to $\lambda < 1/2$. Crucially, this is true even when the width is very small compared to all other timescales in the system. In Figure 8.5, the effective braiding phase close to $t = 0$ deviates significantly from the theoretical predictions for zero-width anyons even when the anyon width is a hundred times smaller than the average spacing between subsequent anyons. Moreover, the finite width of anyons does not impact the phase significantly when $\lambda < 1/2$.

8.2.5. Finite width changes sign of tunneling current

Let us recall the problem we are trying to solve for many pages now. In Chapter 7, we saw that while the anyon collider experiment agrees well with theory at $\nu = 1/3$ FQHE, there is a significant discrepancy between theory and experiment at $\nu = 2/5$. There is a sign mismatch between the theoretically predicted value of the $P-$factor in Equation (8.27), and its experimentally measured value (see Figure 7.5). We were able to locate the precise source of discrepancy: theory predicts a negative tunneling current while

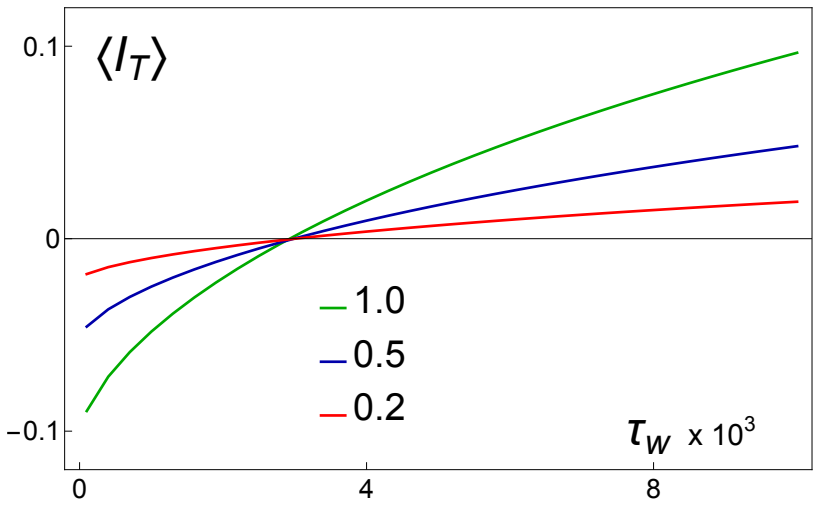


Figure 8.7.: Tunneling current $\langle I_T \rangle$ of the anyon collider as a function of the scaled width for different values of current asymmetry $x = 0.2, 0.5, 1$, and $\lambda = 3/5$, corresponding to the 2/5 FQHE. For small τ_w, the tunneling current is negative in contradiction with experiments. As the scaled width is increased, $\langle I_T \rangle$ starts to increase and becomes positive at $\tau_w \sim 0.003$.

experiments observe an unambiguous positive tunneling current [37, 38]. This leads to the discrepancy by virtue of (derivative of) the tunneling current sitting in the denominator in Equation (8.27). We made several attempts to resolve this discrepancy between theory and experiments, throughout Section 7.7, albeit without much success.

We find now that accounting for the finite width of anyons leads to a natural resolution to this problem. Indeed, the decrease of effective braiding phase $f(t, \lambda, \tau_w)$ close to $t = 0$ discussed in Section 8.2.4 has a direct bearing on all transport quantities of the system, most importantly the tunneling current at the QPC, given in Equation (8.20).

The integrand of the tunneling current in Equation (8.20) contains the sine of $\mathrm{Im} f(t, \lambda, \tau_w)$. For zero-width anyons, the latter quantity is strictly negative, and hence so is its sine, leading to a net negative tunneling current. However, for $t_w \neq 0$, close to $t = 0$, $\mathrm{Im} f(t, \lambda, \tau_w)$ is positive. As the rest of the integrand in Equation (8.20) is peaked close to $t = 0$, a sizable contribution to the tunneling current comes from the $t \simeq 0$ region. In the latter region, the sine of the imaginary phase returns a positive value. We find that this results in an average positive tunneling current for $\lambda = 3/5$, as opposed to a negative average tunneling current seen for zero-width anyons. This is shown in Figure 8.7 where the mean current $\langle I_T \rangle$ is plotted as a function of the scaled width τ_w for different values of the asymmetry x of the incoming currents. One readily sees that $\langle I_T \rangle$ grows from negative to positive as τ_w is increased. For Lorentzian-shaped anyons, $\langle I_T \rangle$ changes sign at $\tau_w \sim 0.003$; for other shapes of finite width anyons (not shown), the qualitative behavior is the same.

The physical interpretation of tunneling current sign change is not too difficult. Since the anyons have a finite width, they are now only partially enclosed inside the braiding loops formed by anyon-antianyon pairs tunneling at the QPC, as shown schematically in Figure 8.1. This means that the effective phase produced by this braiding of the incoming finite width anyon with the tunneling anyon-antianyon pairs is less than the original, expected phase. It then follows that starting from an exchange phase of $\lambda > 1/2$, large enough widths of the anyons could lead to an effective exchange phase less than $1/2$, making the current positive.

The above interpretation also explains why the effect of finite width of anyons is not as dramatic when $\lambda < 1/2$. Since the effect of the finite width is to decrease the effective braiding phase, when $\lambda < 1/2$ the effective braiding phase would only decrease further. This does not change the sign of the tunneling current, but only its magnitude slightly (tunneling current changes sign across $\lambda = 1/2$). This explains why it is not necessary to account for the finite width of anyons in the anyon collider at $\nu = 1/3$ where $\lambda = 1/3$, and the theory of zero-width anyons agrees well with the experiments.

Interestingly, the impact of the finite width of anyons on the tunneling noise is not as dramatic as that on the tunneling current. This can be traced back to the cosine of the imaginary part of the braiding phase in Equation (8.23). Since the cosine is not sensitive to change in signs, the impact of finite width on the tunneling noise is only on a quantitative level, changing its magnitude. However, finite width does change signs of the tunneling current derivatives in Equations (8.25) and (8.26). Nevertheless, for physically reasonable values of the scaled width (see next section) the sign changes of the latter quantities conspire to produce a net negative current cross-correlation.

8.3. Scaled width and source QPC transparency

We show in this section that the scaled width of the anyons is related to the transparency of the source QPCs. The transparency of the source QPCs, $\mathcal{T}$ is defined as the ratio of the incoming current at the QPC with that outgoing from the QPC

$$\mathcal{T} = \frac{I_{u/d}}{I_{in}} \tag{8.28}$$

where $I_{in} = G_0 V$, is simply the conductance of the edge times the voltage applied at the input of the QPC, giving us

$$\mathcal{T} = \frac{h I_{u/d}}{\nu V e^2} \tag{8.29}$$

The wavepacket approach to electron transport gives the width of electron wavepackets to be $\hbar/eV$ [157]. Inspired by this non-interacting picture, it is natural to think that anyon wavepackets at a QPC have a width $t_w \sim \hbar/q_{\boldsymbol{g_2}} V$ [39, 87]. Plugging this in to the

expression for QPC transparency, we find

$$\mathcal{T} = \frac{2\pi}{\nu}\left(\frac{q_{\boldsymbol{g_2}}}{e}\right)^2 \frac{I_{u/d}}{q_{\boldsymbol{g}_\alpha}} t_w \tag{8.30}$$

The collider is characterized by two input currents $I_{u/d}$ from the two source QPCs. There are two extreme possibilities: the balanced case, where the two input currents are equal, giving us $I_+ = 2I_{u/d}$, or the asymmetric case, where one of the currents is zero, giving us $I_+ = I_{u/d}$, with the intermediate cases interpolating linearly between these values. We hence have the relation $1/2 \leq I_{u/d}/I_+ \leq 1$, with the proportionality factor being less than 1.

Then, using the fact that the average spacing between incoming quasiparticles is $t_s = q_{\boldsymbol{g_2}}/I_+$, we can write

$$\mathcal{T} \sim \frac{2\pi}{\nu}\left(\frac{q_{\boldsymbol{g}_\alpha}}{e}\right)^2 \tau_w \tag{8.31}$$

Hence, the scaled width of the anyons bears a direct proportionality with the transparency of the source QPC, with a proportionality constant of order unity. In cases of experimental relevance of the $\nu = 1/3$ and $\nu = 2/5$ FQHE, the constant of proportionality is of order unity. It is also interesting to note that the scaled width does not depend on the input voltage at the QPC, but only the QPC transparency. Indeed, the applied voltage V before a source QPC can be seen as a regular stream of incoming excitations whose spacing is equal to their width, $t_w \sim \hbar/q_{\boldsymbol{g_2}}V$, set by the voltage. As only a fraction $\mathcal{T}$ of these excitations is transmitted through the QPC, it gives a scaled width $\tau_w \sim \mathcal{T}$.

It is true that introducing anyon width as parameter in the system offers flexibility in fitting experimental data. But the direct relation between the widths and QPC transparency established in this section holds significance for several reasons. Associating anyon width with QPC transparency imposes constraints on the plausible range of widths, ensuring that the τ_w remains physically meaningful. This relation also provides a means to experimentally manipulate the anyons by adjusting QPC transparency, thus exploring how system properties vary with anyon width. Beyond data fitting, this relation grants predictive power, allowing us to investigate how system quantities evolve with changes in QPC transparency. Predicting how quantities vary with QPC transparency enables more robust comparisons with experimental results.

However, it should be noted that in the absence of a microscopic connection between the scaled width and the QPC transparency, the constants relating them should be taken with a grain of salt.

8.4. Comparison with experiment

We now examine the consequence of the finite width of the incoming anyons on the experimentally measured generalized Fano factor defined in Equation (8.27). This so-called $P-$value was measured in recent experiments [34, 37, 38, 158] to extract anyon statistics in FQHE. For $\nu = 1/3$ FQHE, the experiments find an excellent agreement with the theory of Ref. [33] where the incoming anyons are assumed to have zero width. On the other hand, for $\nu = 2/5$, the experiments are in strong disagreement with the theoretical calculations, as the $P-$value is predicted to be positive and quite large (close to 6), while the experiments measure negative values of the order of -1. We now make quantitative comparisons of our theory of finite-width anyons with experimental data for both these filling fractions.

8.4.1. $\nu = 2/5$

First, we consider the pressing issue of $\nu = 2/5$ where there is a clear contradiction between theory and experiment. We plot the $P-$value for $\nu = 2/5$ FQHE ($\lambda = 3/5, \delta = 3/5$) in Fig. 8.8 for different values of the scaled width τ_w. Experimental data points from Ref. [37] are shown in brown. The black curve denotes the predictions of Ref. [33] where $\tau_w = 0$, and is in complete disagreement with the experimental data. With a non-zero τ_w, the curves have now negative values, getting closer to the experimental data. The inset zooms into the region around the data points; we find that $\tau_w \sim 0.075$ agrees well with the experiments. Using Equation (8.31) the scaled width found to fit the data in Figure 8.8 can be used to find the related QPC transparency. The two bosonic modes of conductance 1/3 and 1/15 on the edge of the $\nu = 2/5$ FQHE (see Sections 1.2.3 and 2.2 for example) are spatially separated in experiments [37–39]. Hence, for tunneling of $e/5$ anyons, we have $q_{\boldsymbol{g_2}} = e/5$ and $\nu = 1/15$ since the tunneling of $e/5$ anyons can be thought to occur only on the 1/15 bosonic mode. Using these, we find $\mathcal{T} \approx 0.29$, which is quite close to the experimentally used value of 0.35 in Ref. [37] for the data shown in Figure 8.8. We note that after submission of the article related to this work, other works [159] appeared, presenting results consistent with those discussed here.

8.4.2. $\nu = 1/3$

We now compare the prediction of the theory of finite width anyons in the collider, with experimental data at several values of the QPC transparency. Such data is available for $\nu = 1/3$. While Figure 8.8 compares theory and experiment at a fixed transparency, for different values of the current asymmetry, here we will consider fixed current asymmetry and compare theory and experiment as a function of QPC transparency. We consider the exchange phase λ, and the constant relating τ_w and $\mathcal{T}$, that we denote w, to be fitting

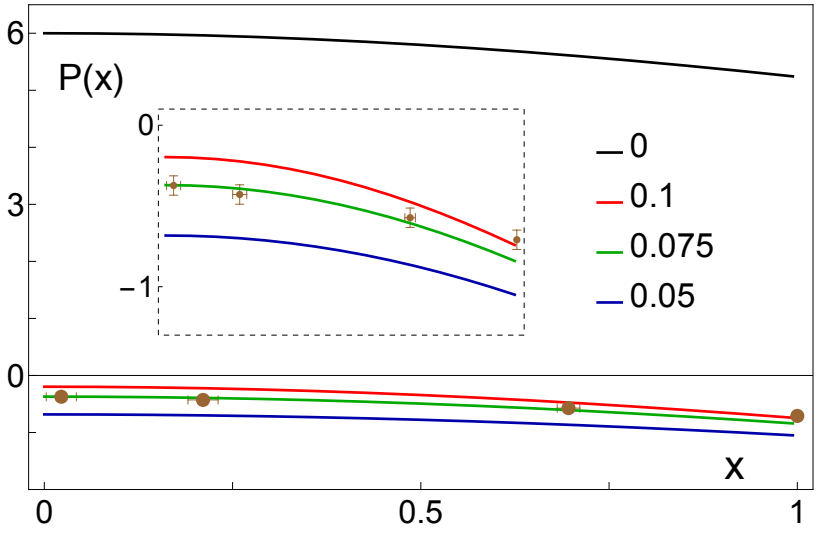


Figure 8.8.: Fano factor $P(x)$ of Equation (8.27) as a function of the current asymmetry x for different values of scaled width: $\tau_w = 0, 0.05, 0.075, 0.1$. Experimental data from Ref. [37] are shown as brown points with error bars. $P(x)$ is in contradiction even with the sign of the experimentally measured values for $\tau_w = 0$, but becomes compatible with the experimental data for $\tau_w \simeq 0.075$. Inset zooms into the region close to the experimental data points. Curves on both panels were obtained in the regime of negligible temperature.

parameters. It is emphasized that although the number w can be argued to be of order unity, its precise value is difficult to estimate from first principles.

We consider two different regimes here: the balanced regime, where equal currents are sent from both source QPCs, and the fully asymmetric regime where current is injected fully from only a single source QPC. In the latter regime, a different quantity, called the $F-$factor is used for comparison. It is defined simply as

$$F = \frac{\langle S_T \rangle}{q_g \langle I_T \rangle} \tag{8.32}$$

Let us first compare theory and experiment in the balanced regime by looking at the $P-$factor in Figure 8.9. Two runs of experimental data (blue and green points) for different QPC transparencies [149] are compared with the theory of finite width anyons applied to two different possibilities.

First, we consider rectangular anyons incident on the QPC. The best fit is given by parameters: $\lambda \sim 1/3$ and $w \sim 1$, giving a nice agreement with the experimental data. We also consider Lorentzian shaped anyons. Here, the best fit is given by parameters: $\lambda \sim 1/3 \times 1.1$, and $w \sim 1/5$. The latter phenomenological choices allow a satisfying agreement between our theory and the experimental data. The value $\lambda \sim 1/3 \times 1.1$ although deviating from the predictions of theory should not be too surprising. Indeed,

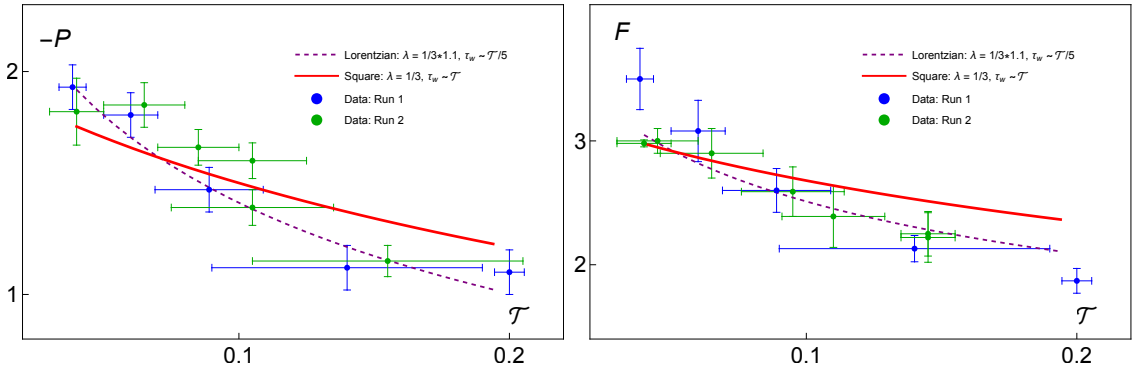


Figure 8.9.: Comparison between theoretical predictions of the $P-$factor in the balanced regime (left) and the $F-$factor in the asymmetric regime (right), and the respective experimental data. We consider two different shapes of the anyons: square and Lorentzian. While the latter fits well with additional phenomenological input, the rectangular anyons naturally agree well with the data.

errors up to 10% in the measured quantities such as charge or statistics are routine in FQHE edge experiments [36, 37]. Moreover, the constant relating the scaled width and QPC transparency does not have a microscopic justification, allowing us some flexibility in changing the latter. Nevertheless, choosing rectangular-shaped anyons fits the data rather well without any additional phenomenological input.

The same story is true in the fully asymmetric regime, where we consider the $F-$factor instead. Lorentzian anyons plus additional phenomenological input and simple rectangular anyons both agree rather well with the experimental data. This convincing agreement between our theory and experimental data underscores the success of our theory in explaining the anyon braiding physics occurring in the anyon collider.

8.5. Discussion and conclusion

This chapter focused on the consequences the finite width of anyons has on their braiding signatures. While typically the finite width of particles can be safely ignored, we explicitly show that the width of anyons plays a crucial role due to their non-trivial braiding statistics. Moreover, the finite width of anyons has a profound impact on observables associated with the braiding statistics of anyons – it has the effect of changing even the sign of the current due to anyons. These properties were first illustrated by studying the current due to single anyon hitting a QPC. This observation has great implications for the anyon collider in $\nu = 2/5$. There, the theory of zero width anyons predicts a negative tunneling current as the exchange phase of the anyons is greater than $\pi/2$. However, experiments observe a clear positive current.

Accounting for the finite width of anyons, we show that the effective time-domain braiding phase of anyons seen at the QPC *decreases*. An exchange phase theoretically predicted to be large than $\pi/2$ could become effectively smaller than $\pi/2$ due to the finite width of anyons. This leads to a change in the sign of the tunneling current. We are able to show that the finite width of anyons changes the sign of the tunneling current in 2/5 FQHE, consistent with the experimental observations. Thanks to the direct relation between width of anyons on FQHE edges and the transparency of QPCs established here, the resolution is placed on a firm quantitative footing. We find an excellent agreement of our theory with data at $\nu = 2/5$ for $\mathcal{T} \sim 0.29$, very close to experimentally used values of QPC transparency.

Our calculations also explain why the first experiments at $\nu = 1/3$ found agreement with the theoretical predictions of zero-width anyons. Indeed, throughout this chapter, we found that for $\lambda = 1/3$ (and more generally for $\lambda < 1/2$), the impact of the finite width of anyons on the physical quantities was markedly limited. Not only was there not a dramatic qualitative change like the sign of the tunneling current, but even the quantitative change was minimal. Nevertheless, it is worth noting that the initial experiments used a fixed transparency $\mathcal{T}$, keeping the scaled width of the anyons constant. Changing $\mathcal{T}$ indeed changes the scaled width, leading to quantitative changes in the physical quantities. We compare our theory with data at $\nu = 1/3$ as a function of $\mathcal{T}$, finding an excellent agreement.

The decrease in the effective braiding phase can be understood as a result of incoming finite-width anyons being only partially enclosed within the loops formed by tunneling anyons at the QPC. This can be seen as a consequence of the "temporal proximity" between the incoming and tunneling anyons. This interpretation opens up an intriguing scenario for further exploration of the consequences of finite anyon width. Consider, for instance, a dilute stream of anyons encountering not just a single QPC, but two QPCs forming a Fabry-Pérot interferometer. In this setup, the incoming anyons would experience both time-domain braiding with the tunneling anyons at the QPCs and conventional braiding with the anyons located in the island between the two QPCs. As a result, edge observables become sensitive to both braiding phases. In this case, only the time-domain braiding phase is expected to be sensitive to effects such as the finite width of anyons, while the conventional phase is expected to retain the theoretically predicted value. Investigating the interplay between these two distinct manifestations of anyon braiding phase could provide deeper insights into the physics of anyons and the extent to which edge physics influences the topological properties of anyons.

Perspectives

This thesis contributes to further our understanding of anyons in a general Abelian FQHE state. We not only propose setups to unambiguously measure the fractional charge, scaling dimension, and braiding statistics of anyons, but also account for edge physics which might lead to observations different from the predictions of pristine theory. The thesis solves many problems in detecting anyons, but it also opens up several avenues to pursue further.

In the context of fractional charges, it might be interesting to use the formalism developed in Chapter 3 to address minimal excitations called Levitons on the FQHE edges [98, 99]. These are excitations with an integer charge and no accompanying quasiparticle-quasihole pairs, potentially useful in flying qubit applications [160]. While we addressed the Andreev reflection like processes in the Laughlin FQHE in Chapter 4, similar processes that might occur in non-Laughlin fractions such as $\nu = 2/5$, where $e/5$ anyon could hit QPCs admitting only $e/3$ anyons, remain unexplored. Although the latter sounds like a trivial generalization of the Laughlin system, in the Laughlin case the fact that anyons braid trivially with electrons led to a considerable simplification. However, it is not clear if such simplifications would occur in the interactions of $e/3$ and $e/5$ anyons in the $\nu = 2/5$ FQHE, or in more general scenarios.

The temperature gradient between edges in Chapter 5 yielded precious information about the scaling dimension of anyons. However, thermal gradients in setups involving multiple quantum point contacts could yield information also about braiding statistics. Beyond the FQHE, this might bear implications for chiral spin liquid states where the anyonic excitations are neutral [161–166].

The anyon collider setup detailed in Chapters 6–8 has yielded remarkable observation of anyonic braiding phase in the $\nu = 1/3$ and $\nu = 2/5$ systems through the time-domain braiding processes. However, as we saw, the finite width of anyons leads to an effectively smaller braiding phase experienced by the system. The Fabry-Pérot geometry, where edge anyons braid with bulk anyons in the conventional sense, implemented at $\nu = 2/5$ agrees with well with simple theoretical predictions [40]. It is hence quite an interesting prospect to study the interplay of time-domain braiding of anyons and the conventional $2D$ braiding of anyons. The Fabry-Pérot system offers a natural way to investigate this interplay. Indeed, we can imagine sending a dilute stream of anyons on the Fabry-Pérot interferometer via an upstream source QPC. The incoming anyons then not only braid in the time-domain with anyons tunneling at the QPC, but also braid spatially with the bulk

anyons located in the island between the two QPCs of the Fabry-Pérot interferometer. Is it possible in this setup that the effective exchange phase experienced by the system is greater than $\pi/2$, thus producing a *negative* tunneling current not seen in the anyon collider?

Of course, this thesis focused throughout on anyons in Abelian FQHE states. A natural question is how do the results described in this thesis fare in non-Abelian FQHE systems [17]? The edge theory of non-Abelian FQHE can in fact be described in a very similar way as the Abelian FQHE. The free edge theory, in addition to chiral bosons, also acquires for example chiral Majorana fermions in the 5/2 FQHE [19]. Anyons tunneling at the QPC present a greater challenge [167, 168]. Non-Abelian anyons are characterized by multiple *fusion channels* (in addition to fractional braiding phases). Fusion is the outcome of bringing together two anyons. Think of Abelian $e/3$ anyons; bringing two of them together creates a $2e/3$ anyon – a fixed outcome. This is not the case for non-Abelian anyons. Indeed, bringing together two σ anyons in the 5/2 FQHE either annihilates them or creates a neutral fermion. Non-Abelian anyons are thus characterized by *multiple fusion channels* and it is thus necessary to specify the fusion channel of the tunneling terms in non-Abelian FQHE. However, in simple QPCs and the limit of long edge states, complications involving multiple fusion channels are avoided in single QPC geometries. The calculations in the latter case thus proceed in a fashion largely similar to those of Abelian anyons. Hence, the results of Chapters 3 and 5 extend readily to non-Abelian FQHE. The Andreev reflection physics of Chapter 4 could also extend in a straightforward manner as long as non-Abelian anyons from an upstream QPC are incident on a QPC that tunnels electrons. This must be true since all anyons, Abelian or non-Abelian, braid trivially with electrons.

Things get interesting when we consider extending the results of Chapters 6–8 to non-Abelian FQHE. In this case, the fusion multiplicity of non-Abelian anyons – their defining characteristic – starts playing a crucial role. Indeed, when non-Abelian anyons are braided in the time domain, owing to the fusion multiplicity, there is not just a fractional phase, but also a rotation of the fusion channel. The question we must ask is if this physics of fusion multiplicity and rotation of fusion channels is accessible in the anyon collider geometry? Recent works that have extended the anyon collider to non-Abelian FQHE seem to answer the latter question in the negative [87]. Granted, the collider is shown to be able to distinguish different topological orders of the non-Abelian FQHE states. However, the fusion multiplicity turns out to be inaccessible as contributions from non-trivial fusion channels to the physical observables turn out to be subleading compared to those from the trivial fusion channel. This means that the collider cannot distinguish between Abelian and non-Abelian anyons. Hence, more work is needed to understand if these subleading contributions, which are the defining signatures of non-Abelian physics, are accessible in the same or related geometries.

To conclude, we comment briefly on the fate of the physics discussed in this thesis in fractional Chern insulators (FCI), realizations of FQHE physics in the absence of

magnetic fields [169]. Indeed, the topological properties of anyons are universal and independent of the platform on which the topological phases are realized. While ideas such as time-domain braiding could extend to cold atomic FCI, the techniques and measurable quantities discussed here are geared towards electronic systems, and probably are not of direct relevance to the former system. However, in recent years, FCI in Moiré materials like twisted bilayer graphene and transition metal dichalcogenides have attracted prolific attention [170]. The non-uniform berry curvature in these systems implies that their low-energy physics is not described by the Laughlin wavefunction, but possibly by its non-trivial generalizations called *vortexable bands* [171]. Here, we lose some nice properties of Laughlin states that make the bulk-boundary correspondence transparent. Indeed, it is well-known that electron correlators on the FQHE edges are related to the bulk Laughlin wavefunction [19]. The absence of this structure in vortexable bands puts into question the direct applicability of chiral boson theory in these systems. Hence, effort is needed to understand the edge theory of Moiré FCIs, and from there the possibilities of unambiguously detecting anyons in these systems. Since these systems are electronic, there is hope that the measurable quantities discussed in this thesis could be adapted to look for anyons in the latter systems.

Appendix A.

Berry Phase

$$\frac{d\gamma}{dt} = i \left\langle \psi_m^{+z_0}(z_i,t) \left| \frac{d}{dt} \right| \psi_m^{+z_0}(z_i,t) \right\rangle = \left\langle \psi_m^{+z_0}(z_i,t) \left| \frac{d}{dt} \psi_m^{+z_0}(z_i,t) \right\rangle \tag{A.1}$$

From the form of the wavefunction in Equation **??**, the Berry phase takes the form

$$\frac{d\gamma}{dt} = i \left\langle \psi_m^{+z_0}(z_i,t) \left| \frac{d}{dt} \left(\sum_i \log\left(z_i - z_0(t)\right) \right) \right| \psi_m^{+z_0}(z_i,t) \right\rangle \tag{A.2}$$

Introducing in the above equation some Dirac-delta functions

$$\frac{d\gamma}{dt} = i \left\langle \psi_m^{+z_0}(z_i,t) \left| \frac{d}{dt} \left(\int d^2z \sum_i \delta(z - z_i) \log\left(z - z_0(t)\right) \right) \right| \psi_m^{+z_0}(z_i,t) \right\rangle \tag{A.3}$$

we identify the single-particle electron density in the presence of the quasihole $\rho^{+z_0} = \langle \psi_m^{+z_0} | \sum_i \delta(z - z_i) | \psi_m^{+z_0} \rangle$ and hence express the Berry phase as

$$\frac{d\gamma}{dt} = i \int d^2z \ \rho^{+z_0} \ \frac{d}{dt} \log\left(z - z_0(t)\right) \tag{A.4}$$

We have $\rho^{+z_0} = \rho_0 + \delta\rho^{+z_0}$, where ρ_0 is the average electron density, and $\delta\rho^{+z_0}$ denotes the change is electron density due to the quasihole. Since the quasihole influences the electronic density only to a distance l_B around it, the latter quantity is negligible as long as the radius of the path traced by the quasihole is large compared to the magnetic length. We hence write

$$\gamma = i \int d^2z \ \rho_0 \oint \frac{dz_0}{z - z_0} \tag{A.5}$$

z_0 is integrated over a radius R in a clockwise sense. Hence, all $|z| < R$ contribute a factor $2\pi i$ to the integral, and the integral vanishses for all $|z| > R$. We hence find the Berry phase to be $\gamma = 2\pi\rho_0\pi R^2$, the number of electrons contained in the circle of radius R

times 2π. From earlier calculations, we know the number of electrons in a region is equal to the number of flux quanta in the regio times the filling fraction, giving us

$$\gamma = 2\pi\nu\frac{\phi}{\phi_0} \tag{A.6}$$

where ϕ denotes the flux contained in the circle of radius R.

Appendix B.

Bosonic Greens Function

In this Appendix, we derive the most fundamental physical quantities used throughout this thesis: bosonic Greens function and quasiparticle Greens function. Here, we start from the action of a chiral boson – a bosonic field that propagates in a single direction, with no backscattering. For a more general derivation, which appropriately defines the chiral boson starting from the more familiar non-chiral boson, we refer the reader to Ref. [172].

B.1. Derivation of bosonic Greens function for a single chiral boson

Let us start with a single chiral boson whose action is given by

$$S = \frac{1}{4\pi}\int dxdt\left[-\chi\partial_x\phi\partial_t\phi - v(\partial_x\phi)^2\right] \tag{B.1}$$

where v is the velocity of the boson, and χ its chirality. Putting it in a box of length L, we quantize the real-space boson in terms of momentum-space bosons.

$$\phi(x,t) = \frac{2\pi}{L}\sum_{k>0}\frac{e^{-ka}/2}{\sqrt{k}}\left[a_k e^{ik(vt-\chi x)} + a_k^\dagger e^{-k(vt-\chi x)}\right] \tag{B.2}$$

Where a is an ultra-violet cutoff, and $a_k, a_k^\dagger$ are bosonic operators in the momentum space satisfying $\left[a_k, a_q^\dagger\right] = \delta_{kq}$. Note that the mode-expansion ensures that the boson is real. We only sum over the $k > 0$ momenta since the boson is right-moving. We use this mode-expansion of the chiral boson as a starting point. In the limit $L \to \infty$, we can express the sum as an integral:

$$\phi(x,t) = \int_0^\infty dk\frac{e^{-ka}/2}{\sqrt{k}}\left[a_k e^{ik(vt-\chi x)} + a_k^\dagger e^{-k(vt-\chi x)}\right]. \tag{B.3}$$

We are concerned with evaluating the following two-point correlation function

$$\mathcal{G}(x,t) = \langle 0|\, \phi(x,t)\phi(0,0)\, |0\rangle - \langle 0|\, \phi(0,0)\phi(0,0)\, |0\rangle \tag{B.4}$$

which we refer to as the *bosonic Greens function*. Here, $|0\rangle$ denotes the ground state of the bosonic edge theory. To calculate the Greens function, we plug in the mode-expansion of Equation B.3 into Equation B.4. This gives us

$$\mathcal{G}(x,t) = \int_0^\infty dkdq \frac{e^{-(k+q)a/2}}{\sqrt{kq}} \left[\left\langle a_k^\dagger a_q \right\rangle \left(e^{-ik(vt-\chi x)} - 1\right) + \left\langle a_k a_q^\dagger \right\rangle \left(e^{ik(vt-\chi x)} - 1\right) \right] \tag{B.5}$$

where $\langle . \rangle$ denotes average on the ground state $|0\rangle$. The bosonic correlation functions in momentum space are simple:

$$\begin{aligned} \left\langle a_k^\dagger a_q \right\rangle &= \delta(k-q) n_k, \\ \left\langle a_k a_q^\dagger \right\rangle &= \delta(k-q)(1+n_k). \end{aligned} \tag{B.6}$$

$n_k = 1/(e^{vk/T} - 1)$ is the Bose-Einstein distribution, where within a low-energy approximation, the bosons are assumed to disperse linearly. We can hence express the bosonic Greens function as

$$\mathcal{G}(x,t) = \int_0^\infty dk \frac{e^{-ka}}{k} \left\{ \left(e^{ik(vt-\chi x)} - 1\right) - n_k \left[\left(e^{ik(vt-\chi x)} - 1\right) \left(e^{-ik(vt-\chi x)} - 1\right) \right] \right\} \tag{B.7}$$

Let us split the integral into two parts, $\mathcal{G}(x,t) = I_1(x,t) - I_2(x,t)$ and evaluate them separately.

The first integral

$$I_1(x,t) = \int_0^\infty dk\ \frac{e^{-k[a-i(vt-\chi x)]} - e^{-ka}}{k} \tag{B.8}$$

is tabulated in Ref.[125], 3.434 (2), giving us

$$I_1(x,t) = \log\left(\frac{i\tau_0}{i\tau_0 + t - \chi x/v}\right) \tag{B.9}$$

where $\tau_0 = a/v$ is a temporal cutoff. The second integral

$$I_2(x,t) = \int_0^\infty dk\ \frac{\left(e^{ik(vt-\chi x)} - 1\right)\left(e^{-ik(vt-\chi x)} - 1\right) e^{-ka}}{e^{vk/T} - 1} \tag{B.10}$$

evaluates similarly after some coordinate transformations. We multiply the numerator and denominator by $e^{-vk/T}$, and make the transformation $u = vk/T$ to find

$$I_2(x,t) = \int_0^\infty du \, \frac{\left(e^{iuT(t-\chi x/v)} - 1\right)\left(e^{-iuT(t-\chi x/v)} - 1\right) e^{-k(a+v/T)}}{1 - e^{-u}} \tag{B.11}$$

which is tabulated again in Ref. [125], 3.413 (1). We then find the second piece to take the following formidable form:

$$I_2(x,t) = \log\left[\frac{\Gamma\left(1+\tau_0 T\right)\Gamma\left(1+\tau_0 T\right)}{\Gamma\left(1+\tau_0 T + iT\left(t-\chi x/v\right)\right)\Gamma\left(1+\tau_0 T - iT\left(t-\chi x/v\right)\right)}\right]. \tag{B.12}$$

In the limit $\tau_0 \to 0$, we are free to flip the sign of τ_0 in one of the Gamma functions in both the numerator and denominator, without affecting the convergence of the integral. This allows us to use the identity $\Gamma(1+ix)\Gamma(1-ix) = x/\sinh \pi x$, which simplifies the integral heavily.

$$I_2(x,t) = \log\left\{\frac{i\tau_0}{i\tau_0 + t - \chi x/v}\frac{\sinh\left[\pi T\left(i\tau_0 + t - \chi x/v\right)\right]}{\sinh\left(i\pi T\tau_0\right)}\right\} \tag{B.13}$$

Putting together the two contributions, we find the time-ordered finite-temperature bosonic Greens function to take the form

$$\mathcal{G}(x,t) = \log\left\{\frac{\sinh\left(i\pi T\tau_0\right)}{\sinh\left[\pi T\left(i\tau_0 + t - \chi x/v\right)\right]}\right\} \tag{B.14}$$

The zero temperature Greens function follows readily, since for $T = 0$, $n_k = 0$ and hence the zero temperature Greens function is given simply by I_1.

$$\mathcal{G}(x,t) = \log\left(\frac{i\tau_0}{i\tau_0 + t - \chi x/v}\right) \tag{B.15}$$

B.2. Extension to multiple chiral bosons

The action of multiple chiral bosonic modes such as those found on the edge of a general Abelian FQHE is shown below:

$$S = \frac{1}{4\pi}\int dxdt \sum_{j=1}^{N}\left[-\chi_j \partial_x\phi_j\partial_t\phi_j - v_j(\partial_x\phi_j)^2\right] \tag{B.16}$$

It is a system of N bosons with v_j and χ_j denoting the velocity and chirality of the $j-$th boson. We define the Greens function of the $j-$th bosonic field to be:

$$\mathcal{G}_j(x,t) = \langle\phi_j(x,t)\phi_j(0,0)\rangle - \langle\phi_j(0,0)\phi_j(0,0)\rangle \tag{B.17}$$

Since the bosons do not interact with each other, it is clear that they each have the same Greens function, derived in the previous section. We can hence readily write

$$\mathcal{G}_j(x,t) = \log\left\{\frac{\sinh\left(i\pi T\tau_{j0}\right)}{\sinh\left[\pi T\left(i\tau_{j0}+t-\chi_j x/v_j\right)\right]}\right\} \tag{B.18}$$

where $\tau_{j0} = a/v_j$. Working in the limit $\tau_{j0} \to 0$ for all j, we choose $\tau_0 < \tau_{0j}$ for all j, giving us the same Greens function for all the bosonic fields.

$$\mathcal{G}_j(x,t) = \log\left\{\frac{\sinh\left(i\pi T\tau_{0}\right)}{\sinh\left[\pi T\left(i\tau_{0}+t-\chi_j x/v_j\right)\right]}\right\} \tag{B.19}$$

B.3. Correlation function of exponentiated boson operators

We know that anyonic quasiparticles or electrons on FQHE edges are related to the bosonic fields by:

$$\psi_{\boldsymbol{g\alpha}} = e^{i\boldsymbol{g\alpha}\cdot\boldsymbol{\phi}}. \tag{B.20}$$

Throughout this thesis, we are interested in calculating $N-$point correlation functions of the above operators.

Hence, in this section, we want to calculate generic correlation functions of exponentiated bosonic fields of the form:

$$O(\{x_k,t_k\}) = \left\langle e^{\boldsymbol{\alpha_1}\cdot\boldsymbol{\phi}(x_1,t_1)}\dots e^{\boldsymbol{\alpha_n}\cdot\boldsymbol{\phi}(x_n,t_n)}\right\rangle \tag{B.21}$$

where $\alpha_k = (\alpha_{1k},\dots,\alpha_{Nk})$ is a vector of complex numbers, and $\boldsymbol{\phi} = (\phi_1,\dots,\phi_N)$.

B.3.1. Single harmonic oscillator

It is instructive to see how this calculation goes for a single harmonic oscillator. Consider a harmonic oscillator with creation and annihilation operators satisfying $[a,a^\dagger]=1$. These are characterized by a ground state $|0\rangle$ satisfying $a\,|0\rangle = 0$.

Mimicking Equation (B.21), we want to calculate the following correlator here:

$$\tilde{O} = \langle 0| : e^{A_1} :: e^{A_2} : \cdots : e^{A_n} : |0\rangle\,, \tag{B.22}$$

where $: e^{A_i} :$ is the analog of the quasiparticle operator, and it reads:

$$: e^{A_i} : \ = e^{\alpha_i a^\dagger} e^{\alpha_i a}, \tag{B.23}$$

where α_i are complex numbers, and the normal ordering (denoted by the symbol $: \ :$) pushes the annihilation operators to the right. The calculation proceeds by commuting the annihilation operators to the right, giving us:

$$\tilde{O} = \langle 0| \, e^{(\alpha_1 + \cdots + \alpha_n) a^\dagger} e^{(\alpha_1 + \cdots + \alpha_n) a} \, |0\rangle \, e^{\sum_{i<j} \alpha_i \alpha_j}. \tag{B.24}$$

Here, the final term is a complex number, which by using the relation between creation and annihilation operators, can be shown to be expressed as:

$$e^{-\sum_{i<j} \alpha_i \alpha_j} \equiv \exp\left[\sum_{i<j} \langle 0| \, A_i A_j \, |0\rangle \right]. \tag{B.25}$$

Moreover, the correlation function of Equation (B.24) vanishes unless $\sum_i \alpha_i = 0$. If the latter condition is satisfied, the correlation function reads:

$$\tilde{O} = \langle 0| : e^{A_1} :: e^{A_2} : \cdots : e^{A_n} : |0\rangle = \exp\left[\sum_{i<j} \langle 0| \, A_i A_j \, |0\rangle \right] \tag{B.26}$$

That is, the correlation function of exponentiated bosons is equal to the exponential of the sum of the bosonic correlators, provided the sum of the coefficients α_i of the bosons vanish. The correlation function vanishes otherwise since in Equation (B.24), the annihilation operators act on the ground state.

B.3.2. Bosonic fields

Let us quickly rewrite, the correlation function of Equation (B.21) more explicitly:

$$O(\{x_k, t_k\}) = \prod_{j=1}^{N} \left\langle e^{\alpha_{1j} \phi_j(x_1, t_1)} \ldots e^{\alpha_{nj} \phi_j(x_n, t_n)} \right\rangle \tag{B.27}$$

From Equation (B.2), it is clear that each bosonic field is simply a linear combination of many harmonic oscillator creation and annihilation operators. Hence, we can simply express the correlation function as:

$$O(\{x_k, t_k\}) = \prod_{j=1}^{N} \exp\left[\sum_{k<l} \alpha_{kj} \alpha_{lj} \, \langle 0| \, \phi_{jk}(x_k, t_k) \phi_{jk}(x_l, t_l) \, |0\rangle \right], \tag{B.28}$$

where to avoid confusion, we remind the reader that j indicates the bosonic mode index in the vector $\boldsymbol{\phi} = (\phi_1, \ldots, \phi_N)$, while k and l refer to the different operators inserted in the correlator. The objects within the square brackets are precisely the bosonic Greens function of Equation (B.19). We can hence write:

$$O(\{x_k, t_k\}) = \prod_{j=1}^{N} \exp\left[\sum_{k<l} \alpha_{kj}\alpha_{lj}\mathcal{G}(x_k - x_l, t_k - t_l)\right]. \tag{B.29}$$

given $\sum_k \alpha_k = 0$. This result can be used to quite generally calculate $N-$point functions of anyon or electron operators on FQHE edges.

B.4. Quasiparticle Greens function

We very often encounter the two-point function of anyon or electron operators in this thesis:

$$\begin{aligned} O_2(x_1 - x_2, t_1 - t_2) &= \left\langle e^{i\boldsymbol{g_\alpha}\cdot\boldsymbol{\phi}(x_1,t_1)} e^{-i\boldsymbol{g_\alpha}\cdot\boldsymbol{\phi}(x_2,t_2)} \right\rangle \\ &= \prod_{j=1}^{N} \left\langle e^{ig_{\alpha j}\phi_j(x_1,t_1)} e^{-ig_{\alpha j}\phi_j(x_2,t_2)} \right\rangle \end{aligned} \tag{B.30}$$

Using Equation (B.29), we can write the above two-point function as:

$$O_2(x_1 - x_2, t_1 - t_2) = \prod_{j=1}^{N} \exp\left[g_{\alpha j}^2 \mathcal{G}(x_1 - x_2, t_1 - t_2)\right]. \tag{B.31}$$

Recalling now that $\sum_j g_{\alpha j}^2 = \delta_{\boldsymbol{g}_\alpha}$, the scaling dimension of type$-\alpha$ quasiparticle, the quasiparticle Greens function is expressed simply as:

$$\left\langle e^{i\boldsymbol{g_\alpha}\cdot\boldsymbol{\phi}(x_1,t_1)} e^{-i\boldsymbol{g_\alpha}\cdot\boldsymbol{\phi}(x_2,t_2)} \right\rangle = \exp\left[\delta_{\boldsymbol{g}_\alpha} \mathcal{G}(x_1 - x_2, t_1 - t_2)\right]. \tag{B.32}$$

Appendix C.

DC shot noise: general Abelian edge

Plugging in the expressions of the tunneling current and tunneling Hamiltonian operators from the previous section, we find

$$\begin{aligned}\langle I_T\rangle = -\frac{i}{2}\sum_{\eta\eta'\epsilon\epsilon'}\epsilon\eta'\sum_{\alpha\beta}\int dt' i q_{\boldsymbol{g}_\alpha}\Big[\Gamma_{\boldsymbol{g}_\alpha}e^{iq_{\boldsymbol{g}_\alpha}Vt}\Big\langle T_K\Big\{\psi^{u\dagger}_{\boldsymbol{g_\alpha}}(0,t^\eta)\psi^{d}_{\boldsymbol{g_\alpha}}(0,t^\eta)\Big]^{\epsilon}\\ \Big[\Gamma_{\boldsymbol{g_\beta}}e^{iq_{\boldsymbol{g}_\beta}Vt'}\psi^{u\dagger}_{\boldsymbol{g_\beta}}(0,t^\eta)\psi^{d}_{\boldsymbol{g_\beta}}(0,t^\eta)\Big]^{\epsilon'}\Big\}\Big\rangle\end{aligned} \tag{C.1}$$

Charge conservation of each bosonic field implies $\alpha=\beta$ and $\epsilon'=-\epsilon$, allowing us to get rid of some summation indices

$$\begin{aligned}\langle I_T\rangle = \sum_{\eta\eta'\epsilon\alpha}\epsilon\eta'\frac{q_{\boldsymbol{g}_\alpha}|\Gamma_{\boldsymbol{g}_\alpha}|^2}{2}\int dt' e^{-iq_{\boldsymbol{g}_\alpha}\epsilon V(t-t')}\\ \Big\langle\Big\{T_K\Big[\psi^{u\dagger}_{\boldsymbol{g}_\alpha}(0,t^\eta)\psi^{d}_{\boldsymbol{g}_\alpha}(0,t^\eta)\Big]^{\epsilon}\Big[\psi^{u\dagger}_{\boldsymbol{g}_\alpha}(0,t^\eta)\psi^{d}_{\boldsymbol{g}_\alpha}(0,t^\eta)\Big]^{-\epsilon}\Big\}\Big\rangle\end{aligned} \tag{C.2}$$

Using then the independence of the upper and lower edges, we can separate the correlator into parts each on the upper and the lower edge

$$\begin{aligned}\langle I_T\rangle = \sum_{\eta\eta'\epsilon\alpha}\epsilon\eta'\frac{q_{\boldsymbol{g}_\alpha}|\Gamma_{\boldsymbol{g}_\alpha}|^2}{2}\int dt' e^{iq_{\boldsymbol{g}_\alpha}\epsilon V(t-t')}\\ \Big\langle\Big\{T_K e^{i\epsilon\boldsymbol{g}_\alpha\cdot\phi^u(0,t^\eta)}e^{-i\epsilon\boldsymbol{g}_\alpha\cdot\phi^u(0,t'^{\eta'})}\Big\}\Big\rangle\Big\langle\Big\{T_K e^{-i\epsilon\boldsymbol{g}_\alpha\cdot\phi^d(0,t^\eta)}e^{i\epsilon\boldsymbol{g}_\alpha\cdot\phi^d(0,t'^{\eta'})}\Big\}\Big\rangle\end{aligned} \tag{C.3}$$

These correlators are calculated in full detail in Appendix B and we use the result to write

$$\langle I_T\rangle = \sum_{\eta\eta'\epsilon\alpha}\epsilon\eta'\frac{q_{\boldsymbol{g}_\alpha}|\Gamma_{\boldsymbol{g}_\alpha}|^2}{2}\int dt' e^{iq_{\boldsymbol{g}_\alpha}\epsilon V(t-t')}e^{\delta_{\boldsymbol{g}_\alpha}\mathcal{G}_u^{\eta\eta'}(t-t')}e^{\delta_{\boldsymbol{g}_\alpha}\mathcal{G}_d^{\eta\eta'}(t-t')} \tag{C.4}$$

where $\mathcal{G}^{\eta\eta'}_{u/d}(t-t')$ is the Keldysh Greens function of the bosonic fields on the upper/lower edge. At finite temperatures, this is given by

$$\mathcal{G}^{\eta\eta'}_{u/d}(t-t') = \ln\left(\frac{\sinh\left[i\pi\tau_0 T_{u/d}\right]}{\sinh\left[\pi T_{u/d}\left(i\tau_0 + \chi^{t-t'}_{\eta\eta'}(t-t')\right)\right]}\right) \tag{C.5}$$

where $T_{u/d}$ is the temperature of the upper/lower edge, τ_0 is a temporal UV cutoff of the bosonic field, and

$$\sigma^{t-t'}_{\eta\eta'} = \frac{1}{2}\left[(\eta'-\eta) + \mathrm{sgn}(t-t')(\eta'+\eta)\right] \tag{C.6}$$

accounts for the Keldysh time ordering of the fields. At zero temperatures, the bosonic Greens function simplifies to a power law

$$\mathcal{G}^{\eta\eta'}_{u/d}(t-t') = \ln\left(\frac{i\tau_0}{i\tau_0 + \chi^{t-t'}_{\eta\eta'}(t-t')}\right) \tag{C.7}$$

Working for now at finite temperatures, but taking $T_u = T_d \equiv T$, and hence $\mathcal{G}_u = \mathcal{G}_d \equiv \mathcal{G}$, we continue calculating the average tunneling current

$$\langle I_T\rangle = \sum_{\eta\eta'\alpha} i\eta' q_{\boldsymbol{g}_\alpha} |\Gamma_{\boldsymbol{g}_\alpha}|^2 \int d\tau \sin\left(q_{\boldsymbol{g}_\alpha} V\tau\right)\left(\frac{\sinh\left[i\pi\tau_0 T\right]}{\sinh\left[\pi T\left(i\tau_0 + \chi^{\tau}_{\eta\eta'}\tau\right)\right]}\right)^{2\delta_{\boldsymbol{g}_\alpha}} \tag{C.8}$$

where we have summed over ϵ and performed the coordinate transformation $t-t'=\tau$. Summing now over the Keldysh indices, and using Equation C.6, we can write

$$\langle I_T\rangle = \sum_{\alpha} 2i q_{\boldsymbol{g}_\alpha} |\Gamma_{\boldsymbol{g}_\alpha}|^2 \int d\tau \sin\left(q_{\boldsymbol{g}_\alpha} V\tau\right)\left(\frac{\sinh\left[i\pi\tau_0 T\right]}{\sinh\left[\pi T\left(i\tau_0 - \tau\right)\right]}\right)^{2\delta_{\boldsymbol{g}_\alpha}} \tag{C.9}$$

This integral can be evaluated using known results [125], giving us the final form of the current

$$\langle I_T\rangle = \sum_{\alpha} 2 q_{\boldsymbol{g}_\alpha} |\Gamma_{\boldsymbol{g}_\alpha}|^2 \tau_0 (2\pi T\tau_0)^{2\delta_{\boldsymbol{g}_\alpha}-1} \sinh\left(\frac{q_{\boldsymbol{g}_\alpha} V}{2T}\right) \frac{\left|\Gamma\left(\delta_{\boldsymbol{g}_\alpha} + i\frac{q_{\boldsymbol{g}_\alpha} V}{2\pi T}\right)\right|^2}{\Gamma(2\delta_{\boldsymbol{g}_\alpha})} \tag{C.10}$$

We now proceed to calculate the tunneling noise. We first specify the fluctuations of the tunneling current about its average value, which is expressed in the Keldysh formalism as

$$\left\langle \delta I_T^2 \right\rangle = \sum_{\eta\eta'} \left\langle \left\{ T_K I_T(t^{\eta}) I_T(t'^{\eta'}) e^{-i\int_K dt H_T(t)} \right\} \right\rangle - \langle I_T\rangle^2 \tag{C.11}$$

where the final term on the right subtracts the average value of the current, thus isolating the fluctuations around the mean. At lowest order in the tunneling amplitudes (order 2), we can safely discard the latter term as it is an order 4 term. Within this order, there is also no need to expand the interaction Hamiltonian. Thus, we can simply express the current fluctuations as

$$\left\langle \delta I_T^2 \right\rangle = \sum_{\eta\eta'} \left\langle \left\{ T_K I_T(t^\eta) I_T(t'^{\eta'}) \right\} \right\rangle \tag{C.12}$$

Then the zero-frequency DC noise is defined as the zero-frequency fourier transform of the current fluctuations

$$\langle S_T \rangle = \sum_{\eta\eta'} \int dt' \left\langle \left\{ T_K I_T(t^\eta) I_T(t'^{\eta'}) \right\} \right\rangle \tag{C.13}$$

The calculation of the tunneling noise then proceeds in the same manner, yielding quite a similar expression

$$\langle S_T \rangle = \sum_\alpha 4 q_{\boldsymbol{g}_\alpha}^2 |\Gamma_{\boldsymbol{g}_\alpha}|^2 \tau_0 (2\pi T \tau_0)^{2\delta_{\boldsymbol{g}_\alpha}-1} \cosh\left(\frac{q_{\boldsymbol{g}_\alpha} V}{2T}\right) \frac{\left|\Gamma\left(\delta_{\boldsymbol{g}_\alpha} + i\frac{q_{\boldsymbol{g}_\alpha} V}{2\pi T}\right)\right|^2}{\Gamma(2\delta_{\boldsymbol{g}_\alpha})} \tag{C.14}$$

The ratio of the tunneling noise to the tunneling current is called the *Fano factor* and it probes the charge of the excitations tunneling at the QPC.

To see this, let us first specialize to the case of single type of quasiparticle tunneling at the QPC, corresponding to Laughlin filling fractions. We can get rid of the sum over α, allowing us to express the current and noise as below.

$$\begin{aligned} \langle I_T \rangle &= 2 q_{\boldsymbol{g}} |\Gamma_{\boldsymbol{g}}|^2 \tau_0 (2\pi T \tau_0)^{2\delta_{\boldsymbol{g}}-1} \sinh\left(\frac{q_{\boldsymbol{g}} V}{2T}\right) \frac{\left|\Gamma\left(\delta_{\boldsymbol{g}} + i\frac{q_{\boldsymbol{g}} V}{2\pi T}\right)\right|^2}{\Gamma(2\delta_{\boldsymbol{g}})} \\ \langle S_T \rangle &= 4 q_{\boldsymbol{g}}^2 |\Gamma_{\boldsymbol{g}}|^2 \tau_0 (2\pi T \tau_0)^{2\delta_{\boldsymbol{g}}-1} \cosh\left(\frac{q_{\boldsymbol{g}} V}{2T}\right) \frac{\left|\Gamma\left(\delta_{\boldsymbol{g}} + i\frac{q_{\boldsymbol{g}} V}{2\pi T}\right)\right|^2}{\Gamma(2\delta_{\boldsymbol{g}})} \end{aligned} \tag{C.15}$$

It is clear that the ratio of these two quantities gives the charge of the quasiparticles in the limit $q_{\boldsymbol{g}} V \gg k_B T$

$$\langle S_T \rangle = 2 q_{\boldsymbol{g}} \langle I_T \rangle \tag{C.16}$$

Indeed, this technique of measuring the charge of tunneling entities gave the first evidence of fractional charges in the Laughlin FQHE.

Let us now consider the situation when multiple types of quasiparticles tunnel across the QPC, but each with the same scaling dimension ($\delta_{\boldsymbol{g}_\alpha} \equiv \delta_{\boldsymbol{g}}$ for all α), relevant for

composite fractions of the FQHE. We hence restore the sum over quasiparticles types, in which case the tunneling current and noise are

$$\begin{aligned}\langle I_T\rangle &= \sum_\alpha 2q_{\boldsymbol{g}_\alpha}|\Gamma_{\boldsymbol{g}_\alpha}|^2\tau_0(2\pi T\tau_0)^{2\delta_{\boldsymbol{g}}-1}\sinh\left(\frac{q_{\boldsymbol{g}_\alpha}V}{2T}\right)\frac{\left|\Gamma\left(\delta_{\boldsymbol{g}}+i\frac{q_{\boldsymbol{g}}V}{2\pi T}\right)\right|^2}{\Gamma(2\delta_{\boldsymbol{g}})}\\ \langle S_T\rangle &= \sum_\alpha 4q_{\boldsymbol{g}_\alpha}^2|\Gamma_{\boldsymbol{g}_\alpha}|^2\tau_0(2\pi T\tau_0)^{2\delta_{\boldsymbol{g}}-1}\cosh\left(\frac{q_{\boldsymbol{g}_\alpha}V}{2T}\right)\frac{\left|\Gamma\left(\delta_{\boldsymbol{g}}+i\frac{q_{\boldsymbol{g}_\alpha}V}{2\pi T}\right)\right|^2}{\Gamma(2\delta_{\boldsymbol{g}})}\end{aligned} \tag{C.17}$$

but find now in the large voltage limit

$$\langle S_T\rangle = 2\frac{\sum_\alpha|\Gamma_{\boldsymbol{g}_\alpha}|^2q_{\boldsymbol{g}_\alpha}^2q_{\boldsymbol{g}_\alpha}^{2\delta_{\boldsymbol{g}}-1}}{\sum_\alpha|\Gamma_{\boldsymbol{g}_\alpha}|^2q_{\boldsymbol{g}_\alpha}q_{\boldsymbol{g}_\alpha}^{2\delta_{\boldsymbol{g}}-1}}\langle I_T\rangle \tag{C.18}$$

We emphasize that $|\Gamma_{\boldsymbol{g}_\alpha}|^2$ gives the relative weight for the tunneling of type$-\alpha$ quasiparticle. Hence, for composite fractions where different quasiparticles may tunnel across the QPC simultaneously, the DC Fano factor mixes the charge of different quasiparticles tunneling across the QPC.

Appendix D.

Finite-frequency ΔT noise: C_2 analytics

Here, we briefly go over the evaluation of the integrals in Equations (**??**) and (**??**). The perturbatively expanded noise is given by

$$S_+(\omega, T_u, T_d) = \sum_\alpha S_0^{(\alpha)}(\omega, \bar{T}) \left[1 + \left(\frac{\Delta T}{2\bar{T}}\right)^2 C_2^{(\alpha)}(\omega, \bar{T})\right] \tag{D.1}$$

where

$$S_0^{(\alpha)}(\omega, \bar{T}) = \left(q_{\boldsymbol{g}_\alpha}\Gamma_{\boldsymbol{g}_\alpha}\right)^2 \int d\tau e^{i\omega\tau} \left[\frac{\sinh\left(i\pi\bar{T}\tau_0\right)}{\sinh\left(\pi\bar{T}(i\tau_0+\tau)\right)}\right]^{2\delta_{\boldsymbol{g}_\alpha}} \tag{D.2}$$

and

$$\begin{aligned} C_2^{(\alpha)}(\omega, \bar{T}) = \frac{1}{S_0^{(\alpha)}(\bar{T}, \omega)} \left(q_{\boldsymbol{g}_\alpha}\Gamma_{\boldsymbol{g}_\alpha}\right)^2 \int d\tau\ e^{i\omega\tau} \left[\frac{\sinh\left(i\pi\bar{T}\tau_0\right)}{\sinh\left(\pi\bar{T}(i\tau_0+\tau)\right)}\right]^{2\delta_{\boldsymbol{g}}} \\ \left[\frac{\delta_{\boldsymbol{g}_\alpha}(\pi(i\tau_0+\tau))^2}{\sinh\big(\pi\bar{T}(i\tau_0+\tau)\big)} - \frac{\delta_{\boldsymbol{g}_\alpha}(i\pi\tau_0)^2}{\sinh\big(i\pi\tau_0\bar{T}\big)}\right] \end{aligned} \tag{D.3}$$

Absorbing the constants into the variables, the key integral to be evaluated takes the following generic form

$$A_{\delta_{\boldsymbol{g}_\alpha}}(z) = \int du\ e^{-iz(u-i\alpha)} \left[\frac{\sinh(i\alpha)}{\sinh(i\alpha-u)}\right]^{2\delta_{\boldsymbol{g}_\alpha}}. \tag{D.4}$$

Rewriting the hyperbolic sine in terms of exponentials, the integral can be recast as

$$A_{\delta_{\boldsymbol{g}_\alpha}}(z) = (1-e^{-2i\alpha})^{2\delta_{\boldsymbol{g}_\alpha}} e^{-z\alpha} \int du \frac{e^{-(2\delta_{\boldsymbol{g}_\alpha}+iz)u}}{\left[e^{-2u}+e^{i(\pi-2\alpha)}\right]^{2\delta_{\boldsymbol{g}_\alpha}}}. \tag{D.5}$$

This integral can be evaluated using Ref. [125] (3.314) which gives us

$$\int dx \frac{e^{-\tilde{\mu}x}}{\left[e^{-x/\tilde{\gamma}} + e^{\tilde{\beta}/\tilde{\gamma}}\right]^{\tilde{\nu}}} = \tilde{\gamma} \exp\left[\tilde{\beta}\left(\tilde{\mu} - \frac{\tilde{\nu}}{\tilde{\gamma}}\right)\right] \frac{\Gamma\left(\tilde{\nu} - \tilde{\gamma}\tilde{\mu}\right)\Gamma\left(\tilde{\gamma}\tilde{\mu}\right)}{\Gamma\left(\tilde{\nu}\right)}, \tag{D.6}$$

provided the conditions $\mathrm{Re}\left(\frac{\tilde{\nu}}{\tilde{\gamma}}\right) > \mathrm{Re}\ \tilde{\mu} > 0$ and $|\mathrm{Im}\ \tilde{\beta}| < \pi\ \mathrm{Re}\ \tilde{\gamma}$ are satisfied. Here, $\Gamma(x)$ is the Euler-Gamma function. For the integral in Equation (D.5), we can identify $\tilde{\beta} = i(\pi/2 - \alpha)$, $\tilde{\gamma} = 1/2$, $\tilde{\nu} = 2\delta_{\boldsymbol{g}_\alpha}$ and $\tilde{\mu} = 2\delta_{\boldsymbol{g}_\alpha} + iz$, which satisfies all the conditions. We then finally have

$$A_{\delta_{\boldsymbol{g}_\alpha}}(z) = \frac{1}{2}(2\sin\alpha)^{2\delta_{\boldsymbol{g}_\alpha}} e^{-\frac{\pi}{2}z} \frac{\left|\Gamma\left(\delta_{\boldsymbol{g}_\alpha} + i\frac{z}{2}\right)\right|^2}{\Gamma(2\delta_{\boldsymbol{g}_\alpha})}. \tag{D.7}$$

The first integral in Equation (**??**) can be evaluated, after trivial manipulations, directly using Equation (D.7). The second term in the second integral can be evaluated similarly. The first term in the second integral of Equation (D.7) is a bit more involved and is related to the second derivative of Equation (D.7) with respect to z. This can be seen from Equation (D.4), where a z-derivative will bring down a factor $(u - i\alpha)$. The second derivative of Equation (D.7) can be expressed as

$$\begin{aligned}\partial_z^2 A_{\delta_{\boldsymbol{g}_\alpha}}(z) = \frac{1}{2}\frac{(2\sin\alpha)^{2\delta_{\boldsymbol{g}_\alpha}}}{\Gamma(2\delta_{\boldsymbol{g}_\alpha})} e^{-\frac{\pi}{2}z} \left|\Gamma\left(\delta_{\boldsymbol{g}_\alpha} + i\frac{z}{2}\right)\right|^2 \frac{1}{4}\Bigg\{\pi^2 - \left[\psi\left(\delta_{\boldsymbol{g}_\alpha} + i\frac{z}{2}\right) - \psi\left(\delta_{\boldsymbol{g}_\alpha} - i\frac{z}{2}\right)\right]^2 \\ -2i\pi\left[\psi\left(\delta_{\boldsymbol{g}_\alpha} + i\frac{z}{2}\right) - \psi\left(\delta_{\boldsymbol{g}_\alpha} - i\frac{z}{2}\right)\right] - \left[\psi'\left(\delta_{\boldsymbol{g}_\alpha} + i\frac{z}{2}\right) + \psi'\left(\delta_{\boldsymbol{g}_\alpha} - i\frac{z}{2}\right)\right]\Bigg\},\end{aligned} \tag{D.8}$$

where $\psi(z)$ is the digamma function and $\psi'(z)$ its z-derivative. Finally, using Equations (D.7) and (D.8), we can express the full noise, in the limit $\tau_0 \longrightarrow 0$ as

$$\begin{aligned}S_+(\omega, T_R, T_L) = \sum_\alpha \left(q_{\boldsymbol{g}_\alpha}\Gamma_{\boldsymbol{g}_\alpha}\right)^2 \tau_0 \left[2\pi\tau_0\bar{T}\right]^{2\delta_{\boldsymbol{g}_\alpha}-1} e^{-\frac{\omega}{2\bar{T}}} \frac{\left|\Gamma\left(\delta_{\boldsymbol{g}_\alpha} + \frac{i\omega}{2\pi\bar{T}}\right)\right|^2}{\Gamma(2\delta_{\boldsymbol{g}_\alpha})} \\ \Bigg\{1 + \left(\frac{\Delta T}{2\bar{T}}\right)^2 \delta_{\boldsymbol{g}_\alpha}\Bigg[-1 + \frac{\left|\delta_{\boldsymbol{g}_\alpha} + \frac{i\omega}{2\pi\bar{T}}\right|^2}{2\delta_{\boldsymbol{g}_\alpha}(2\delta_{\boldsymbol{g}_\alpha}+1)}\Bigg(\pi^2 + 4\pi\mathrm{Im}\left[\psi\left(\delta_{\boldsymbol{g}_\alpha} + 1 + \frac{i\omega}{2\pi\bar{T}}\right)\right] \\ +4\left\{\mathrm{Im}\left[\psi\left(\delta_{\boldsymbol{g}_\alpha} + 1 + \frac{i\omega}{2\pi\bar{T}}\right)\right]\right\}^2 - 2\mathrm{Re}\left[\psi'\left(\delta_{\boldsymbol{g}_\alpha} + 1 + \frac{i\omega}{2\pi\bar{T}}\right)\right]\Bigg)\Bigg]\Bigg\}\end{aligned} \tag{D.9}$$

From this, we can extract the coefficient C_2 which isolates the non-equilibrium contributions in second order of the temperature difference

$$C_2^{(\alpha)}\left(\frac{\omega}{2\pi\bar{T}}\right) = \delta_{\boldsymbol{g}_\alpha}\left[-1+\frac{\left|\delta_{\boldsymbol{g}_\alpha}+\frac{i\omega}{2\pi\bar{T}}\right|^2}{2\delta_{\boldsymbol{g}_\alpha}(2\delta_{\boldsymbol{g}_\alpha}+1)}\left(\pi^2+4\pi\mathrm{Im}\left[\psi\left(\delta_{\boldsymbol{g}_\alpha}+1+\frac{i\omega}{2\pi\bar{T}}\right)\right]\right.\right.$$
$$\left.\left.+4\left\{\mathrm{Im}\left[\psi\left(\delta_{\boldsymbol{g}_\alpha}+1+\frac{i\omega}{2\pi\bar{T}}\right)\right]\right\}^2-2\mathrm{Re}\left[\psi'\left(\delta_{\boldsymbol{g}_\alpha}+1+\frac{i\omega}{2\pi\bar{T}}\right)\right]\right)\right] \quad \text{(D.10)}$$

Appendix E.

Quasiparticle Andreev Reflection: Integrals

In this Appendix, we summarize the integrals used in the zero-temperature and finite-temperature evaluation of cross-correlation, auto-correlation, and tunneling current in the Andreev geometry.

E.1. Zero temperature: useful contour integrals

First, we need to evaluate the following integral

$$J_1^{\eta_3\eta_4}(t_2,\tau) = \int dT \frac{1}{\left[T - \frac{\tau}{2} + i\eta_4\tau_0\right]\left[T - t_2 + \frac{\tau}{2} + i\eta_3\tau_0\right]}. \tag{E.1}$$

We will use the residue theorem to go about this. J_1 has two single poles located at $T = \frac{\tau}{2} - i\eta_4\tau_0$ and $T = t_2 - \frac{\tau}{2} - i\eta_3\tau_0$. Firstly, we note that if $\eta_3 = \eta_4$, then both poles lie on the same side of the real axis. This means that we can close the contour over the opposite half-plane which encloses no poles and hence gives zero, that is, $J_1^{\eta\eta}(t_2,\tau) = 0$.

We then focus on the only nonzero case, namely $\eta_4 = -\eta_3$. We choose to always close the contour over the half-plane enclosing the pole at $T = \frac{\tau}{2} - i\eta_4\tau_0$, thus picking an overall sign η_3, ultimately yielding

$$J_1^{\eta_3\eta_4}(t_2,\tau) = \frac{2i\pi\eta_3}{\tau - t_2 + 2i\eta_3\tau_0}\delta_{\eta_3,-\eta_4}. \tag{E.2}$$

The second integral of interest reads

$$J_2^{\eta_1\eta_3}(\tau) = \int dt_2 \frac{t_2}{(t_2 - i\eta_1\tau_0)^{\frac{2}{\nu}}\,(t_2 - \tau - 2i\eta_3\tau_0)}. \tag{E.3}$$

The integrand of J_2 has a relatively complicated $\frac{2}{\nu}$-order pole at $t_2 = i\eta_1\tau_0$, and a simple first-order pole at $t_2 = \tau + 2i\eta_3\tau_0$. As for J_1, the resulting integral vanished if both poles lie on the same half-plane, i.e. if $\eta_1 = \eta_3$. We thus focus again on the only nonzero case, namely $\eta_1 = -\eta_3$. We choose to close the contour over the half-plane enclosing the single pole, thus picking up an overall sign η_3, ultimately yielding

$$J_2^{\eta_1\eta_3}(\tau) = 2i\pi\eta_3 \frac{\tau + 2i\eta_3\tau_0}{(\tau + 3i\eta_3\tau_0)^{2/\nu}} \delta_{\eta_3,-\eta_1}. \tag{E.4}$$

E.2. Finite temperature calculation

Several elements of the derivation are common between auto- and cross-correlations and we try to present the two together as much as possible.

Our starting point is given by the auto- and cross-correlations expressed in terms of the Keldysh finite temperature bosonic Green's function

$$\mathcal{G}^{\eta_1\eta_2}(x,\tau) = \log\left(\frac{\sinh(i\pi T\tau_0)}{\sinh\left[\pi T\left(i\tau_0 - \chi_{12}(\tau)(\tau - x/v_F)\right)\right]}\right). \tag{E.5}$$

The expressions for cross- and auto-correlation are obtained from Equations (4.17) and (4.27)

$$\begin{aligned}
S_{23} = {} & \frac{2e^2v_F^2}{(2\pi i)^2}\frac{\Gamma_L^2\Gamma_R^2}{(2\pi a)^{2\nu+2/\nu}}\int dt dt_1\ldots dt_4 \sum_{\{\eta_k\}} \eta_1\ldots\eta_4\ e^{ie^*Vt_{34}} e^{2\nu\mathcal{G}^{\eta_3\eta_4}(0,t_{34})} e^{\frac{2}{\nu}\mathcal{G}^{\eta_1\eta_2}(0,t_{12})} \\
& \times \partial_x\left[-\mathcal{G}^{-\eta_1}(x-L,t-t_1) + \mathcal{G}^{-\eta_2}(x-L,t-t_2) - \nu\mathcal{G}^{-\eta_3}(x,t-t_3) + \nu\mathcal{G}^{-\eta_4}(x,t-t_4)\right] \\
& \times \partial_y\left[\mathcal{G}^{+\eta_1}(y-L,-t_1) - \mathcal{G}^{+\eta_2}(y-L,-t_2)\right] \\
& \times \left[e^{-\mathcal{G}^{\eta_1\eta_3}(L,t_{13})} e^{\mathcal{G}^{\eta_1\eta_4}(L,t_{14})} e^{\mathcal{G}^{\eta_2\eta_3}(L,t_{23})} e^{-\mathcal{G}^{\eta_2\eta_4}(L,t_{24})} - 1\right], \\
S_{33}^{\text{exc}} = {} & \frac{2e^2v_F^2}{(2\pi i)^2}\frac{\Gamma_L^2\Gamma_R^2}{(2\pi a)^{2\nu+2/\nu}}\int dt dt_1\ldots dt_4 \sum_{\{\eta_k\}} \eta_1\ldots\eta_4\ e^{ie^*Vt_{34}} e^{2\nu\mathcal{G}^{\eta_3\eta_4}(0,t_{34})} e^{\frac{2}{\nu}\mathcal{G}^{\eta_1\eta_2}(0,t_{12})} \\
& \times \partial_x\left[\mathcal{G}^{-\eta_1}(x-L,t-t_1) - \mathcal{G}^{-\eta_2}(x-L,t-t_2)\right] \partial_y\left[\mathcal{G}^{+\eta_1}(y-L,-t_1) - \mathcal{G}^{+\eta_2}(y-L,-t_2)\right] \\
& \times \left[e^{-\mathcal{G}^{\eta_1\eta_3}(L,t_{13})} e^{\mathcal{G}^{\eta_1\eta_4}(L,t_{14})} e^{\mathcal{G}^{\eta_2\eta_3}(L,t_{23})} e^{-\mathcal{G}^{\eta_2\eta_4}(L,t_{24})} - 1\right]
\end{aligned} \tag{E.6}$$

E.2.1. $t-$ and t_1-integrals

The first complication arising at finite temperature comes from the the $t-$ and t_1-integrals as the Green's function derivative no longer reduces to a simple delta function. Instead of

Equation (4.20), one has at finite temperature

$$\partial_x \mathcal{G}^{\eta_1\eta_2}(x,\tau) = -\frac{\pi\chi_{12}(\tau)T/v_F}{\tanh\left[\pi T\left(i\tau_0 - \chi_{12}(\tau)(\tau - x/v_F)\right)\right]}, \tag{E.7}$$

allowing us to write the general integrated form as (assuming here $x > 0$)

$$\int dt\partial_x \left[\mathcal{G}^{\eta\eta_1}(x, t-t_1) - \mathcal{G}^{\eta\eta_2}(x, t-t_2)\right] = i\frac{\pi(1-2T\tau_0)}{v_F}\left(\eta_1 - \eta_2\right) - \frac{2\pi T}{v_F}\left(t_1 - t_2\right). \tag{E.8}$$

This, in turn, enables us to write (up to leading order in the cutoff)

$$\begin{aligned} S_{23} = \frac{e^2\Gamma_L^2\Gamma_R^2}{2(2\pi a)^{2\nu+2/\nu}} \int dt_2 dT d\tau \sum_{\{\eta_k\}} \eta_1 \ldots \eta_4 \; e^{ie^*V\tau} e^{2\nu\mathcal{G}^{\eta_3\eta_4}(0,\tau)} e^{\frac{2}{\nu}\mathcal{G}^{\eta_1\eta_2}(0,t_2)} \left[i\left(\eta_1 - \eta_2\right) - 2Tt_2\right] \\ \times \left[i\left(\eta_1 - \eta_2\right) - 2Tt_2 + i\nu\left(\eta_3 - \eta_4\right) - 2\nu T\tau\right] \left[\frac{e^{\mathcal{G}^{\eta_1\eta_4}(L,-\tilde{t}+\tau/2)} e^{\mathcal{G}^{\eta_2\eta_3}(L,-t_2-\tilde{t}-\tau/2)}}{e^{\mathcal{G}^{\eta_1\eta_3}(L,-\tilde{t}-\tau/2)} e^{\mathcal{G}^{\eta_2\eta_4}(L,-t_2-\tilde{t}+\tau/2)}} - 1\right], \end{aligned} \tag{E.9}$$

$$\begin{aligned} S_{33}^{\text{exc}} = -\frac{e^2\Gamma_L^2\Gamma_R^2}{2(2\pi a)^{2\nu+2/\nu}} \int dt_2 d\tilde{t} d\tau \sum_{\{\eta_k\}} \eta_1 \ldots \eta_4 \; e^{ie^*V\tau} e^{2\nu\mathcal{G}^{\eta_3\eta_4}(0,\tau)} e^{\frac{2}{\nu}\mathcal{G}^{\eta_1\eta_2}(0,t_2)} \left[i\left(\eta_1 - \eta_2\right) - 2Tt_2\right]^2 \\ \times \left[\frac{e^{\mathcal{G}^{\eta_1\eta_4}(L,-\tilde{t}+\tau/2)} e^{\mathcal{G}^{\eta_2\eta_3}(L,-t_2-\tilde{t}-\tau/2)}}{e^{\mathcal{G}^{\eta_1\eta_3}(L,-\tilde{t}-\tau/2)} e^{\mathcal{G}^{\eta_2\eta_4}(L,-t_2-\tilde{t}+\tau/2)}} - 1\right], \end{aligned} \tag{E.10}$$

where we flipped the sign of t_2 and, following the same steps as the zero-temperature calculation, we changed variables from t_3, t_4 to $\tilde{t} = (t_3 + t_4)/2$ and $\tau = t_3 - t_4$.

E.2.2. $\tilde{t}-$integral

At this point, one notices that the variable $\tilde{t}$ is only present in the final term, allowing us to perform the corresponding integral yielding

$$\begin{aligned} F_{\eta_3,\eta_4}(t_2,\tau) = \int d\tilde{t} \left[\frac{e^{\mathcal{G}^{\eta_1\eta_4}(L,-\tilde{t}+\tau/2)} e^{\mathcal{G}^{\eta_2\eta_3}(L,-t_2-\tilde{t}-\tau/2)}}{e^{\mathcal{G}^{\eta_1\eta_3}(L,-\tilde{t}-\tau/2)} e^{\mathcal{G}^{\eta_2\eta_4}(L,-t_2-\tilde{t}+\tau/2)}} - 1\right] \\ = -\frac{2}{\pi T}\frac{\sinh\left(\pi T t_2\right)\sinh\left(\pi T\tau + i\alpha(\eta_3 - \eta_4)\right)}{\sinh\left(\pi T(t_2+\tau) + i\alpha(\eta_3 - \eta_4)\right)} \left[\pi T\left(t_2 + \tau\right) + i\alpha\left(\eta_3 - \eta_4\right) - i\frac{\pi}{2}\left(\eta_3 - \eta_4\right)\right], \end{aligned} \tag{E.11}$$

with the shorthand notation $\alpha = \frac{\pi T a}{v_F}$.

This then leaves us with the following expressions for the current correlations

$$S_{23} = \frac{e^2\Gamma_L^2\Gamma_R^2}{2(2\pi a)^{2\nu+2/\nu}} \int dt_2 d\tau \sum_{\{\eta_k\}} \eta_1 \dots \eta_4 \; e^{ie^*V\tau} e^{2\nu\mathcal{G}^{\eta_3\eta_4}(0,\tau)} e^{\frac{2}{\nu}\mathcal{G}^{\eta_1\eta_2}(0,t_2)} \left[i\left(\eta_1-\eta_2\right) - 2Tt_2\right]$$
$$\times \left[i\left(\eta_1-\eta_2\right) - 2Tt_2 + i\nu\left(\eta_3-\eta_4\right) - 2\nu T\tau\right] F_{\eta_3,\eta_4}(t_2,\tau), \tag{E.12}$$

$$S_{33}^{\text{exc}} = -\frac{e^2\Gamma_L^2\Gamma_R^2}{2(2\pi a)^{2\nu+2/\nu}} \int dt_2 d\tau \sum_{\{\eta_k\}} \eta_1 \dots \eta_4 \; e^{ie^*V\tau} e^{2\nu\mathcal{G}^{\eta_3\eta_4}(0,\tau)} e^{\frac{2}{\nu}\mathcal{G}^{\eta_1\eta_2}(0,t_2)}$$
$$\left[i\left(\eta_1-\eta_2\right) - 2Tt_2\right]^2 F_{\eta_3,\eta_4}(t_2,\tau). \tag{E.13}$$

E.2.3. t_2-integral

Performing explicitly the summations over η_i, and making use of the symmetries in t_2 and τ, one is left with

$$S_{23} = -S_{33}^{\text{exc}} + \nu \frac{4e^2\Gamma_L^2\Gamma_R^2}{(2\pi a)^{2\nu+2/\nu}} \int d\tau \cos(e^*V\tau) e^{2\nu\mathcal{G}(-\tau)}$$
$$\times \int dt_2 \left(e^{\frac{2}{\nu}\mathcal{G}(t_2)} - e^{\frac{2}{\nu}\mathcal{G}(-t_2)}\right) \left\{F_{+1}(t_2,\tau) - iT\tau\left[F_0(t_2,\tau) - F_{+1}(t_2,\tau)\right]\right\},$$

$$S_{33}^{\text{exc}} = -\frac{4e^2\Gamma_L^2\Gamma_R^2}{(2\pi a)^{2\nu+2/\nu}} \int d\tau \cos(e^*V\tau) e^{2\nu\mathcal{G}(-\tau)}$$
$$\times \int dt_2 \left[\left(e^{\frac{2}{\nu}\mathcal{G}(t_2)} + e^{\frac{2}{\nu}\mathcal{G}(-t_2)}\right) - 2iTt_2\left(e^{\frac{2}{\nu}\mathcal{G}(t_2)} - e^{\frac{2}{\nu}\mathcal{G}(-t_2)}\right)\right] \left[F_0(t_2,\tau) - F_{+1}(t_2,\tau)\right],$$

where we introduced the shorter notation $\mathcal{G}(t) = \mathcal{G}^{-+}(0,t)$ along with $F_{\frac{\eta_3-\eta_4}{2}}(t_2,\tau) = F_{\eta_3,\eta_4}(t_2,\tau)$.

Carrying out the integration over t_2, one can show, after rather lengthy but straightforward derivations, that

$$S_{23} = -S_{33}^{\text{exc}} + \nu \frac{8\pi}{(\pi T)^2} \frac{e^2\Gamma_R^2\Gamma_L^2}{(2\pi a)^{2\nu+2/\nu}} \int d\tau \cos\left(e^*V\tau\right) e^{2\nu\mathcal{G}(-\tau)} \left[iH_0(\tau) - \left(1+iT\tau\right) M_0(\tau)\right], \tag{E.14}$$

$$S_{33}^{\text{exc}} = -\frac{8\pi}{(\pi T)^2} \frac{e^2\Gamma_R^2\Gamma_L^2}{(2\pi a)^{2\nu+2/\nu}} \int d\tau \cos\left(e^*V\tau\right) e^{2\nu\mathcal{G}(-\tau)} \left(1+2iT\tau\right) M_0(\tau), \tag{E.15}$$

where

$$M_0(\tau) = \mathrm{Re}\left\{\alpha^{2/\nu} 2\pi(-1)^{1/\nu} \frac{\sinh^2(\pi T\tau)}{\left[\sinh(\pi T\tau + 3i\alpha)\right]^{2/\nu}}\right\},$$
$$H_0(\tau) = (2\alpha)^{2/\nu} e^{-\pi T\tau} \sinh(\pi T\tau) \frac{\Gamma\left(1+\frac{1}{\nu}\right)\Gamma\left(\frac{1}{\nu}\right)}{\Gamma\left(1+\frac{2}{\nu}\right)} {}_2F_1\left(1, \frac{1}{\nu}, \frac{2}{\nu}, 1 - e^{-2\pi T\tau}\right) \quad \text{(E.16)}$$

E.2.4. Final $\tau-$integral

We are now left with a set of three integrals remaining. Two of those can be carried out for generic values of the filling factor. Indeed, using known results, [125] one can readily compute the intermediate function

$$\kappa_0(z) = \int dv e^{izv} \left(\frac{\sinh(i\alpha)}{\sinh(v+i\alpha)}\right)^{2\nu} \frac{1}{\left[\sinh(v+3i\alpha)\right]^{2/\nu-2}}$$
$$= -2^{2/\nu+2\nu-3}\alpha^{2\nu}(-1)^{1/\nu} e^{-\pi z/2} \frac{\left|\Gamma\left(\frac{1}{\nu}+\nu-1+i\frac{z}{2}\right)\right|^2}{\Gamma\left(\frac{2}{\nu}+2\nu-2\right)}, \quad \text{(E.17)}$$

and from this obtain

$$\int d\tau \cos(e^*V\tau)\, e^{2\nu\mathcal{G}(-\tau)} M_0(\tau) = \frac{(-1)^{1/\nu}\alpha^{2/\nu}}{T}\left[\kappa_0\left(\frac{e^*V}{\pi T}\right) + \kappa_0\left(-\frac{e^*V}{\pi T}\right)\right], \quad \text{(E.18)}$$

as well as

$$\int d\tau \cos(e^*V\tau)\, e^{2\nu\mathcal{G}(-\tau)} T\tau M_0(\tau) = \frac{(-1)^{1/\nu}\alpha^{2/\nu}}{\pi T}\left[\frac{1}{i}\,\partial_z\kappa_0(z)|_{z=\frac{e^*V}{\pi T}} + \frac{1}{i}\,\partial_z\kappa_0(z)|_{z=-\frac{e^*V}{\pi T}}\right]. \quad \text{(E.19)}$$

The final integral remaining involves the function $H_0(\tau)$ defined in Equation (E.16). While it cannot be performed formally, one can make progress by noticing that the hypergeometric function only involves integer coefficients thus enabling a finite order expansion. The resulting coefficients, however, depend on the inverse filling factor $1/\nu$ in a nontrivial way. While the expansion can be carried out for any Laughlin filling factor, we choose to show only the results at $\nu = 1/3$. One then has

$${}_2F_1\left(1,3,6,1-e^{-2\pi T\tau}\right) = \quad \text{(E.20)}$$
$$\frac{-30}{12\left(e^{-2\pi T\tau}-1\right)}\left[\frac{24\pi T\tau e^{-4\pi T\tau}}{\left(e^{-2\pi T\tau}-1\right)^4} + \frac{12}{\left(e^{-2\pi T\tau}-1\right)^3} + \frac{18}{\left(e^{-2\pi T\tau}-1\right)^2} + \frac{4}{\left(e^{-2\pi T\tau}-1\right)} - 1\right].$$

Substituting this back into Equation (E.16), one is able to carry out the only remaining integral, namely

$$\begin{aligned}
&\int d\tau \cos\left(e^*V\tau\right) e^{\frac{2}{3}\mathcal{G}(-\tau)} H_0(\tau) \\
&= i\frac{(2\alpha)^{20/3}}{8\pi T}\left(\frac{\left|\Gamma\left(\frac{7}{3}+i\frac{eV}{6\pi T}\right)\right|^2}{\Gamma\left(\frac{14}{3}\right)}\left\{\pi\cosh\left(\frac{eV}{6T}\right)-2\sinh\left(\frac{eV}{6T}\right)\mathrm{Im}\left[\psi\left(\frac{7}{3}+i\frac{eV}{6\pi T}\right)\right]\right\}\right. \\
&\left.-\frac{\left|\Gamma\left(\frac{1}{3}+i\frac{eV}{6\pi T}\right)\right|^2}{\Gamma\left(\frac{5}{3}\right)}\frac{eV}{6\pi T}\sinh\left(\frac{eV}{6T}\right)\left[\frac{23}{120}+\frac{9}{160}\left(\frac{eV}{3\pi T}\right)^2\right]\right). \qquad \text{(E.21)}
\end{aligned}$$

Combining all these results, this finally leaves us with the final expressions for the current correlations at finite temperature and filling factor $\nu = 1/3$

$$\begin{aligned}
S_{23} = -\frac{2}{3}\frac{4e^2\Gamma_L^2\Gamma_R^2}{\pi^2 v_F^3}\left(\frac{T}{v_F}\right)^{11/3}&\left\{\sinh\left(\frac{eV}{6T}\right)\frac{\left|\Gamma\left(\frac{7}{3}+i\frac{eV}{6\pi T}\right)\right|^2}{\Gamma\left(\frac{14}{3}\right)}\mathrm{Im}\left[\psi\left(\frac{7}{3}+i\frac{eV}{6\pi T}\right)\right]\right. \\
&\left.-\frac{1}{8}\frac{\left|\Gamma\left(\frac{1}{3}+i\frac{eV}{6\pi T}\right)\right|^2}{\Gamma\left(\frac{5}{3}\right)}\frac{eV}{6\pi T}\sinh\left(\frac{eV}{6T}\right)\left[\frac{23}{120}+\frac{9}{160}\left(\frac{eV}{3\pi T}\right)^2\right]\right\}, \qquad \text{(E.22)}
\end{aligned}$$

$$S_{33}^{\mathrm{exc}} = \frac{4e^2\Gamma_L^2\Gamma_R^2}{\pi^2 v_F^3}\left(\frac{T}{v_F}\right)^{11/3}\sinh\left(\frac{eV}{6T}\right)\frac{\left|\Gamma\left(\frac{7}{3}+i\frac{eV}{6\pi T}\right)\right|^2}{\Gamma\left(\frac{14}{3}\right)}\mathrm{Im}\left[\psi\left(\frac{7}{3}+i\frac{eV}{6\pi T}\right)\right] \qquad \text{(E.23)}$$

presented in the main text.

We note that the zero-temperature contour integrals relied on $1/\nu$ being an integer to perform contour integrals over simple poles. The finite-temperature calculations are more general, and up to Equation E.16 do not rely on $1/\nu$ being an integer. The only element of the calculation which relies on $1/\nu$ being an integer is the expansion of the hypergeometric function in Equation E.21. Nevertheless, it is possible to quite easily evaluate the final τ integral numerically to obtain the cross- and auto-correlation.

Why do we mention this generalization? Recall that $1/\nu$ is indeed the theoretically predicted scaling dimension of the second QPC, while ν is that of the first QPC. As mentioned several times in the thesis, scaling dimensions typically assume a non-universal value. A generalization to arbitrary values of $1/\nu$ hence allows a proper comparison with experiments.

Appendix F.

Time-domain braiding phase from 4−branch Keldysh contour

In this appendix, we show how the four-branch Keldysh contour can be used to analyze the braiding of incoming anyons with anyons tunneling at a QPC in a technically complete manner. The four-branch contour is a generalization of the standard Keldysh contour discussed in Section 2.3.5, and is shown in Figure F.1. As indicated in the figure, the times on the first branch precede time on all other branch. The times on the second branch occur after those on the first branch, but before the second and first, and so on. The times on the fourth branch of course occur the last. Time ordering within a branch is given by the directions of the respective branches.

These properties of the four-branch Keldysh contour can be leveraged to make our calculation of the anyon braiding phase technically complete. Indeed, to calculate the average tunneling current due to a single incoming anyon, we make use of the augmented state of Equation (6.17):

$$|\varphi\rangle \equiv \sum_{\beta} p_{\boldsymbol{g_\beta}} e^{-i\boldsymbol{g_\beta}.\boldsymbol{\phi^u}(-\mathcal{L},-\mathcal{T})} |0\rangle \,, \tag{F.1}$$

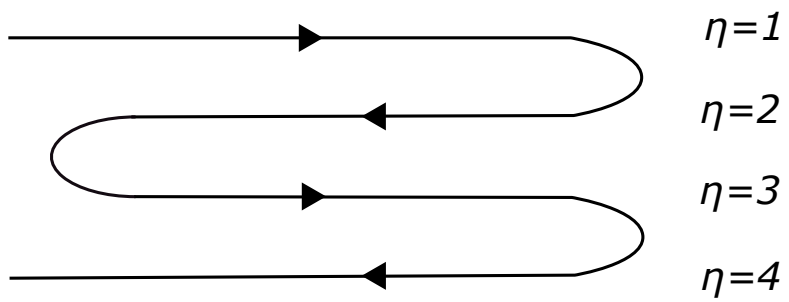


Figure F.1.: Four branch Keldysh contour.

with the average tunneling current on this state defined in the standard Keldysh formalism as:

$$\langle I_T(t_1)\rangle = \langle\varphi|\, I_T(t_1^-)\; e^{-i\int_K dt_2 H_T(t_2)}\,|\varphi\rangle\,. \tag{F.2}$$

To proceed with the calculation, we need to take the incoming anyons inside the Keldysh ordering. This was accomplished in Chapter 6 by assuming $\mathcal{T}\to\infty$, which then naturally places the incoming anyon of the ket to the extreme right, and the incoming anyon of the bra to the extreme left, as seen in Equation (6.19).

While this assumption of $\mathcal{T}\to\infty$ is physically meaningful, we can avoid it by working on the four-branch Keldysh contour. Indeed, here the incoming anyons on the bra and the ket are placed on the first and the fourth branches respectively. Similarly, the tunneling current operator is placed on the third branch. Hence, we express the average tunneling current in the four-branch Keldysh formalism as:

$$\langle I(t_1)\rangle = \sum_{\beta\gamma} p^*_{\boldsymbol{g_\beta}} p_{\boldsymbol{g_\gamma}}\,\langle 0|\, T_{K_4}\; e^{i\boldsymbol{g_\beta}\cdot\boldsymbol{\phi^u}(-\mathcal{L},-\mathcal{T}^{(4)})}\; I_T(t_1^{(3)}) e^{-i\int_{K_4} dt_2 H_T(t_2)}\; e^{-i\boldsymbol{g_\gamma}\cdot\boldsymbol{\phi^u}(-\mathcal{L},-\mathcal{T}^{+})}\,|0\rangle\,, \tag{F.3}$$

where T_{K_4} denotes time ordering on the four-branch Keldysh contour, while the subscript K_4 in the integral of the time-evolution operator denotes an integral over the Keldysh contour. The superscripts on the time arguments indicate the branch on which the respective operators are inserted. Expanding the time-evolution operator to the lowest order in the tunneling amplitudes, we find the following expression for the tunneling current:

$$\begin{aligned}\langle I(t_1)\rangle = \sum_{\alpha}\frac{q_{\boldsymbol{g}_\alpha}|\Gamma_{\boldsymbol{g}_\alpha}|^2}{2}\sum_{\beta\gamma} p^*_{\boldsymbol{g_\beta}} p_{\boldsymbol{g_\gamma}}\sum_{\epsilon}\epsilon\sum_{\eta=1}^{4}(-1)^{1+\eta}\int dt_2\\ \langle 0|\, T_{K_4}\; e^{i\boldsymbol{g_\beta}\cdot\boldsymbol{\phi^u}(-\mathcal{L},-\mathcal{T}^{(4)})} e^{i\epsilon\boldsymbol{g_\alpha}\cdot\boldsymbol{\phi^u}(0,t_1^{(3)})} e^{-i\epsilon\boldsymbol{g_\alpha}\cdot\boldsymbol{\phi^d}(0,t_1^{(3)})}\\ e^{i\epsilon\boldsymbol{g_\alpha}\cdot\boldsymbol{\phi^d}(0,t_2^{(\eta)})} e^{-i\epsilon\boldsymbol{g_\alpha}\cdot\boldsymbol{\phi^u}(0,t_2^{(\eta)})} e^{-i\boldsymbol{g_\gamma}\cdot\boldsymbol{\phi^u}(-\mathcal{L},-\mathcal{T}^{(1)})}\,|0\rangle\,.\end{aligned} \tag{F.4}$$

The calculation proceeds as in the main text, employing a generalized Wicks theorem:

$$\left\langle T_{K_4}\left\{\prod_{s=1}^{n} e^{ia_s\phi_j^{u/d}\left(x_s,t_s^{\eta_s}\right)}\right\}\right\rangle = \exp\left[\sum_{s=1}^{n}\sum_{p=s+1}^{n} a_s a_p\; \mathcal{G}_j^{(4)\eta_s\eta_p}(x_s-x_p,t_s-t_p)\right], \tag{F.5}$$

which is non-zero only when $\sum_s a_s = 0$. $\mathcal{G}_j^{(4)\eta\eta'}(x,t)$ denotes the four-branch Keldysh bosonic Greens function of the $j-$th bosonic mode, given at finite temperature by:

$$\mathcal{G}^{(4)\eta\eta'}(x,\tau) = \log\left(\frac{\sinh(i\pi T\tau_0)}{\sinh\left[\pi T\left(i\tau_0-\sigma^{(4)}_{\eta\eta'}(\tau)(\tau-\chi_j x/v_j)\right)\right]}\right), \tag{F.6}$$

where

$$\sigma^{(4)}_{\eta\eta'}(t) = \begin{cases} \mathrm{sgn}(\eta - \eta'), & \text{if } \eta \neq \eta' \\ (-1)^{1+\eta}\mathrm{sgn}(t - t'), & \text{if } \eta = \eta' \end{cases} . \tag{F.7}$$

Using these results, the tunneling current naturally leads to the same results as Equation (6.25), without making any assumptions about the injection time $\mathcal{T}$.

Appendix G.

Anyon Collider: Fluctuation-Dissipation Theorem

This Appendix aims to explicitly show the fluctuation-dissipation theorem quoted in Equation (G) of the main text. The latter relation relates tunneling current-edge current correlation with the derivatives of the average tunneling current with respect to the incoming currents.

Let us start by calculating the tunneling current – edge current correlator, denoted $\left\langle \delta I_T \delta \tilde{I}_u \right\rangle = \left\langle I_T \tilde{I}_u \right\rangle - \langle I_T \rangle \left\langle \tilde{I}_u \right\rangle$. We start with the definition of the conserved current on the edge

$$\begin{aligned} \tilde{I}_u &= \frac{1}{2\pi} \sum_j Q_j \partial_x \phi_j^u \\ &= -\frac{1}{2\pi} \sum_j Q_j \partial_t \phi_j^u \end{aligned} \tag{G.1}$$

The quantity $\left\langle I_T \tilde{I}_u \right\rangle$ is given in the Keldysh formalism as:

$$\left\langle I_T \tilde{I}_u \right\rangle = \int dt'' \left\langle T_K \left\{ I_T(t^-) \tilde{I}_u(t''^+) e^{-i \int_K dt' H_T(t')} \right\} \right\rangle \tag{G.2}$$

The calculation proceeds in the usual manner. We expand the time evolution operator to lowest non-vanishing order in the tunneling amplitudes:

$$\left\langle I_T \tilde{I}_u \right\rangle = -i \int dt' dt'' \sum_{\eta'} \eta' \left\langle \left\{ T_K I_T(t^-) \tilde{I}_u(t''^+) H_T(t'^{\eta'}) \right\} \right\rangle . \tag{G.3}$$

Using the expressions of the tunneling Hamiltonian and current operators from the main text, and the edge current operator given here, we write:

$$\left\langle I_T \tilde{I}_u \right\rangle = -\frac{1}{2\pi} \sum_{\alpha} q_{\boldsymbol{g}_\alpha} |\Gamma_{\boldsymbol{g}_\alpha}|^2 \sum_{\eta'} \eta' \sum_{\epsilon} \epsilon \int dt' dt'' \\ \left\langle \left\{ T_K e^{i\epsilon \left[\boldsymbol{g_\alpha}.\bar{\boldsymbol{\phi}}^{\boldsymbol{u}}(0,t^-) - \boldsymbol{g_\alpha}.\bar{\boldsymbol{\phi}}^{\boldsymbol{d}}(0,t^-) \right]} e^{-i\epsilon \left[\boldsymbol{g_\alpha}.\bar{\boldsymbol{\phi}}^{\boldsymbol{u}}(0,t'^{\eta'}) - \boldsymbol{g_\alpha}.\bar{\boldsymbol{\phi}}^{\boldsymbol{d}}(0,t'^{\eta'}) \right]} \sum_j q_j \partial_{t''} \bar{\phi}_j^u(0,t''^+) \right\} \right\rangle, \tag{G.4}$$

where $\bar{\phi^{u/d}}$ denote bosonic fields augmented with solitonic excitations:

$$\bar{\phi}_j^{u/d}(t) = \phi_j^{u/d}(t) + 2\pi \sum_{k=1}^{N} g_{\beta j} \theta(t - t_k^{u/d}). \tag{G.5}$$

We proceed with the evaluation of this correlation function by seperating the bosonic fields on the upper and lower edges, giving us:

$$\left\langle I_T \tilde{I}_u \right\rangle = -\frac{1}{2\pi} \sum_{\alpha} q_{\boldsymbol{g}_\alpha} |\Gamma_{\boldsymbol{g}_\alpha}|^2 \sum_{\eta'} \eta' \sum_{\epsilon} \epsilon \int dt' \\ \left\langle \left\{ T_K e^{-i\epsilon \boldsymbol{g_\alpha}.\bar{\boldsymbol{\phi}}^{\boldsymbol{d}}(0,t^-)} e^{i\epsilon \boldsymbol{g_\alpha}.\bar{\boldsymbol{\phi}}^{\boldsymbol{d}}(0,t'^{\eta'})} \right\} \right\rangle \\ \int dt'' \left\langle \left\{ T_K e^{i\epsilon \boldsymbol{g_\alpha}.\bar{\boldsymbol{\phi}}^{\boldsymbol{u}}(0,t^-)} e^{-i\epsilon \boldsymbol{g_\alpha}.\bar{\boldsymbol{\phi}}^{\boldsymbol{u}}(0,t'^{\eta'})} \sum_j q_j \partial_{t''} \bar{\phi}_j^u(0,t''^+) \right\} \right\rangle. \tag{G.6}$$

From Section 7.3, we know that the correlation function of the lower edge is given by:

$$\left\langle \left\{ T_K e^{-i\epsilon \boldsymbol{g_\alpha}.\bar{\boldsymbol{\phi}}^{\boldsymbol{d}}(0,t^-)} e^{i\epsilon \boldsymbol{g_\alpha}.\bar{\boldsymbol{\phi}}^{\boldsymbol{d}}(0,t'^{\eta'})} \right\} \right\rangle = e^{\delta_{\boldsymbol{g}_\alpha} \mathcal{G}^{-\eta'}(0,t-t')} e^{-\gamma_d |t-t'| (1 - \sum_\beta P_\beta e^{-2i\pi \boldsymbol{g_\alpha}.\boldsymbol{g_\beta}})}. \tag{G.7}$$

The main objective of this appendix is to evaluate the upper edge correlator. Let us focus on the latter quantity, written in the third line in the above equation and given below:

$$\mathcal{C}^u(t^-, t'^{\eta'}) = \int_{-\infty}^{\infty} dt'' \left\langle \left\{ T_K e^{i\epsilon \boldsymbol{g_\alpha}.\bar{\boldsymbol{\phi}}^{\boldsymbol{u}}(0,t^-)} e^{-i\epsilon \boldsymbol{g_\alpha}.\bar{\boldsymbol{\phi}}^{\boldsymbol{u}}(0,t'^{\eta'})} \sum_j q_j \partial_{t''} \bar{\phi}_j^u(0,t''^+) \right\} \right\rangle. \tag{G.8}$$

We write out separately the equilibrium bosonic fields and the non-equilibrium solitonic excitations, resulting in the following expression:

$$\mathcal{C}^u(t^-, t'^{\eta'}) = \prod_j \int_{-\infty}^{\infty} dt'' \Big\langle \Big\{ T_K e^{i\epsilon \phi_j^u(0,t^-)} e^{-i\epsilon \phi_j^u(0,t'^{\eta'})} \; e^{2\pi i \epsilon g_{\alpha j} g_{\beta j} \sum_{k=1}^{N} [\theta(t-t_k) - \theta(t'-t_k)]} \\ \sum_j q_j \partial_{t''} \left[\phi_j^u(0,t''^+) + 2\pi g_{\beta j} \sum_{k=1}^{N} \theta(t'' - t_k) \right] \Big\} \Big\rangle. \tag{G.9}$$

Let us now further split this into two parts:

$$\begin{aligned}\mathcal{C}^u(t^-,t'^{\eta'}) = &\\ &\prod_j \int_{-\infty}^{\infty} dt'' \Bigg\{ \Big[\left\langle \left\{ T_K e^{i\epsilon\phi_j^u(0,t^-)} e^{-i\epsilon\phi_j^u(0,t'^{\eta'})} \sum_j q_j \partial_{t''}\phi_j^u(0,t''^+) \right\} \right\rangle \\ &\times \left\langle e^{2\pi i\epsilon g_{\alpha j} g_{\beta j} \sum_{k=1}^N [\theta(t-t_k)-\theta(t'-t_k)]} \right\rangle_{\text{n-eq}} \Big] \\ &+ \left\langle \left\{ T_K e^{i\epsilon\phi_j^u(0,t^-)} e^{-i\epsilon\phi_j^u(0,t'^{\eta'})} \right\} \right\rangle \\ &\times \left\langle e^{2\pi i\epsilon g_{\alpha j} g_{\beta j} \sum_{k=1}^N [\theta(t-t_k)-\theta(t'-t_k)]} \sum_j 2\pi q_j g_{\beta j} \sum_{k=1}^N \partial_{t''}\theta(t''-t_k) \right\rangle_{\text{n-eq}} \Bigg\}\end{aligned} \tag{G.10}$$

The equilibrium correlator in the first line above can be calculated using bosonic identities of Appendix B, and being careful about branch cuts of the bosonic Greens functions. We do not show the details here, but the final result yields:

$$\begin{aligned}\int_{-\infty}^{+\infty} dt'' \left\langle \left\{ T_K e^{i\epsilon\phi_j^u(0,t^-)} e^{-i\epsilon\phi_j^u(0,t'^{\eta'})} \sum_j q_j \partial_{t''}\phi_j^u(0,t''^+) \right\} \right\rangle & \\ = e^{\delta_{\boldsymbol{g}_\alpha} \mathcal{G}^u(\sigma^{-\eta'}(t-t'))}\ q_{\boldsymbol{g}_\alpha} 2\pi T t'.&\end{aligned} \tag{G.11}$$

where we have used that $\sum_j q_j g_{\alpha j} = q_{\boldsymbol{g}_\alpha}$, which is true for all the examples of edge theories we will encounter in this thesis (fully chiral edges, or counter-propagating modes that are *neutral*). Clearly, this contribution vanishes in the zero temperature limit. We will hence discard this contribution from now since we work in the zero-temperature limit:

$$\begin{aligned}\mathcal{C}^u(t^-,t'^{\eta'}) = &\prod_j e^{g_{\alpha j}^2 \mathcal{G}^{-\eta'}(t-t')} \\ \times &\int_{-\infty}^{\infty} dt'' \left\langle e^{2\pi i\epsilon g_{\alpha j} g_{\beta j} \sum_{k=1}^N [\theta(t-t_k)-\theta(t'-t_k)]} \sum_j 2\pi q_j g_{\beta j} \sum_{k=1}^N \partial_{t''}\theta(t''-t_k) \right\rangle_{\text{n-eq}},\end{aligned} \tag{G.12}$$

We turn our attention to the more interesting non-equilibrium correlator on the final line of Equation (G.12). To evaluate this correlator, we need to operate the so-called Markovian approximation [33]. In this context, the latter approximation means that the tunneling current and edge current are correlated only in the time-interval where incoming anyons are incident on the QPC. Indeed, only when the anyons are incident on the QPC is there a simultaneous non-zero tunneling current (due to incoming anyons breaking the particle-hole symmetry at the QPC) and a non-zero edge current (due to the incoming anyons themselves). This means that $\left\langle I_T \tilde{I}_u \right\rangle = \langle I_T \rangle \left\langle \tilde{I}_u \right\rangle$ for $t'' \in (-\infty, t'] \cup [t, +\infty)$ and

hence $\left\langle \delta I_T \delta \tilde{I}_u \right\rangle = 0$ except when $t'' \in [t', t]$. With this in mind, we go ahead with the calculation of the non-equilibrium correlator where the range of the t''-integral is restricted to $[t', t]$:

$$\begin{aligned}\mathcal{C}^u(t^-, t'^{\eta'}) &= \prod_j e^{g_{\alpha j}^2 \mathcal{G}^{-\eta'}(t-t')} \\ &\times \left\langle e^{2\pi i \epsilon g_{\alpha j} g_{\beta j} \sum_{k=1}^N [\theta(t-t_k)-\theta(t'-t_k)]}\ 2\pi q_{\boldsymbol{g_\beta}} \sum_{k=1}^N [\theta(t-t_k)-\theta(t'-t_k)] \right\rangle_{\text{n-eq}} \\ &= \prod_j e^{2g_{\alpha j}^2 \mathcal{G}^{-\eta'}(t-t')}\ 2\pi \frac{\partial}{\partial(i\zeta)} \left\langle e^{i\zeta q_{\boldsymbol{g_\beta}} \sum_{k=1}^N [\theta(t-t_k)-\theta(t'-t_k)]} \right\rangle_{\text{n-eq}} \Bigg|_{\zeta = \frac{2\pi g_{\alpha j} g_{\beta j}}{q_{\boldsymbol{g_\beta}}}}.\end{aligned} \tag{G.13}$$

where we have evaluated the t'' integral. The non-equilibrium correlator above can be easily calculated with the methods of Section 7.3, giving us the upper edge correlator to be:

$$\mathcal{C}^u(t^-, t'^{\eta'}) = \prod_j e^{g_{\alpha j}^2 \mathcal{G}^{-\eta'}(t-t')} \times 2\pi \frac{\partial}{\partial(i\zeta)} e^{-\gamma_u |t-t'| \left(1 - \sum_\beta P_\beta e^{i\gamma q_{\boldsymbol{g_\beta}}}\right)} \Bigg|_{\zeta = \frac{2\pi g_{\alpha j} g_{\beta j}}{q_{\boldsymbol{g_\beta}}}}. \tag{G.14}$$

Subsequently, the derivative is acted on the correlator, yielding the following expression for the non-equilibrium correlator:

$$\begin{aligned}\mathcal{C}^u(t^-, t'^{\eta'}) &= -2\pi\gamma_u |t-t'| \times e^{\delta_{\boldsymbol{g}_\alpha} \mathcal{G}^{-\eta'}(t-t')} \\ &\times e^{\gamma_u |t-t'| \left(1 - \sum_\beta P_\beta e^{i2\pi \boldsymbol{g_\alpha} \cdot \boldsymbol{g_\beta}}\right)} \sum_\beta P_\beta q_{\boldsymbol{g_\beta}} e^{i2\pi \boldsymbol{g_\alpha} \cdot \boldsymbol{g_\beta}}.\end{aligned} \tag{G.15}$$

Plugging the above expression for the upper edge correlator, back into the tunneling current - edge current correlator, we find:

$$\begin{aligned}\left\langle I_T \tilde{I}_u \right\rangle = \sum_\alpha q_{\boldsymbol{g}_\alpha} |\Gamma_{\boldsymbol{g}_\alpha}|^2 \sum_{\eta'} \eta' \sum_\epsilon \epsilon \int dt' e^{2\delta_{\boldsymbol{g}_\alpha} \mathcal{G}^{-\eta'}(0, t-t')} \\ e^{-\gamma_u |t-t'| (1 - \sum_\beta P_\beta e^{2i\pi \boldsymbol{g_\alpha} \cdot \boldsymbol{g_\beta}})} e^{-\gamma_d |t-t'| (1 - \sum_\beta P_\beta e^{-2i\pi \boldsymbol{g_\alpha} \cdot \boldsymbol{g_\beta}})} \\ \gamma_u |t-t'| \sum_\sigma P_\beta q_{\boldsymbol{g_\sigma}} e^{i2\pi \boldsymbol{g_\alpha} \cdot \boldsymbol{g_\sigma}}\end{aligned} \tag{G.16}$$

From this, to arrive at $\left\langle \delta I_T \delta \tilde{I}_u \right\rangle$ it is not too difficult to subtract $\langle I_T \rangle \left\langle \tilde{I}_u \right\rangle$ from the above expression. Indeed, $\langle I_T \rangle$ is simply the first two lines of the above expression (see Equation (7.22)), while $\left\langle \tilde{I}_u \right\rangle$ is calculated from Equation (G.14) by setting $\zeta = 0$. We

hence find:

$$\begin{aligned}\left\langle \delta I_T \delta \tilde{I}_u \right\rangle = \sum_\alpha q_{\boldsymbol{g}_\alpha} |\Gamma_{\boldsymbol{g}_\alpha}|^2 \sum_{\eta'} \eta' \sum_\epsilon \epsilon \int dt' e^{2\delta_{\boldsymbol{g}_\alpha} \mathcal{G}^{-\eta'}(0,t-t')} \\ e^{-\gamma_u |t-t'|(1-\sum_\beta P_\beta e^{2i\pi \boldsymbol{g_\alpha}\cdot\boldsymbol{g_\beta}})} e^{-\gamma_d |t-t'|(1-\sum_\beta P_\beta e^{-2i\pi \boldsymbol{g_\alpha}\cdot\boldsymbol{g_\beta}})} \\ \gamma_u |t-t'| \sum_\sigma P_\beta q_{\boldsymbol{g_\sigma}} \left(1 - e^{i2\pi \boldsymbol{g_\alpha}\cdot\boldsymbol{g_\sigma}}\right)\end{aligned} \tag{G.17}$$

Following the same steps, we can calculate $\left\langle \delta I_T \delta \tilde{I}_d \right\rangle$ which will look quite similar except for some signs.

It is not difficult to see that the above quantities can be expressed as a derivative of the tunneling current (see Equation (7.22)):

$$\left\langle \delta I_T \delta \tilde{I}_u \right\rangle = \sum_\beta q_{\boldsymbol{g_\sigma}} \gamma_u P_\beta \frac{\partial}{\partial(\gamma_u P_\beta)} \langle I_T \rangle \tag{G.18}$$

And similarly,

$$\left\langle \delta I_T \delta \tilde{I}_d \right\rangle = \sum_\beta q_{\boldsymbol{g_\sigma}} \gamma_d P_\beta \frac{\partial}{\partial(\gamma_d P_\beta)} \langle I_T \rangle \tag{G.19}$$

The current cross-correlation is given by

$$\langle \delta I_u \delta I_d \rangle = -\langle S_T \rangle + \left\langle \delta I_T \delta \tilde{I}_u \right\rangle - \left\langle \delta I_T \delta \tilde{I}_d \right\rangle \tag{G.20}$$

Putting these together, we can conveniently express the cross correlation in terms of the tunneling noise and derivatives of the tunneling current

$$\langle \delta I_u \delta I_d \rangle = -\langle S_T \rangle + \sum_\beta q_{\boldsymbol{g_\sigma}} \left(\gamma_u P_\beta \frac{\partial}{\partial(\gamma_u P_\beta)} - \gamma_d P_\beta \frac{\partial}{\partial(\gamma_d P_\beta)} \right) \langle I_T \rangle , \tag{G.21}$$

which generalizes the fluctuation-dissipation theorem quoted in Ref. [33]. This result applied to general Abelian quantum Hall edges. Changing the variables to γ_+, γ_-, this becomes

$$\langle \delta I_u \delta I_d \rangle = -\langle S_T \rangle + \sum_\beta Q_\beta \left(\gamma_+ P_\beta \frac{\partial}{\partial(\gamma_- P_\beta)} + \gamma_- P_\beta \frac{\partial}{\partial(\gamma_+ P_\beta)} \right) \langle I_T \rangle , \tag{G.22}$$

obtaining the result quoted in the main text.

Bibliography

[1] Philip W Anderson. *Basic notions of condensed matter physics*. en. Ed. by Philip W Anderson. London, England: CRC Press, June 2019.

[2] LD Landau. "Theory of phase transformations II. Phys". In: *Z. Sowjet* 11 (1937), p. 545.

[3] LD Landau and EM Lifshitz. *Statistical Physics, Course of Theoretical Physics*. 1965.

[4] K. v. Klitzing, G. Dorda, and M. Pepper. "New Method for High-Accuracy Determination of the Fine-Structure Constant Based on Quantized Hall Resistance". In: *Phys. Rev. Lett.* 45 (6 1980), pp. 494–497. DOI: 10.1103/PhysRevLett.45.494.

[5] D. C. Tsui, H. L. Stormer, and A. C. Gossard. "Two-Dimensional Magnetotransport in the Extreme Quantum Limit". In: *Phys. Rev. Lett.* 48 (22 1982), pp. 1559–1562. DOI: 10.1103/PhysRevLett.48.1559.

[6] Daniel C. Tsui. "Nobel Lecture: Interplay of disorder and interaction in two-dimensional electron gas in intense magnetic fields". In: *Rev. Mod. Phys.* 71 (4 1999), pp. 891–895. DOI: 10.1103/RevModPhys.71.891.

[7] D. J. Thouless et al. "Quantized Hall Conductance in a Two-Dimensional Periodic Potential". In: *Phys. Rev. Lett.* 49 (6 1982), pp. 405–408. DOI: 10.1103/PhysRevLett.49.405.

[8] R. B. Laughlin. "Anomalous Quantum Hall Effect: An Incompressible Quantum Fluid with Fractionally Charged Excitations". In: *Phys. Rev. Lett.* 50 (18 1983), pp. 1395–1398. DOI: 10.1103/PhysRevLett.50.1395.

[9] E. H. Hall. "On a new action of the magnet on electric currents". In: *American Journal of Mathematics* 2 (3 1879), p. 287. DOI: 10.2307/2369245.

[10] Xiao-Gang Wen. "Topological order: From long-range entangled quantum matter to a unified origin of light and electrons". en. In: *ISRN Condens. Matter Phys.* 2013 (Mar. 2013), pp. 1–20.

[11] Xiao-Gang Wen. *Quantum Field Theory of Many-Body Systems: From the Origin of Sound to an Origin of Light and Electrons*. Oxford University Press, Sept. 2007. ISBN: 9780199227259. DOI: 10.1093/acprof:oso/9780199227259.001.0001.

[12] E. Witten. "Quantum field theory and the jones polynomial". In: *Communications in Mathematical Physics* 121 (3 1989), pp. 351–399. DOI: 10.1007/bf01217730.

[13] J. M. Leinaas and J. Myrheim. "On the theory of identical particles". In: *Il Nuovo Cimento B (1971-1996)* 37.1 (1977), pp. 1–23. ISSN: 1826-9877. DOI: 10.1007/BF02727953.

[14] Frank Wilczek. "Quantum Mechanics of Fractional-Spin Particles". In: *Phys. Rev. Lett.* 49 (14 1982), pp. 957–959. DOI: 10.1103/PhysRevLett.49.957.

[15] Daniel Arovas, J. R. Schrieffer, and Frank Wilczek. "Fractional Statistics and the Quantum Hall Effect". In: *Phys. Rev. Lett.* 53 (7 1984), pp. 722–723. DOI: 10.1103/PhysRevLett.53.722.

[16] A. Kitaev. "Fault-tolerant quantum computation by anyons". In: *Annals of Physics* 303 (1 2003), pp. 2–30. DOI: 10.1016/s0003-4916(02)00018-0.

[17] Chetan Nayak et al. "Non-Abelian anyons and topological quantum computation". In: *Rev. Mod. Phys.* 80 (3 2008), pp. 1083–1159. DOI: 10.1103/RevModPhys.80.1083.

[18] R. Willett et al. "Observation of an even-denominator quantum number in the fractional quantum Hall effect". In: *Phys. Rev. Lett.* 59 (15 1987), pp. 1776–1779. DOI: 10.1103/PhysRevLett.59.1776.

[19] G. W. Moore and N. Read. "Nonabelions in the fractional quantum hall effect". In: *Nuclear Physics B* 360 (2-3 1991), pp. 362–396. DOI: 10.1016/0550-3213(91)90407-o.

[20] D E Feldman and Bertrand I Halperin. "Fractional charge and fractional statistics in the quantum Hall effects". In: *Reports on Progress in Physics* 84.7 (2021), p. 076501. DOI: 10.1088/1361-6633/ac03aa.

[21] "The quantum hall effect". In: *Graduate Texts in Contemporary Physics* (1990). DOI: 10.1007/978-1-4612-3350-3.

[22] X. G. Wen. "Electrodynamical properties of gapless edge excitations in the fractional quantum Hall states". In: *Phys. Rev. Lett.* 64 (18 1990), pp. 2206–2209. DOI: 10.1103/PhysRevLett.64.2206.

[23] X. Wen. "Chiral luttinger liquid and the edge excitations in the fractional quantum hall states". In: *Physical Review B* 41 (18 1990), pp. 12838–12844. DOI: 10.1103/physrevb.41.12838.

[24] X. Wen. "Topological orders and edge excitations in fractional quantum hall states". In: *Advances in Physics* 44 (5 1995), pp. 405–473. DOI: 10.1080/00018739500101566.

[25] B. J. van Wees et al. "Quantized conductance of point contacts in a two-dimensional electron gas". In: *Phys. Rev. Lett.* 60 (9 1988), pp. 848–850. DOI: 10.1103/PhysRevLett.60.848.

[26] T. Martin. "Course 5 noise in mesoscopic physics". In: *Nanophysics: Coherence and Transport, École d'Été De Physique Des Houches Session LXXXI* (2005), pp. 283–359. DOI: 10.1016/s0924-8099(05)80047-2.

[27] D. Christian Glattli. "Tunneling Experiments in the Fractional Quantum Hall Effect Regime". In: *The Quantum Hall Effect: Poincaré Seminar 2004*. Ed. by Benoît Douçot et al. Basel: Birkhäuser Basel, 2005, pp. 163–197. ISBN: 978-3-7643-7393-1. DOI: 10.1007/3-7643-7393-8_5.

[28] M. Carrega et al. "Anyons in quantum hall interferometry". In: *Nature Reviews Physics* 3 (10 2021), pp. 698–711. DOI: 10.1038/s42254-021-00351-0.

[29] C. L. Kane and Matthew P. A. Fisher. "Nonequilibrium noise and fractional charge in the quantum Hall effect". In: *Phys. Rev. Lett.* 72 (5 1994), pp. 724–727. DOI: 10.1103/PhysRevLett.72.724.

[30] L. Saminadayar et al. "Observation of the $e/3$ Fractionally Charged Laughlin Quasiparticle". In: *Phys. Rev. Lett.* 79 (13 1997), pp. 2526–2529. DOI: 10.1103/PhysRevLett.79.2526.

[31] R. de Picciotto et al. "Direct observation of a fractional charge". In: *Nature* 389 (6647 1997), pp. 162–164. DOI: 10.1038/38241.

[32] M. Reznikov et al. "Observation of quasiparticles with one-fifth of an electron's charge". In: *Nature* 399 (6733 1999), pp. 238–241. DOI: 10.1038/20384.

[33] Bernd Rosenow, Ivan P. Levkivskyi, and Bertrand I. Halperin. "Current Correlations from a Mesoscopic Anyon Collider". In: *Phys. Rev. Lett.* 116 (15 2016), p. 156802. DOI: 10.1103/PhysRevLett.116.156802.

[34] H. Bartolomei et al. "Fractional statistics in anyon collisions". In: *Science* 368 (6487 2020), pp. 173–177. DOI: 10.1126/science.aaz5601.

[35] C. de C. Chamon et al. "Two point-contact interferometer for quantum Hall systems". In: *Phys. Rev. B* 55 (4 1997), pp. 2331–2343. DOI: 10.1103/PhysRevB.55.2331.

[36] J. Nakamura et al. "Direct observation of anyonic braiding statistics". In: *Nature Physics* 16 (9 2020), pp. 931–936. DOI: 10.1038/s41567-020-1019-1.

[37] M. Ruelle et al. "Comparing Fractional Quantum Hall Laughlin and Jain Topological Orders with the Anyon Collider". In: *Phys. Rev. X* 13 (1 2023), p. 011031. DOI: 10.1103/PhysRevX.13.011031.

[38] P. Glidic et al. "Cross-Correlation Investigation of Anyon Statistics in the $\nu = 1/3$ and 2/5 Fractional Quantum Hall States". In: *Phys. Rev. X* 13 (1 2023), p. 011030. DOI: 10.1103/PhysRevX.13.011030.

[39] J. M. Lee et al. "Partitioning of diluted anyons reveals their braiding statistics". In: *Nature* 617 (7960 2023), pp. 277–281. DOI: 10.1038/s41586-023-05883-2.

[40] J. Nakamura et al. "Fabry-Pérot Interferometry at the $\nu = 2/5$ Fractional Quantum Hall State". In: *Phys. Rev. X* 13 (4 2023), p. 041012. DOI: 10.1103/PhysRevX.13.041012.

[41] Noah L. Samuelson et al. *Anyonic statistics and slow quasiparticle dynamics in a graphene fractional quantum Hall interferometer*. 2024. arXiv: 2403.19628 [cond-mat.mes-hall].

[42] Thomas Werkmeister et al. *Anyon braiding and telegraph noise in a graphene interferometer*. 2024. arXiv: 2403.18983 [cond-mat.mes-hall].

[43] Noam Schiller et al. *Scaling tunnelling noise in the fractional quantum Hall effect tells about renormalization and breakdown of chiral Luttinger liquid*. 2024. arXiv: 2403.17097 [cond-mat.mes-hall].

[44] A. Veillon et al. "Observation of the scaling dimension of fractional quantum hall anyons". In: *Nature* (2024). DOI: 10.1038/s41586-024-07727-z.

[45] Mélanie Ruelle et al. *Time-domain braiding of anyons*. 2024. arXiv: 2409.08685 [cond-mat.mes-hall].

[46] B. I. Halperin. "Statistics of Quasiparticles and the Hierarchy of Fractional Quantized Hall States". In: *Phys. Rev. Lett.* 52 (18 1984), pp. 1583–1586. DOI: 10.1103/PhysRevLett.52.1583.

[47] J. K. Jain. "Composite-fermion approach for the fractional quantum Hall effect". In: *Phys. Rev. Lett.* 63 (2 1989), pp. 199–202. DOI: 10.1103/PhysRevLett.63.199.

[48] O. Shtanko, K. Snizhko, and V. Cheianov. "Nonequilibrium noise in transport across a tunneling contact between $\nu = \frac{2}{3}$ fractional quantum Hall edges". In: *Phys. Rev. B* 89 (12 2014), p. 125104. DOI: 10.1103/PhysRevB.89.125104.

[49] Y. C. Chung, M. Heiblum, and V. Umansky. "Scattering of Bunched Fractionally Charged Quasiparticles". en. In: *Physical Review Letters* 91.21 (Nov. 2003), p. 216804. ISSN: 0031-9007, 1079-7114. DOI: 10.1103/PhysRevLett.91.216804.

[50] Aveek Bid et al. "Shot Noise and Charge at the 2/3 Composite Fractional Quantum Hall State". In: *Phys. Rev. Lett.* 103 (23 2009), p. 236802. DOI: 10.1103/PhysRevLett.103.236802.

[51] M. Dolev et al. "Dependence of the tunneling quasiparticle charge determined via shot noise measurements on the tunneling barrier and energetics". In: *Phys. Rev. B* 81 (16 2010), p. 161303. DOI: 10.1103/PhysRevB.81.161303.

[52] S. Biswas et al. "Shot noise does not always provide the quasiparticle charge". In: *Nature Physics* 18 (12 2022), pp. 1476–1481. DOI: 10.1038/s41567-022-01758-x.

[53] T. Ando, A. B. Fowler, and F. Stern. "Electronic properties of two-dimensional systems". In: *Reviews of Modern Physics* 54 (2 1982), pp. 437–672. DOI: 10.1103/revmodphys.54.437.

[54] P. Drude. "Zur elektronentheorie der metalle". In: *Annalen Der Physik* 306 (3 1900), pp. 566–613. DOI: 10.1002/andp.19003060312.

[55] F. D. M. Haldane. "Fractional Quantization of the Hall Effect: A Hierarchy of Incompressible Quantum Fluid States". In: *Phys. Rev. Lett.* 51 (7 1983), pp. 605–608. DOI: 10.1103/PhysRevLett.51.605.

[56] Gerald V. Dunne. *Aspects of Chern-Simons Theory*. 1999. arXiv: hep-th/9902115 [hep-th].

[57] David Tong. *Lectures on the Quantum Hall Effect*. 2016. arXiv: 1606.06687 [hep-th].

[58] Ganpathy Murthy. *Lectures on quantum Hall effect*. https://www.icts.res.in/event/page/26665. 2023.

[59] A. Bid et al. "Observation of neutral modes in the fractional quantum hall regime". In: *Nature* 466 (7306 2010), pp. 585–590. DOI: 10.1038/nature09277.

[60] Murray Gell-Mann and Francis Low. "Bound States in Quantum Field Theory". In: *Phys. Rev.* 84 (2 1951), pp. 350–354. DOI: 10.1103/PhysRev.84.350.

[61] G. Nenciu and G. Rasche. "Adiabatic theorem and Gell-Mann-Low formula". In: *Helvetica Physica Acta* 62.4 (1989), pp. 372–388.

[62] L. V. Keldysh. "Diagram technique for nonequilibrium processes". In: *Zh. Eksp. Teor. Fiz.* 47 (1964), pp. 1515–1527.

[63] L.P. Kadanoff and G. Baym. *Quantum Statistical Mechanics*. New York: W.A. Benjamin Inc., 1962.

[64] W. Schottky. "Über spontane stromschwankungen in verschiedenen elektrizitätsleitern". In: *Annalen Der Physik* 362 (23 1918), pp. 541–567. DOI: 10.1002/andp.19183622304.

[65] R. Bisognin et al. "Microwave photons emitted by fractionally charged quasiparticles". In: *Nature Communications* 10 (1 2019). DOI: 10.1038/s41467-019-09758-x.

[66] M. Kapfer et al. "A josephson relation for fractionally charged anyons". In: *Science* 363 (6429 2019), pp. 846–849. DOI: 10.1126/science.aau3539.

[67] V. J. Goldman and B. Su. "Resonant tunneling in the quantum hall regime: measurement of fractional charge". In: *Science* 267 (5200 1995), pp. 1010–1012. DOI: 10.1126/science.267.5200.1010.

[68] D. Ferraro et al. "Charge tunneling in fractional edge channels". en. In: *Physical Review B* 82.8 (Aug. 2010), p. 085323. ISSN: 1098-0121, 1550-235X. DOI: 10.1103/PhysRevB.82.085323.

[69] D. Ferraro et al. "Relevance of Multiple Quasiparticle Tunneling between Edge States at $\nu = p/(2np+1)$". en. In: *Physical Review Letters* 101.16 (Oct. 2008), p. 166805. ISSN: 0031-9007, 1079-7114. DOI: 10.1103/PhysRevLett.101.166805.

[70] D Ferraro et al. "Finite-frequency noise for edge states at a filling factor $\nu = 2/5$". In: *Physica Scripta* 2012.T151 (2012), p. 014025. DOI: 10.1088/0031-8949/2012/T151/014025.

[71] J. Rech et al. "Negative Delta-T Noise in the Fractional Quantum Hall Effect". In: *Phys. Rev. Lett.* 125 (8 2020), p. 086801. DOI: 10.1103/PhysRevLett.125.086801.

[72] Hiromi Ebisu, Noam Schiller, and Yuval Oreg. "Fluctuations in Heat Current and Scaling Dimension". In: *Phys. Rev. Lett.* 128 (21 2022), p. 215901. DOI: 10.1103/PhysRevLett.128.215901.

[73] Bruno Bertin-Johannet et al. "Photoassisted current in the fractional quantum Hall effect as a probe of the quasiparticle operator scaling dimension". In: *Phys. Rev. B* 108 (16 2023), p. 165425. DOI: 10.1103/PhysRevB.108.165425.

[74] Matteo Acciai, Gu Zhang, and Christian Spånslätt. *Role of scaling dimensions in generalized noises in fractional quantum Hall tunneling due to a temperature bias*. 2024. arXiv: 2408.04525 [cond-mat.mes-hall].

[75] Kyrylo Snizhko and Vadim Cheianov. "Scaling dimension of quantum Hall quasiparticles from tunneling-current noise measurements". In: *Phys. Rev. B* 91 (19 2015), p. 195151. DOI: 10.1103/PhysRevB.91.195151.

[76] Noam Schiller, Yuval Oreg, and Kyrylo Snizhko. "Extracting the scaling dimension of quantum Hall quasiparticles from current correlations". In: *Phys. Rev. B* 105 (16 2022), p. 165150. DOI: 10.1103/PhysRevB.105.165150.

[77] T. Jonckheere et al. "Anyonic Statistics Revealed by the Hong-Ou-Mandel Dip for Fractional Excitations". In: *Phys. Rev. Lett.* 130 (18 2023), p. 186203. DOI: 10.1103/PhysRevLett.130.186203.

[78] I. Safi, P. Devillard, and T. Martin. "Partition Noise and Statistics in the Fractional Quantum Hall Effect". In: *Phys. Rev. Lett.* 86 (20 2001), pp. 4628–4631. DOI: 10.1103/PhysRevLett.86.4628.

[79] Smitha Vishveshwara. "Revisiting the Hanbury Brown–Twiss Setup for Fractional Statistics". In: *Phys. Rev. Lett.* 91 (19 2003), p. 196803. DOI: 10.1103/PhysRevLett.91.196803.

[80] Smitha Vishveshwara and N. R. Cooper. "Correlations and beam splitters for quantum Hall anyons". In: *Phys. Rev. B* 81 (20 2010), p. 201306. DOI: 10.1103/PhysRevB.81.201306.

[81] Gabriele Campagnano et al. "Hanbury Brown–Twiss Interference of Anyons". In: *Phys. Rev. Lett.* 109 (10 2012), p. 106802. DOI: 10.1103/PhysRevLett.109.106802.

[82] Gabriele Campagnano et al. "Hanbury Brown and Twiss correlations in quantum Hall systems". In: *Phys. Rev. B* 88 (23 2013), p. 235415. DOI: 10.1103/PhysRevB.88.235415.

[83] Christophe Mora. *Anyonic exchange in a beam splitter*. 2022. arXiv: 2212.05123 [cond-mat.mes-hall].

[84] K. T. Law, D. E. Feldman, and Yuval Gefen. "Electronic Mach-Zehnder interferometer as a tool to probe fractional statistics". In: *Phys. Rev. B* 74 (4 2006), p. 045319. DOI: 10.1103/PhysRevB.74.045319.

[85] H. K. Kundu et al. "Anyonic interference and braiding phase in a mach-zehnder interferometer". In: *Nature Physics* 19 (4 2023), pp. 515–521. DOI: 10.1038/s41567-022-01899-z.

[86] Byeongmok Lee, Cheolhee Han, and H.-S. Sim. "Negative Excess Shot Noise by Anyon Braiding". In: *Phys. Rev. Lett.* 123 (1 2019), p. 016803. DOI: 10.1103/PhysRevLett.123.016803.

[87] J. M. Lee and H. S. Sim. "Non-abelian anyon collider". In: *Nature Communications* 13 (1 2022). DOI: 10.1038/s41467-022-34329-y.

[88] Gabriel Gasse et al. "Observation of quantum oscillations in the photoassisted shot noise of a tunnel junction". In: *Phys. Rev. B* 88 (24 2013), p. 241402. DOI: 10.1103/PhysRevB.88.241402.

[89] L.-H. Reydellet et al. "Quantum Partition Noise of Photon-Created Electron-Hole Pairs". In: *Phys. Rev. Lett.* 90 (17 2003), p. 176803. DOI: 10.1103/PhysRevLett.90.176803.

[90] R. J. Schoelkopf et al. "Observation of "Photon-Assisted" Shot Noise in a Phase-Coherent Conductor". In: *Phys. Rev. Lett.* 80 (11 1998), pp. 2437–2440. DOI: 10.1103/PhysRevLett.80.2437.

[91] Gordey B. Lesovik, Thierry Martin, and Julien Torrès. "Josephson frequency singularity in the noise of normal-metal–superconductor junctions". In: *Phys. Rev. B* 60 (17 1999), pp. 11935–11938. DOI: 10.1103/PhysRevB.60.11935.

[92] A. A. Kozhevnikov, R. J. Schoelkopf, and D. E. Prober. "Observation of Photon-Assisted Noise in a Diffusive Normal Metal–Superconductor Junction". In: *Phys. Rev. Lett.* 84 (15 2000), pp. 3398–3401. DOI: 10.1103/PhysRevLett.84.3398.

[93] C. de C. Chamon, D. E. Freed, and X. G. Wen. "Tunneling and quantum noise in one-dimensional Luttinger liquids". In: *Phys. Rev. B* 51 (4 1995), pp. 2363–2379. DOI: 10.1103/PhysRevB.51.2363.

[94] Xiao-Gang Wen. "Edge transport properties of the fractional quantum Hall states and weak-impurity scattering of a one-dimensional charge-density wave". In: *Phys. Rev. B* 44 (11 1991), pp. 5708–5719. DOI: 10.1103/PhysRevB.44.5708.

[95] I. Safi and E. V. Sukhorukov. "Determination of tunneling charge via current measurements". In: *Europhysics Letters* 91.6 (2010), p. 67008. DOI: 10.1209/0295-5075/91/67008.

[96] Adeline Crépieux, Pierre Devillard, and Thierry Martin. "Photoassisted current and shot noise in the fractional quantum Hall effect". In: *Phys. Rev. B* 69 (20 2004), p. 205302. DOI: 10.1103/PhysRevB.69.205302.

[97] P. K. Tien and J. P. Gordon. "Multiphoton Process Observed in the Interaction of Microwave Fields with the Tunneling between Superconductor Films". In: *Phys. Rev.* 129 (2 1963), pp. 647–651. DOI: 10.1103/PhysRev.129.647.

[98] J. Keeling, I. Klich, and L. S. Levitov. "Minimal Excitation States of Electrons in One-Dimensional Wires". In: *Phys. Rev. Lett.* 97 (11 2006), p. 116403. DOI: 10.1103/PhysRevLett.97.116403.

[99] J. Rech et al. "Minimal Excitations in the Fractional Quantum Hall Regime". In: *Phys. Rev. Lett.* 118 (7 2017), p. 076801. DOI: 10.1103/PhysRevLett.118.076801.

[100] Inès Safi. "Driven strongly correlated quantum circuits and Hall edge states: Unified photoassisted noise and revisited minimal excitations". In: *Phys. Rev. B* 106 (20 2022), p. 205130. DOI: 10.1103/PhysRevB.106.205130.

[101] M. Tinkham. *Introduction to Superconductivity*. International series in pure and applied physics. McGraw Hill, 1996. ISBN: 9780070648784.

[102] J. C. Cuevas, A. Martín-Rodero, and A. Levy Yeyati. "Hamiltonian approach to the transport properties of superconducting quantum point contacts". In: *Phys. Rev. B* 54 (10 1996), pp. 7366–7379. DOI: 10.1103/PhysRevB.54.7366.

[103] T. Jonckheere et al. "Multipair dc Josephson resonances in a biased all-superconducting bijunction". In: *Phys. Rev. B* 87 (21 2013), p. 214501. DOI: 10.1103/PhysRevB.87.214501.

[104] Thierry Martin. "Wave packet approach to noise in NS junctions". In: *Physics Letters A* 220.1 (1996), pp. 137–142. ISSN: 0375-9601. DOI: https://doi.org/10.1016/0375-9601(96)00484-7.

[105] Patrik Recher, Eugene V. Sukhorukov, and Daniel Loss. "Andreev tunneling, Coulomb blockade, and resonant transport of nonlocal spin-entangled electrons". In: *Phys. Rev. B* 63 (16 2001), p. 165314. DOI: 10.1103/PhysRevB.63.165314.

[106] Olivier Sauret, Denis Feinberg, and Thierry Martin. "Quantum master equations for the superconductor–quantum dot entangler". In: *Phys. Rev. B* 70 (24 2004), p. 245313. DOI: 10.1103/PhysRevB.70.245313.

[107] D. Chevallier et al. "Current and noise correlations in a double-dot Cooper-pair beam splitter". In: *Phys. Rev. B* 83 (12 2011), p. 125421. DOI: 10.1103/PhysRevB.83.125421.

[108] B. Pannetier and H. Courtois. "Andreev Reflection and Proximity effect". In: *Journal of Low Temperature Physics* 118 (5/6 2000), pp. 599–615. DOI: 10.1023/a:1004635226825.

[109] C. L. Kane and Matthew P. A. Fisher. "Shot noise and the transmission of dilute Laughlin quasiparticles". In: *Phys. Rev. B* 67 (4 2003), p. 045307. DOI: 10.1103/PhysRevB.67.045307.

[110] E. Bocquillon et al. "Electron quantum optics in ballistic chiral conductors". In: *Annalen Der Physik* 526 (1-2 2013), pp. 1–30. DOI: 10.1002/andp.201300181.

[111] C. Grenier et al. "Electron quantum optics in quantum hall edge channels". In: *Modern Physics Letters B* 25 (12n13 2011), pp. 1053–1073. DOI: 10.1142/s0217984911026772.

[112] E. Comforti et al. "Bunching of fractionally charged quasiparticles tunnelling through high-potential barriers". In: *Nature* 416 (6880 2002), pp. 515–518. DOI: 10.1038/416515a.

[113] Y. C. Chung et al. "Anomalous chiral Luttinger liquid behavior of diluted fractionally charged quasiparticles". In: *Phys. Rev. B* 67 (20 2003), p. 201104. DOI: 10.1103/PhysRevB.67.201104.

[114] P. Glidic et al. "Quasiparticle andreev scattering in the $\nu = 1/3$ fractional quantum hall regime". In: *Nature Communications* 14 (1 2023). DOI: 10.1038/s41467-023-36080-4.

[115] Nancy P. Sandler, Claudio de C. Chamon, and Eduardo Fradkin. "Andreev reflection in the fractional quantum Hall effect". In: *Phys. Rev. B* 57 (19 1998), pp. 12324–12332. DOI: 10.1103/PhysRevB.57.12324.

[116] M. Hashisaka et al. "Andreev reflection of fractional quantum Hall quasiparticles". In: *Nature Communications* 12.1 (2021), p. 2794. ISSN: 2041-1723. DOI: 10.1038/s41467-021-23160-6.

[117] I. Safi and H. J. Schulz. "Transport in an inhomogeneous interacting one-dimensional system". In: *Phys. Rev. B* 52 (24 1995), R17040–R17043. DOI: 10.1103/PhysRevB.52.R17040.

[118] Dmitrii L. Maslov and Michael Stone. "Landauer conductance of Luttinger liquids with leads". In: *Phys. Rev. B* 52 (8 1995), R5539–R5542. DOI: 10.1103/PhysRevB.52.R5539.

[119] Liam A. Cohen et al. "Universal chiral Luttinger liquid behavior in a graphene fractional quantum Hall point contact". In: *Science* 382.6670 (2023), pp. 542–547. DOI: 10.1126/science.adf9728. eprint: https://www.science.org/doi/pdf/10.1126/science.adf9728.

[120] Ivan P. Levkivskyi. "Universal nonequilibrium states at the fractional quantum Hall edge". In: *Phys. Rev. B* 93 (16 2016), p. 165427. DOI: 10.1103/PhysRevB.93.165427.

[121] C. Han et al. "Topological vacuum bubbles by anyon braiding". In: *Nature Communications* 7 (1 2016). DOI: 10.1038/ncomms11131.

[122] Tom Morel et al. "Fractionalization and anyonic statistics in the integer quantum Hall collider". In: *Phys. Rev. B* 105 (7 2022), p. 075433. DOI: 10.1103/PhysRevB.105.075433.

[123] Gu Zhang et al. *Fractional-statistics-induced entanglement from Andreev-like tunneling*. 2023. arXiv: 2312.16556 [cond-mat.mes-hall].

[124] G. Zhang et al. "Measuring statistics-induced entanglement entropy with a hong–ou–mandel interferometer". In: *Nature Communications* 15 (1 2024). DOI: 10.1038/s41467-024-47335-z.

[125] I. S. Gradshteyn et al. "Table of integrals, series, and products". In: (2015). DOI: 10.1016/c2010-0-64839-5.

[126] K. Iyer et al. "Quasiparticle Andreev reflection in the Laughlin fractions of the fractional quantum Hall effect". In: *Phys. Rev. B* 108 (15 2023), p. 155404. DOI: 10.1103/PhysRevB.108.155404.

[127] G. B. Lesovik and R. Loosen. "On the detection of finite-frequency current fluctuations". In: *Journal of Experimental and Theoretical Physics Letters* 65 (3 1997), pp. 295–299. DOI: 10.1134/1.567363.

[128] U. Gavish, Y. Levinson, and Y. Imry. "Detection of quantum noise". In: *Phys. Rev. B* 62 (16 2000), R10637–R10640. DOI: 10.1103/PhysRevB.62.R10637.

[129] LD Landau and EM Lifshitz. "JB Sykes, JS Bell, and ME Rose. Quantum mechanics, non-relativistic theory: Vol. 3 of course of theoretical physics". In: *Physics Today* 11 (1958), p. 56.

[130] Ramón Aguado and Leo P. Kouwenhoven. "Double Quantum Dots as Detectors of High-Frequency Quantum Noise in Mesoscopic Conductors". In: *Phys. Rev. Lett.* 84 (9 2000), pp. 1986–1989. DOI: 10.1103/PhysRevLett.84.1986.

[131] A. Mahé et al. "Current correlations of an on-demand single-electron emitter". In: *Phys. Rev. B* 82 (20 2010), p. 201309. DOI: 10.1103/PhysRevB.82.201309.

[132] Audrey Cottet, and Wolfgang Belzig. "Finite Frequency Noise of a Superconductor-Ferromagnet Quantum Point Contact". In: *Phys. Rev. Lett.* 101 (25 2008), p. 257001. DOI: 10.1103/PhysRevLett.101.257001.

[133] P.-M. Billangeon et al. "Emission and Absorption Asymmetry in the Quantum Noise of a Josephson Junction". In: *Phys. Rev. Lett.* 96 (13 2006), p. 136804. DOI: 10.1103/PhysRevLett.96.136804.

[134] R. Deblock et al. "Detection of quantum noise from an electrically driven two-level system". In: *Science* 301 (5630 2003), pp. 203–206. DOI: 10.1126/science.1084175.

[135] J. Basset et al. "Measurement of Quantum Noise in a Carbon Nanotube Quantum Dot in the Kondo Regime". In: *Phys. Rev. Lett.* 108 (4 2012), p. 046802. DOI: 10.1103/PhysRevLett.108.046802.

[136] O. Shein-Lumbroso et al. "Electronic noise due to temperature differences in atomic-scale junctions". In: *Nature* 562 (7726 2018), pp. 240–244. DOI: 10.1038/s41586-018-0592-2.

[137] Samuel Larocque et al. "Shot Noise of a Temperature-Biased Tunnel Junction". In: *Phys. Rev. Lett.* 125 (10 2020), p. 106801. DOI: 10.1103/PhysRevLett.125.106801.

[138] E. Sivre et al. "Electronic heat flow and thermal shot noise in quantum circuits". In: *Nature Communications* 10 (1 2019), p. 257001. DOI: 10.1038/s41467-019-13566-8.

[139] Ludovico Tesser et al. "Charge, spin, and heat shot noises in the absence of average currents: Conditions on bounds at zero and finite frequencies". In: *Phys. Rev. B* 107 (7 2023), p. 075409. DOI: 10.1103/PhysRevB.107.075409.

[140] Jakob Eriksson et al. "General Bounds on Electronic Shot Noise in the Absence of Currents". In: *Phys. Rev. Lett.* 127 (13 2021), p. 136801. DOI: 10.1103/PhysRevLett.127.136801.

[141] Masahiro Hasegawa and Keiji Saito. "Delta-T noise in the Kondo regime". In: *Phys. Rev. B* 103 (4 2021), p. 045409. DOI: 10.1103/PhysRevB.103.045409.

[142] A. Mu et al. "Origin of the anomalous electronic shot noise in atomic-scale junctions". In: *The Journal of Physical Chemistry C* 123 (39 2019), pp. 23853–23862. DOI: 10.1021/acs.jpcc.9b06766.

[143] A. Popoff et al. "Scattering theory of non-equilibrium noise and delta t current fluctuations through a quantum dot". In: *Journal of Physics: Condensed Matter* 34 (18 2022), p. 185301. DOI: 10.1088/1361-648x/ac5200.

[144] Giacomo Rebora et al. "Delta-T noise for fractional quantum Hall states at different filling factor". In: *Phys. Rev. Res.* 4 (4 2022), p. 043191. DOI: 10.1103/PhysRevResearch.4.043191.

[145] Gu Zhang, Igor V. Gornyi, and Christian Spånslätt. "Delta-T noise for weak tunneling in one-dimensional systems: Interactions versus quantum statistics". In: *Phys. Rev. B* 105 (19 2022), p. 195423. DOI: 10.1103/PhysRevB.105.195423.

[146] K. Iyer et al. "Colored delta-T noise in fractional quantum Hall liquids". In: *Phys. Rev. B* 108 (24 2023), p. 245427. DOI: 10.1103/PhysRevB.108.245427.

[147] K. Schwab et al. "Measurement of the quantum of thermal conductance". In: *Nature* 404.6781 (25 2000), pp. 974–977. ISSN: 1476-4687. DOI: 10.1038/35010065.

[148] Mitali Banerjee et al. "Observed quantization of anyonic heat flow". In: *Nature* 545.7652 (25 Apr. 2017), 75–79. ISSN: 1476-4687. DOI: 10.1038/nature22052.

[149] Gwendal Fève. *Private communication.* 2008. DOI: 10.1103/PhysRevLett.101.257001.

[150] D. E. Feldman and Moty Heiblum. "Why a noninteracting model works for shot noise in fractional charge experiments". In: *Phys. Rev. B* 95 (11 2017), p. 115308. DOI: 10.1103/PhysRevB.95.115308.

[151] Emiliano Papa and A. H. MacDonald. "Interactions Suppress Quasiparticle Tunneling at Hall Bar Constrictions". In: *Phys. Rev. Lett.* 93 (12 2004), p. 126801. DOI: 10.1103/PhysRevLett.93.126801.

[152] Noam Schiller et al. *Scaling tunnelling noise in the fractional quantum Hall effect tells about renormalization and breakdown of chiral Luttinger liquid.* 2024. DOI: 10.1103/PhysRevLett.101.257001. arXiv: 2403.17097 [cond-mat.mes-hall].

[153] Noam Schiller et al. "Anyon Statistics through Conductance Measurements of Time-Domain Interferometry". In: *Phys. Rev. Lett.* 131 (18 2023), p. 186601. DOI: 10.1103/PhysRevLett.131.186601.

[154] G. Last and M. D. Penrose. "Lectures on the poisson process". In: *Phys. Rev. Lett.* 101 (25 2017), p. 257001. DOI: 10.1017/9781316104477.

[155] C. L. Kane, Matthew P. A. Fisher, and J. Polchinski. "Randomness at the edge: Theory of quantum Hall transport at filling ν=2/3". In: *Phys. Rev. Lett.* 72 (26 1994), pp. 4129–4132. DOI: 10.1103/PhysRevLett.72.4129.

[156] C. L. Kane and Matthew P. A. Fisher. "Impurity scattering and transport of fractional quantum Hall edge states". In: *Phys. Rev. B* 51 (19 1995), pp. 13449–13466. DOI: 10.1103/PhysRevB.51.13449.

[157] T. Martin and R. Landauer. "Wave-packet approach to noise in multichannel mesoscopic systems". In: *Physical Review B* 45 (4 1992), pp. 1742–1755. DOI: 10.1103/physrevb.45.1742.

[158] J. M. Lee et al. "Partitioning of diluted anyons reveals their braiding statistics". In: *Nature* 617 (7960 2023), pp. 277–281. DOI: 10.1038/s41586-023-05883-2.

[159] Matthias Thamm and Bernd Rosenow. "Effect of the Soliton Width on Nonequilibrium Exchange Phases of Anyons". In: *Phys. Rev. Lett.* 132 (15 2024), p. 156501. DOI: 10.1103/PhysRevLett.132.156501.

[160] Hermann Edlbauer et al. "Semiconductor-based electron flying qubits: review on recent progress accelerated by numerical modelling". In: *EPJ Quantum Technology* 9.1 (25 Aug. 2022), p. 257001. ISSN: 2196-0763. DOI: 10.1140/epjqt/s40507-022-00139-w.

[161] Lucile Savary and Leon Balents. "Quantum spin liquids: a review". In: *Reports on Progress in Physics* 80.1 (25 2016), p. 016502. DOI: 10.1088/0034-4885/80/1/016502.

[162] Kai Klocke et al. "Time-Domain Anyon Interferometry in Kitaev Honeycomb Spin Liquids and Beyond". In: *Phys. Rev. Lett.* 126 (17 2021), p. 177204. DOI: 10.1103/PhysRevLett.126.177204.

[163] Kai Klocke et al. "Thermal Probes of Phonon-Coupled Kitaev Spin Liquids: From Accurate Extraction of Quantized Edge Transport to Anyon Interferometry". In: *Phys. Rev. X* 12 (1 2022), p. 011034. DOI: 10.1103/PhysRevX.12.011034.

[164] Yue Liu et al. "Dynamical Anyon Generation in Kitaev Honeycomb Non-Abelian Spin Liquids". In: *Phys. Rev. Lett.* 129 (3 2022), p. 037201. DOI: 10.1103/PhysRevLett.129.037201.

[165] M. McGinley, M. Fava, and S. A. Parameswaran. "Anomalous thermal relaxation and pump-probe spectroscopy of two-dimensional topologically ordered systems". In: *Physical Review B* 109 (7 2024), p. 257001. DOI: 10.1103/physrevb.109.075108.

[166] M. McGinley, M. Fava, and S. Parameswaran. "Signatures of fractional statistics in nonlinear pump-probe spectroscopy". In: *Physical Review Letters* 132 (6 2024), p. 257001. DOI: 10.1103/physrevlett.132.066702.

[167] Paul Fendley, Matthew P. A. Fisher, and Chetan Nayak. "Dynamical Disentanglement across a Point Contact in a Non-Abelian Quantum Hall State". In: *Phys. Rev. Lett.* 97 (3 2006), p. 036801. DOI: 10.1103/PhysRevLett.97.036801.

[168] Paul Fendley, Matthew P. A. Fisher, and Chetan Nayak. "Edge states and tunneling of non-Abelian quasiparticles in the $\nu = 52$ quantum Hall state and $p + ip$ superconductors". In: *Phys. Rev. B* 75 (4 2007), p. 045317. DOI: 10.1103/PhysRevB.75.045317.

[169] S. A. Parameswaran, R. Roy, and S. L. Sondhi. "Fractional quantum hall physics in topological flat bands". In: *Comptes Rendus. Physique* 14 (9-10 2013), pp. 816–839. DOI: 10.1016/j.crhy.2013.04.003.

[170] Z. Liu and E. J. Bergholtz. "Recent developments in fractional chern insulators". In: *Encyclopedia of Condensed Matter Physics* 101 (25 2024), pp. 515–538. DOI: 10.1016/b978-0-323-90800-9.00136-0.

[171] Patrick J. Ledwith, Ashvin Vishwanath, and Daniel E. Parker. "Vortexability: A unifying criterion for ideal fractional Chern insulators". In: *Phys. Rev. B* 108 (20 2023), p. 205144. DOI: 10.1103/PhysRevB.108.205144.

[172] David Tong. *Gauge Theory*. 2008. DOI: 10.1103/PhysRevLett.101.257001.